UNIVERSITY of CALIFORNIA
Santa Barbara

Topological Quantum Computing with Majorana Zero Modes and Beyond

A dissertation submitted in partial satisfaction of the
requirements for the degree of

Doctor of Philosophy

in

Physics

by

Christina Paulsen Knapp

Committee in charge:

Professor Chetan Nayak, Chair

Professor Leon Balents

Professor Andrea F. Young

June 2019

The dissertation of Christina Paulsen Knapp is approved:

Professor Leon Balents

Professor Andrea F. Young

Professor Chetan Nayak, Chair

June 2019

Of course it is happening in your head, Harry, but why on earth should that mean it is not real?
-J.K. Rowling, *Harry Potter and the Deathly Hallows*

To my grandparents, John and Betsy Tower, and Harold and Barbara Knapp,
for instilling in me the value of learning.

Acknowledgements

I am immensely grateful to many people for making graduate school a successful and enjoyable experience.

First, I would like to thank my advisor Chetan Nayak for introducing me to the field of topological phases and for his patience and guidance throughout my Ph.D. Chetan's balance of providing direction when necessary and encouraging independence when possible has been essential for my growth as a physicist. His good humor and breadth of expertise has fostered a particularly fun and vibrant group that I feel incredibly fortunate to have joined.

Next, I would like to thank Parsa Bonderson, who has in many ways acted as my unofficial co-advisor. In addition to leading me deeper into diagrammatic calculus than I ever anticipated I would dive, Parsa's meticulous revisions of paper drafts and practice talks have held me to a higher standard than I would have otherwise achieved. I am indebted to him for hours of career advice, scientific guidance, and social commentary.

I am extremely grateful to my committee members Leon Balents and Andrea Young for their time and advice. Leon's group meetings have provided me a glimpse into the greater world of topological physics. Andrea graciously welcomed me onto a project that introduced me to the wizardry of graphene experiments and significantly broadened my research directions.

I have been extraordinarily fortunate to work with and learn from numerous collaborators. Roman Lutchyn has advised me on several projects, extensively improved my familiarity with field theory, and been a driving force behind my participation in Majorana-based research. Torsten Karzig has been an MVP coauthor, providing lively discussions and reinvigorating my interest in projects at their dullest moments. Dima Pikulin's optimistic demeanor and grasp of mesoscopic physics, combined with Michael Beverland's fault tolerance perspective led to a particularly enjoyable collaboration. My foray into fractional Chern insulator physics would not have been possible without Mike Zaletel's expertise and enthusiasm; his mentorship let to a fascinating project with many interesting future directions. Discussions with Eric Spanton have sharpened my understanding of "experimental accessibility" and improved my intuition for a new system. Meng Cheng and Dong Liu were extremely helpful, and patient, collaborators on my first project. Kaushal Patel endured my frenzied calculations of anyonic entanglement entropies for years and was a calm check on my descent into diagrammatic madness. I continue to learn and benefit from working with Jukka Vayrynen and Dave Aasen.

My graduate school experience has been shaped by the past and present Station Q community. My unofficial office in the seminar room has led to many helpful and interesting discussions with Zhenghan Wang, Bela Bauer, Michael Freedman, Chao-Ming Jian, Maissam Barkeshli, David Clarke, Andrey Antipov, and Anna Keselman. I am particularly grateful for Jen Cano's mentorship, and to all the Q and UCSB graduate students for helpful discussions and a collaborative environment. Every day in Elings has been brightened by Sean Fraer's friendly greeting and organizational mastery.

Finally, I have been supported throughout the last six years and my entire life by an amazing network of friends and family. Their love, encouragement, and much-needed distractions have made me a healthier, happier, and better person.

Curriculum Vitæ

Christina Paulsen Knapp

Education

2019	Ph.D. in Physics (expected), University of California, Santa Barbara Advisor: Chetan Nayak
2016	M.A. in Physics, University of California, Santa Barbara Advisor: Chetan Nayak
2013	B.A. in Physics (highest honors) & Math, Williams College, Williamstown, MA Advisor: William K. Wootters

Awards

2016-2018	NSF Graduate Research Fellow
2016-2019	Outstanding Service to the Department, UCSB Physics
2014	Oustanding Teaching Assistant, UCSB Physics
2013	Ferrando-Fithian Award, UCSB Physics
2013	Phi Beta Kappa and Sigma Xi Honor Societies

Publications

"Fractional Chern insulator edge states and layer-resolved lattice contacts," Christina Knapp, Eric M. Spanton, Andrea F. Young, Chetan Nayak, and Michael P. Zaletel. *Physical Review B* 99, 081114 (2019), arXiv:1810.02325.

"Modeling noise and error correction for Majorana-based quantum computing," Christina Knapp, Michael Beverland, Dmitry I. Pikulin, and Torsten Karzig. *Quantum* 2, 88 (2018), arXiv:1806.01275.

"Dephasing of Majorana-based qubits," Christina Knapp, Torsten Karzig, Roman Lutchyn, and Chetan Nayak. *Physical Review B* 97, 125404 (2018), arXiv:1711.03968.

"Anyonic Entanglement and Topological Entanglement Entropy," Parsa Bonderson, Christina Knapp, and Kaushal Patel. *Annals of Physics* 385 (2017), arXiv:1706.09420.

"Scalable Designs for Quasiparticle-Poisoning-Protected Topological Quantum Computation with Majorana Zero Modes," Torsten Karzig, Christina Knapp, Roman Lutchyn, Parsa Bonderson, Matthew Hastings, Chetan Nayak, Jason Alicea, Karsten Flensberg, Stephan Plugge, Yuval Oreg, Charles Marcus, and Michael Freedman. *Physical Review B* 95, 235305 (2017), arXiv:1610.05289.

"Nature and Correction of Diabatic Errors in Anyon Braiding," Christina Knapp, Michael P. Zaletel, Dong E. Liu, Meng Cheng, Parsa Bonderson, and Chetan Nayak. *Physical Review X* 6, 041003 (2016), arXiv:1601.05790.

Abstract

Topological Quantum Computing with Majorana Zero Modes and Beyond

by

Christina Paulsen Knapp

Topological quantum computing seeks to store and manipulate information in a protected manner using topological phases of matter. Information encoded in the degenerate state space of pairs of non-Abelian anyons or defects is robust to local perturbations, reducing its susceptiblity to environmental errors and potentially providing a scalable approach to quantum computing. However, topological quantum computing faces significant challenges, not least of which is identifying an experimentally accessible platform supporting non-Abelian topological physics. In this thesis, we critically analyze topological quantum computing with Majorana zero modes, non-Abelian defects of a topological superconductor. We identify intrinsic error sources for Majorana-based systems and propose quantum computing architectures that minimize their effects. Additionally, we consider a new approach for realizing and detecting non-Abelian topological defects in fractional Chern insulators.

Topological quantum computing is predicated on the idea that braiding non-Abelian anyons adiabatically can implement quantum gates fault tolerantly. However, any braiding experiment will necessarily depart from the strict adiabatic limit. We begin by analyzing the nature of diabatic errors for anyon braiding, paying particular attention to how such errors scale with

braiding time. We find that diabatic errors are unfavorably large and worryingly sensitive to details of the time evolution. We present a measurement-based correction protocol for such errors, and illustrate its application in a particular Majorana-based qubit design.

We next propose designs for Majorana-based qubits operated entirely by a measurement-based protocol, thereby avoiding the diabatic errors discussed above. Our designs can be scaled into large two dimensional arrays amenable to long-term quantum computing goals, whose core components are testable in near-term devices. These qubits are robust to quasiparticle poisoning, anticipated to be one of the dominant error sources coupling to Majorana zero modes. We demonstrate that our designs support topologically protected Clifford operations and can be augmented to a universal gate set without requiring additional control parameters.

While topological protection greatly suppresses errors, residual coupling to noise limits the lifetimes of our proposed Majorana-based qubits. We analyze the dephasing times for our quasiparticle-poisoning-protected qubits by calculating their charge distribution using a particle number-conserving formalism. We find that fluctuations in the electromagnetic environment couple to an exponentially suppressed topological dipole moment. We estimate dephasing times due to $1/f$ noise, thermal quasiparticle excitations, and phonons for different qubit sizes.

The residual errors discussed above will necessarily require error correction for a sufficiently long quantum computation. We develop physically motivated noise models for Majorana-based qubits that can be used to analyze the performance of a quantum error correcting code. We apply this noise model to estimate pseudo-thresholds for a small subsystem code, identi-

fying the relative importance of difference error processes from a fault tolerance perspective. Our results emphasize the necessity of suppressing long-lived quasiparticle excitations that can spread across the code.

Finally, we turn our attention to a different platform that could host non-Abelian topological defects: fractional Chern insulators in graphene. We study the edge states of fractional Chern insulators using the field theory of fractional quantum Hall edges supplemented with a symmetry action. We find that lattice symmetries impose a quantized momentum difference for edge electrons in a fractional state of a $C = 2$ Chern band. This momentum difference can be used to selectively contact the different edge states, thereby allowing detection of topological defects in the bulk with a standard four terminal measurement. Our proposal could be implemented in graphene subject to an artificially patterned lattice.

Contents

Chapter 1

Introduction: Topological phases and topological quantum computing

Keep it secret. Keep it safe.

-Gandalf, *The Fellowship of the Ring*

Condensed matter physics is the study of systems in which many particles are strongly interacting with each other, such that it becomes impractical to track all the degrees of freedom of the system. The focus thus shifts from the behavior of individual electrons and atoms to the collective behavior of the system. Generally, there will be a range of parameters (e.g., temperature, pressure, electric and magnetic fields) for which the collective behavior is qualitatively the same: we call the system for this parameter range a *phase of matter*. When the collective behavior changes discontinuously after a point in parameter space, for instance above some

critical temperature, the system has undergone a phase transition.

Prior to the discovery of the quantum Hall effect, condensed matter physicists believed that phases of matter could be classified by the degree to which they break symmetries of the Hamiltonian. This elegant idea is known as the Landau paradigm, and states that different phases can be distinguished by their local order parameters: local observables of the system that quantify the strength and character of symmetry breaking. A non-zero local order parameter indicates a spontaneously broken symmetry of the Hamiltonian. As the system transitions from an ordered phase to a disordered phase, the local order parameter shrinks, vanishes at the phase transition, then remains zero throughout the disordered phase. For instance, the magnetization is a local order parameter distinguishing a ferromagnet from a paramagnet.

Topological phases of matter are striking contradictions to the Landau paradigm. These are gapped phases of matter which cannot be distinguished by their symmetries. [1] The physical observables only depend on global properties of the system (e.g., dimensionality, genus, and boundary conditions) and are invariant under smooth deformations of the spacetime manifold [193]. Order parameters distinguishing topological phases are *topological invariants*, which are quantized to take integer values and generally depend on integrating over the full system (and are therefore non-local). In Chapter 7, we will discuss one such invariant, the Chern number of an isolated energy band in 2D. Most importantly for our purposes, the emergent quasiparticles of a topological phase are *anyons* [264], whose collective states depend on the history of how they have moved around and merged with each other.

The name "topological phase" derives from the fact that the universal behavior of the sys-

[1] Although, as we shall discuss in Chapters 7 and 8, symmetries can enrich a topological phase.

tem can be understood by applying the mathematical theory of topology, in which local quantities, such as distances and angles, are unimportant, and only global properties, such as dimensionality and the number of non-contractible cycles of the manifold, play a role. In this thesis, we will focus on topological phases in one and two spatial dimensions, with either anyonic quasiparticles or extrinsic topological defects. It is worth noting that the field of topological physics is much broader, and includes higher dimensional systems, topological insulators with no intrinsic topological order, and even gapless phases known as topological semimetals. All of these phases are intimately related to topological invariants, but manifest their connection to topology in different ways.

1.1 Anyons

Fundamental particles can be divided into two categories distinguished by their exchange statistics. This classification stems from two observations: (1) fundamental particles of the same species (e.g., electrons with the same spin) are identical, and (2) we live in a universe with three spatial dimensions. The first point implies that exchanging a pair of identical particles does not change the many body state of the system, therefore such an exchange can only change the many body wavefunction by a phase, $\psi(x_1, x_2, \ldots, x_N) \rightarrow e^{i\theta}\psi(x_2, x_1, \ldots, x_N)$. The second point tells us that exchanging a pair of particles twice can be smoothly deformed to a process in which one particle is wound around the other, and this trajectory can then be contracted to a point. Therefore, exchanging a pair of identical particles twice must result in the initial many-body wavefunction, which restricts the phase θ to be an integer multiple of π. As a result,

exchanging two identical fundamental particles either changes the many body wavefunction by a sign or leaves it invariant, corresponding to *fermions* and *bosons*, respectively. Exchange statistics are intimately connected to the spin of the particle (half-integer for fermions, integer for bosons), and are the underlying reason for such phenomena as the Pauli exclusion principle (fermions) and Bose-Einstein condensation (bosons).

The same arguments do not hold in two spatial dimensions. A trajectory in which one particle winds around another cannot be contracted to a point without passing one particle through the other. Therefore, this process does not need to return the initial state and the phase θ can take *any* value. This is the origin of the name *anyon* [264], a particle which does not satisfy bosonic or fermionic exchange statistics but rather can pick up any phase when wound around another. Mathematically, exchanges of N identical fermions or bosons are described by the permutation group S_N, since we only need to keep track of the the initial and final configurations of the system. Conversely, exchanges of N anyons are described by the braid group B_N, and the final state of the system depends on the topology of how the anyons have moved around each other. Furthermore, the above arguments indicate that exchanging anyons of different types can also result in the many-body wavefunction picking up a phase, provided that the final configuration is the same as the initial configuration, up to permutations of anyons of the same type.

Fundamental particles live in 3D space and are thus necessarily bosons or fermions, however quasiparticles (localized disturbances above the ground state in a gapped phase) in 2D can be anyonic. Following the discussion in Ref. [193], recall that when a state undergoes

cyclic adiabatic evolution of the system parameters, the many body wavefunction acquires a phase. This phase can be separated into a time-dependent dynamical piece, $\int dt\varepsilon(\mathbf{R}(t))$, and a time-independent Berry phase [29]

$$\gamma = i \int d\mathbf{R} \cdot \langle \psi(\mathbf{R}) | \nabla_{\mathbf{R}} | \psi(\mathbf{R}) \rangle. \tag{1.1}$$

In general, γ has both a geometric and topological contribution. When $\mathbf{R}$ corresponds to the quasiparticle positions, the latter only depends on the braid formed by the quasiparticle trajectories. This topological contribution can result in quantized relative phases when comparing different braids.

More explicitly, provided the quasiparticles are kept well-separated at all times, the energy is $\mathcal{O}\left(e^{-|x|/\xi}\right)$ and the dynamical phase is exponentially suppressed. This is a direct result of the topological phase having an energy gap and no local order parameter. In general, the geometric part of the Berry phase could result in a non-universal overall phase acquired by the state. To appreciate why this does not destroy the anyonic exchange statistics, compare the phase acquired by the manybody wavefunction when (1) quasiparticle q_1 follows the contour C encircling stationary quasiparticle q_2, and (2) q_1 follows C without a quasiparticle in the center. The geometric phase only depends on C and will therefore be the same in both cases. The topological piece contributes a quantized relative phase, resulting in anyonic exchange statistics. In Chapter 7, we will see that in the fractional quantum Hall effect, quasiparticles are quantized charge-flux composites and the topological part of the Berry phase is exactly the Aharonov-Bohm phase $\varphi = q\Phi_B$ acquired by the charge q of one quasiparticle winding around

the flux Φ_B of another.

Remarkably, a more exotic scenario is possible when we consider degenerate many-body state spaces. When the Hilbert space associated to a given collection of anyons is multi-dimensional, the integrand in Eq. (1.1) generalizes to the Berry matrix for a degenerate state space [265],

$$\mathbf{m}_{ab} = \langle \psi_a(\mathbf{R}) | \nabla_{\mathbf{R}} | \psi_b(\mathbf{R}) \rangle, \tag{1.2}$$

and under the adiabatic cyclic evolution the states transform as

$$\psi_a \to \mathcal{P}\text{exp}\left(i \int d\mathbf{R} \cdot \mathbf{m}_{ab} \right) \psi_b, \tag{1.3}$$

where $\mathcal{P}$ denotes path-ordering. It turns out that the geometric contribution to the Berry matrix will always be an overall phase, and relative phases between the different states will only be from the topological contribution. The above expression tells us that braiding anyons can rotate the many-body state within its degenerate state space. In fact, in a topological phase, braiding anyons is the only way to implement non-trivial unitary operations [193].

1.1.1 Anyon models

Distinct systems can give rise to the same topological phase. When considering universal properties of topological phases, it is useful to separate the topological content, described by an *anyon model*, from the microscopic details of the underlying physics. An anyon model

contains the following data: (1) the distinct anyon types in the system; (2) how these anyons combine together; and (3) the effect of braiding pairs of anyons [148].

(1) Two anyons are only distinct if there is no local process (e.g., addition of an electron) that maps one to the other. We say that anyons belong to different superselection sectors, and we label these superselection sectors with a topological charge. In the fractional quantum Hall effect, the topological charge corresponds to a fraction of the electric charge, but this is not always the case. Every topological phase has a finite set of topological charges, which includes a trivial particle (locally deformable to the vacuum). We generally label the trivial particle by 1. Mathematically, an anyon model corresponds to a modular tensor category $\mathcal{C}$, and the topological charges a are labels in that category, $a \in \mathcal{C}$.

(2) Anyons are well-defined when they are separated from each other by more than a correlation length. When two anyons are brought close together, they fuse to form a new anyon. This process is described by a collection of fusion rules, written as

$$a \times b = \sum_{c \in \mathcal{C}} N_{ab}^{c} c, \tag{1.4}$$

where $\{a, b, c\}$ label topological charges of the phase, and the *multiplicity* N_{ab}^{c} is an integer counting the number of distinct processes through which anyons a and b can fuse to c. Throughout this thesis, we will assume $N_{ab}^{c} \in \{0, 1\}$. When all the fusion rules take the form $a \times b = c$ (i.e., there is a unique fusion channel for each pair of topological charges), the many-body state space is one-dimensional. In this case, the anyons are *Abelian*. In contrast, when there are multiple cs for which $N_{ab}^{c} \neq 0$, anyons a and b have multiple fusion channels and are *non-Abelian*.

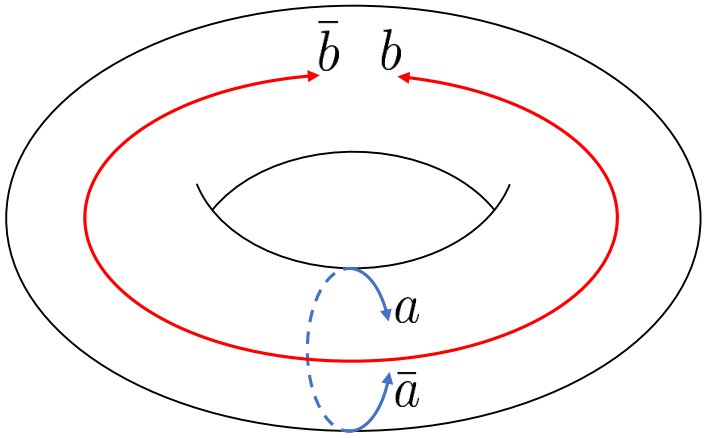

Figure 1.1: The ground state degeneracy of a topological phase is topology-dependent. The processes shown above for which anyons traverse different cycles are non-commuting

The Hilbert space of a and b is spanned the possible fusion channels, e.g., $|a, b; c_1\rangle$ and $|a, b; c_2\rangle$ when $a \times b = c_1 + c_2$.

More concretely, the largest eigenvalue of the matrix $(N_a)_{bc} = N_{ab}^c$ is the *quantum dimension* d_a of anyon a. The state space of N anyons of topological charge a grows asymptotically as d_a^N. For Abelian anyons, $d_a = 1$, while for non-Abelian anyons $d_a > 1$. This implies an internal dimensionality associated with non-Abelian anyons. Note that d_a does not need to be integer-valued.

(3) Braiding can be described by operators R_{ab} that exchange the positions of anyons a. For Abelian anyons, R_{ab} is a phase $e^{i\theta_{ab}}$, while for non-Abelian anyons R_{ab} can be a matrix. Therefore, braiding operations commute for Abelian anyons, while they generally do not commute for non-Abelian anyons (justifying the names). Crucially, note that braiding non-Abelian anyons can rotate the many-body state within the degenerate state space.

For every topological charge a, there is a unique conjugate charge $\bar{a}$ such that a and $\bar{a}$ can

fuse to the vacuum,

$$a \times \bar{a} = 1 + \ldots, \tag{1.5}$$

where the ellipses indicate that there could be additional fusion channels. This fusion rule has important consequences for the ground state degeneracy when the phase lives on a higher-genus surface. Consider a phase living on the torus, as shown in Fig. 1.1. There exists a process (blue) in which a pair of anyons a, $\bar{a}$ are nucleated from the vacuum, circle a non-trivial cycle of the torus, then pair-annihilate. The initial and final states have no excitations and are thus ground states. These states are distinct, as can be seen from a similar process on the other non-trivial cycle of the torus with a pair of anyons b, $\bar{b}$ (red) that braid non-trivially with a, $\bar{a}$. As these two processes do not commute, the second can serve as a measurement of whether the first has occurred. The ground state degeneracy (gsd) is topology-dependent: a genus g surface has

$$|\text{gsd}| = \mathcal{D}^g, \tag{1.6}$$

where $\mathcal{D} = \sqrt{\sum_{a \in \mathcal{C}} d_a^2}$ is the *total quantum dimension of the phase* [2]. For an Abelian phase, $\mathcal{D}$ is equal to the number of distinct anyons.

The information underlying the discussion above is encoded in the $\mathcal{S}$-matrix of an anyon model. The $\mathcal{S}$-matrix together with the $\mathcal{T}$-matrix (corresponding to an anyon circling both

[2]The total quantum dimension can be used to identify a topological phase from the ground state entanglement entropy by contributing a subleading term, $-\log \mathcal{D}$, known as the *topological entanglement entropy* [149, 166, 42].

non-contractible cycles of the torus before being pair-annihilated), forms the modular data of an anyon model and is often enough to completely specify the phase [221] [3]. Additional data comes from imposing associativity of fusion and braiding, which results in two consistency conditions known as the pentagon and hexagon equations. When working with anyon models, it is often useful to employ a diagrammatic formalism [148, 40, 43], which we review in Appendix A.

1.1.2 Topological defects

Anyons are quasiparticle excitations; they have a finite energy cost and are dynamical objects. A topological phase can also host point-like extrinsic defects with topological properties, such as non-Abelian fusion and braiding. Here, "extrinsic" means that the Hamiltonian of the system has to be modified to include the defects, which are not freely moving. The theory of anyon models can be extended to include topological defects [19].

Practically speaking, topological defects provide one of the most promising avenues for experimentally realizing non-Abelian fusion and braiding. Phases with non-Abelian anyons are exceedingly rare and despite some promising results in certain fractional quantum Hall phases [189, 218, 82, 214, 267, 14], they have never been definitively observed. Abelian topological phases are believed to be much more common and experimentally accessible. Non-Abelian topological defects can arise in an otherwise Abelian phase, or significantly enrich the braiding structure of a simple non-Abelian phase [17].

This thesis will explore two physical platforms hosting non-Abelian topological defects:

[3] A recent counterexample was provided by Ref. [187] and discussed in Ref. [41].

Majorana zero modes in topological superconductors [146] and genons in fractional Chern insulators [21]. At present, engineering Majorana zero modes from semiconductor/superconductor heterostructures [224, 181, 200] appears to be the most experimentally accessible approach to accessing non-Abelian topological physics. Genons are more exotic topological defects, whose presence effectively changes the genus of the system, thereby increasing the topologically protected ground state degeneracy. A recent experiment demonstrating fractional Chern insulator physics in graphene [238] has positioned genons as an alternative experimentally feasible route to non-Abelian topological physics.

1.2 Topological quantum computing

The field of quantum computing seeks to build a computer that operates quantum mechanically [212, 198]. Information is stored in *qubits* (two level quantum systems), manipulated through unitary operations (quantum gates), and readout using measurements. The differences between a quantum and classical computer originate from superposition and entanglement. A qubit can be in any superposition of its two basis states, thus a system of N qubits has a 2^N dimensional Hilbert space. In contrast, classical computers store their information in bits, which can either be in one state or the other. Quantum computers are therefore more naturally suited for simulating a quantum system, as the number of qubits needed to encode a many-body state grows polynomially with system size, in contrast to exponential growth for classical bits [91]. Entanglement enriches the type of operations that can be performed on a quantum computer, thereby allowing for the existence of new algorithms to address classically intractable prob-

lems. Building a large scale quantum computer would revolutionize the information industry, with far-reaching impacts on developing new technologies and drug design through quantum simulation [143, 272], breaking modern encryption schemes [236] and replacing them with inherently secure cryptography [27], among many other applications. As such, quantum computing has attracted intense interest from academic researchers, government agencies, large corporations, and technology start-ups.

There are many different proposals for how to build a quantum computer, including storing qubit states in trapped ions, spins in quantum dots, superconducting circuits, or even photon polarization. While these approaches have enjoyed success in realizing small systems of qubits, they all suffer from sensitivity to local environmental noise. This fragility comes from both the fact that a quantum mechanical state is encoded in continuous variables (such as the relative phase between two basis states), for which slight deviations can accumulate over time to decohere the information; and from accidental measurements collapsing the state of the system, thereby removing the benefit of using qubits over classical bits. One way to overcome the detrimental effects of coupling to a noisy environment is to implement a quantum error correcting code. Essentially, this spreads the information over many qubits (the exact number depends on both the code and the noisy environment for the given system). Subsets of these qubits can be measured to detect errors without collapsing the encoded quantum mechanical state. If noise events are sufficiently rare, faults in the system can be corrected and error rates for the encoded information can be made arbitrarily small. However, increasing the number of qubits needed to encode one unit of information can make scaling the quantum computer to large system sizes

prohibitively difficult.

An attractive alternative is to store information non-locally in the degenerate state space of non-Abelian anyons or topological defects [147, 193]. These states are indistinguishable by any local observable, up to exponentially suppressed corrections in ratios of macroscopic parameters of the system that can be made large. Information thus encoded is robust to a local noisy environment, and is said to be *topologically protected*. Furthermore, braiding performs unitary operations in a protected manner: the encoded information remains insensitive to the local environment, and systematic errors are avoided because the braiding phase is independent of the details of the quasiparticle trajectories. *Topological quantum computing* therefore implements fault-tolerance (robustness to noise) at the hardware level. Heuristically, topological quantum computing obviates long-term scalability concerns, at the expense of utilizing a more complicated qubit.

1.3 This thesis

Topological quantum computing faces many challenges. Non-Abelian topological phases are rare in nature, and have proven experimentally challenging to study. Non-Abelian topological defects are believed to be more accessible, but pose new challenges including how to braid and measure given that defects are generally hard to move and non-local measurements are difficult to implement. Not all non-Abelian anyons or topological defects support universal quantum computing from braiding alone; in fact, all actively-pursued platforms for non-Abelian topological physics would require an additional unprotected operation. Furthermore, physical real-

ities such as finite temperature, operational time, and system size result in residual errors that may need to be corrected for sufficiently long computations. This thesis addresses these issues at length.

In Chapter 2, we consider the first challenge of finding an experimentally accessible platform for topological quantum computing by reviewing Majorana zero modes, non-Abelian defects of a topological superconductor. We review the topological nature of Majorana zero modes, their potential physical realization, and the supporting experimental evidence thereof. We then explain how Majorana zero modes can be used to encode a qubit, and address the subtleties of implementing braiding in such a system.

Chapter 3 addresses what happens when braiding is implemented in a finite amount of time, and thus is not strictly adiabatic. We identify how diabatic errors arise in anyon braiding, and the scaling of the associated error rates. We further develop a correction scheme and illustrate its application to a particular Majorana-based qubit proposal.

We next turn our attention to long-term visions for topological quantum computing that can be tested in the near-future. Chapter 4 presents scalable designs for Majorana-based quantum computing. We discuss five different qubit architectures, all of which support universal quantum computing and are protected from dominant noise sources. The key concepts underlying these designs should be testable with only modest changes to currently existing devices.

In Chapter 5, we consider how noise limits the lifetimes of the qubits presented in the previous chapter. In particular, we calculate the charge distribution of these qubits in a number conserving formalism, illustrating how it couples to the topologically encoded information. We

estimate dephasing times due to different noise sources for reasonable parameter values.

Chapter 6 addresses the residual errors affecting a Majorana-based quantum computer by presenting physically motivated noise models for such a system. These noise models can be used to analyze the performance of a quantum error correcting code, and thereby help determine which types of errors affecting the system are most problematic from a fault-tolerance perspective. We apply our noise models to estimate pseudo-thresholds for a small subsystem code.

Majorana zero modes are not the only platform for topological quantum computing. Chapter 7 reviews the theory of the fractional quantum Hall effect and fractional Chern insulators, the latter of which can host non-Abelian topological defects at lattice dislocations. We summarize a recent experiment observing fractional Chern insulator physics in graphene.

In Chapter 8, we study the edge physics of fractional Chern insulators to propose an experiment for detecting non-Abelian topological defects at lattice dislocations in the bulk. The interplay of lattice symmetry with topological order can effectively create a multi-layered system, where the layer degree of freedom physically corresponds to different lattice sites. Lattice symmetries along the edge of the sample impose a quantized momentum difference between the edge states, which can be used to selectively contact the edge electron associated with one layer. This provides the missing ingredient for using the edge states to detect defects in the bulk using a standard four-terminal measurement. The system studied here could be implemented in graphene subject to an artificially patterned lattice potential.

Finally, in Chapter 9 we summarize the status and future directions of the studies presented

in this thesis. We then outline two new projects stemming from the work contained here.

Chapter 2

Review: Majorana zero modes

Life is infinitely stranger than anything which the mind of man could invent.

-Sir Arthur Conan Doyle, *The Complete Adventures of Sherlock Holmes*

In this chapter, we review the search for Majorana zero modes and their potential application to topological quantum computing. We begin by disentangling the concepts of Majorana fermions, Majorana operators, and Majorana zero modes. We next illustrate the salient topological properties of Majorana zero modes in a 1D toy model [146]. The topological phase described by this model can be realized in semiconductor-superconductor heterostructures [181, 200]; we discuss both the theoretical proposals for realizing and detecting this phase and the experimental evidence in support of Majorana zero modes. Finally, we present the basic ideas underlying Majorana-based quantum computing, paying particular focus to different proposals for implementing braiding in experimentally feasible systems.

2.1 Majorana fermions, Majorana operators, and Majorana zero modes

Historically, Majorana fermions were first proposed in the context of high energy physics as a fundamental particle described by a real wavefunction. Since then, the label 'Majorana' refers to something (particle, quasiparticle, bound state, or gapless edge mode) with fermionic self-statistics that acts as its own antiparticle. As the terminology is not consistently applied throughout the literature, we take some time here to sharpen the meaning of these different entities.

As reviewed in the previous chapter, all fundamental particles are either bosons or fermions, where the labels refer to the self-statistics of identical particles with dramatic implications for their collective behavior. Within these two categories there are several different species that can be distinguished by the properties of their wavefunctions. Dirac fermions, such as electrons, are described by solutions to the Dirac wave equation. Notably, Dirac fermions are physically distinct from their corresponding antiparticles. Mathematically, this is manifested by Dirac fermions having complex wavefunctions, whose complex conjugates are the wavefunctions of the corresponding antiparticles.

In 1937, Ettore Majorana realized that the Dirac equation can be rewritten as a pair of wave equations admitting real solutions. Physically, these solutions are wavefunctions describing fermionic particles that are physically indistinguishable from their own antiparticles. There remains an ongoing search for whether such *Majorana fermions* exist as fundamental particles. [1]

[1] For instance, neutrinos have been postulated to be Majorana fermions [10].

It is often convenient to work in second quantized formalism rather than with wave equations. In this language, a Dirac fermion is described by a (non-Hermitian) Dirac operator c_i that satisfies fermionic anticommutation relations,

$$\{c_i, c_j\} = \{c_i^\dagger, c_j^\dagger\} = 0, \qquad \{c_i, c_j^\dagger\} = \delta_{ij}. \tag{2.1}$$

In contrast, Majorana fermions are described by Hermitian operators

$$\gamma_i = \gamma_i^\dagger, \tag{2.2}$$

satisfying fermionic anticommutation relations

$$\{\gamma_i, \gamma_j\} = 2\delta_{ij}. \tag{2.3}$$

Equations (2.2) and (2.3) define a *Majorana operator*, with Eq. (2.2) sometimes referred to as 'the Majorana condition.'

Formally, we can rewrite a Dirac operator as a pair of Majorana operators,

$$c_j = \frac{1}{2}\left(\gamma_j - i\bar{\gamma}_j\right), \tag{2.4}$$

or equivalently

$$\gamma_j = c_j + c_j^\dagger, \qquad \bar{\gamma}_j = \frac{c_j - c_j^\dagger}{i}. \tag{2.5}$$

It is straightforward to check that Eq. (2.4) satisfies Eq. (2.1). The physical implication of Eq. (2.4) is that a pair of Majorana fermions forms a Dirac fermion. Another way of writing this is to note that the product of Majorana operators corresponds to the fermion parity of the Dirac operator:

$$i\gamma_j\bar{\gamma}_j = 1 - 2c_j^\dagger c_j. \tag{2.6}$$

Importantly, a single Majorana fermion does not have a well-defined fermion parity. As fermion parity is a conserved quantity in nature, Majorana fermions necessarily occur in pairs. Equations (2.4-2.6) are not particularly meaningful when Majorana fermions are spatially intertwined. Rather, we shall be interested in the realization of spatially separated Majorana fermions, whose collective description corresponds to a non-local Dirac fermion.

In condensed matter physics, the interest is in an emergent quasiparticle or defect described by a Majorana operator. A natural place to search for such an object is in superconductors, where quasiparticles are superpositions of electrons and holes. Conventional s-wave superconductors pair electrons of opposite spin; their quasiparticle operators schematically take the form

$$d = uc_\downarrow + vc_\uparrow^\dagger. \tag{2.7}$$

In this case, spin prevents quasiparticle operators from satisfying Eq. (2.2). We therefore turn our attention to spinless superconductors, which necessarily have odd momentum space pair-

ing to satisfy the Pauli exclusion principle. Particle hole symmetry imposes the additional constraint that a quasiparticle operator at energy E must be equal to the quasihole operator at energy $-E$: $d(E) = d^\dagger(-E)$. The superconducting gap prevents the existence of such zero energy modes except at domain walls, for instance the endpoints of a 1D p-wave superconductor or vortices of a 2D p+ip superconductor. Superconductors that bind a Majorana fermion at a domain wall are characterized by a non-trivial topological invariant, and are thus called topological superconductors. The combination of a Majorana fermion bound to a domain wall is called a *Majorana zero mode* (MZM) or equivalently a *Majorana bound state*. In the next section, we illustrate how MZMs appear in a toy model of a 1D p-wave superconductor.

MZMs are topological defects with non-Abelian fusion and braiding statistics. A pair of MZMs can either fuse to vacuum (denoted 1) or to a Dirac fermion (denoted ψ); since the MZM is pinned to zero energy (up to exponentially small corrections that we return to later), these fusion channels are degenerate. Using the anyon model language reviewed in the previous chapter, the non-trivial fusion rules for MZMs are

$$\gamma \times \gamma = 1 + \psi \tag{2.8}$$

$$\gamma \times \psi = \gamma \tag{2.9}$$

$$\psi \times \psi = 1. \tag{2.10}$$

At the operator level, Eq. (2.8) can be understood from Eq. (2.6). The operator $i\gamma_j\bar{\gamma}_j$ can have eigenvalues ± 1, for which the corresponding Dirac fermion is either occupied ($\langle c_j^\dagger c_j \rangle = 1$) or not. We call the latter case the "vacuum." As each pair of MZMs contributes two degener-

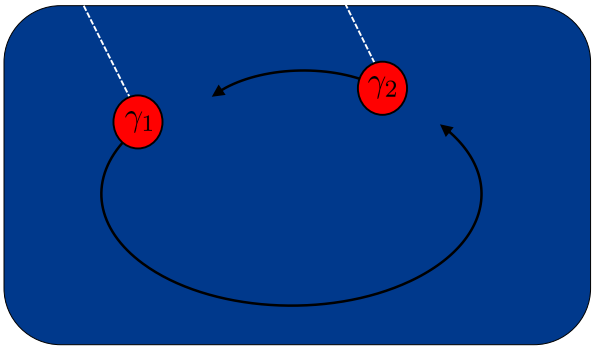

Figure 2.1: Braiding Majorana zero modes (red) in a 2D p+ip superconductor (blue). Each vortex has a branch cut emanating from it (dashed white line). For the process shown, only the vortex associated with operator γ_2 crosses a branch cut, and thus picks up the corresponding sign change. Therefore, the braid shown corresponds to the operators transforming as $\gamma_1 \to \gamma_2$ and $\gamma_2 \to -\gamma_1$.

ate fusion channels, the ground state degeneracy of a system with $2n$ MZMs grows as $\sqrt{2}^{2n}$. Therefore, the quantum dimension of a single MZM is $\sqrt{2}$. We also note that Eq. (2.3) implies that we cannot simultaneously be in fermion parity eigenstates of $i\gamma_j\gamma_k$ and $i\gamma_j\gamma_l$; it follows that measurements of non-commuting pairs of MZMs can be used for state teleportation. We return to this point at the end of this chapter.

The non-Abelian braiding statistics can be intuitively understood by considering MZMs in a spinless p+ip superconductor [132]. Spinless fermion operators necessarily flip sign when the superconducting phase changes by 2π, as happens around a vortex. To track these sign changes, we can draw branch cuts emanating from each vortex that, for instance, terminate on the upper boundary of the superconductor as drawn in Fig. 2.1. When exchanging a pair of MZMs, we would expect their associated operators to transform into each other, up to a possible phase. As only one of MZMs crosses a branch cut line (γ_2 for the depicted counterclockwise exchange), we have $\gamma_1 \to \gamma_2$ and $\gamma_2 \to -\gamma_1$. It follows that a counterclockwise

braid is given by the operator

$$R^{(12)} = \frac{1 + \gamma_1 \gamma_2}{\sqrt{2}}. \tag{2.11}$$

Interesting physics occurs when we consider a system of four MZMs and adiabatically exchange a pair of them. Let us work in the basis $|0\rangle = |i\gamma_1\gamma_2 = i\gamma_3\gamma_4 = 1\rangle$ and $|1\rangle = |i\gamma_1\gamma_2 = i\gamma_3\gamma_4 = -1\rangle$. Applying $R^{(23)}$ to the initial state $|0\rangle$ yields

$$R^{(23)}|0\rangle = \frac{1}{\sqrt{2}} \left(|0\rangle + i|1\rangle\right), \tag{2.12}$$

that is, braiding MZMs can rotate the state (within the fixed total parity state space). It is important to note that the non-Abelian braiding of MZMs is intimately tied to the fact that Majorana fermions are bound to vortex cores. Exchanging two freely moving Majorana fermions would simply rotate the wavefunction by π, as does exchanging any pair of identical fermions.

Finally, we conclude this section with a couple of comments. (1) The fusion and braiding statistics of MZMs are closely related to those of Ising anyons, which are proposed to be the quasiparticles of a $\nu = 5/2$ fractional quantum Hall phase [189]. For this reason, such anyons are sometimes referred to as Majorana fermions. We avoid this terminology, as it can be easily confused with Majorana fermions with trivial fermionic exchange statistics. Ising anyons generally arise in phases that admit an effective description as a p+ip superconductor, see for instance the discussion in Ref. [218]. (2) Topological phases hosting Ising anyons can have a gapless edge mode whose wavefunction is a solution of the Majorana wave equation.

Name	Type	Majorana reason
Majorana fermion	fundamental particle	solves Majorana wave equation
Majorana zero mode Majorana bound state	non-Abelian top. defect	Majorana operator description
Ising anyon	non-Abelian anyon	same fusion/similar braiding to MZMs
chiral Majorana mode	gapless edge state	solves Majorana wave equation

Table 2.1: Majorana-labeled entities. In this thesis, we will primarily be concerned with Majorana zero modes (MZMs), which are Majorana fermions bound to domain walls of a topological superconductor (vortices in 2D, boundaries in 1D). MZMs exhibit non-Abelian fusion and braiding statistics, which make them attractive candidates for topological quantum computing. Closely related concepts are: Ising anyons (quasiparticles rather than extrinsic defects), which have the same fusion as and similar braiding to MZMs (and are sometimes referred to as Majorana fermions in the literature); and chiral Majorana modes, which are gapless edge states of 2D topological superconductors or certain topological phases. The latter often appear in conjunction with MZMs or Ising anyons, but are not themselves non-Abelian topological defects or anyons.

These edge modes are thus Majorana fermions and appear in conjunction with, but do not themselves satisfy, non-Abelian statistics. Again, to avoid confusion, we will refer to these states as *chiral Majorana modes*.

2.2 Kitaev chain

The following toy model introduced by Kitaev [146] describes a chain of spinless electrons c_i with chemical potential μ, hopping parameter t, p-wave pairing amplitude Δ, and superconducting phase ϕ:

$$H = -\mu \sum_i c_i^\dagger c_i - \frac{1}{2} \sum_i \left(t c_i^\dagger c_{i+1} + \Delta e^{i\phi} c_i c_{i+1} + h.c. \right). \tag{2.13}$$

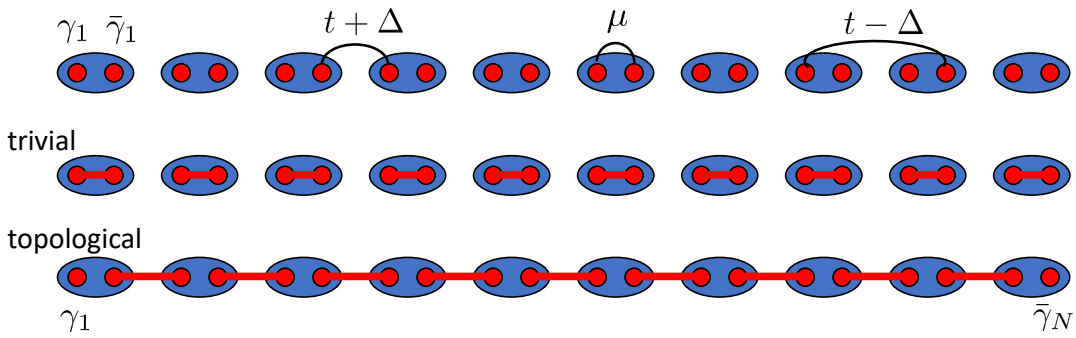

Figure 2.2: Kitaev chain. A spinless electron (blue oval) can be rewritten as a pair of Majorana operators (red circles). The chemical potential μ pairs Majorana operators belonging to the same electron, while hopping and pair tunneling terms pair Majorana operators belonging to adjacent electrons. In the trivial phase, all Majorana operators are paired. In the topological phase, there are two unpaired Majorana operators, describing the MZMs at either end of the system.

This model is mathematically equivalent to the transverse field Ising model, which can be seen by applying a Jordan Wigner transformation to the latter.

Before searching for isolated MZMs, we first identify the different phases of the model by studying the bulk properties of the system. It is convenient to take periodic boundary conditions, so that after a Fourier transform the Hamiltonian can be written in Bogoliubov-de Gennes form as

$$H = -\frac{1}{2}\sum_k \left(c_k^\dagger, c_{-k}\right) \begin{pmatrix} \mu + t\cos(ka) & i\Delta e^{-i\phi}\sin(ka) \\ -i\Delta e^{i\phi}\sin(ka) & -\mu - t\cos(ka) \end{pmatrix} \begin{pmatrix} c_k \\ c_{-k}^\dagger \end{pmatrix}. \tag{2.14}$$

(As alluded to in the previous section, the Pauli exclusion principle dictates that the superconducting pairing must be odd in momentum for a spinless system. This is reflected above by the

pairing term being proportional $\sin(ka)$.) The bulk energies are thus

$$E(k) = \sqrt{(\mu + t\cos(ka))^2 + \Delta^2 \sin^2(ka)}. \tag{2.15}$$

Importantly, the bulk is gapped except at the points $\mu = \pm t$. The regimes $\mu > t$ and $\mu < -t$ can be related by a particle hole transformation, so we will focus on the former.

Clearly, in the limit $\mu \to \infty$ the ground state corresponds to an atomic insulator with each site occupied; we identify this phase as trivial. Cooper pairs in this "strong-pairing" phase are formed from tightly bound fermions and have exponentially localized wavefunctions. In contrast, the phase at $|\mu| < t$ has "weak pairing," and the Cooper pair wavefunction is constant across the system [218]. It turns out that these two phases are distinguished by a topological invariant.

We follow the presentation in Ref. [6]. Identifying the matrix in Eq. (2.14) as $\mathcal{H}_k$, we can use the relation $\mathcal{H}_k = \mathbf{h}(k) \cdot \sigma$ to define a vector $\mathbf{h}(k)$ (here σ is the vector of Pauli matrices). The topological invariant is the winding number of the corresponding unit vector $\hat{\mathbf{h}}(k) = \mathbf{h}(k)/|\mathbf{h}(k)|$ as k is varied over the Brillouin zone, with trivial winding corresponding to the trivial phase. Particle hole symmetry constrains the form of $\mathbf{h}(k)$ such that $h_{x,y}(k) = -h_{x,y}(-k)$ and $h_z(k) = h_z(-k)$. Therefore, at $k = 0$ and π/a, $h_{x,y}(k)$ vanishes, and the winding of $\hat{\mathbf{h}}(k)$ can be reduced to considering whether $\hat{\mathbf{h}}(0)$ is parallel or antiparallel to $\hat{\mathbf{h}}(\pi/a)$, corresponding to trivial or non-trivial winding number, respectively. The winding number can only change when the bulk gap vanishes. The limit of $\mu \to \infty$ indicates that $\mathbf{h}(0)$ is parallel to $\mathbf{h}(\pi/a)$, and thus has trivial winding. As anticipated, the strong pairing phase

is topologically trivial. When $\mu < |t|$, $h_z(\pi/a)$ can flip sign compared to $h_z(0)$. The weak pairing phase has non-trivial winding and corresponds to the topological phase. This analysis holds in the presence of perturbations that preserve translation symmetry.

We will now consider a finite chain and see that the topological phase hosts MZMs at its boundaries. Rewriting Eq. (2.13) in terms of Majorana operators using

$$c_i = \frac{e^{-i\phi/2}}{2}\left(\gamma_i + i\bar{\gamma}_i\right) \tag{2.16}$$

(a trivial redefinition of Eq. (2.4)), the Hamiltonian becomes

$$H = -\mu \sum_{i=1}^{N} \frac{1 - i\gamma_i\bar{\gamma}_i}{2} + \frac{1}{4}\sum_{i=1}^{N-1}\left((t-\Delta)i\gamma_i\bar{\gamma}_{i+1} - (t+\Delta)i\bar{\gamma}_i\gamma_{i+1}\right). \tag{2.17}$$

There are two fine-tuned points for which the physics becomes especially clear. First, when $t = \Delta = 0$ and $|\mu| \neq 0$, the Hamiltonian reduces to

$$H_{\text{triv}} = -\mu \sum_i \frac{1 - i\gamma_i\bar{\gamma}_i}{2}, \tag{2.18}$$

which has a unique ground state corresponding to all sites on the chain occupied or unoccupied, depending on the sign of μ. In particular, all Majorana operators are paired at the same site, thus we have no isolated Majorana zero modes. This is illustrated schematically in Fig. 2.2. While the exact Majorana operator pairing becomes more complicated away from this fine-tuned point, the gapped bulk implies that the ground state degeneracy does not change throughout

the phase $|\mu| > t$.

Next, consider the Hamiltonian at the point $t = \Delta \neq 0$ and $\mu = 0$:

$$H_{\text{top}} = -\frac{\Delta}{2} \sum_{i=1}^{N-1} i\bar{\gamma}_i \gamma_{i+1}. \tag{2.19}$$

Crucially, the Majorana operators γ_1 and $\bar{\gamma}_N$ do not appear in the sum and thus commute with the Hamiltonian,

$$[H_{\text{top}}, \gamma_1] = [H_{\text{top}}, \bar{\gamma}_N] = 0. \tag{2.20}$$

These Majorana operators correspond to Majorana zero modes at either end of the chain, see Fig. 2.2. Together, they form a non-local Dirac fermion with operator $f = (\gamma_1 + i\bar{\gamma}_N)/2$. There is a two-fold ground state degeneracy corresponding to $f^\dagger f = 0$, or 1. Once again, the pairing of Majorana operators becomes more complicated away from this fine-tuned point, but the essential physics remains the same. In particular, there exist two Majorana operators $\gamma_{L/R} = \sum_{i=1}^{N} (\alpha_i \gamma_i + \beta_i \bar{\gamma}_i)$ (where α_i and β_i depend on μ, t, and Δ) satisfying

$$[H_{\text{top}}, \gamma_{L/R}] \sim e^{-L/\xi}, \tag{2.21}$$

where $L = Na$ is the length of the chain and ξ is the correlation length. The system therefore retains a two-fold ground state degeneracy, up to exponentially suppressed corrections.

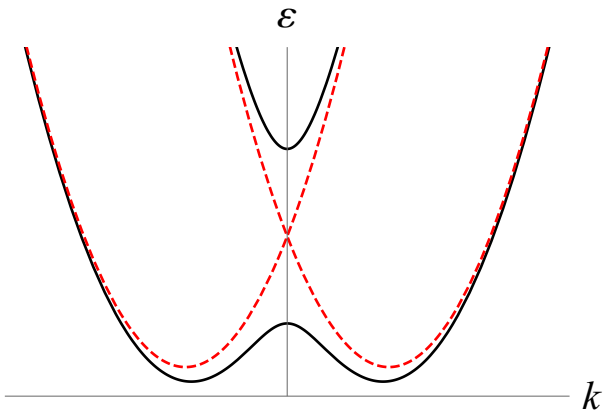

Figure 2.3: Energy bands for Eq. (2.22). Red-dashed lines are for $h = 0$. Black lines are for $h > 0$. When the chemical potential lies in the energy gap, the system is effectively spinless. Proximity coupling to a superconductor introduces pairing between the electrons in the lower band at $\pm k$.

2.3 Majorana zero modes in semiconductor/superconductor heterostructures

The toy model reviewed in the previous section provides an intuitive understanding of a system realizing spatially separated MZMs, however from the experimental realization standpoint it has two notable drawbacks. First, the model relies on p-wave pairing, which is exceedingly rare in nature. Second, the model assumes spinless electrons, which are a theoretical construct. Given these complications, the emphasis is to engineer a system realizing the topological phase of the Kitaev chain, rather than to search for a naturally occurring phase of matter [103, 224, 181, 200].

We will focus on the proposals presented in Refs. [181, 200], which combine strong spin orbit coupling in a semiconductor nanowire with an external magnetic field to create an effectively spinless system. When this nanowire is proximity coupled to a conventional s-wave su-

perconductor, Cooper pairs hopping across the semiconductor-superconductor interface induce p-wave superconductivity. For the appropriate values of magnetic field, chemical potential, and superconducting gap, this system can be tuned into a topological phase smoothly connected to that of the Kitaev chain.

Following the presentation in Ref. [6], the nanowire can be described by the Hamiltonian

$$H_{\text{NW}} = \int dx \psi^\dagger_\sigma(x) \left(-\frac{\partial_x^2}{2m^*} - \mu - i\alpha\sigma_y\partial_x + h\sigma_z \right)_{\sigma,\sigma'} \psi_{\sigma'}(x), \tag{2.22}$$

where m^* is the effective mass, μ is the chemical potential, α characterizes the strength of spin-orbit interactions, and h is the spin-splitting induced by an applied magnetic field. We assume the wire has a single occupied mode. As depicted in Fig. 2.3, when $h = 0$ spin-orbit coupling shifts the bands associated with different spins (red-dashed curves). For $h > 0$, these bands hybridize near $k = 0$ to open an energy gap

$$\varepsilon_\pm(k) = \frac{k^2}{2m} - \mu \pm \sqrt{(\alpha k)^2 + h^2}. \tag{2.23}$$

When μ sits within the gap, the system is effectively spinless.

When the semiconductor nanowire is near an s-wave superconductor, Cooper pair hopping across the interface contributes a term to the Hamiltonian

$$H_\Delta = \int dx \left(\Delta\psi^\dagger_\uparrow(x)\psi^\dagger_\downarrow(x) + h.c. \right), \tag{2.24}$$

where Δ is the induced pairing in the nanowire. If we reexpress the Hamiltonian in terms of operators $\psi_\pm(k)$ which add electrons to bands $\varepsilon_\pm(k)$, then Eq. (2.24) contributes an interband s-wave pairing term and an intraband p-wave pairing term:

$$H_\Delta = \int \frac{dk}{2\pi} \left\{ \sum_{a=\pm} \frac{\Delta_p(k)}{2} \left(\psi_a(-k)\psi_a(k) + h.c.\right) + \Delta_s(k) \left(\psi_-(-k)\psi_+(k) + h.c.\right) \right\}, \quad (2.25)$$

where

$$\Delta_p(k) = \frac{\alpha k \Delta}{\sqrt{(\alpha k)^2 + h^2}}, \qquad \Delta_s(k) = \frac{h\Delta}{\sqrt{(\alpha k)^2 + h^2}}. \quad (2.26)$$

The p-wave pairing arises because electrons within a band at momenta $\pm k$ have misaligned spins (due to the competition between the magnetic field and spin-orbit coupling) and can therefore Cooper pair. The quasiparticle energies are

$$\varepsilon'_\pm(k) = \sqrt{\Delta^2 + \frac{\varepsilon_+^2 + \varepsilon_-^2}{2} \pm (\varepsilon_+ - \varepsilon_-)\sqrt{\Delta_s^2 + \mu^2}}. \quad (2.27)$$

At $h = \sqrt{\Delta^2 + \mu^2}$, $\varepsilon'_-(0) = 0$ and the quasiparticle energy gap closes. When h is above this critical value, the nanowire is no longer effectively spinless and the wire is in a trivial state. In contrast, when

$$h > \sqrt{\Delta^2 + \mu^2} \quad (2.28)$$

the wire enters a topological superconducting phase with MZMs at the endpoints.

The three essential ingredients for this proposal are (1) strong spin orbit coupling, (2) proximity-induced superconductivity, and (3) time reversal symmetry breaking, provided here by a semiconductor nanowire, s-wave superconductor, and external magnetic field, respectively. Separately, each ingredient is easily available to an experimental group; the challenge arises in making them compatible with each other. In the next section we mention some tensions in achieving this compatibility.

Finally, we note that there are many variations on the proposal reviewed here. An earlier proposal used topological insulators in place of semiconducting wires to provide spin orbit coupling [103]. Another variant is to replace the external magnetic field with magnetic atoms [104] or micromagnets [150]. More recent proposals utilize planar Josephson junctions [206], or the Little-Parks effect in a semiconductor nanowire with a superconducting shell coating the full circumference [182]. Much of the discussion in this thesis could be straightforwardly generalized to these alternate proposals for engineering topological superconductivity.

2.4 Experiments

Since the proposals of Refs. [181, 200], there has been an explosion in experimental progress towards engineering MZMs [190, 79, 74, 65, 95, 80, 191, 222, 5, 78, 197, 113, 274, 250]. In this section, we describe current approaches towards experimentally realizing and detecting MZMs.

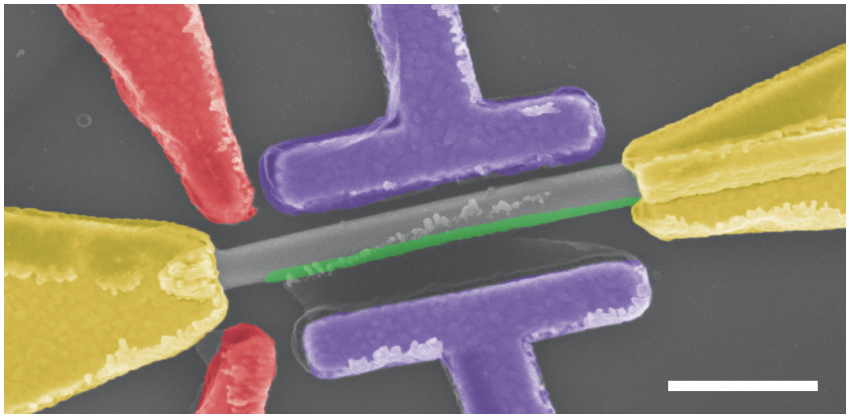

Figure 2.4: Micrograph of VLS Majorana nanowire used for zero bias peak transport experiment, scale bar is 500 nm. An InSb nanowire (gray) is coated on one side with 10 nm thick Al (green). Side gates (red) control the tunnel gate voltage, while T-shaped gates (purple) are used to tune the chemical potential of the proximitized wire. Reprinted with permission from Ref. [274].

2.4.1 Realizations

Despite utilizing conventional ingredients, the above proposal has proven difficult to realize experimentally. First, materials must satisfy certain conditions. The semiconductor must have large spin orbit coupling and Landé g-factor to maximize the effectively spinless regime in the presence of a magnetic field. The superconductor ideally has a large superconducting gap with no subgap states. Next, the materials must be compatible with each other, and with the application of an external magnetic field. The superconductor must be able to induce superconductivity in the semiconductor, while also being sufficiently thin so that a parallel magnetic field does not drive the system normal. The presence of the magnetic field along the axis of the wire constrains the possible geometric layouts of 1D topological superconducting wire networks (see Section 2.5.1). Finally, the ultimate goal of achieving topological protection of the joint MZM parity necessitates realization of a hard induced superconducting gap. The

semiconductor, superconductor, and their interface must be uniform to avoid the presence of disorder-induced subgap states. This final constraint requires resource-intensive fabrication of the heterostructures, thereby severely limiting the number of experimental groups that can pursue MZM physics in these systems.

Experiments have focused on InAs and InSb semiconducting wires with epitaxial growth of thin Al superconducting shells (original experiments used NbTiN [190], but given the presence of subgap states most experiments now use Al). InAs has g-factor of $8-15$ and spin orbit coupling strength $\alpha = 0.2 - 0.8\,\text{eV}\cdot\text{Å}$, and can be lattice matched to Al to provide an exceptionally clean interface [157, 233]. InSb has slightly better parameters of g-factor $40 - 50$ and $\alpha = 0.2 - 1\,\text{eV}\cdot\text{Å}$. While it does not benefit from lattice matching, it can none-the-less form a clean interface with Al [106]. The superconducting gap and critical field of Al depends on its thickness; for $10 - 20\,\text{nm}$ thick films the gap is between $0.2 - 0.3\,\text{meV}$ and the critical field is $10\,\text{mT}$. For sufficiently clean samples in zero field, the induced gap for both InSb and InAs is $0.2\,\text{meV}$. All parameters are taken from Ref. [179] and references therein.

Currently, there are three leading approaches to fabricating 1D topological superconductors from semiconductor-superconductor heterostructures: Vapor Liquid Solid (VLS) nanowires, lithography of 2D electron gasses (2DEGs), and selective area grown wires (SAG wires). The first is a bottom up approach, in which epitaxial nanowires (InAs or InSb) are grown in vacuum and have superconductor (Al) deposited in situ to form a clean semiconductor-superconductor interface. The wires are typically 80-100 nm in diameter and up to $10\,\mu\text{m}$ long [179]. VLS nanowires have provided the cleanest evidence thus far for MZMs [274], but are not scalable

to larger systems. In contrast, the second and third approaches are better suited for fabricating networks of topological superconductors. 2DEGs begin with a high mobility semiconductor quantum well, on which Al is lithographically patterned. Electrostatic gates are then used to deplete electrons from all regions in the semiconductor not forming the desired 1D wire network. Early experiments on MZM nanowires fabricated from 2DEGs have been encouraging [197], but complications remain (see e.g., Ref. [179]). SAG wires use lithography to only grow semiconductor in selected areas (i.e., in the shape of the desired network), which can then be covered with Al. One promising aspect of SAG wires is that the process provides greater control over the dimensions of the wire than 2DEGs or VLS wires. This control could result in more uniform wires, which might then be more reproducibly tuned into the topological phase. Thus far, experiments have realized SAG wires with a hard induced superconducting gap [251], but have not yet shown transport signatures of MZMs in the presence of a magnetic field.

2.4.2 Detection

MZMs appear at the endpoints of a 1D p-wave superconductor tuned into the topological phase. Therefore, any experimental evidence of MZMs must appear only when all the necessary criteria for a topological phase are met, and must persist over the range of parameter values for which the system remains in that phase. Additionally, evidence supporting MZMs should reflect their topological origin.

Below, we review two transport experiments for detecting MZMs. The first uses tunneling spectroscopy into the end of a grounded semiconductor-superconductor wire to search for zero

bias peaks in the differential conductance, indicating the presence of a zero energy state. When the states have a topological origin (i.e., are MZMs), the zero bias conductance peaks should be quantized to $2e^2/h$ for a range of parameter values. While there have been numerous zero bias peak experiments beginning with Ref. [190], we focus here on two recent experiments [274, 197].

The second detection scheme uses a two-terminal conductance measurement for a floating 1D superconductor in the Coulomb-blockaded regime to determine the ground state periodicity. For a trivial superconducting phase, the ground state energy should have a $2e$ periodic dependence on gate voltage, indicating that single electrons cannot tunnel into the wire except at charge degenerate points. For the topological phase, the pair of MZMs provide a non-local fermionic state whose occupation does not cost energy (up to corrections $\mathcal{O}\left(e^{-L/\xi}\right)$), thus the ground state energy should become approximately $1e$ periodic with the deviations given by the exponentially suppressed degeneracy splitting.

Zero bias peaks

The most-pursued signature of MZMs is a quantized zero bias conductance peak [232, 162, 225, 97, 94]. The basic experimental layout is shown in Fig. 2.4. A semiconducting nanowire with a grounded superconducting shell is separated from a normal metal lead by a tunneling barrier. When the bias voltage between the lead and the nanowire is sufficient to overcome the superconducting gap, electrons can tunnel into the nanowire, producing a finite current. When the bias voltage is below the superconducting gap ($eV < \Delta$), electrons are reflected back into the lead at the tunnel barrier and there is no current. The differential conductance

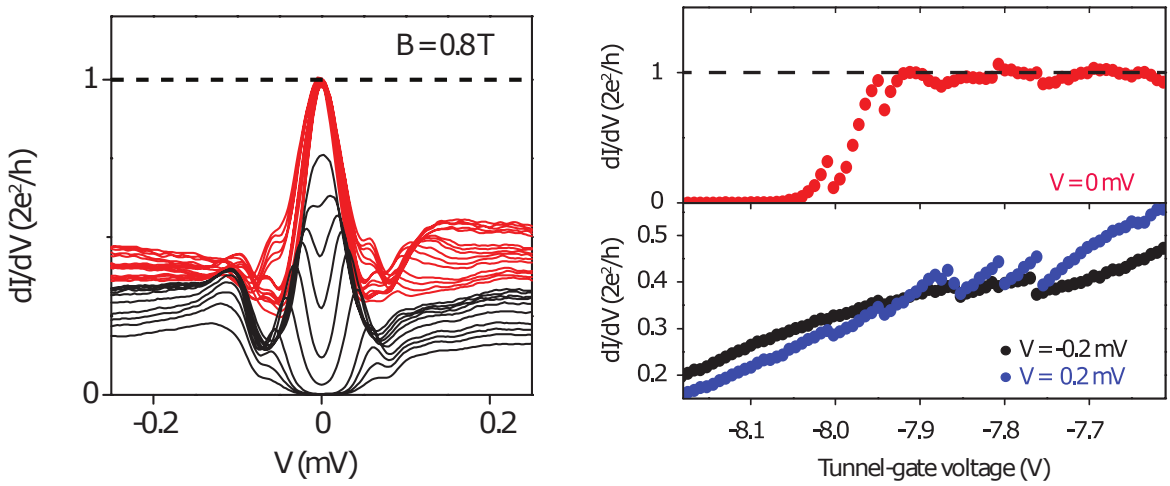

Figure 2.5: Quantized zero bias peaks. Left panel: differential conductance plotted against bias voltage for different tunnel gate voltage values with magnetic field strength $B = 0.8\,\mathrm{T}$. The red traces show that the zero bias peak height is quantized to $2e^2/h$ for a range of tunnel gate voltage. Top right panel: Zero bias peak height plotted against tunnel gate voltage. Bottom right panel: Differential conductance at $V = \pm 0.2$ mV for the same range of tunnel gate voltage. Thus while the height of the tunnel barrier continues to affect the differential conductance away from zero bias, the peak height retains a quantized value. Reprinted with permission from Ref. [274].

$G(V) = \frac{dI}{dV}$ should therefore take the form of the bottom-most black curves in the left panel of Fig. 2.5, where the separation in V between the shoulders of the curve are a measure of the superconducting gap (and any signal at lower bias voltage indicate nonvanishing subgap density of states in the wire).

By applying a magnetic field along the axis of the wire, we expect the semiconductor-superconductor nanowire to be driven into a topological phase with MZMs at its endpoints. These should be observable by the appearance of a zero bias peak in $G(V)$. The MZM is expected to drive the system to the perfect Andreev reflection fixed point: an electron incident on the tunnel barrier from the lead should be reflected as a hole, with a Cooper pair absorbed into the nanowire. As a result, the height of the zero bias peak should be quantized to $G(0) = 2e^2/h$ for a range of magnetic fields, backgate voltages, and tunnel barrier height.

Recent experiments have measured quantized zero bias peaks in Al/InAs VLS nanowires [274] and zero bias peaks approaching quantization in Al/InAs 2DEGs [197]. In the former, the peak height remains pinned over a range of tunnel gate barrier height (Fig. 2.5) and magnetic field. The zero bias peaks only appear when all the conditions for topological superconductivity are met (magnetic field parallel to the wire with strength sufficient to drive the system into the spinless regime without driving the superconductor normal). The 2DEG experiment demonstrates zero bias peaks that appear to approach quantization as temperature is lowered and can be fit to a theoretical model in which finite temperature combined with tunnel broadening of the MZM contribute to the peak height not being quantized [197]. For both experiments, the wire has a hard superconducting gap at zero magnetic field.

Zero bias peaks can also arise from non-topological effects, caused for instance by trivial Andreev bound states forming at the end of the wire. Numerous studies have argued that such states could form in the presence of smooth chemical potential variations [210, 144, 242] and even stick to zero energy [177, 178] to mimic the experimental results of Ref. [274]. These numerical studies have been supported by an experiment on proximitized InAs quantum dots that found similar transport signatures despite definitely not hosting MZMs [163]. Therefore, while the results of Refs. [274] and [197] are certainly encouraging, they have not definitively demonstrated the existence of MZMs. We return to this point at the end of this section.

Coulomb blockade

We next consider transport in the Coulomb-blockaded regime to detect the trivial to topological phase transition of a floating 1D superconductor. The setup is shown in Fig. 2.6. A proximitized semiconductor wire is separated by tunnel barriers on either end from two normal metal leads. When the charging energy of the wire E_C is smaller than the induced superconducting gap, a single electron can only tunnel into the wire at the charge degenerate point between two Coulomb valleys. In the trivial superconducting phase, these valleys are $2e$ periodic, which is reflected in a two-terminal conductance measurement. For the topological phase, these valleys are $1e$ periodic, indicating the presence of the zero energy state shared between the MZM pair. This crossover from $2e$ to $1e$ periodicity as the magnetic field is increased is indirect evidence of MZMs.

Taken independently, observing the transition from $2e$ to $1e$ periodicity in the two-terminal conductance could simply indicate that the superconductor is being driven normal by the mag-

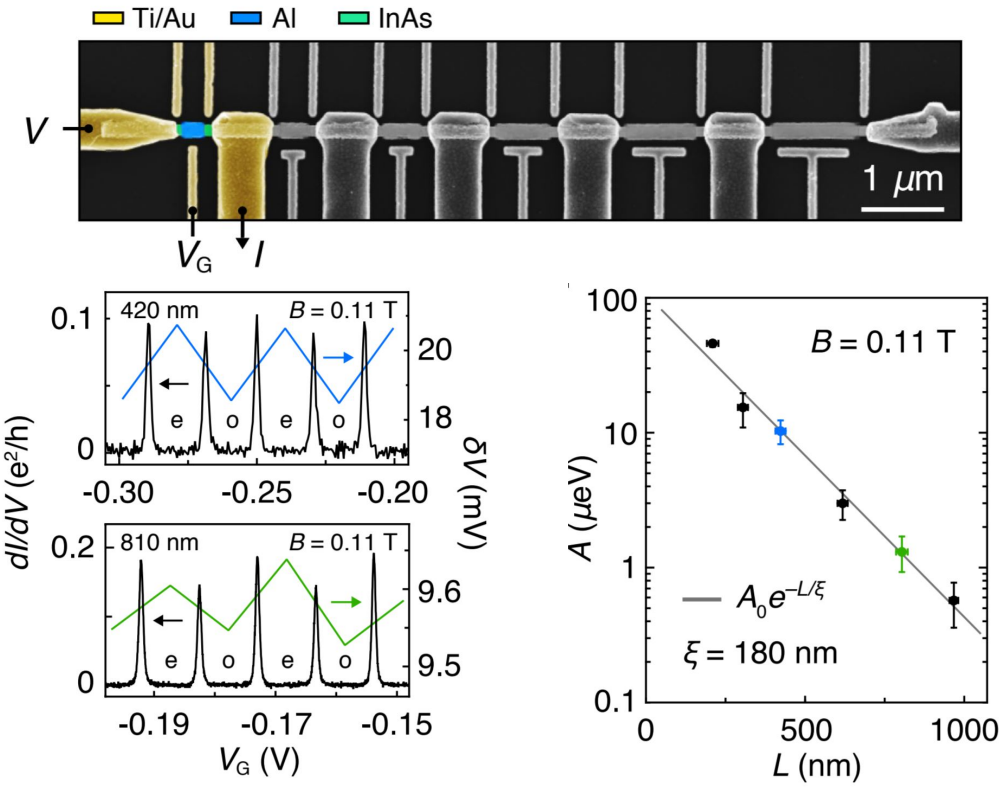

Figure 2.6: Coulomb-blockade on full shell Majorana nanowire. Top panel: Micrograph of device with six different proximitized regions, ranging from 210 nm (highlighted segment) to 970 nm. Left panel: Adjacent Coulomb valleys have slight even-odd effect, interpreted as resulting from the MZM hybridization across the proximitized segment. Left axis is the fine-scale Coulomb peak conductance, right axis (colored traces) is the valley spacing. Right panel: Averaged even-odd peak spacing differences for the six proximitized regions shown in (a), fit to an exponential. Reprinted with permission from Ref. [250].

netic field. The stronger evidence for this being a signature of the topological phase transition instead comes from quantifying deviations from perfect $1e$ periodicity. For a finite wire, the two parity states of the MZMs will be split in energy by an amount that scales as $e^{-L/\xi}$. This degeneracy splitting will result in an even-odd effect, where odd valleys are slightly narrower than even valleys (or vice versa). References [5, 250] argued that by averaging over many valleys they were able to quantify the even-odd effect and thereby extract the degeneracy split-

ting [2]. Comparing the degeneracy splitting over different wire lengths (for multiple devices in Ref. [5] and for different regions of the same wire for Ref. [250]) allowed them to analyze how this degeneracy splitting scales with wire length. Both experiments fit their data to an exponential curve.

After the publication of Ref. [5], a numerical study called into question whether the exponential fit could be interpreted as an indication of topological protection, arguing that to reproduce the experimental results with a theoretical model required the presence of both MZMs and trivial Andreev bound states [64]. Other concerns regarding the experimental data of both Refs. [5, 250] are that the exponential fit only comes from a limited number of points, and that the interpretation of several of these points is subtle [3]. Other subtleties arise when considering the averaging procedure over many Coulomb valleys to extract the degeneracy splittings for different lengths, and whether we actually expect different devices to exhibit the same ξ and thus fall onto such an exponential curve. [4]

Discussion

Experimental evidence for MZMs from transport signatures remains controversial for the reasons mentioned above. The most natural explanation to describe the multitude of experimental results [190, 79, 74, 65, 95, 80, 191, 222, 5, 78, 197, 113, 274, 250] is as signatures of MZMs,

[2]Reference [250] uses a different approach to engineer topological superconductivity than the other experiments discussed, replacing the role of the Zeeman splitting in Refs. [181, 200] with the superconducting phase winding in a full-shell nanowire [182].

[3]The top-most point indicates a degeneracy splitting greater than the induced superconducting gap, while the bottom-most is below the temperature of the system.

[4]For instance, theory predicts that the degeneracy splitting have non-universal oscillatory behavior in addition to the envelope exponential scaling, see discussion in Chapter 5.

however, none of these experiments taken independently definitively demonstrates the realization of a topological superconductor. As such, there is a strong interest in the community in moving beyond transport experiments to directly probe the topological nature of MZMs. Some proposals for near-term directions along these lines are given in Ref. [1] and at the end of Chapter 4.

In this thesis, we take the view that while experiments have not yet engineered MZMs capable of supporting topological quantum computation, the promising trajectory suggests that such MZMs will be realized in the not-too-distant future. We therefore turn our attention to Majorana-based quantum computation, and assume that the current issues affecting MZM experiments (e.g., soft superconducting gap in the presence of a magnetic field, reproducibility of electrostatic environments, scalability of fabrication techniques) will be resolved. For the remainder of this thesis, we will consider MZMs occurring at the endpoints of a 1D superconductor deep in the topological phase.

2.5 Majorana-based quantum computing

We finally turn to how MZMs could be utilized for topological quantum computation. The basic idea behind all Majorana-based quantum computing proposals is to store information in the fermion parity of pairs of MZMs and to manipulate this information through braiding and measurement. Provided the MZMs are kept well-separated at all times, the stored information will be robust to local environmental noise. More specifically, errors occur from processes that couple the MZMs. Finite spatial separation L and temperature T result in error rates that scale

as $e^{-L/\xi}, e^{-\Delta/T}$, where Δ and ξ are the topological superconducting gap and correlation length, respectively. Additionally, since a topological superconductor is technically a fermion parity-protected topological phase [38] rather than a true topological phase, it is also vulnerable to quasiparticle poisoning (processes which add an electron to the system) [108, 51, 216]. Later chapters will discuss the effect of these error processes at length.

A single topological superconducting wire hosts two MZMs and consequently has two degenerate ground states. However, conservation of fermion parity dictates that a floating superconductor must at all times remain in a definite fermion parity state. [5] Therefore, to prepare a superposition state, we need at least four MZMs (two wires) belonging to the same superconducting island. Labeling their corresponding operators as γ_j, for $j \in \{1, 2, 3, 4\}$, one basis choice for the qubit is

$$|0\rangle = |i\gamma_1\gamma_2 = +1, i\gamma_3\gamma_4 = +1\rangle \tag{2.29}$$

$$|1\rangle = |i\gamma_1\gamma_2 = -1, i\gamma_3\gamma_4 = -1\rangle. \tag{2.30}$$

Both $|0\rangle$ and $|1\rangle$ have total fermion parity even: $-\gamma_1\gamma_2\gamma_3\gamma_4 = 1$.

In this section, we first consider braiding MZMs in 1D wire networks. We exemplify three such schemes in proposals for Majorana-based qubits, highlighting the pros and cons of each. We then discuss the limitations of using MZMs for topological quantum computing.

[5] An excellent discussion of this point in a number conserving analysis of a 1D topological superconductor is given in Ref. [93].

2.5.1 Braiding MZMs in 1D wire networks

As reviewed in Section 2.1, adiabatically exchanging a pair of MZMs corresponding to γ_i and γ_j is given by the operator $R^{(ij)} = (1 + \gamma_i\gamma_j)/\sqrt{2}$. For the basis given in Eq. (2.29),

$$R^{(12)} = R^{(34)} = e^{-i\pi/4} \begin{pmatrix} 1 & 0 \\ 0 & i \end{pmatrix}, \qquad R^{(23)} = R^{(14)} = \frac{1}{\sqrt{2}} \begin{pmatrix} 1 & i \\ i & 1 \end{pmatrix}. \tag{2.31}$$

Together with single and two-qubit measurements, the above are sufficient to implement any Clifford gate in a topologically protected way.

Our focus thus far has been on proposals for realizing MZMs in 1D topological superconductors. Clearly, a purely 1D system does not support braiding as MZMs cannot be passed through each other. Below, we sketch several ways to overcome this issue using 1D wire networks.

T-junctions

Figure 2.7 demonstrates that a 1D wire network in the geometry of a T (a so-called "T-junction") can be used to exchange the positions of a pair of MZMs, provided that we are able to physically move the domain wall separating the topological and trivial phases [7]. The braiding protocol utilizes a simple three-point turn, familiar to all fellow directionally challenged drivers. The pressing question is whether such a protocol actually implements the braid operator $R^{(ij)}$. Note that Ivanov's argument for vortices in a p+ip superconductor [132], re-

viewed at the beginning of this chapter, does not apply in this situation.

Amazingly, exchanging MZMs in a T-junction does in fact result in non-Abelian braiding. Following the presentation in Ref. [7], this remarkable result can be understood simply by mapping the problem onto the Kitaev chain with parameters chosen such that the system is purely real. Considering the Hamiltonian in Eq. (2.13), we set $\Delta = 0$ in the trivial phase, and $\Delta \neq 0$ with $\phi = 0, \pi$ in the topological phase. We can pictorially represent $\phi = 0$ with rightward/upward pointing arrows and $\phi = \pi$ with leftward/downward pointing arrows. Studying Fig. 2.7a, we see that to exchange the MZMs at either end of the wire we necessarily reverse the directions of the arrows. Thus, to complete the braid, we need to return the Hamiltonian to its original form using a gauge transformation. This can be done by multiplying all fermionic creation operators by i. In doing so, we see that the non-local fermionic operator composed of the two MZMs transforms as $f^\dagger = (\gamma_1 - i\gamma_2)/2 \to if^\dagger = (\gamma_2 + i\gamma_1)/2$, or equivalently,

$$\gamma_1 \to \gamma_2, \qquad\qquad \gamma_2 \to -\gamma_1. \tag{2.32}$$

We thus recover the same braiding transformations as for a vortices in a 2D p+ip superconductor.

Finally, note that these results hold for the 1D topological superconductor phase realized in semiconductor-superconductor heterostructures, as the Hamiltonian of the latter system can be smoothly connected to the topological phase of the Kitaev chain.

Example: Keyboard gates. The problem now reduces to how can we physically move the

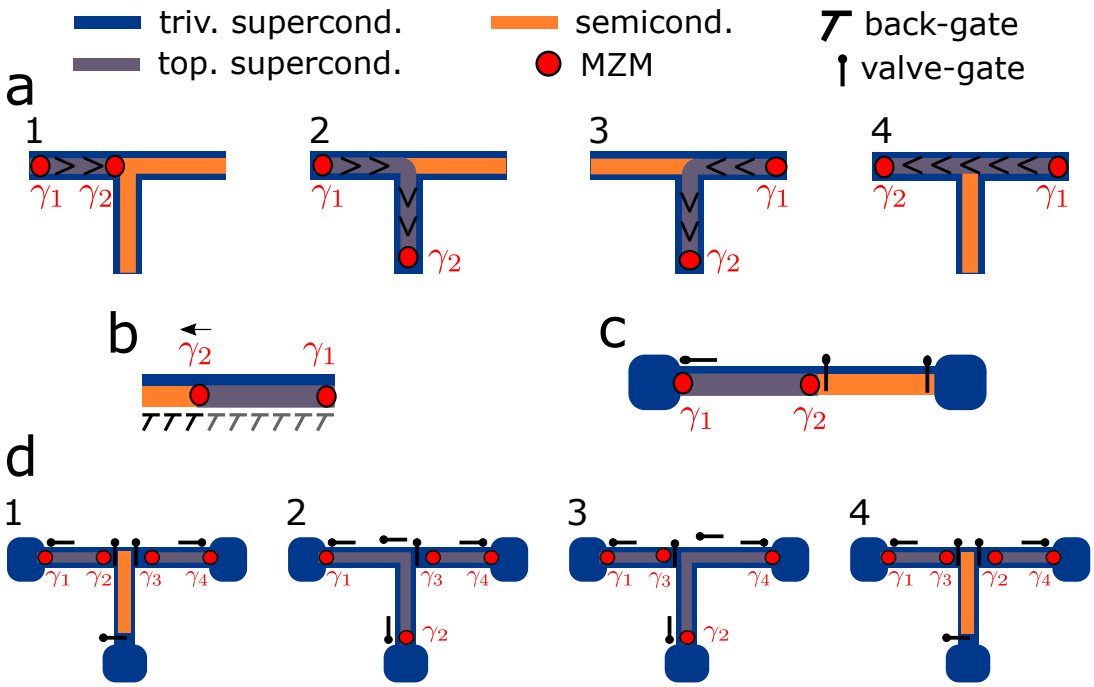

Figure 2.7: Two proposals for implementing braiding MZMs in a semiconductor/superconductor T-junction. a) Proposal of Ref. [7]. Different regions of the semiconductor/superconductor are tuned into the topological phase, hosting MZMs γ_1 and γ_2. By moving the domain wall separating the topological and trivial phase by following steps 1, 2, 3, 4, 1, γ_1 and γ_2 are interchanged. The arrows indicate that to return the system to the initial state, a gauge transformation must be performed, which implements the non-trivial braiding statistics (see discussion in main text). b) The domain walls can be moved using a pattern of backgates, to tune local segments of the semiconductor into and out of the topological phase. This approach is known as "keyboard gates." c) An alternative approach for moving domain walls is to raise and lower "valve-gates", which cut the system into disjoint segments when lowered [1]. The ends of the semiconductor/superconductor wire are contacted by bulk s-wave superconductors. When the valve-gate between the bulk superconductor and the wire is lowered, the wire has a finite charging energy and the MZMs for the associated segment of the T-junction are strongly hybridized. We do not show these MZMs as they occupy a fixed parity state. Conversely, when the valve-gate is open, the associated segment of the T-junction is in a topological phase. d) Braiding in the Aasen proposal can be implemented following the sequence 1, 2, 3, 4.

domain walls of a topological superconductor. Reference [7] proposed using a sequence of "keyboard gates" as depicted in Fig. 2.7b to tune the local chemical potential. Provided we have sufficient tunability of the chemical potential in the semiconductor, we should be able to change which regions are in the topological phase and thereby move the domain walls hosting MZMs.

This proposal presents several challenges. Foremost, screening from the s-wave superconductor limits the tunability of semiconductor's chemical potential; no experiment to date has been able to move the domain wall separating topological and trivial phases. Additionally, at certain stages of the braiding protocol, perpendicular wires must simultaneously be in the topological phase. This requires the existence of perpendicular magnetic fields (for the proposals of Refs. [181, 200]), which could weaken or even destroy the superconducting gap. Finally, there is some worry that the tuning required by this proposal might not be implemented smoothly enough to satisfy the adiabatic condition, and could therefore introduce additional diabatic errors (see Chapter 3).

Example: Aasen proposal. A variant of this approach to braiding was proposed by Ref. [1], shown schematically in Fig. 2.7c and d. In this proposal, keyboard gates are replaced by four gate-tuned valves (c), which can be used to connect/disconnect different regions of the T-junction from each other and bulk superconducting contacts. When the valve between the T-junction and bulk superconducting contact is open, corresponding to Josephson energy E_J much greater than charging energy E_C, the parity states of the wire are degenerate and the wire

hosts MZMs at its endpoints. Conversely, when the valve is closed, $E_C \gg E_J$, the parity states are split in energy and there is a unique ground state. Similarly, when a valve at the center of a T-junction is open, the MZMs at the ends of the two wire segments are strongly hybridized, essentially healing the two segments into a single topological superconductor. When the valve is cut, the MZMs are uncoupled and contribute to the ground state degeneracy. In this proposal, all valve tunings are assumed to be performed adiabatically such that the system remains in the degenerate ground state subspace at all times.

The sequence shown in Fig. 2.7d essentially replaces moving the domain wall separating topological and trivial phases with tuning a full leg of the T-junction into a topological or trivial phase all at once. The hope is that screening from the superconductor will not be as prohibitive to this approach as to keyboard gates. However, the gate-tuned valves introduce a new difficulty, in that we must be able to fully open and fully close them, which is experimentally challenging. Concerns regarding the geometric constraints on the external magnetic field and diabatic errors also remain.

T-junction with tunable couplings

Some of the difficulties associated with the T-junction reviewed above can be circumvented with the T-junction of Fig. 2.8. In this setup, tuning regions into and out of the topological phase is replaced by dynamically changing the coupling between pairs of MZMs [6]. The T-junction is composed of four MZMs. At the initial and final configurations, two of the these

[6]The Aasen proposal could be viewed in the same manner, γ_1, γ_3 in Fig. 2.8 are γ_2, γ_3 in the initial setup of Fig. 2.7d, and the trivial segment of the T-junction really contains two strongly hybridized MZMs.

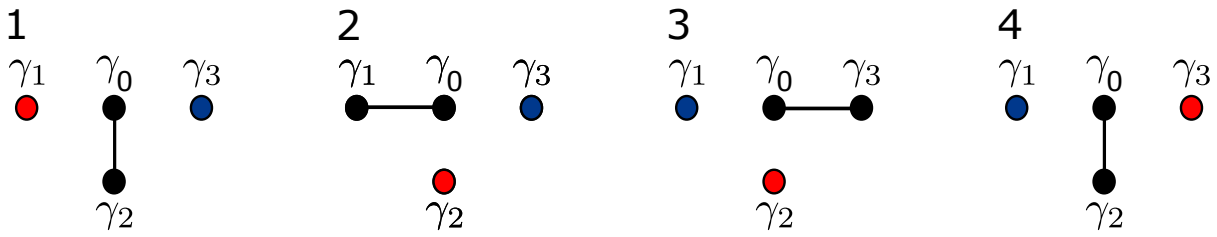

Figure 2.8: Braiding by changing the couplings between different MZMs. The T-junction is formed from four MZMs, γ_1, γ_2, and γ_3 at the endpoints and γ_0 in the center. When the center MZM is coupled to one of the outer MZMs (black-line), the associated parity is fixed and the pair forms an ancilla degree of freedom. By changing the couplings according to the sequence shown, we change which pair of MZMs form the ancilla and teleport the states of γ_1 and γ_3 to implement a counter-clockwise braid.

MZMs are completely decoupled (up to exponentially suppressed corrections) and will, in part, comprise the topological qubit, while the other two MZMs are an ancillary pair that are coupled to each other. The braiding operation is partitioned into three steps, that end at time t_1, t_2, and t_3, respectively. Each step changes which MZMs are decoupled (and correspond to the topological qubit pair) and which MZMs are coupled (and correspond to the ancillary pair). We call the configurations at the end of each step a turning point.

The Hamiltonian for the system takes the form

$$H = -\sum_{j=1}^{3} \Delta_j(t) i\gamma_j\gamma_0, \tag{2.33}$$

where $\Delta_j(t)$ ranges between 0 and $\Delta > 0$. In each panel of Fig. 2.8, the dots represent MZMs and the line connecting two dots represents a Hamiltonian of the form of Eq. (2.33) with the corresponding $\Delta_i = \Delta$ and all other $\Delta_i = 0$. By changing which MZM is coupled to the central MZM in an adiabatic manner, the topological state information is teleported between MZMs, so as to always be encoded in the uncoupled MZMs. Following the indicated sequence of such

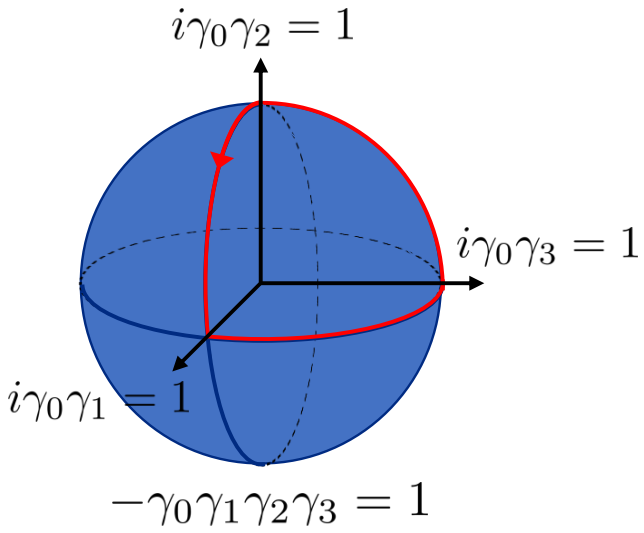

Figure 2.9: In the total fermion parity even subspace, the sequence of Fig. 2.8 sweeps out an octant of the Bloch sphere, corresponding to a phase of $\pi/4$. This phase is topologically protected provided accidental couplings between MZMs are exponentially suppressed.

teleportations results in a braiding transformation of the topological qubit pair of MZMs.

It is worth elaborating on why this braiding protocol is a topologically protected operation. The key idea is that the information is at all times stored in degenerate (up to exponentially small corrections) states because one of the computational MZMs is decoupled at all times. Following the presentation in Ref. [137], it is helpful to visualize the braiding protocol on the Bloch sphere for the even parity sector, as shown in Fig. 2.9. The protocol outlined above corresponds to tracing out an octant of the Bloch sphere (i.e., picking up a phase $\pi/4$ during the process; the odd parity sector will pick up the opposite phase). Deviations from this trajectory contribute errors to the relative phase error (braiding phase error), and are caused by accidentally coupling to the fourth MZM. Provided these accidental couplings remain exponentially suppressed, the relative phase generated by this protocol is quantized (up to the resulting exponentially small corrections), and the braid is topologically protected. In contrast,

if we wanted to introduce a different relative phase corresponding to some other trajectory on the Bloch sphere, we would not necessarily be able to impose that one of the MZMs remains decoupled at all times. In this case, we would need to fine-tune the magnitudes of the Δ_j and errors would not, in general, be exponentially suppressed.

Example: Top-transmon. One proposal that utilizes this braiding scheme embeds Majorana nanowires onto superconducting islands that can be tunably coupled to each other via Josephson junctions [252, 129]. This set-up can be embedded into a type of superconducting qubit known as a "transmon" [155], and is therefore called a "topological transmon" or "top-transmon" for short [120]. We will return to this proposal in Chapter 3 to illustrate the nature of diabatic errors and how they can be corrected.

The T-junction is shown in Fig. 2.10. Three superconducting islands, each hosting a semiconductor nanowire tuned to have a MZM on either end, are connected via split Josephson junctions to a superconducting phase ground. We label the MZMs at the endpoints of the T γ_1, γ_2, and γ_3. The MZMs γ_1', γ_2', and γ_3' at the center of the T are coupled via a Majorana-Josephson potential. This potential hybridizes the three MZMs in the low-energy subspace, leaving behind a single MZM (γ_0 from Fig. 2.8), which is a linear combination of the γ_j's.

Ignoring the excited states associated with the γ_j's, the low-energy Hamiltonian is given by Eq. (2.33). The couplings Δ_j depend sensitively on the ratio of the Josephson coupling

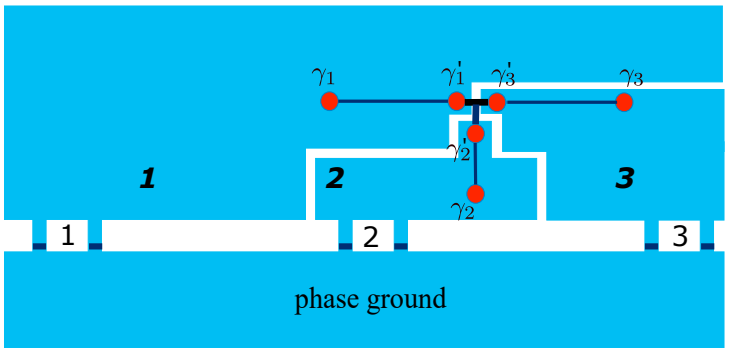

time	$\lvert\Phi_1\rvert$	$\lvert\Phi_2\rvert$	$\lvert\Phi_3\rvert$
0	0	Φ_{max}	0
t_1	Φ_{max}	0	0
t_2	0	0	Φ_{max}
t_3	0	Φ_{max}	0

Figure 2.10: The tunable T-junction proposed in Refs. [252, 129]. The black lines are nanowires hosting MZMs (red dots) at their endpoints. Light blue areas are superconducting islands. The island labeled **j** hosts MZMs γ_j, γ_j' and is connected to the phase ground by Josephson junction j. The magnetic flux through Josephson junction j is Φ_j. We tune the fluxes between 0 and $\Phi_{\text{max}} < \frac{1}{2}\Phi_0$ to change the strength of the Coulomb coupling between the MZM pairs γ_j and γ_j'. The schedule shown in the right panel implements the sequence shown in Fig. 2.8. When $|\Phi_i| = \Phi_{\text{max}}$, Δ_i is maximized and γ_i is coupled to the center MZM γ_0, formed out of a linear combination of the γ_j's.

$E_{J,j}(\Phi_j)$ and charging energy $E_{C,j}$ of each island [129]:

$$\Delta_j \sim \exp\left\{\sqrt{\frac{8E_{J,j}(\Phi_j)}{E_{C,j}}}\right\}. \tag{2.34}$$

The Josephson energy depends on the flux Φ_j threaded through the junction,

$$E_{J,j}(\Phi_j) = E_{J,j}(0)\cos\left(\pi\frac{\Phi_j}{\Phi_0}\right). \tag{2.35}$$

When operated such that $E_{J,j}(0) \gg E_{C,j}$, the couplings Δ_j can be tuned between a maximum value at $\Phi_j = \Phi_{\text{max}} < \Phi_0/2$ and an exponentially vanishing magnitude at $\Phi_j \approx 0$. Therefore, this set-up supports tunable T-junction braiding. The schedule shown in the right panel of Fig. 2.10 implements the counter-clockwise braid of Fig. 2.8.

Finally, we note some of the pros and cons of this proposal. Most notably, the set-up shown

in Fig. 2.10 does not require physically moving domain walls, and thus might be simpler to operate experimentally. The design operation borrows existing techniques from superconducting qubits, only requiring slight modification. However, these schemes still rely on a T-junction architecture and as depicted would require perpendicular magnetic fields. This difficulty could potentially be circumvented by replacing the shape of a T with the shape of an h (so that all topological wire segments are parallel), but is nonetheless believed to suffer from banal engineering issues [199]. Additionally, using grounded superconducting islands means the qubit is susceptible to quasiparticle poisoning.

Measurement-based braiding

Dynamically changing the couplings between pairs of MZMs can be replaced by a sequence of projective parity measurements of the MZM pairs. The scheme outlined in the previous section relied on the assumption that the ancillary pair of MZMs is in the even parity state at each turning point. This was achieved using the adiabatic condition that a gapped system will remain in its ground state at all times if the system evolves sufficiently slowly. By adiabatically changing the parameters of the Hamiltonian in Eq. (2.33), the system evolves according to Fig. 2.8. However, if we could guarantee that a measurement of the ancillary MZMs projects the pair into the even parity state, we do not need to evolve the couplings Δ_i smoothly in time.

More explicitly, the operator $\Pi_0^{(jk)} = (1 + i\gamma_j\gamma_k)/2$ projects the MZMs j and k into the even fermion parity state. Using the anticommutation relations of Majorana operators, we see

that a braid $R^{(12)}$ can be implemented by the following sequence:

$$\Pi_0^{(03)}\Pi_0^{(10)}\Pi_0^{(20)}\Pi_0^{(03)} = \frac{1+i\gamma_0\gamma_3}{2}\frac{1+i\gamma_1\gamma_0}{2}\frac{1+i\gamma_2\gamma_0}{2}\frac{1+i\gamma_0\gamma_3}{2} \tag{2.36}$$

$$= 2^{-4}\left(1-i\gamma_0\gamma_3\right)\left(1-i\gamma_1\gamma_0-i\gamma_2\gamma_0+\gamma_1\gamma_2\right)\left(1-i\gamma_0\gamma_3\right) \tag{2.37}$$

$$= 2^{-4}(1+\gamma_1\gamma_2)\left(1-i\gamma_0\gamma_3\right)^2 \tag{2.38}$$

$$= 2^{-3}\left(1+\gamma_1\gamma_2\right)\left(1-i\gamma_0\gamma_3\right) \tag{2.39}$$

$$= 2^{-3/2}R^{(12)}\otimes\Pi_0^{(03)}. \tag{2.40}$$

(Whether the operator $R^{(12)}$ describes a clockwise or counterclockwise exchange of the MZMs is a matter of convention since the γ_i operators can be changed by a sign via a gauge transformation. Here, we define it as a counterclockwise exchange to match the setup in Fig. 2.8.)

Of course, since operators $\{\gamma_j,\gamma_k\} = 2\delta_{jk}$, there is no way to guarantee the outcome of a measurement of $i\gamma_j\gamma_0$ when the system begins in a definite parity state of $i\gamma_k\gamma_0$. This issue can be overcome by employing "forced measurement." This is a repeat-until-success protocol involving alternating measurements between the pair of MZMs that is to become ancillary and the pair that was ancillary, until the desired measurement outcome is achieved. As each measurement outcome occurs with probability $1/2$, the probability that after n subsequent measurements we have not obtained the desired results decays as 2^{-n}. On average, two successive measurements are required. The process of repeating former measurements only contributes an overall phase and thus does not change the encoded computational state.

The measurement-based braiding protocol described here is topologically protected in the

same sense as the previous proposal. For each stage of the braid, one of the computational MZMs does not participate in any measurements. Errors to the relative phase again only occur from accidental coupling to this MZM, and are exponentially suppressed for the same reasons as for idle MZMs.

Example: Hexon. An obvious benefit of measurement-based braiding is that it frees up the allowed geometry of the MZMs, provided that we can implement pair-wise MZM measurements. One recently proposed Majorana-based qubit operating on this proposal is the "hexon" shown in Fig. 2.11 [141]. We now sketch the essential concepts behind this design, Chapter 4 will be a detailed discussion of this proposal with subsequent chapters analyzing its susceptibility to various noise sources.

The qubit consists of three floating (not grounded) 1D topological superconductors hosting MZMs at either end. The topological superconductors are connected by a strip of s-wave superconductor in the center (the "backbone" of the qubit) to form a single superconducting island. As the superconducting backbone does not need to be tuned to a topological phase, the magnetic field needed to tune the three 1D topological superconductors can be aligned in the same direction (thereby greatly simplifying the previously discussed proposals).

When operated away from charge degeneracies, i.e., in Coulomb valleys, the overall parity of the hexon $-i\prod_{j=1}^{6}\gamma_j$ will be fixed and the charging energy will protect the system from quasiparticle poisoning (unpaired fermionic quasiparticles hopping onto or off of the island). Explicitly, quasiparticle poisoning events will be suppressed by $\exp(-E_C/T)$. As such, the

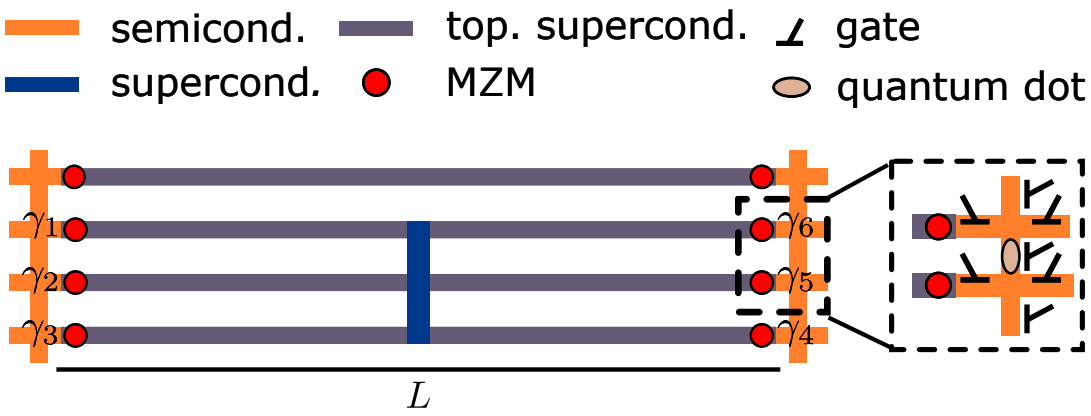

Figure 2.11: The hexon consists of three 1D topological superconductors (gray), joined into a single superconducting island by the vertical superconducting backbone (dark blue). We label the six MZMs (red dots) forming the hexon γ_j, $j \in \{1, \ldots, 6\}$. The hexon is connected at either end to a semiconducting wire network (orange), that can be used to connect multiple hexons into a scalable architecture and to perform MZM parity measurements. Above the hexon is a coherent link (floating 1D topological superconductor), which can be used to facilitate parity measurements involving MZMs on either end of the hexon. The inset shows that quantum dots can be tuned into the semiconductor using electrostatic gates, which can then be used to facilitate measurements of the MZM parity. Chapter 4 is a detailed analysis of this and similar Majorana-based qubit designs.

hexon has a four-dimensional (nearly) degenerate ground state subspace, which can encode a qubit and an ancilla. (A quasiparticle poisoning event would constitute a leakage error, transitioning the system out of the ground state subspace.) To avoid errors from splitting the ground state degeneracies of the MZMs, it is important both that the 1D topological superconductors be long ($L \gg \xi$), and that the relative charging energy between the wires we suppressed. Provided there is a strong connection between the superconducting backbone and the superconducting shell of the 1D topological superconductors, the latter requirement can be satisfied (see Chapter 4 for details). Hexons are therefore expected to exhibit exceptionally long coherence times when these conditions are satisfied (see Chapter 5).

Braiding is implemented by measurements, which can be done by coupling MZMs to an

adjacent quantum dot in the semiconducting structure connected to the ends of the hexon. Any pair of MZMs belonging to the same side of the wire can be measured by connecting them to a single quantum dot and then probing the ground state energy, charge, or capacitance of the quantum dot. Two-MZM measurements involving both sides of the hexon can be implemented by using a coherent link (floating 1D topological superconductor) above the hexon. The MZMs of the coherent link are in a definite parity state, thus a four-MZM measurement can be used to infer the desired two-MZM parity. Additionally, four-MZM measurements between different hexons can be used to entangle the qubits. These measurements are described in detail in Chapter 4.

The hexon overcomes many of the issues facing previous MZM braiding proposals: (1) the magnetic field can point in a single direction, (2) measurement-based braiding avoids diabatic errors, (3) the device is quasiparticle-poisoning-protected, and (4) the fabrication appears significantly simpler than that of Fig. 2.10. Remaining difficulties include: determining the best approach for fabricating the superconducting backbone such that subgap states are not introduced and the superconductor is not killed by the magnetic field; and implementing the quantum dot-assisted measurements of MZMs.

2.5.2 Quantum information constraints

One benefit of Majorana-based quantum computing is that Clifford operations may be implemented with topological protection via braiding and measurement. However, the Gottesman-Knill theorem demonstrates that Clifford operations (which can be generated from the Hadamard

gate, Phase gate, and CNOT gate) can be efficiently modeled on a classical computer by updating the list of stabilizers that define the ground state vector at each computational step [110]. Nevertheless, Clifford operations are valuable because they can be augmented by a single additional (non-Clifford gate) to support universal quantum computation [45] and they play a significant role in prominent error correction protocols [109].

A popular approach to implementing a non-Clifford (and thus not topologically protected in a Majorana-based architecture) gate is to use magic state distillation to produce T-gates. Below, we outline the basic idea behind magic state distillation. We then highlight how residual error sources will affect the qubit operation, and how these can be further reduced using quantum error correction.

T-gates and magic state distillation

This section originally appeared in Ref. [141] and is reprinted with permission.

While the addition of any non-Clifford gate suffices [194, 195, 52], an attractive choice is the T gate (also known as the $\pi/8$ phase gate)

$$T \equiv \begin{pmatrix} 1 & 0 \\ 0 & e^{i\pi/4} \end{pmatrix}. \tag{2.41}$$

Given the ability to perform Clifford gates and perform measurements, the ability to apply a T

gate is equivalent to the ability to generate ancillary qubits in a "magic state," such as

$$\frac{1}{\sqrt{2}}\left(|0\rangle + e^{i\pi/4}|1\rangle\right). \tag{2.42}$$

The fundamental virtue of magic states is that they may be distilled using only Clifford operations [47]. In its original formulation, magic state distillation is a process that consumes 15 low fidelity approximations to the magic state and produces one copy of the magic state with improved fidelity, using only Clifford operations. This procedure requires only very modest fidelity of $1-\epsilon$, where $\epsilon \lesssim 0.14$, for the 15 input magic states to commence and asymptotically yields a magic state with fidelity of $1 - \text{const} \times \epsilon^3$. Much work has since been done on optimizing distillation protocols and related strategies for crossing the divide between Clifford completeness to universal quantum computation, see Refs. [85, 46, 53]. Note that the distillation can either be performed on the physical topological qubits for low-depth circuits, or at the level of logical qubits in error-correcting codes. In the following, we will focus on magic state preparation and distillation for the physical topological qubits. Once an approximate magic state can be prepared on the level of physical qubits, the high fidelity Clifford gates also allow preparation of an approximate logical magic state.

Magic state distillation will constitute the bulk of the work of any quantum computer of a few hundred qubits with topologically protected Clifford gates. For larger quantum computers, the cost of communication, i.e., use of Swap gates, could rival distillation as an expense until long-range communication is properly addressed. For this reason, the circuit depth for magic state distillation is a good surrogate for the overall efficiency of the layout of a quantum computer.

Magic state distillation is often presented without a concrete qubit architecture in mind, where all unitary Clifford gates and measurements are possible on all qubits and all pairs of qubits (a complete graph model). Essentially, one needs the ability to prepare approximate magic states. The closer these states are to Eq. (2.42), the fewer rounds of distillation are necessary. Conceptually, the simplest way to prepare a magic state in a Majorana-based architecture is to split the degeneracy between the qubit states given in Eq. (2.29) for a fixed amount of time so that the dynamical phase $e^{i\int dt\varepsilon_{\text{hyb}}(t)}$ introduces a relative phase of $\pi/4$ between the basis states $|0\rangle$ and $|1\rangle$. Clearly this state preparation is unprotected as it depends sensitively on the magnitude of the hybridization energy $\varepsilon_{\text{hyb}}(t)$ and the timing of coupling. More sophisticated procedures are proposed in Refs. [228, 67, 129, 18, 66, 137, 142].

Quantum error correction

Thus far, the emphasis of Majorana-based quantum computation has been on realizing MZMs experimentally and understanding how to encode qubits in their degenerate ground state space so that errors scale as $e^{-L/\xi}, e^{-\Delta/T}, e^{-E_C/T}$. These intrinsic error rates set an upper bound on the lifetime of a Majorana-based qubit. In order to store information for a longer time, it is necessary to perform quantum error correction on the system. For a given quantum error correcting code, if the physical error rate is below a particular value, known as the code's pseudo-threshold, the qubit's lifetime is increased and a longer quantum computation can be performed. Studying the effectiveness of quantum error correcting codes for Majorana-based systems is a relatively recent development [48, 246, 50, 256, 168, 254, 158, 207, 167, 175, 174, 122, 255, 176]. Here we note several open questions regarding quantum error correction

of Majorana-based qubits.

Firstly, some of the dominant errors expected in a Majorana-based quantum computer are quasiparticle poisoning events that change the total fermion parity of the qubit and thus take the system out of the computational space. Such errors are not generally included in standard analyses of quantum error correcting codes. Understanding both how problematic such errors are, and which codes are best equipped to correct for them, is an important open question. Chapter 6 make preliminary progress towards addressing this issue.

Additionally, a quantum computer operated using the measurement-based braiding protocol outlined above will be highly sensitive to measurement errors. Before pursuing such an approach, it will be crucial to understand the impact of faulty measurements, and crucially whether measurement-only topological quantum computing can be made fault tolerant. The answer to this question will have significant impact on which Majorana-based qubit architectures are ultimately pursued.

Lastly, we note that storing quantum information in a degenerate state space means that there is no preferred qubit basis, and similarly no preferred basis in which to perform measurements. This feature could potentially be used to optimize certain operations of a quantum error correcting code. In general, the quantum error correcting codes best suited to a Majorana-based system could be quite different than those best suited to alternate hardwares, because of the differences in how noise affects the system, the topological protection of certain operations, and the ability to perform measurements in any basis.

Chapter 3

Diabatic errors for anyon braiding

Infinity is a dreadfully poor place. They can never manage to make ends meet.

-Norton Juster, *The Phantom Tollbooth*

Topological phases of matter are a potential platform for the storage and processing of quantum information with intrinsic error rates that decrease exponentially with inverse temperature and with the length scales of the system, such as the distance between quasiparticles. However, it is less well-understood how error rates depend on the speed with which non-Abelian quasiparticles are braided. These "diabatic errors" are the subject of this chapter.

In general, diabatic corrections to the holonomy or Berry's matrix vanish at least inversely with the length of time for the braid, with faster decay occurring as the time-dependence is made smoother. We show that such corrections will not affect quantum information encoded in topological degrees of freedom, unless they involve the creation of topologically nontriv-

ial quasiparticles. Moreover, we show how measurements that detect unintentionally created quasiparticles can be used to control this source of error.

3.1 Introduction

Topological phases of matter can protect quantum information indefinitely at zero temperature, so long as all quasiparticles in the system are kept infinitely far apart and all processes are performed infinitely-slowly [147, 193]. If the temperature is not zero and quasiparticles are a finite distance L apart, then errors will occur with a rate $\Gamma \sim \max(e^{-\beta\Delta}, e^{-L/\xi})$, where β is the inverse temperature, Δ is the energy gap to topologically nontrivial quasiparticles, and $\xi \sim 1/\Delta$ is the correlation length [147, 38]. The exponential suppression of thermal and finite-size errors makes topological phases a promising avenue for quantum computing, provided that it is possible to control errors caused by moving quasiparticles in a finite duration of time.

For a system in a topological phase, the energy gap to topologically nontrivial quasiparticles determines a natural time scale, $1/\Delta$. In order to avoid unintentionally exciting quasiparticles, all operations should be performed in a time t_{op} that is much larger than this time scale. On the other hand, the topological degeneracy of non-Abelian anyons is not exact, except when all length scales are infinite, as there will generically be a small energy splitting $\delta E \sim E_0 e^{-L/\xi}$

between all nearly-degenerate states [31]. (Here E_0 is an energy scale related to the kinetic energy of quasiparticles, i.e. an "attempt frequency" for quantum tunneling events.) Rotations between states in this nearly-degenerate state space will only occur so long as braiding is *fast* compared to $1/\delta E$. Attempting to drag charged anyons through a disordered environment presents a similar upper limit on the braiding time [145]. Therefore, we narrow our focus to the regime $1/\Delta \ll t_{\text{op}} \ll 1/\delta E$ and ask the question: within this range of time scales, how does the error rate decrease as t_{op} is increased?

The unitary transformations effected by braiding non-Abelian quasiparticles in a gapped topological phase can be understood as a manifestation of the non-Abelian generalization [265] of Berry's geometric phase [29]. More specifically, in the adiabatic limit, the unitary time evolution can be split into contributions from the dynamical phase, the Berry's matrix, and the instantaneous energy eigenbasis transformation. The dynamical phase is t_{op}-dependent. The combination of the Berry's matrix and the instantaneous energy eigenbasis transformation is known as the *holonomy* and is t_{op}-independent. Consequently, corrections to the braiding transformations due to the finite completion time for a braiding operation can be viewed as a special case of diabatic corrections to the holonomy. In considering such corrections, it is important to keep in mind that, away from the adiabatic limit [44], the time evolution of states does not cleanly separate into a t_{op}-independent holonomy and a t_{op}-dependent dynamical phase. In other words, for diabatic evolution, what one considers to be the dynamical phase is somewhat arbitrary. For the purpose of comparing with the adiabatic limit, it will be most convenient for us to call the quantity $-\int_0^{t_{\text{op}}} dt E(t)$ the "dynamical phase," where $E(t)$ is the instantaneous

ground-state energy of the time-dependent Hamiltonian, even when we are not working in the adiabatic limit. Factoring this dynamical phase out of the (diabatic) time evolution operator, the remainder will generally depend strongly on the details of the Hamiltonian and will no longer simply be equivalent to the holonomy (which it equals in the adiabatic limit). The deviation of the remainder from its adiabatic limit is precisely what we wish to analyze for braiding transformations of topological quasiparticles.

Generically, diabatic corrections to the transition amplitude from a ground state to an excited state vanish as $\mathcal{O}(1/t_{\text{op}})$ as t_{op} is taken to infinity [44]. However, the scaling of diabatic corrections is sensitive to the precise time-dependence of the parameters in the Hamiltonian. In particular, the corrections are $\mathcal{O}(1/t_{\text{op}}^{k+1})$ when the time-dependence is C^k smooth [169, 263, 3], and are exponentially suppressed when the time-dependence is analytic [105, 135, 136, 196, 134]. (Infinitely smooth C^∞ time-dependence may result in stretched exponential decay of corrections.) As transitions out of the ground state subspace may affect the topological degrees of freedom, diabatic corrections to braiding do not appear to exhibit the nice topological protection, i.e. exponential suppression of errors, that thermal and finite-size corrections exhibit. Moreover, they seem to depend on details to a worrisome extent, though one may question whether this dependence is stable against noise in these parameters, as may arise from coupling to a bath.

On the other hand, quantum information encoded in a topological state space is expected to be corrupted only by the uncontrolled motion of quasiparticles. This is the reason for the temperature and length dependence of error rates: the density of thermally-excited quasiparti-

cles, which decohere the topological states by diffusing through the system, scales as $e^{-\beta\Delta}$; the amplitude for virtual quasiparticles to be transferred between two quasiparticles separated by a distance L scales as $e^{-L/\xi}$, which generically splits degeneracies of their topological states. Hence, one would expect that diabatic corrections to the holonomy would only affect the overall phase of a state, rather than the quantum information encoded in it, unless quasiparticles are created or braided in an unintended manner. In other words, it seems possible for diabatic corrections to be large, but only entering as overall phases when there is no uncontrolled quasiparticle motion, allowing the encoded quantum information to remain topologically-protected.

This is, indeed, the case. Diabatic errors are due to the uncontrolled creation or motion of quasiparticles; other diabatic corrections to the holonomy do not affect the topologically-encoded quantum information. Since these quasiparticles are created by the diabatic variation of specific terms in the Hamiltonian, they can only occur in specific places, i.e. in the vicinity of the quasiparticles' motion paths. These errors can, therefore, be diagnosed by corresponding measurements and corrected. Such protocols apply to diabatic errors, but they cannot correct all errors, such as those due to tunneling or thermally-excited quasiparticles, which must be minimized by increasing quasiparticle separations and lowering the temperature, or by engineering a shorter correlation length and larger energy gap. If all of these different sources of errors were significant, it would require a full-blown error-correcting code to contend with them. In this paper, we focus on corrections which are not exponentially suppressible and we leave implicit errors due to non-zero correlation length and finite gaps.

Previous studies have considered the effects of diabatic evolution on particular topolog-

ical systems. Refs. [59, 140, 229] have investigated the stability of Majorana zero modes (MZMs) [218, 257, 146] outside the adiabatic limit and other papers have suggested methods of reducing the diabatic error for MZMs [139, 138] and for Kitaev surface codes and color codes [55]. In this paper, we consider diabatic error for braiding more broadly. We present results on the magnitude, origin, and correction of diabatic errors for general anyonic braiding. We further apply our results to the braiding of MZMs. In particular, we concentrate on MZMs in topological superconducting nanowires [146, 181, 200, 6], both for concreteness and also because experimentally such systems have been successfully realized and signatures of MZMs have been observed [190, 74, 79, 95, 220, 65, 191, 80, 125]. The braiding transformations of MZMs in such systems can be implemented in a quasi-one-dimensional geometry by slow variations of the couplings in a nanowire T-junction [7, 226, 252, 129]. We will critically analyze the practical aspects of our theory applied to the braiding and measurement schemes introduced in Refs. [120, 252, 129].

This chapter is structured as follows. After briefly reviewing previous literature on quasi-adiabatic evolution of two-level systems in Section 3.2.1, we investigate the effect of dissipative coupling to a thermal bath in Section 3.2.2. In Section 3.3, we consider the motion of one anyon around a second anyon fixed at the origin within a Chern-Simons effective field theory with fixed anyon number. We show that diabatic corrections to the holonomy do not affect the braiding phase unless diabatic variation of the Hamiltonian parameters causes the moving anyon to have a non-vanishing amplitude of following trajectories that wind a different number of times than intended around the stationary anyon. In Section 3.4.1, we compute the

diabatic corrections to the braiding transformation of MZMs. We show that these corrections are of the form of generic diabatic corrections: the transition amplitude vanishes as $1/t_{\text{op}}^2$. In Section 3.4.2, we show that these errors can be diagnosed by measurements and corrected by a repeat-until success protocol. We generalize this error-correction protocol to generic non-Abelian anyon braiding in Section 3.5. In Section 3.6, we apply our results to the proposal of Ref. [129] and introduce a variation of the qubit therein to facilitate measurements. We critically assess the feasibility of such a correction scheme with current technology in Section 3.7. Finally, we address time scales for anyon braiding in Section 5.5.

3.2 Quasi-adiabatic evolution of two-level systems

3.2.1 Landau-Zener effect and the dependence on turn-on/off

Diabatic corrections to the adiabatic limit asymptotically decrease with the operation time t_{op} with a functional form which depends on the smoothness of the time dependence in the Hamiltonian. In particular, if the time dependence of the Hamiltonian is analytic (within a strip around the real axis), diabatic corrections decay exponentially in the inverse of the rate at which the Hamiltonian evolves. A classic example was provided by Landau [159] and Zener [273], who considered a two-level system with the following time-dependent Hamiltonian:

$$H_{\text{LZ}}(t) = ct\sigma_z - \lambda\sigma_x. \tag{3.1}$$

We will assume $c > 0$ in the following. The state of the system takes the form

$$|\psi(t)\rangle = a(t)\ |\uparrow\rangle + b(t)\ |\downarrow\rangle\,. \tag{3.2}$$

We consider a time evolution starting from $t = -\infty$ and ending at t large, given by

$$\begin{pmatrix} a(t) \\ b(t) \end{pmatrix} = \begin{bmatrix} S_1 & S_2 \\ -S_2^* & S_1^* \end{bmatrix} \begin{pmatrix} a(-\infty) \\ b(-\infty) \end{pmatrix}. \tag{3.3}$$

The matrix elements are (dropping subleading contributions)

$$S_1 = e^{-\frac{\pi}{2}\Lambda} \tag{3.4}$$

$$S_2 = -2\sqrt{\frac{\pi}{\Lambda}} \frac{e^{-\frac{\pi}{4}\Lambda}}{\Gamma(-i\frac{\Lambda}{2})} e^{i\frac{\pi}{4} - i\Phi(t)}, \tag{3.5}$$

where we have defined $\Lambda = \frac{\lambda^2}{c}$ and $\Phi(t) = ct^2 + \Lambda \ln|2ct|$. In the above we take the $t \to \infty$ limit, but keep the time dependence in the oscillatory phase $\Phi(t)$ as it does not have a well-defined limit (this does not affect the diabatic transition probability).

When the system is initially in the ground state, i.e. $a(-\infty) = 1$ and $b(-\infty) = 0$, the final state's probability for a transition into the excited state is given by

$$P_{\mathrm{G}\to\mathrm{E}} = |a(t \to \infty)|^2 = |S_1|^2 = e^{-\pi\frac{\lambda^2}{c}}. \tag{3.6}$$

If the goal is to remain in the ground state, then this is an error, but it is an error that is exponentially small in Λ, the inverse of the speed with which the system is moved through the avoided crossing.

A few comments are in order. In the model in Eq. (3.1), the spectral gap goes to infinity at large times. One might worry that the exponential protection in the Landau-Zener model is an artifact of an infinite asymptotic gap. Since we will generally be interested in Hamiltonians which have a spectral gap that is approximately constant, it is important to see that such protection applies to such Hamiltonians as well. To this end, consider the family of Hamiltonians

$$H_\theta(t) = E_0 \cos(\theta(t))\, \sigma_z + E_0 \sin(\theta(t))\, \sigma_x \tag{3.7}$$

The Hamiltonian $H_{\rm LZ}(t)/\sqrt{c^2t^2+\lambda^2}$ is of this form, with $\cos(\theta(t)) = ct/\sqrt{c^2t^2+\lambda^2}$, $\sin(\theta(t)) = -\lambda/\sqrt{c^2t^2+\lambda^2}$, and $E_0 = 1$. A change of variables to $\tilde{t}(t)$ with $d\tilde{t}/dt = \sqrt{c^2t^2+\lambda^2}$ applied to Schrödinger's equation brings the Hamiltonian $H_{\rm LZ}(t)$ to the form $H_\theta(\tilde{t})$. If the function $\tilde{t}(t)$ is bounded by a polynomial, then the protection will remain exponential in the new time variable, in terms of which the Hamiltonian has a constant gap. Since $\tilde{t} \sim \lambda t$ for small t and $\tilde{t} \sim \pm\frac{1}{2}ct^2$ for large t, this is satisfied.

Although the speed with which the Hamiltonian evolves, as measured by $|\dot{H}|/|H|$, is roughly c/λ near the avoided crossing, the total time of the adiabatic evolution is infinite. This was the price that we paid in order to evolve the system in a completely analytic manner. If the time dependence changes more sharply, so that the total operation time is finite, then the exponential protection will disappear. To see an example of this, we modify the Hamiltonian of Eq. (3.1) to one in which the time dependence occurs over a finite interval. There are several ways to do this; we focus on one that will have relevance to later sections of the paper. We consider a time dependent Hamiltonian of the form

$$H(t) = h(t)\sigma_z - \lambda\sigma_x \tag{3.8}$$

with

$$h(t) = \begin{cases} -ct_{\rm op} & \text{for} \quad t \le -t_{\rm op} \\ ct & \text{for} \quad -t_{\rm op} \le t \le t_{\rm op} \\ ct_{\rm op} & \text{for} \quad t_{\rm op} \le t \end{cases} \tag{3.9}$$

In the adiabatic limit, this Hamiltonian rotates the state of the system between non-orthogonal initial and final states. In the long-time regime, where $\sqrt{c}t_{\rm op} \gg 1$ and $ct_{\rm op} \gg \lambda$, we find that the time evolution operator acquires a correction to its diagonal components (see Appendix A

of Ref. [153] for a derivation):

$$S_1 = e^{-\frac{\pi}{2}\Lambda} - \sqrt{\frac{\pi}{c}}\frac{e^{-\frac{\pi}{4}\Lambda}}{\Gamma(-i\frac{\Lambda}{2})t_{\text{op}}}e^{-i\frac{\pi}{4}+i\Phi(t)}. \tag{3.10}$$

The transition probability is given by

$$P_{\text{G}\to\text{E}} = \frac{\lambda^2}{4c^2 t_{\text{op}}^2} + \mathcal{O}\Big(\frac{e^{-\frac{\pi\lambda^2}{2c}}}{\sqrt{c}t_{\text{op}}}, e^{-\frac{\pi\lambda^2}{c}}\Big). \tag{3.11}$$

Here we only worry about the corrections that do not decay exponentially with Λ.

The $\mathcal{O}(t_{\text{op}}^{-2})$ diabatic transition probability is characteristic of any continuous, but otherwise generic, time dependence. A set of more general results show that errors become smaller as the evolution becomes smoother [169, 263, 3]. If the first k derivatives of the Hamiltonian exist and are continuous, then the diabatic corrections to the transition probability vanish as $\mathcal{O}(t_{\text{op}}^{-2k-2})$. Our primary interest will be diabatic corrections to the holonomy, the scaling of which we will return to at the end of Section 3.3. Previous studies were done in the context of adiabatic quantum computing and thus did not address diabatic corrections to the holonomy.

3.2.2 Effects of dissipation due to coupling to a bath

Although this dependence on the differentiability of the Hamiltonian is mathematically correct, one may worry about its relevance to experimental solid state systems, for which noise and dissipation are unavoidable. At the turn-on and turn-off of the time dependence, when the time derivatives of the Hamiltonian are small, but perhaps not quite zero (hence, requiring a discontinuity in the next higher derivative), noise could wash out some of the sensitivity to the precise values of these derivatives. Hence, it is interesting to study the effect of coupling

to a dissipative bath, which is effectively like randomly adding discontinuities to the time dependence of the system Hamiltonian.

In anticipation of our eventual application to MZMs, we consider the product of *two* two-level systems, which we can think of as spins with the corresponding Pauli operators $\vec{\sigma}$ and $\vec{\tau}$. The two-level systems are coupled to a bath through bath operators B_j as described by the Hamiltonian

$$H = \sum_{j=1}^{3} \left[-\Delta_j(t)(1 + B_j)\sigma_j \otimes \tau_z + H_{Bj} \right]. \tag{3.12}$$

The system has an exact two-fold degeneracy labeled by $\tau_z = \pm 1$, which we think of as distinct "sectors." The bosonic bath, which is a proxy for all of the environmental degrees of freedom other than the two spins, is modeled by a collection of oscillators through the terms

$$B_j = \sum_{\alpha} \tilde{\lambda}_{j\alpha}(a^{\dagger}_{j\alpha} + a_{j\alpha}) \tag{3.13}$$

$$H_{Bj} = \sum_{\alpha} \omega_{j\alpha} a^{\dagger}_{j\alpha} a_{j\alpha}. \tag{3.14}$$

The bath couplings $\tilde{\lambda}$ are chosen to model a zero-temperature Ohmic bath. Each spin component σ_j couples to a different subset of the oscillators $a_{j\alpha}$. The crucial features of this Hamiltonian, which are not generic to all two-level systems, are that σ_j is only coupled to the bath when $\Delta_j(t) \neq 0$ and that the bath is uncorrelated for different σ_j. The first feature was chosen for reasons that will become clear in Section 3.4.1, when we discuss the braiding of MZMs, the choice of uncorrelated noise will be explained in Section 3.6.2.

We choose the time dependence of the $\Delta_j(t)$ to consist of three steps through which the

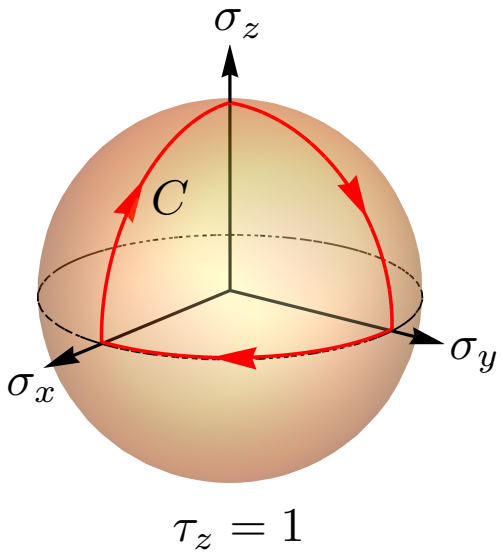

Figure 3.1: In the $\tau_z = 1$ sector the instantaneous eigenstates of $H(t)$ trace out an octant of the Bloch sphere, shown above as the contour C. At times $t = 0, t_1, t_2, t_{\text{op}}$ only one of the Δ_i is non-zero. At these times, σ_i commutes with the Hamiltonian and the corresponding point on the contour is one of the corners or "turning points." The holonomic phase at the end of the evolution is half the solid angle traced out by the contour C, $\frac{\Omega(C)}{2} = -\frac{\pi}{4}$.

instantaneous eigenstates of H circumscribe an octant of the Bloch sphere, as shown in Fig. 3.1. Specifically, we interpolate linearly in time between $(\Delta_1, \Delta_2, \Delta_3) = (0, \Delta, 0)$ at time $t = 0$ and $(\Delta, 0, 0)$ at $t = t_1$; between $(\Delta, 0, 0)$ at $t = t_1$ and $(0, 0, \Delta)$ at $t = t_2$; and finally between $(0, 0, \Delta)$ at $t = t_2$ and $(0, \Delta, 0)$ at $t = t_{\text{op}}$. This evolution is similar to "adiabatic gate teleportation," as discussed in Ref. [11]. In the $\tau_z = 1$ sector, the ground state acquires the holonomic (geometric) phase $-\pi/4$. In the $\tau_z = -1$ sector, the handedness is reversed, and the ground state acquires the holonomic phase $\pi/4$. The dynamical phase, on the other hand, is identical for the two sectors, since they are related by an anti-unitary symmetry which takes $\sigma_j \to -\sigma_j$. Thus, the dynamical phase can be canceled by comparing the $\tau_z = 1$ and $\tau_z = -1$ sectors, and the $\tau_z = -1$ sector picks a $\pi/2$ holonomic phase relative to the $\tau_z = 1$ sector

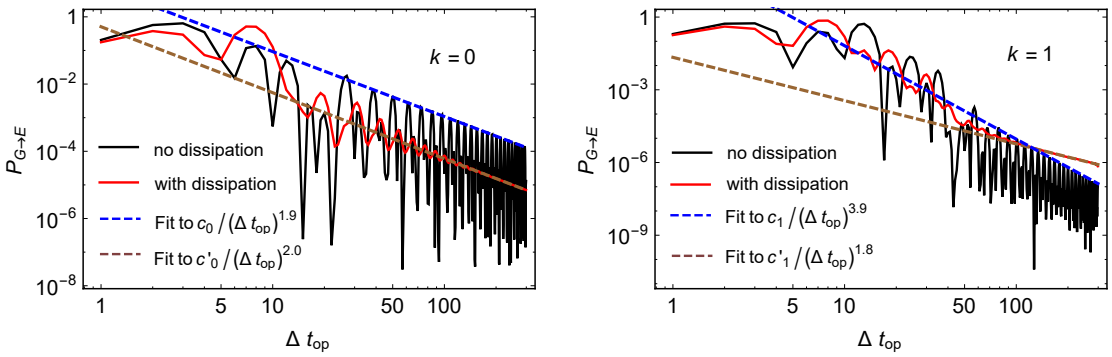

Figure 3.2: With dissipation (red solid line), transition probability $P_{\mathrm{G}\to\mathrm{E}}$ vs the gap multiplied by the total evolution time Δt_{op}, due to diabatic effects for k=0 (left), and k=1 (right). The long time tail is fitted to $c_0/(\Delta t_{\mathrm{op}})^x$ with $x \approx 2$ (brown dashed line). We choose the cutoff $\omega_c = 10\Delta$, Ohmic bath at low temperature $T = 1/\beta = 0.001\Delta$, system-bath coupling $\lambda_1 = \lambda_2 = \lambda_3 = 0.01\Delta$. The black solid line shows the results without dissipation, and the envelope function for long time is is fitted to $c_0'/(\Delta t_{\mathrm{op}})^x$ with $x \approx 2k + 2$ (blue dashed line).

during the time evolution in the adiabatic limit.

In order to quantitatively study the effects of the bath, we numerically solve the master equation for a time-dependent Hamiltonian coupled to a bath (see Ref. [153], Appendix C). We initialize the system in a certain superposition of $|\sigma_y = +1; \tau_z = +1\rangle$ and $|\sigma_y = -1; \tau_z = -1\rangle$, which we expect to yield results that are qualitatively representative of a general input. We first compute the probability of a transition out of the ground state manifold into an excited state for the $\tau_z = 1$ sector, $P_{\mathrm{G}\to\mathrm{E}}$; the $\tau_z = -1$ sector has similar behavior. In Fig. 3.2, we plot $P_{\mathrm{G}\to\mathrm{E}}$ as a function of the total evolution time t_{op}, both with and without dissipation. The left panel shows it for a stepwise linear time dependence ($k = 0$). The right panel shows it for a smoothed-out time dependence ($k = 1$) in which the first derivatives exist and are continuous everywhere, i.e. they vanish at the beginning and end of each time step (see Ref. [153], Appendix D). In the absence of dissipation, the envelope of the decay follows the expected scaling as t_{op}^{-2} and t_{op}^{-4} for $k = 0$ and 1, respectively. As may be seen in the plots, the dissipation suppresses oscillations in

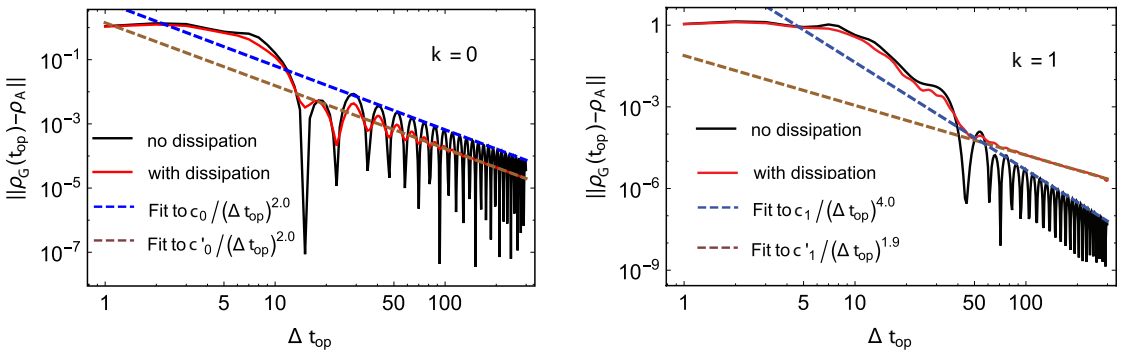

Figure 3.3: The deviation of the density matrix after projection onto the ground state, $||\rho_{\rm G}(t_{\rm op}) - \rho_A||$, versus the gap multiplied by the total evolution time, $\Delta t_{\rm op}$. The parameters are the same as in Fig. 3.2.

the transition probability. For $k = 0$, the dissipative case has the same $t_{\rm op}^{-2}$ falloff at long times. For $k = 1$, however, dissipation has an important qualitative effect at long times: the excitation probability again goes as $t_{\rm op}^{-2}$, rather the $t_{\rm op}^{-4}$ behavior that occurs without dissipation. This can be understood as follows: the suppressed excitation rate for the non-dissipative $k = 1$ protocol relies on the smoothness of the time evolution of the system's Hamiltonian, i.e. the smoothness of the $\Delta_j(t)$. With dissipation, this smoothness is washed out by the random discontinuities added by the bath. For shorter $t_{\rm op}$, however, there remains a quantitative difference between the $k = 0$ and 1 protocols, which suggests some level of engineering the time dependence of the system Hamiltonian remains beneficial.

If we measure the system and find that it remains in the two-fold degenerate ground state manifold, then a phase gate has been applied to this subspace, due to the sector-dependent holonomic phase of $\pm\frac{\pi}{4}$. However, there may have been intermediate diabatic excitations which relaxed, causing the final state to deviate from the adiabatic result. This deviation is quantified

by $||\rho_{\mathrm{G}}(t_{\mathrm{op}}) - \rho_A||$, where ρ_A is the final density matrix obtained in the adiabatic limit,

$$\rho_{\mathrm{G}}(t_{\mathrm{op}}) = \frac{\Pi_G \rho(t_{\mathrm{op}}) \Pi_G}{\mathrm{Tr}\left(\Pi_{\mathrm{G}} \rho(\mathrm{t_{op}})\right)} \tag{3.15}$$

is the density matrix for finite t_{op} projected into the ground state manifold, where Π_G is the projection operator into the ground state and $\rho(t_{\mathrm{op}})$ is the density matrix before the projection measurement, and $||\ldots||$ denotes the trace norm. $||\rho_{\mathrm{G}}(t_{\mathrm{op}}) - \rho_A||$ measures the deviation of the state from the ideal/adiabatic limit result. As shown in Fig. 3.3, $||\rho_{\mathrm{G}}(t_{\mathrm{op}}) - \rho_A||$ exhibits behavior similar to that of $P_{\mathrm{G}\to\mathrm{E}}$. In particular, without dissipation, the long-time asymptotics exhibit t_{op}^{-2k-2} scaling, while the inclusion of dissipation suppresses oscillations in $||\rho_{\mathrm{G}}(t_{\mathrm{op}}) - \rho_A||$ and leads to a power-law decay t_{op}^{-2} at long times.

We believe the t_{op}^{-2} is universal for diabatic transitions in the presence of dissipation. A heuristic explanation is to consider the rate equation for the occupation number of the excited level N_E in the instantaneous basis. Phenomenologically, we postulate that the time evolution of N_E is governed by the following rate equation:

$$\frac{dN_E}{dt} = h(t) - \Gamma(t) N_E. \tag{3.16}$$

Here $h(t)$ describes the generation of excitations due to the matrix element between the ground state $|G\rangle$ and excited state $|E\rangle$, and $\Gamma(t)$ characterizes the relaxation of the excitations. Importantly, in the model Eq. (3.12), the bath coupling is assumed to be synchronized with the time-dependent couplings of the Hamiltonian, whose time variation is responsible for diabatic transitions. Therefore, as a zeroth order approximation we can assume that $h(t)$ and $\Gamma(t)$ have the same time dependence. Furthermore, we have $h(t) \sim \mathcal{O}\left(|\langle E|\partial_t H|G\rangle|^2\right)$. We expect that if t_{op} becomes longer, the speed at which the Hamiltonian changes on average should decrease as

t_{op}^{-1}. To capture this dependence on t_{op} we make a crude estimate of $h(t)$ to be $h(t) = \frac{\Delta}{t_{\text{op}}^2} f(t)$, where $f(t)$ is a dimensionless function whose range is $[0, 1]$, and write $\Gamma(t) = \Gamma f(t)$. The rate equation can now be integrated with the initial condition $N_E(t = 0) = 0$, and the result is

$$N_E(t) = \frac{\lambda}{\Gamma t_{\text{op}}^2} \left[1 - e^{-F(t)}\right], \tag{3.17}$$

where $F(t) = \int_0^t ds f(s)$. It is not hard to see that $F(t_{\text{op}})$ grows at least linearly with t_{op}, so asymptotically we find $N_E(t_{\text{op}}) = \mathcal{O}(t_{\text{op}}^{-2})$.

To summarize, diabatic corrections (to both the transition probability from the ground state to an excited state and to the phase acquired if the system remains in the ground state) are non-universal and dependent on the detailed time dependence of the Hamiltonian in the absence of dissipation. In the presence of dissipation, however, the scaling of diabatic corrections appears to become universal in the limit of large operation time.

3.3 Diabatic corrections to braiding transformations of anyons

In the previous section, we saw that diabatic corrections to the holonomy are only polynomially suppressed in the time t_{op} of the evolution and, for the system of Eq. (3.12), can be as bad as $\mathcal{O}(t_{\text{op}}^{-2})$. This is especially worrisome if the holonomy in question determines the braiding transformations in a topological quantum computer. However, we argue in this section that diabatic corrections to the braiding transformations of anyons originate from the uncontrolled creation or motion of anyons.

We justify this claim by studying the diabatic time evolution for two theories with fixed anyon number, where one anyon braids around the other. We perform these calculations using

Maxwell-Chern-Simons theory [81], which has a finite gap to gauge field excitations. In the first theory, the anyons are forced to move along a specific trajectory. In this case, we find that the corrections to the braiding transformations are independent of the braiding time and are exponentially suppressed by the separation of anyons. In the second theory, the anyons are transported via a pinning potential. In this case, the anyons have some amplitude to tunnel out of the potential trap and possibly wind around the other anyon a number of times that does not match that of the trap motion. The sum over such topologically distinct trajectories, i.e. with different winding numbers, destroys the quantization of the braiding transformation.

Consider an Abelian Maxwell-Chern-Simons theory for two anyons carrying charges a and b, respectively. Anyon b sits at the origin for all time and anyon a sits a distance R away until time $t = 0$, at which it circles the origin and then returns to its initial position. We use $x = (t, \mathbf{r})$ to denote the space-time coordinates collectively. The action is

$$\mathcal{S} = \int d^3x \left(\frac{k}{4\pi} \epsilon_{\mu\nu\lambda} a^\mu \partial^\nu a^\lambda - \frac{1}{4g^2} f_{\mu\nu} f^{\mu\nu} - j^\mu a_\mu \right). \tag{3.18}$$

Between $t = 0$ and $t = t_{\text{op}}$ the moving anyon has current (in the polar coordinate (r, θ)):

$$j_a^0(x) = \frac{a}{r} \delta(r - R) \delta\Big(\theta - \frac{2\pi t}{t_{\text{op}}}\Big) \tag{3.19}$$

$$j_a^\theta(x) = a \frac{2\pi R}{r t_{\text{op}}} \delta(r - R) \delta\Big(\theta - \frac{2\pi t}{t_{\text{op}}}\Big) \tag{3.20}$$

and the stationary anyon has current

$$j_b^0(x) = b \delta^{(2)}(\mathbf{r}). \tag{3.21}$$

All other currents vanish. For a pure Abelian Chern-Simons theory we would expect the braiding transformation to be the phase factor $e^{i2\pi ab/k}$. Adding the Maxwell term gives the in-

teraction a non-topological component, which is exponentially-decaying. Hence, the braiding transformation is expected to have corrections that are exponentially-small in R.

Integrating out a_μ gives the effective action

$$\mathcal{S}_{\text{eff}} = \int d^3x d^3x' \left[j^\mu(x) G^{(1)}_{\mu\nu}(x,x') j^\nu(x') - \frac{g^2}{2} j_\alpha(x) G^{(2)}(x,x') j^\alpha(x') \right]. \tag{3.22}$$

Here, the two propagators are given by

$$G^{(1)}_{\mu\lambda}(x,x') = \frac{\pi}{k} \langle x | \frac{\epsilon_{\mu\nu\lambda}\partial^\nu}{\partial^2(1+\frac{\partial^2}{g^4k^2/4\pi^2})} | x' \rangle \tag{3.23}$$

$$G^{(2)}(x,x') = \langle x | \frac{1}{\partial^2 + g^4k^2/4\pi^2} | x' \rangle. \tag{3.24}$$

Both terms in Eq. (3.22) can be evaluated by transforming to momentum space. One can show that the first term Eq. (3.22) contributes a braiding transformation $e^{i\Phi}$, with the phase

$$\Phi = \frac{2\pi ab}{k} \left(1 - \sqrt{\frac{\pi g^2 kR}{4\pi}} e^{-g^2kR/2\pi} \right) + \mathcal{O}\left(e^{-g^2kR/2\pi} \right), \tag{3.25}$$

which has finite-R corrections, but is independent of the braiding speed [153]. Evaluation of the second term in the action shows that it grows linearly in t_{op} and is the *same for all braiding processes*, i.e. it is independent of the charge of the second anyon at the origin, as is expected for a dynamical phase. If there are diabatic corrections to braiding, they must arise from effects not allowed in this simple theory.

We now modify our theory such that anyon a is dynamical. Its position is no longer a classical parameter but is, instead, controlled by a pinning potential. We move the pinning potential in order to transport anyon a around static anyon b. We again set b to have fixed

position. The effective action reads

$$\mathcal{S} = \int dt \Big[\int d^2\mathbf{r} \left(\frac{k}{4\pi} \epsilon_{\mu\nu\lambda} a^\mu \partial^\nu a^\lambda - j^\mu a_\mu \right) + \frac{1}{2} m \Big(\frac{d\mathbf{q}}{dt} \Big)^2 - V_a(\mathbf{q} - \mathbf{R}(t)) \Big]. \tag{3.26}$$

Here $\mathbf{q}$ is the coordinate of the particle, which is now a dynamical variable. $\mathbf{R}(t)$ parameterizes the trajectory of the pinning potential V_q.

To proceed, we first integrate out a_μ. As before, this will generate a Hopf term for the worldlines and, in the present configuration, this term is just the winding number of $\mathbf{q}(t)$ around the origin.

We can simplify this problem further by ignoring the radial motion of particle a, which is an inessential complication, so we only need to keep the polar angle θ. The above action now can be reduced to the problem of a particle on a ring with a flux tube in the center. However, we still have the external "driving" force that moves the anyon, which is given by the time dependent pinning potential $V_a(\mathbf{q}(t) - \mathbf{R}(t))$:

$$\mathcal{S} = \int_0^{t_{\text{op}}} dt \left[\frac{1}{2} I \dot{\theta}^2 + \frac{ab}{k} \dot{\theta} - V_a \Big(\theta - \frac{2\pi t}{t_{\text{op}}} \Big) \right]. \tag{3.27}$$

Here I is the effective rotational inertia. In the following, we assume that the pinning potential is moving with a constant angular velocity and that the pinning potential completes one circuit and returns to $\theta = 0$ after time t_{op}. The path integral representation of the transition amplitude is

$$\langle \theta \equiv 0 | U(t_{\text{op}}, 0) | \theta \equiv 0 \rangle = \sum_{n=-\infty}^{\infty} \int_{\theta(0)=0}^{\theta(t_{\text{op}})=2\pi n} \mathcal{D}\theta(t) e^{i\mathcal{S}}. \tag{3.28}$$

Notice that we need to sum over different winding number sectors for $\theta(t)$. Let us make

the change of variable $\theta = \tilde{\theta} + \frac{2\pi t}{t_{\rm op}}$, so that $\tilde{\theta}(0) = 0$ and $\tilde{\theta}(t_{\rm op}) = 2\pi(n-1)$. This yields

$$\mathcal{S} = \Big(\frac{2\pi I}{t_{\rm op}} + \frac{ab}{k}\Big)\Big[\tilde{\theta}(t_{\rm op}) - \tilde{\theta}(0)\Big] + \frac{2\pi^2 I}{t_{\rm op}} + \frac{2\pi ab}{k} + \int_0^{t_{\rm op}} dt\,\Big[\frac{1}{2}I\dot{\tilde{\theta}}^2 - V_a(\tilde{\theta})\Big]. \tag{3.29}$$

Let us denote

$$\mathcal{S}_m = \int_{\theta(0)=0}^{\theta(t_{\rm op})=2\pi m} \mathcal{D}\theta(t)\exp\left\{i\int_0^{t_{\rm op}} dt\,\left[\frac{1}{2}I\dot{\theta}^2 - V_a(\theta)\right]\right\}. \tag{3.30}$$

The transition amplitude is then

$$\langle\theta\equiv 0|U(t_{\rm op},0)|\theta\equiv 0\rangle = e^{i\frac{2\pi ab}{k}}\sum_{n=-\infty}^{\infty} e^{i\frac{4\pi^2 I}{t_{\rm op}}(n+\frac{1}{2})+i\frac{2\pi abn}{k}}\mathcal{S}_n. \tag{3.31}$$

In order to find the braiding transformation, we need to compare the above transition amplitude with the case there is no anyon b sitting at the origin. If we let $H_0(t)$ denote the Hamiltonian in this case, we find

$$\langle\theta\equiv 0|U_0(t_{\rm op},0)|\theta\equiv 0\rangle = \sum_{n=-\infty}^{\infty} e^{i\frac{4\pi^2 I}{t_{\rm op}}(n+\frac{1}{2})}\mathcal{S}_n. \tag{3.32}$$

The braiding transformation is, thus, given by the ratio of these two amplitudes, resulting in the phase factor:

$$e^{i\Phi} = \frac{e^{i\frac{2\pi ab}{k}}\sum\limits_{n=-\infty}^{\infty} e^{i\frac{4\pi^2 I}{t_{\rm op}}n}e^{i\frac{2\pi abn}{k}}\mathcal{S}_n}{\sum\limits_{n=-\infty}^{\infty} e^{i\frac{4\pi^2 I}{t_{\rm op}}n}\mathcal{S}_n}. \tag{3.33}$$

The quantization of Φ is destroyed in general because the moving anyon now has some amplitude $\mathcal{S}_{n\neq 0}$ of escaping the pinning potential and tunneling around the static anyon an additional n times. In the adiabatic limit, the system remains in the instantaneous ground state at all

times, so the moving anyon remains trapped in the pinning potential. In this limit, $\mathcal{S}_n = 0$ for all $n \neq 0$, and the braiding phase is quantized to $\Phi = 2\pi ab/k$.

We note that Eq. (3.33) ignores coupling to an environment. Realistically, the environment will detect the sectors associated with distinct winding numbers n, since these are macroscopically different trajectories. This "which-path" information will remove the interference between n-sectors in Eq. (3.33), resulting in a decohered state. Presumably the bath can help to the extent it relaxes the escaped anyon back into the moving trap before it is left behind.

Clearly a theory that does not fix anyon number will also have diabatic corrections to the braiding transformation. A pair of anyons with nontrivial topological charge could be created. If one of the anyons circles a or b before annihilating with its antiparticle, the braiding transformation will be affected. If we braid two anyons with a fixed fusion channel in a non-Abelian Chern-Simons theory, we can reduce the calculation to a calculation in Abelian Chern-Simons theory, since the result must be a phase. So long as we do not allow any type of quasiparticle creation (real or virtual), the fusion channel will remain fixed, so the preceding calculation is, in fact, completely general and pinpoints the source of diabatic errors in the general case.

We have seen that both sources of diabatic corrections to the braiding transformation arise from transitions out of the ground state subspace that result in the uncontrolled motion of anyons – either the anyon a winds around b too many or too few times, or else an anyon pair is created and one of the new anyons winds around a and/or b. We are now in a position to understand the power law behavior of corrections to the braiding transformation shown in Fig. 3.3. Corrections to the braiding transformation must be the result of two transitions: a transition out

of the ground state, causing the error, and a transition back into the ground state allowing us to define an operation within the ground state subspace. As shown in Refs. [169, 263, 3], for $\mathcal{C}^k$ smooth time evolution, the transition amplitude is $\mathcal{O}\left(t_{\text{op}}^{-k-1}\right)$, therefore corrections to the braiding transformations are $\mathcal{O}\left(t_{\text{op}}^{-2k-2}\right)$.

3.4 A correction scheme for diabatic errors to the braiding of MZMs in T-junctions

In the previous section, we found that errors in the braiding transformation caused by diabatic effects originate from the uncontrolled creation or motion of anyons. We now use this result to devise a correction scheme for such diabatic errors. In this section, we focus on the particular example of braiding MZMs in a T-junction and provide concrete proposals in this context. In Section 3.5, we will generalize our diabatic error correction scheme to systems supporting arbitrary types of non-Abelian anyons or defects.

3.4.1 Relation between two-level systems and braiding MZMs at T-junctions

Section 3.2 focused on the adiabatic evolution of two-level systems. Since our main interest is the braiding of quasiparticles in a topological phase, in particular the braiding of MZMs, we pause now to map the braiding and two-level problems onto each other. With such a mapping in hand, we can translate the results discussed in Section 3.2 to the context of quasiparticle braiding in a topological phase. More specifically, we consider braiding of MZMs in a network

of topological superconducting wires. The essential building block of the network is a so-called T-junction.

Recall the tunable T-junction shown in Fig. 2.8 of the previous chapter. At the initial and final configurations, two of the four MZMs comprising the junction are decoupled (up to exponentially suppressed corrections), while the other two form an ancillary pair. (Eventually, it will be convenient to have three MZMs replacing the one in the middle, following Ref. [129], but we will focus on the simpler situation here.) Changing the couplings allows us to change which pair of MZMs form the ancilla. Following the sequence depicted in Fig. 2.8 effectively braids the decoupled pair of MZMs by teleporting the topological state of the MZMs.

As discussed previously, the Hamiltonian for these MZMs takes the form

$$H = -\sum_{j=1}^{3} \Delta_j(t)\, i\gamma_j\gamma_0 \tag{3.34}$$

where $\{\gamma_i, \gamma_j\} = 2\delta_{ij}$ for $i, j = 0, 1, 2, 3$ and $\Delta_j(t)$ ranges between 0 and $\Delta > 0$.

The overall fermion parity of these four MZMs is even when $\gamma_0\gamma_1\gamma_2\gamma_3 = -1$ and odd when $\gamma_0\gamma_1\gamma_2\gamma_3 = +1$. If we fix the overall fermion parity of these four MZMs, they share a two-dimensional topological state space, which we map to a spin-$1/2$ system according to the representation of the Pauli operators $\sigma_j = i\gamma_0\gamma_j$ for overall parity even, and $\sigma_j = -i\gamma_0\gamma_j$ for overall parity odd.

This representation reveals the equivalence between the MZM Hamiltonian of Eq. (3.34) and the spin Hamiltonian of Eq. (3.12) without the bath coupling. In particular, the even and odd overall parity sectors of the four-MZMs Hamiltonian are mapped to the $\tau_z = +1$ and -1 sectors of the two-spin Hamiltonian, respectively. The difference between the holonomies in

the sectors of the two-spin model is mapped to the difference between the holonomies in the even and odd fermion parity sectors of the MZMs, giving the relative phase of the braiding transformation.

Let us focus in more detail on the first step of this process, which transfers the state information initially encoded in γ_1 to γ_2, and occurs between $t = 0$ and $t = t_1$. Consider varying the couplings linearly during this time segment:

$$\Delta_1(t) = \Delta\frac{t}{t_1} \tag{3.35}$$

$$\Delta_2(t) = \Delta\left(1 - \frac{t}{t_1}\right) \tag{3.36}$$

$$\Delta_3(t) = 0, \tag{3.37}$$

so that the $\tau_z = +1$ sector of the spin Hamiltonian (corresponding even fermion parity) takes the following form for $0 \leq t \leq t_1$:

$$H = \Delta\left[\frac{t}{t_1}\sigma_x + \left(1 - \frac{t}{t_1}\right)\sigma_y\right]. \tag{3.38}$$

If we define the following unitary transformation

$$M = \frac{1}{2\sqrt{2+\sqrt{2}}}\Big[i(\sigma_z + \sigma_y)(1+\sqrt{2}) - (i\sigma_x + 1)\Big], \tag{3.39}$$

then

$$MHM^\dagger = \frac{\Delta}{\sqrt{2}}\left[h(t)\,\sigma_z - \sigma_x\right], \tag{3.40}$$

where $h(t) = 1 - \frac{2t}{t_1}$. Thus, we obtain $MHM^\dagger$ to be in the same form as the Landau-Zener Hamiltonian in Eq. (3.8). The other steps in the braiding protocol can also be mapped to Landau-Zener problems that can be pieced together.

The relation between a MZM T-junction and a two-level system implies that the diabatic

errors that we encountered in the latter case will also arise in the former. Consequently, if braiding is not done infinitely-slowly, the resulting unitary transformation will generically differ from the expected adiabatic result by $\mathcal{O}(1/t_{\text{op}})$ errors. This can be improved to $\mathcal{O}(1/t_{\text{op}}^{k+1})$ if the time-dependence of the control parameters of the Hamiltonian is $\mathcal{C}^k$, which requires fine-tuning the time-dependence by setting k derivatives of the Hamiltonian to zero at the initial and final times. On the other hand, Section 3.3 leads us to anticipate that errors in the braiding transformation must be due to the creation or uncontrolled movement of topological quasiparticles. In the next section, we show that this is, indeed, the case: if a sequence of measurements shows that no quasiparticles have been created at intermediate steps of the evolution, then the braiding phase is fixed to its topologically-protected value. Moreover, this fact allows us to specify a protocol for detecting and correcting diabatic error that would affect the braiding transformation.

3.4.2 Error correction through measurement

In this section, we show that projecting the system into the ground state at the turning points during the T-junction braiding process is sufficient to fix all diabatic errors within the MZM system. This suggests an error correction scheme for braiding MZMs, based on a repeat-until-success protocol, that produces topologically-protected gates. For now, we focus on errors occurring within the low energy subspace of the four MZMs, because we expect these errors to be the most prevalent. We address diabatic transitions out of this subspace in Section 3.6.2.

We consider the time evolution depicted in Fig. 2.8. At any point in the system's time

evolution, the energy levels in the even parity sector $\gamma_0\gamma_1\gamma_2\gamma_3 = -1$ are the same as those of the odd parity sector $\gamma_0\gamma_1\gamma_2\gamma_3 = +1$. This follows from the fact that there is always a pair of MZMs that is decoupled from the Hamiltonian (the one that is unaffected during that step of the protocol and a linear combination of the other three), and switching the parity of this pair does not affect the energy. This correspondence between the spectra in the two sectors implies the dynamical phase is identical for both sectors and, thus, does not affect the braiding transformation.

At each turning point of the braiding process, there are two decoupled MZMs which sit at the endpoints of the T-junction: at $t = 0$, γ_1 and γ_3 are decoupled; at t_1, γ_2 and γ_3 are decoupled; at t_2, γ_1 and γ_2 are decoupled; and, at t_3, γ_1 and γ_3 are decoupled. We can consider the unitary time evolution of each step between turning points, which we denote as U_{ij}, to indicate the Hamiltonian starts with γ_j coupled to γ_0 and γ_i decoupled, and ends with γ_i coupled to γ_0 and γ_j decoupled. In this notation, U_{12} is the evolution from time $t = 0$ to t_1, U_{31} is from t_1 to t_2, and U_{23} is from t_2 to t_3. We emphasize that γ_k for $k \neq 0, i, j$ remains decoupled throughout the step corresponding to U_{ij}, as this fact is crucial for the topological protection of the braiding, and we will utilize it to analyze the diabatic error. (By decoupled, we mean up to the residual, exponentially suppressed couplings due to nonzero correlation length. Such exponentially suppressed corrections can easily be made arbitrarily small and so are left implicit throughout this paper.)

Let us first choose a basis for the Hilbert space of the four MZMs. For calculational purposes, it will be useful to employ the basis $|-\gamma_0\gamma_1\gamma_2\gamma_3 = \pm 1, i\gamma_2\gamma_0 = \pm 1\rangle$, specified by

the overall fermion parity of the four MZMs and the parity of the initial/final ancillary pair of MZM. In this basis, the four MZMs have the following matrix representations

$$\gamma_0 = -\sigma_y \otimes \sigma_y \tag{3.41}$$
$$\gamma_1 = \sigma_x \otimes 1 \tag{3.42}$$
$$\gamma_2 = \sigma_y \otimes \sigma_x \tag{3.43}$$
$$\gamma_3 = \sigma_y \otimes \sigma_z. \tag{3.44}$$

Since the total fermion parity must be conserved (as these four MZMs only interact with each other for the specified Hamiltonian), the unitary evolution operators U_{ij} are block diagonalized into 2×2 blocks U_{ij}^{e} and U_{ij}^{o} corresponding to even and odd fermion parity sectors, respectively:

$$U_{ij} = \begin{bmatrix} U_{ij}^{\mathrm{e}} & 0 \\ 0 & U_{ij}^{\mathrm{o}} \end{bmatrix}. \tag{3.45}$$

The property $[U_{ij}, \gamma_k] = 0$ for $k \neq 0, i, j$ yields the relations between even and odd overall parity sectors

$$U_{12}^{\mathrm{o}} = \sigma_z U_{12}^{\mathrm{e}} \sigma_z \tag{3.46}$$
$$U_{31}^{\mathrm{o}} = \sigma_x U_{31}^{\mathrm{e}} \sigma_x \tag{3.47}$$
$$U_{23}^{\mathrm{o}} = U_{23}^{\mathrm{e}}. \tag{3.48}$$

We now consider what happens if we apply a projective measurement of the fermion parity eigenstates of the ancillary pair of MZMs at each turning point (which are also their energy eigenstates at those points). Later, we will discuss how to do this in a physical setup; for now, we will simply analyze what happens when such projections are applied at the turning points

of the braiding process. We define the projection operators

$$\Pi_s^{(ij)} = \frac{1 + is\gamma_i\gamma_j}{2}, \tag{3.49}$$

which projects to the state with definite fermion parity $i\gamma_i\gamma_j = s = \pm 1$ for the pair of MZMs γ_i and γ_j. For the above representation of MZM operators, the projectors of interest are given by

$$\Pi_{s_0}^{(20)} = \frac{1 + s_0 1 \otimes \sigma_z}{2} \tag{3.50}$$

$$\Pi_{s_1}^{(10)} = \frac{1 + s_1 \sigma_z \otimes \sigma_y}{2} \tag{3.51}$$

$$\Pi_{s_2}^{(30)} = \frac{1 - s_2 1 \otimes \sigma_x}{2}. \tag{3.52}$$

The total evolution operator for the braiding process with fermion parity measurements of the ancillary pairs at the turning points given by

$$W_{\text{Total}} = \Pi_{s_3}^{(20)} U_{23} \Pi_{s_2}^{(30)} U_{31} \Pi_{s_1}^{(10)} U_{12} \Pi_{s_0}^{(20)}, \tag{3.53}$$

where s_j is the measurement outcome at the jth turning point. Clearly this operator is not unitary, in general, since it involves projective measurements. In order to for this operator to represent a braiding operation, the initial and final configurations of the ancillary pair must match, that is, we must have $s_3 = s_0$.

Substituting Eqs. (3.46)-(3.48) and assuming $s_3 = s_0$, we find

$$W_{\text{Total}} = \begin{bmatrix} 1 & 0 \\ 0 & is_0s_1s_2 \end{bmatrix} \otimes W', \tag{3.54}$$

where W' is given by

$$W' = \frac{1+s_3\sigma_z}{2} U_{23}^{\mathrm{e}} \frac{1-s_2\sigma_x}{2} U_{31}^{\mathrm{e}} \frac{1+s_1\sigma_y}{2} U_{12}^{\mathrm{e}} \frac{1+s_0\sigma_z}{2}. \tag{3.55}$$

We notice that W' takes the form $w'\Pi_{s_0}^{(20)}$ for a scalar w' that depends on the precise details of the unitary evolution operators and measurement outcomes. (This scalar encodes the probability of the measurement outcomes, but is otherwise unimportant, since the quantum state is normalized after each measurement.)

In order to obtain the effect of this operation on the topological qubit, it is useful to convert to the more relevant basis given by $|i\gamma_1\gamma_3 = \pm 1, i\gamma_2\gamma_0 = \pm 1\rangle$ (which is obtained by a simple permutation of basis states). In this basis, the total evolution operator is

$$W_{\text{Total}} = [R_{13}]^{s_1 s_2} \otimes w\, \Pi_{s_0}^{(20)}, \tag{3.56}$$

where

$$R_{13} = \begin{bmatrix} 1 & 0 \\ 0 & i \end{bmatrix} \tag{3.57}$$

is the (projective) braiding transformation for exchanging the MZMs γ_1 and γ_3 in a counterclockwise fashion. Once again, $w = -is_1s_2w'$ is an unimportant overall scalar. The parity of the exponent $s_1s_2 = \pm 1$, i.e. the measurements outcomes at the t_1 and t_2 turning points, determines whether W_{Total} acts as a counterclockwise or clockwise braiding transformation.

The preceding argument shows that the braiding process with fermion parity measurements of the ancillary pairs at the turning points acts on the topological qubit pair of MZMs in the same way as the topologically protected braiding transformation R_{13}, so long as a neutral fermion is not created (paying its concomitant energy penalty) throughout the process. When

precisely one of the intermediate measurements finds the ancillary pair to have odd parity, this means that a fermion is transferred from the qubit pair to the ancillary pair during the preceding time step and then transferred back during the following time step.

This can be understood diagrammatically from the arguments of Refs. [34, 35, 32], as summarized in Fig. 3.4. These are shown with labels from the Ising anyon theory, but the same essential arguments hold for MZMs. It follows from the properties of the Ising anyon model that a braiding exchange of two Ising σ non-Abelian anyons with a neutral fermion transferred between them is equivalent to their inverse braid with no fermion transfer, up to an overall phase, as shown in the left panel of Fig. 3.4. The same property is true for MZMs.

At a T-junction governed by the Hamiltonian of Eq. (3.34), the emitted fermion can only be transferred to one place, the ancillary pair of MZMs, since the Hamiltonian does not couple any other degrees of freedom. A pair of such transfers of fermions, which corresponds to the measurements finding the ancillas in their excited state at both t_1 and t_2, essentially cancel each other. In this case, we have $s_1 s_2 = 1$ and the braiding transformation is still R_{13}.

In summary, we can understand the correction of diabatic errors via measurement from the general viewpoint of measurement-only protocol for braiding [34, 35, 32], as depicted in the right panel of Fig. 3.4. One can clearly see that the resulting operation effected by the protocol depends on the outcomes of the two intermediate fusion channel measurements, in agreement with the result we found Eq. (3.57). This analysis reveals that diabatic transition errors that occur between the turning points can be corrected and topological protection of the resulting operation will be recovered if we introduce measurements at the turning points of

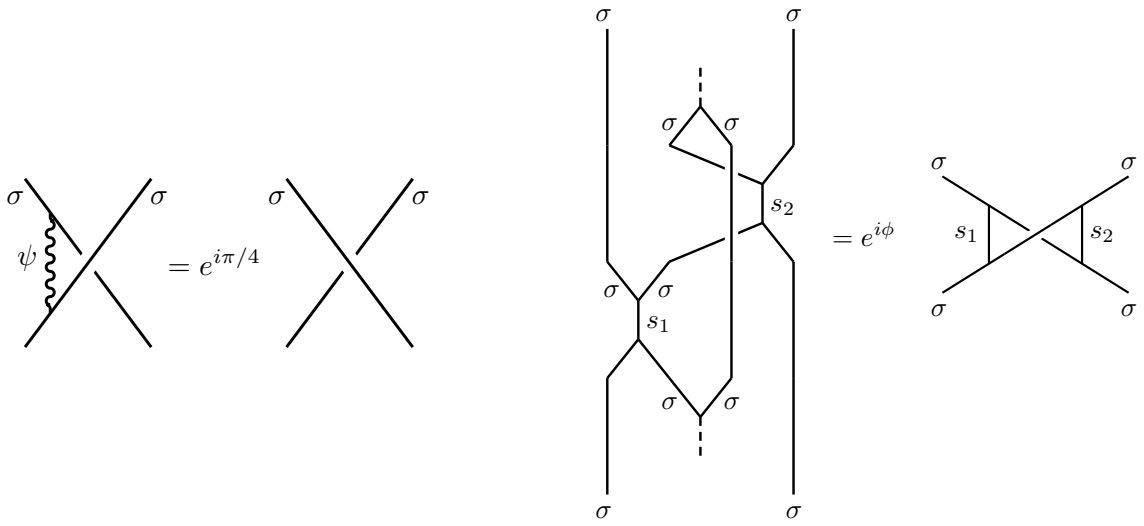

Figure 3.4: Left: The effect of a diabatic error, which transfers a neutral fermion from the qubit to the ancillas, on the braiding. For Ising anyons, it turns a counterclockwise braiding into a clockwise one, up to an overall phase. Right: The measurement-only protocol for braiding. The resulting operation depends on the fusion channels s_1 and s_2 of the intermediate measurements (which can take the values I or ψ). If $s_1 = s_2$, the result is a counterclockwise braid, otherwise it is the inverse braid. See Appendix A for a review of diagrammatic anyon models.

the braiding process. If the measurements do not produce the desired outcomes, the resulting operation, though topologically protected, may not be the intended braiding transformation. Hence, we would like to impose a protocol that guarantees that we obtain the desired outcomes and braiding operation. For this, we now devise a generalization of the forced measurement scheme introduced in Ref. [34] and reviewed in the previous Chapter.

First, let us recall the original forced measurement protocol in the context of this braiding process. Suppose that the first measurement of the fermion parity $i\gamma_1\gamma_0$ returns the undesired outcome $s_1 = -1$ with probability p_0. We can recover from such an undesired outcome by measuring the fermion parity of $i\gamma_2\gamma_0$, which now has equal probability of measurement outcomes $i\gamma_2\gamma_0 = s_0' = \pm 1$ (projecting with $\Pi_{s_0'}^{(20)}$), and then repeating the measurement of $i\gamma_1\gamma_0$, which now also has equal probability of measurement outcomes $i\gamma_1\gamma_0 = s_1' = \pm 1$ (projecting

with $\Pi_{s_1'}^{(10)}$). This process can be repeated as many times as necessary until we obtain the desired measurement outcome $s_1 = 1$. Each recovery attempt has probability $1/2$ of succeeding or failing, so the probability of needing n recovery attempts for the forced measurement process in order to obtain the desired outcome of $s_1 = +1$ is $p_n = p_0 2^{-n}$ and the average number of recovery attempts needed for this will be $\langle n \rangle = 2p_0$. A similar protocol can be used for each of the three segments of the braiding process if the corresponding measurements do not initially yield the desired outcome.

The original forced measurement protocol may be less efficient than is desirable if the measurement times are relatively long, as each recovery attempt only has $1/2$ probability of success. In this case, it may be preferable to utilize a hybrid approach that combines the use of nearly-adiabatic evolution with the forced measurement scheme in order to generate a high probability of success for each recovery attempt. Consider, again, the situation where we reach the first turning point with Hamiltonian $H = -i\Delta\gamma_1\gamma_0$ (we assume $\Delta > 0$), and perform a measurement of the fermion parity $i\gamma_1\gamma_0$ and obtain the undesired outcome $s_1 = -1$ with probability p_0. We can now follow the hybrid adiabatic-measurement recovery protocol:

1. Change the sign of the coupling between γ_0 and γ_1, so that the Hamiltonian goes from $H = -i\Delta\gamma_1\gamma_0$ to $H = i\Delta\gamma_1\gamma_0$.

2. Nearly-adiabatically tune the Hamiltonian from $H = i\Delta\gamma_1\gamma_0$ to $H = -i\Delta\gamma_2\gamma_0$, and then to $H = -i\Delta\gamma_1\gamma_0$.

3. Measure the fermion parity $i\gamma_1\gamma_0$. If the outcome is $s_1 = -1$, go to step 1. If the outcome is $s_1 = +1$, stop.

In step 1, we emphasize that the Hamiltonian only involves the MZMs γ_0 and γ_1, so the process of changing the sign of the coupling does not change the state, i.e. the state remains in the $i\gamma_1\gamma_0 = -1$ state during this process, due to conservation of fermion parity. It just goes from being an excited state to being a ground state. Note that ancillary MZMs' states $i\gamma_1\gamma_0 = \pm 1$ will temporarily become degenerate in this step when the Hamiltonian passes through zero. Clearly, this means that this step will not be adiabatic (nor nearly-adiabatic) with respect to the energy difference between the $i\gamma_1\gamma_0 = \pm 1$ states, but we also want to make sure that it is fast with respect to any of the exponentially suppressed energy splittings between topologically degenerate states. Of course, if the MZMs are embedded in a superconductor, then we must also ensure that the process is slow enough not to excite states above the superconducting gap. In other words, if this process is carried out in time t_{flip}, then we require $\Delta_{\text{SC}}^{-1} \ll t_{\text{flip}} \ll 1/\delta E$.

In step 2, we really just want any adiabatic path from $H = i\Delta\gamma_1\gamma_0$ to $H = -i\Delta\gamma_1\gamma_0$. Taking a path that passes through $H = -i\Delta\gamma_2\gamma_0$ and which only involves γ_0, γ_1, and γ_2 is most convenient, because it limits the possible diabatic errors to transitions involving the three MZMs that we are already manipulating and measuring in this segment of the braiding process. Moreover, as we will discuss later, we may need to pause at $H = -i\Delta\gamma_2\gamma_0$ during this step in order to flip the sign of the possible coupling between γ_0 and γ_1, while its magnitude is at zero and can be done without affecting the state. As long as the Hamiltonian is changed slowly and smoothly (near adiabatically) during this step, the system will remain in the ground state with high probability. In this case, the subsequent measurement in step 3 will have a high probability of obtaining the desired measurement outcome $s_1 = +1$. If the probability of obtaining the

undesired outcome $s_1 = -1$ after one such hybrid recovery attempt is p, the probability of needing n recovery attempts in order to obtain the desired outcome $s_1 = +1$ is $p_n = p_0 p^{n-1}(1-p)$ and the average number of recovery attempts needed for this will be $\langle n \rangle = \frac{p_0}{1-p}$. In this hybrid scheme, p can be made arbitrarily small by making the nearly-adiabatic evolution take a longer amount of time and by making the Hamiltonian time dependence smoother.

If the system is coupled to a dissipative bath of the type described in Section 3.2.2, there is yet another generalization of forced measurement protocol. There is some rate Γ for relaxation to the ground state which vanishes at the turning points and is largest midway between two turning points. In this case, after performing a measurement of the fermion parity $i\gamma_1\gamma_0$ with the undesired outcome $s_1 = -1$, we can follow the dissipation-assisted hybrid recovery protocol:

1. Nearly-adiabatically tune the Hamiltonian from $H = -i\Delta\gamma_1\gamma_0$ to $H = -i\Delta\frac{1}{2}(\gamma_1\gamma_0 + \gamma_2\gamma_0)$.

2. Pause for an amount of time approximately equal to Γ^{-1}.

3. Nearly-adiabatically tune the Hamiltonian from $H = -i\Delta\frac{1}{2}(\gamma_1\gamma_0 + \gamma_2\gamma_0)$ to $H = -i\Delta\gamma_1\gamma_0$.

4. Measure the fermion parity $i\gamma_1\gamma_0$. If the outcome is $s_1 = -1$, go to step 1. If the outcome is $s_1 = +1$, stop.

The effectiveness of this strategy strongly depends on the system-bath coupling. It has the advantage over the previously described hybrid strategy that it does not require the ability to change the sign of couplings.

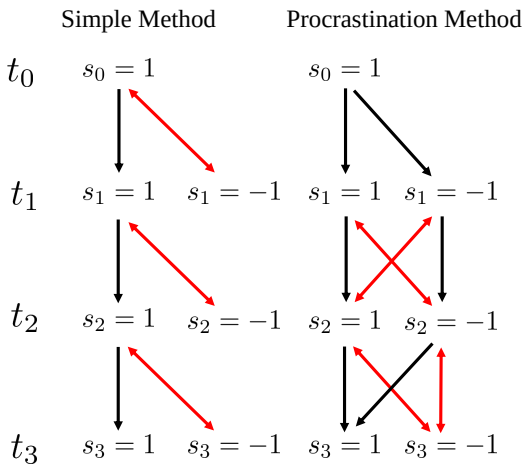

Figure 3.5: The above flow chart outlines the two methods of using forced measurement or its generalizations for recovery protocols, as discussed in the text. The one directional arrows (black) indicate a process that yields a desired or acceptable outcome for which we do not apply a recovery protocol. The bidirectional arrows (red) indicate a process that yields an undesired or unacceptable outcome for which we apply a recovery protocol. We can schematically think of the recovery protocol as backtracking and trying the process again, with a new probability of obtaining a desired outcome. The simple method applies a recovery protocol whenever a turning point measurement outcome indicates a diabatic transition occurred to an excited state. The procrastination method will accept either measurement outcome at the first turning point. However, when the first measurement outcome is $s_1 = -1$, if we procrastinate, we must require the second turning point to have measurement outcome $s_2 = -1$, because we need two wrongs to make a right.

We have outlined three approaches to correcting diabatic errors at each turning point: the forced measurement, hybrid, and dissipation-assisted hybrid protocols. As described above, we can employ one of these recovery schemes as soon as we measure the system in its excited state at each turning point of the braiding process. This is outlined in the left panel of Fig. 3.5. A slightly more efficient method is to procrastinate correcting certain errors. If we measure $s_1 = s_2 = -1$, then as long as we measure $s_3 = s_0$, we will obtain the correct braiding transformation. In other words, two wrongs make a right. Thus if we measure $s_1 = -1$, there

is some chance that, if we continue to evolve, we will find $s_2 = -1$ and $s_3 = s_0$, in which case the system has made the right number of errors to correct itself. The likelihood of such self-correction can be increased by changing the sign of the coupling between γ_0 and γ_3, so that the Hamiltonian is taken from $H = -i\Delta\gamma_1\gamma_0$ at time t_1 to $H = i\Delta\gamma_3\gamma_0$ at time t_2. In this way, if there is no diabatic transition during the second braiding segment, the system will stay in the excited state, and yield $s_1 = s_2 = -1$. If a diabatic error does occur during this segment, yielding the measurement outcome $s_2 = +1$, then we apply a recovery protocol. This procrastination method is shown in the right panel of Fig. 3.5.

3.5 A correction scheme for diabatic errors to the braiding of anyons

We now explain how the previous section's correction scheme for diabatic errors to braiding MZMs can be generalized to the braiding of generic non-Abelian anyons. We will first consider braiding transformations generated using a T-junction type setup with tunable couplings between non-Abelian anyons at fixed locations, as described in Ref. [32]. At the end of this section, we will explain how to correct for diabatic errors in the more general scenario of transporting anyons through a two-dimensional space.

It is straightforward to generalize the MZM braiding protocol depicted in Fig. 2.8 to the braiding of two non-Abelian anyons of topological charge a: replace the labels γ_i with the labels a_i and implement the same sequence of couplings. We explain below why this braiding

scheme holds more generally. [1] For the sake of simplicity, we assume that the anyons a and $\bar{a}$ obey the fusion rule

$$a \times \bar{a} = 0 + c, \tag{3.58}$$

where 0 is the vacuum topological charge and c is some nontrivial topological charge.

As with the example of braiding MZMs, we partition the braiding operation into three steps that end at times $t_{\text{op}}/3$, $2t_{\text{op}}/3$, and t_{op}, which we call the turning points. At each turning point, two anyons are coupled with each other and the other two anyons are decoupled. Each step interpolates between the turning points, changing which two anyons are coupled (or decoupled). The sequence is identical to that in Fig. 2.8, with the labels γ_i replaced by a_i. The corresponding Hamiltonian governing this (sub)system of four anyons can be written as

$$H = -\sum_{j=1}^{3} \Delta_j(t) Z_j \tag{3.59}$$

$$Z_j = |a_j, a_0; 0\rangle\langle a_j, a_0; 0| - |a_j, a_0; c\rangle\langle a_j, a_0; c| \tag{3.60}$$

where $|a_j, a_0; 0\rangle$ and $|a_j, a_0; c\rangle$ correspond to the states in which the anyons a_j and a_0 are in the 0 and c fusion channels (i.e. have collective topological charge of the corresponding values), respectively. The energy splittings given by $\Delta_j(t)$ reflect which pairs of anyons are coupled, as was the case for MZMs. For the (near) adiabatic braiding process, the nonzero values of $\Delta_j(t)$ at the turning points are $\Delta_2(0)$, $\Delta_1(t_{\text{op}}/3)$, $\Delta_3(2t_{\text{op}}/3)$, and $\Delta_2(t_{\text{op}})$.

We assume these energy scales are much smaller than the bulk gap of the system, $|\Delta_j(t)| \ll \Delta_{\text{bulk}}$, so that the dominant diabatic errors will be transitions to excited states within the fu-

[1] The braiding protocol can also be applied to anyons of different topological charge values a and b, provided that they share an Abelian fusion channel [32], but we restrict out attention to the simpler case.

sion state space of these four anyons, rather than to states with additional bulk quasiparticle excitations. Assuming only such dominant diabatic errors, the discussion follows that of Section 3.4.2. In particular, when a diabatic error occurs in a given step of the braiding process, the ancillary (decoupled) pair of anyons at the end of the step will be in the c fusion channel, rather than the 0 fusion channel corresponding to the ground state. In accord with Section 3.3, where we demonstrated that diabatic errors result from uncontrolled creation and movement of anyons, we can interpret such errors as corresponding to an unintended transfer of topological charge c between the anyon being transported and the ancillary pair. (There is nowhere else for the topological charge to come from or go, in the state level of approximation, since the Hamiltonian does not couple to any other degrees of freedom.) If we project the ancillary pair of anyons to their vacuum fusion channel after each step, we recover the braiding transformation for adiabatic evolution. Thus, as we saw with MZMs, a measurement-based error correction protocol can correct all diabatic errors within the four anyon subspace.

Let us focus on the situation where we are tuning between the initial configuration at $t = 0$ with $H = -\Delta Z_2$ and the first turning point at $t = t_{\text{op}}/3$ with $H = -\Delta Z_1$. When we reach the first turning point, we perform a measurement of fusion channel of the pair of anyons a_1 and a_0 and obtain outcome s_1. The precise method of measurement will depend on the details of the system in which the anyons exist. The desired measurement outcome, corresponding to no diabatic error occurring, is $s_1 = 0$. Let us assume the outcome $s_1 = c$, corresponding to a diabatic error, occurs with probability p_0. In the event of this diabatic error, we can apply the following hybrid adiabatic-measurement diabatic error correction protocol:

1. Change the sign of the coupling between a_0 and a_1, so that the Hamiltonian goes from $H = -\Delta Z_1$ to $H = \Delta Z_1$.

2. Nearly-adiabatically tune the Hamiltonian from $H = \Delta Z_1$ to $H = -\Delta Z_2$, and then to $H = -\Delta Z_1$.

3. Measure the fusion channel of a_0 and a_1. If the outcome is $s_1 = c$, go to step 1. If the outcome is $s_1 = 0$, stop.

The above steps are identical to the hybrid adiabatic-measurement recovery protocol outlined for MZMs in Section 3.4.2. In step 1, the Hamiltonian only involves anyons a_0 and a_1, so the process of changing from $H = -\Delta Z_1$ to $H = \Delta Z_1$ does not change the state. It just takes it from being an excited state to being a ground state. In doing so, the fusion channels 0 and c will temporarily become degenerate, thus this step will not be adiabatic (nor nearly-adiabatic) within the four anyon subspace.

Step 2 really just requires any nearly adiabatic path from $H = \Delta Z_1$ to $H = -\Delta Z_1$. The path described limits the possible diabatic errors to involving the three anyons that we are already manipulating and measuring in this segment of the braiding process. As long as the Hamiltonian is changed nearly adiabatically during this step, the system will remain in the ground state with high probability. In this case, the measurement in step 3 will have a high probability of obtaining the desired measurement outcome of $s_1 = 0$. If the probability of an undesired measurement outcome $s_1 = c$ after one such hybrid recovery attempt is p, the probability of needing n recovery attempts in order to correct the diabatic error is $p_n = p_0 p^{n-1}(1-p)$ and the average number of recovery attempts needed for this will be $\langle n \rangle = \frac{p_0}{1-p}$.

In this hybrid scheme, p can be made arbitrarily small by making the nearly-adiabatic evolution take a longer amount of time and by making the Hamiltonian time dependence smoother.

Similarly, one can also adapt the dissipation-assisted hybrid recovery protocol of Section 3.4.2 to apply to non-Abelian anyons, but we will not repeat the details. Of course, we could alternatively use other methods, such as a measurement-only protocol, if they provide preferable time costs.

It is straightforward to generalize the above discussion to the case of general fusion rules $a \times \bar{a} = \sum_c N_{a\bar{a}}^c c$ (note that we always have $N_{a\bar{a}}^0 = 1$, by definition), as it it simply involves keeping track of additional energies levels corresponding to the additional fusion channels and multiplicities. It does, however, require having greater control over the system parameters, because errors corresponding to the different undesired fusion channel measurement outcomes ($s_j \neq 0$) will require tuning the couplings in a manner that is specific to the particular fusion channel.

We note that, for general non-Abelian anyons, one cannot always use the procrastination method, described in Section 3.4.2, for reducing the number of diabatic error correction protocols applied during a complete braiding operation. It can only be used when the undesired fusion channel measurement outcomes at intermediate turning points $s_1 = s_2 = c$ is an Abelian topological charge.

If the diabatic errors associated with creation of quasiparticles in the bulk, i.e. transitions to states above the bulk gap, are not negligible (as we have previously assumed), then we require additional machinery to correct such errors. By locality, such diabatic errors will create

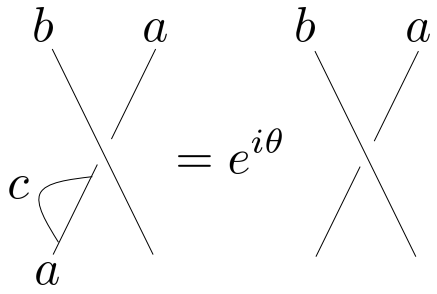

Figure 3.6: The left side shows the braiding diagram corresponding to the diabatic error correction protocol addressing the creation of a bulk quasiparticle. The anyon a can emit an anyon c, which we need to detect, trap, then fuse back together with a. The right side shows that this process is equivalent to the intended braid, up to an unimportant overall phase. Note that the b line is not actually necessary for this statement.

quasiparticles in the vicinity of the "transport path," which is to say along the two legs of the T-junction connecting the three anyons involved in a given step. We must monitor the bulk region along this path to detect whether there is an unintentional creation of a bulk quasiparticle that leaves the T-junction. (If the unintentionally created quasiparticle remains in the T-junction, it will be dealt with by the previous diabatic error correction protocols.) In the event that an emitted quasiparticle is detected, it must be trapped and fused back into the anyons involved in the corresponding transport process.

This protocol also applies more generally to the case where an anyon is being physically transported through the 2D system by some arbitrary method, e.g. being dragged around by a moving pinning potential. This can be understood schematically from the diagrams shown in Fig. 3.6, where we show a moving anyon of topological charge a that emits an anyon of topological charge c. If we trap the anyon c and fuse it back into anyon a, the process is equivalent (in the topological state space) to the process where anyon a is moved without

emitting anyons, up to unimportant overall phase factors.

3.6 Implementation of measurement-based correction in a flux-controlled architecture for Manipulating MZMs

The diabatic error correction scheme of Section 3.4.2 can be adapted to the top-transmon [252, 129], whose basic operating principles were sketched in the previous Chapter and shown in Fig. 2.10. We review the top-transmon, discuss the diabatic errors to which this setup is susceptible, then propose a modification to the superconducting system that allows for correction of the most common diabatic errors.

3.6.1 Review of the top-transmon

Recall from Fig. 2.10 that we can braid MZMs by embedding a MZM T-junction [7, 252] or π-junction [129] inside a system of superconductors, coupled to each other with split Josephson junctions. Changing the magnetic flux through a junction changes the Coulomb couplings between MZMs on the same island. This proposal is appealing both because it does not require careful control over local parameters, as would be necessary to move topological domain walls, and because the sophistication of superconducting qubit technology can be easily transferred to a combined superconductor-topological qubit system. In particular, superconducting qubit experiments are able to carefully control the time evolution of the magnetic flux through a split Josephson junction, so it is feasible to set multiple time derivatives of the flux time dependence

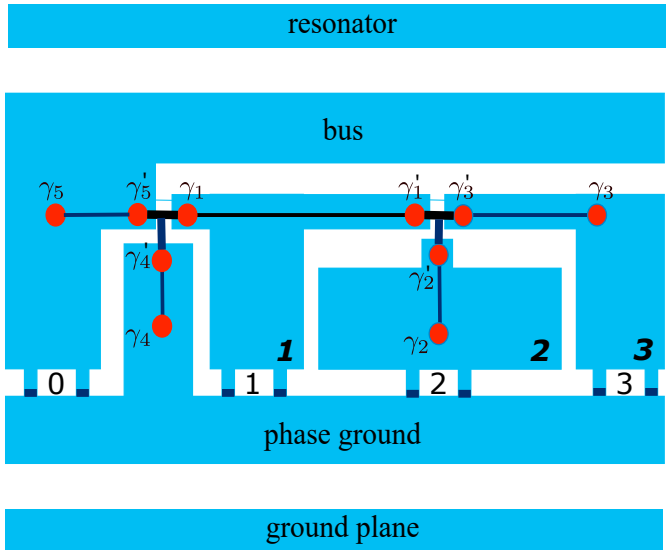

Figure 3.7: The π-junction proposed by Ref. [129]. The MZM system sits inside a superconducting qubit formed by the bus and ground islands. The topological qubit is embedded into a transmission line resonator to allow read-out of the qubit state.

to zero at the beginning and end of the evolution.

The minimal braiding setup is the T-junction shown in Fig. 2.10. The minimal setup that encodes a topological qubit is the π-junction in Fig. 3.7, but most of the underlying physics is already captured by the T-junction.

Fig. 2.10 shows three superconducting islands, each hosting a semiconductor nanowire tuned to have a MZM on either end, connected via split Josephson junctions to a superconducting phase ground. The island hosting MZMs γ_1 and γ_1' is referred to as the "bus" and is assumed to be much larger than islands 2 and 3. The nanowires form a T-junction, with γ_1, γ_2, and γ_3 located at the endpoints of the T and γ_1', γ_2', and γ_3' situated at the center of the T.

The γ_j's are coupled to each other through a Majorana-Josephson potential of strength E_M. This potential couples the three MZMs in the low-energy subspace, leaving behind a single MZM that we denote as γ_0, which is a linear combination of γ_1', γ_2', and γ_3'.

If we ignore the excited states associated with γ_1', γ_2', and γ_3', then the low-energy Hamiltonian (up to small corrections that we will for now assume to be negligible) is

$$H_{\text{eff}} = -\sum_j \Delta_j i\gamma_j\gamma_0. \tag{3.61}$$

Hence, the low-energy effective Hamiltonian of this system is the Hamiltonian of Eq. (3.34) that we analyzed in Section 3.4. The couplings Δ_i are [129]

$$\Delta_i = 16\left(\frac{E_{C,i}E_{J,i}(\Phi_i)^3}{2\pi^2}\right)^{1/4} e^{-\sqrt{8E_{J,i}(\Phi_i)/E_{C,i}}}\cos(q_i\pi/e)f(\alpha) \tag{3.62}$$

where $f(\alpha)$ is a function depending on the Aharanov-Bohm phase shifts which is $\mathcal{O}(1)$ during the braiding process and q_i is the induced charge on island i, controlled through electrostatic gates. The Josephson energy associated with junction i is

$$E_{J,i}(\Phi_i) = E_{J,i}(0)\cos(\pi\frac{\Phi_i}{\Phi_0}), \tag{3.63}$$

and $E_{C,i}$ is the single electron charging energy of junction i. The system is operated in the regime $E_{J,i} \gg E_{C,i}$. Thus, when we tune $\Phi_i \approx 0$, the ratio $E_{J,i}(\Phi_i)/E_{C,i}$ is maximized and the coupling Δ_i is exponentially suppressed. A reasonable parameter choice is $E_{J,i}(0)/E_{C,i} \sim 50$ [155], indicating that Δ_i can be tuned to a minimum value $\sim e^{-20}$. This justifies our approximation in Section 3.4.2 that the system Hamiltonian commutes with γ_k when Δ_k is tuned to its minimum value. When we tune flux $\Phi_i = \Phi_{\text{max}} \lesssim \frac{\Phi_0}{2}$, $E_{J,i}(\Phi_i)/E_{C,i}$ is minimized and Δ_i reaches its maximum value. Note that the sign of Δ_i, which determines which ancilla parity state corresponds to the ground state, depends on the induced charge q_i. By tuning the fluxes according to the schedule shown in Fig. 2.10, we can vary the Hamiltonian with time in

the manner considered in Section 3.4.

To enable measurements, the system is capacitively coupled to a transmission line resonator, as shown schematically for the π-junction in Fig. 3.7. The frequency of the resonator is shifted by the state of the superconducting-MZM system. This results in an energy-dependent transmission amplitude of a microwave sent down the transmission line, which can be used to extract the state of the superconductor-MZM system [223]. A system of a superconducting bus and ground coupled to each other through a split Josephson junction and capacitively coupled to a transmission line resonator is a particular type of superconducting qubit, known as a "transmon" when operated in the regime $E_J \gg E_C$ [155]. The system described here embeds a topological qubit within a transmon. When this system is tuned such that all islands are either phase locked to the bus or the ground it forms a "top-transmon" [120, 252, 129].

3.6.2 Diabatic errors in a top-transmon

Consider the diabatic errors that could occur in the top-transmon. There are errors of the type analyzed in Section 3.4, for which the system remains within the low-energy (four-MZM) subspace. These errors can be identified and corrected by the protocol of Section 3.4.2. We discuss how the necessary measurements can be carried out in Section 3.6.4.

It is also possible for the system to transition out of the low energy subspace. The low energy subspace includes the ground and first excited states, separated by energy gap $\mathcal{O}(\Delta)$. The gap separating these two lowest lying states from the higher excited states is $\mathcal{O}(E_M)$, where E_M is the energy scale of the Majorana-Josephson coupling between γ_1', γ_2', and γ_3'

that splits their shared degeneracy. As discussed in Section 3.2, the probability of diabatic transitions to excited states of energy E_{gap} scales with the operational time as $\mathcal{O}\left(\frac{1}{(t_{\text{op}}E_{\text{gap}})^{2k+2}}\right)$, for $\mathcal{C}^k$ smoothness of the time evolution. Hence, the relative likelihood of errors due to diabatic transition to the second or third excited states [at energies $\mathcal{O}(E_M)$] compared to errors due to diabatic transition to the first excited states [at energies $\mathcal{O}(\Delta)$], which are correctible by the protocol of Section 3.4.2, will scale as $(\Delta/E_M)^{2k+2}$.

Other errors can occur from transitioning to even higher energy levels on the order of the Josephson energy E_J or the bulk superconducting gap Δ_{SC}. One possibility is diabatic-induced quasiparticle poisoning, which can be understood as follows. Tuning the flux at a Josephson junction decreases the energy gap to the continuum for the Andreev bound state (ABS) at that junction. If the ABS transitions to the continuum and travels into the superconducting island i, it changes the induced charge of that island, flipping the sign of Δ_i and thereby interchanging the ground and first excited states. However, we expect the probability of such errors to be suppressed due to both the larger energy scale and the fact that the time evolution of each Josephson junction is "more adiabatic" than the evolution of the six MZM system. This second point is because the Josephson energies in Eq. (3.63) depend less sensitively on changes in the flux than the Coulomb couplings, which depend roughly as $e^{-\sqrt{8E_{J,i}(\Phi_i)/E_{C,i}}}$.

One might also worry that despite the larger gap and the less dramatic time dependence, diabatic transitions above the superconducting gap would be significant due to the continuum of available states. The following argument suggests that the continuum of states above the gap does not introduce significant errors. The system's time dependence arises from changing

the Josephson energy, which is a local quantity. Thus, we expect a diabatic transition to excite a quasiparticle state localized near the junction. Provided the junction is spatially separated from the MZMs, the effect of this excited state on the MZM subspace is very small. In other words, the spectral weight for the local density of states near the MZM wires is small and finite, which implies that the matrix elements between excitations above the superconducting gap and the state of the system are small. Integrating these matrix elements over the continuum of available states will still be small. Combined with the suppressed probability of such a transition, we, thus, expect diabatic transitions above the superconducting gap to be much less significant than errors within the MZM system. Hence, we will satisfy ourselves by correcting the latter. We note that, if we were to braid the MZMs by physically moving them around each other, we would need to take into account diabatic transitions to the continuum of states above the superconducting gap as such excitations would be localized near the MZMs. Such errors could be dealt with using the quasiparticle trap method described schematically at the end of Section 3.5.

Finally, we note that the magnetic fluxes threaded through the split Josephson junctions control the time evolution. Each flux is tuned independently from the others. Thus, noise introduced in one junction will be uncorrelated with noise associated with the flux in a different junction. This justifies our choice of system-bath coupling in Eq. 3.12 and demonstrates that the analysis of Section 3.2.2 applies to a top-transmon.

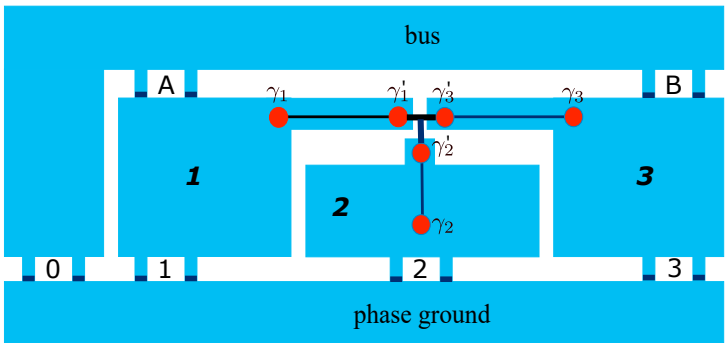

t	$\Phi = 0$ jns	$\lvert\Phi\rvert = \Phi_{\text{max}}$ jns
0	2, A, B	0, 1, 3
t_1	2, 3, A	0, 1, B
t_2	1, 2, B	0, 3, A
t_3	2, A, B	0, 1, 3

Figure 3.8: Top: Modified T-junction structure designed to allow for parity measurements at each turning point. Bottom: Flux values for measurement at the turning points. Note that a junction with $\Phi = 0$ maximizes the Josephson energy and phase locks its neighboring superconductors, while a junction with $|\Phi| = \Phi_{\text{max}}$ minimizes its Josephson energy and essentially decouples the neighboring superconductors. At time t_1, islands 2 and 3 are phase locked to the ground and decoupled from the bus, while island 1 is phase locked to the bus and decoupled from the ground.

3.6.3 Extension to the π-junction

The same analysis holds for π-junctions, with the modification that there are now always four decoupled MZMs. For instance, in Fig. 3.7, γ_4 and γ_5 are always decoupled, as are two of the remaining four MZMs (γ_1', γ_2', and γ_3' are Majorana-Josephson coupled and so effectively comprise one MZM, as is the case with γ_1, γ_4', and γ_5'). In the effective six MZM picture, the two MZMs appearing in the Hamiltonian form the ancilla and the four decoupled MZMs comprise the topological qubit. The two energy levels are determined by the parity of the ancilla. If we fix total parity, each energy level is two-fold degenerate; e.g. for total parity even, at the first turning point the ground state corresponds to ancilla parity even and two degenerate qubit states, $|0\rangle = |i\gamma_4\gamma_5 = +1, i\gamma_2\gamma_3 = +1\rangle$ and $|1\rangle = |i\gamma_4\gamma_5 = -1, i\gamma_2\gamma_3 = -1\rangle$.

3.6.4 Error detection through projective measurement

We now explain how to carry out the projective measurements needed for our error correction protocol. We modify the experimental architecture from that shown in Fig. 2.10 to that of Fig. 3.8. The braiding protocol is the same up to the minor change that the Coulomb couplings of islands 1 and 3 now depend on the magnetic flux tuned through two junctions: $\Delta_1(\Phi_A, \Phi_1),\ \Delta_3(\Phi_B, \Phi_3)$ (recall that Δ_i couples the MZMs γ_i and γ_i'). The essential feature that each Δ_i can be independently tuned between exponentially separated minimum and maximum values is unchanged. As before, we will write the maximum and minimum values of $|\Delta_i|$ as Δ and 0, respectively.

The benefit of the geometry of Fig. 3.8 is that at each turning point the system can be turned into a top-transmon [120], allowing for measurement of the parity of the ancillary pair of MZMs. This is accomplished by decoupling the bus and the ground and connecting each MZM to either the bus or the ground. Measurement returns the parity of the MZMs connected to the bus.

The table in the right panel of Fig. 3.8 shows the necessary flux values that one must have to perform the measurements at each turning point. In order to measure $i\gamma_1\gamma_0$, we couple island 1 to the bus and islands 2 and 3 to the ground. Similarly, to measure $i\gamma_3\gamma_0$, we connect island 3 to the bus and islands 1 and 2 to the ground. To measure $i\gamma_2\gamma_0$, we connect islands 1 and 3 to the bus and island 2 to the ground. Assuming the total parity of the system is fixed, one can infer the parity of $i\gamma_2\gamma_0$ from this measurement. Alternatively, this assumption can be relaxed and one can explicitly check the total parity by introducing additional superconducting

islands [153].

In Section 3.4.2, we discussed several approaches for correcting diabatic error by utilizing measurements: the forced measurement, hybrid, and dissipation-assisted hybrid protocols. We emphasize that utilizing the forced measurement protocol in the architecture of Fig. 3.8 involves tuning fluxes in order to isolate different pairs of MZMs for subsequent measurements. We can implement the hybrid approach if we are able to flip the sign of Δ_i for each island independently. This can be done if the induced charge on each island is independently controlled by external electrostatic gates, as flipping the sign of Δ_i corresponds to changing $q_i \to q_i \pm e$. Note that this swaps the ground and first excited states of the MZMs, but does not introduce electrons into the system and, therefore, does not affect the total fermion parity of the system. We can also use the dissipation-assisted hybrid protocol, which does not require tuning the induced charge, if the system is coupled to a dissipative bath.

Consider the recovery step for the hybrid protocol for the architecture of Fig. 3.8. If we measure $s_1 = -1$, we first need to change the sign of Δ_1. This is done by tuning $q_1 \to q_1' = q_1 \pm e$. We then reverse the time evolution back to $H(0)$. At this point, γ_1 is decoupled from the other MZMs, so that when we tune $q_1' \to q_1' \pm e$ it has no effect on the energy levels of the system. This is in contrast to the initial change of q_1 to q_1', which is intentionally done while γ_1 and γ_1' are coupled, in order to swap the energy level of the occupied level from an excited state to a ground state. We then evolve back to $H(t_1)$ and remeasure s_1.

Once the appropriate islands are coupled to the bus or ground, one measures the state of the system with the transmission line resonator. The system with fixed parity, say even, has four

energy levels: the ground and first excited state, separated by energy $\mathcal{O}(\Delta)$, and the second and third excited state, with energy $\mathcal{O}(E_M)$ above the ground state. For $\Delta > 0$, at the first turning point the ground state and the second excited state correspond $i\gamma_1\gamma_0 = +1$, while the first and third excited states correspond to $i\gamma_1\gamma_0 = -1$ [129]. By sending a microwave through the transmission line resonator and measuring the shift in the resonant frequency, one can infer the parity of $i\gamma_1\gamma_0$. If the system has remained in the lowest two energy states, one can also infer the parity of the qubit.

Noise broadens the effective frequency of the resonator into a normal distribution, thus measurement will only distinguish the different parity states of $i\gamma_1\gamma_0$ provided the peak spacing is sufficiently larger than the width of the distributions. We obtain a rough estimate of the measurement time as follows: the difference in the resonator's effective frequencies determines the peak spacing of the distributions, which in turn sets an upper bound on the width (in frequency) of each distribution. The uncertainty principle allows us to translate an upper bound on the width of the distribution to a lower bound on the measurement time.

For the system under consideration, the measurement must resolve a frequency splitting $\mathcal{O}(\frac{g^2\delta_+}{\delta\omega^2})$, where g is the coupling strength of the transmon to the resonator, $\delta\omega = \Omega_0 - \omega_0$ is the detuning, Ω_0 is the transmon frequency, ω_0 is the bare resonator frequency, and δ_+ is the average dispersion of the transmon energy levels. For the frequency estimates given in Ref. [129], this frequency splitting corresponds to a lower bound on the measurement time of

$$t_{\text{meas}} \gg 20\,\text{ns}. \tag{3.64}$$

Provided the experimental details of the resonator, we could calculate the photon transmission probability, $T_\pm$ corresponding to the parity states $i\gamma_1\gamma_0 = \pm 1$. Let the probability that N photons pass through the resonator during a measurement time t_{meas} when the system is in the state $i\gamma_1\gamma_0 = \pm 1$ be denoted $P(N, t_{\text{meas}}|i\gamma_1\gamma_0 = \pm 1)$. As described in Ref. [129], this probability distribution is Poissonian, and at long measurement times approaches a normal distribution:

$$P(N, t_{\text{meas}}|i\gamma_1\gamma_0 = \pm 1) = \text{Pois}(N, \lambda_\pm) \approx \frac{e^{-\frac{(N-\lambda_\pm)^2}{2\lambda_\pm}}}{\sqrt{2\pi\lambda_\pm}}, \tag{3.65}$$

where $\lambda_\pm \propto T_\pm t_{\text{meas}}$. We see that the peak spacing between the distributions grows linearly in time, while the width of each distribution grows as a square-root in time. Due to the finite overlap of the two possible distributions, there is some probability of incorrectly interpreting a measurement outcome; this separation error decreases exponentially with increasing measurement time. Thus, we expect that a measurement time of 100 ns is sufficient to satisfy the bound in Eq. (3.64).

Recall that γ_0 is a linear combination of $\gamma_1', \gamma_2', \gamma_3'$. There are two other Majorana operators, composed of different linearly-independent combinations of $\gamma_1', \gamma_2', \gamma_3'$. It is the parity of these additional two Majorana operators that determines whether or not the MZMs are in the low energy subspace. These Majorana operators couple less strongly to the resonator and, thus, greater resolution is necessary to determine their parity. In order to detect a transition to the second or third excited states, the measurement needs to resolve a frequency splitting $\mathcal{O}(\frac{g^2\delta_+\delta_-}{\delta\omega^2 E_M})$, where δ_- is half the difference of the dispersion of the transmon energy levels. For

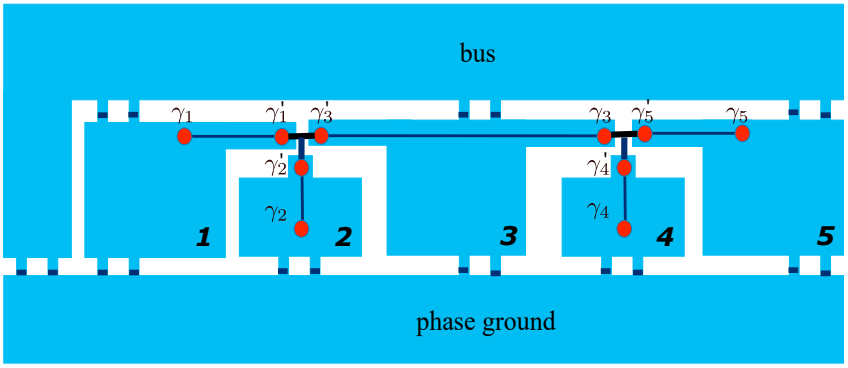

Figure 3.9: A π-junction designed to allow fermion parity measurements at each turning point.

this resolution, the lower bound on the measurement time increases to

$$t_{\text{meas}} \gg 1\,\mu\text{s}. \tag{3.66}$$

Coupling the system to a cold bath can relax the second and third excited states to the first excited state and the ground state respectively. Thus, in the presence of a dissipative bath and with sufficiently slow evolution, the system will relax into the lowest two energy levels and the more precise measurement resolution is unnecessary.

Finally, we note that we can easily generalize from a T-junction [252]) to a π-junction [129] while still maintaining the ability to measure the parity at each corner of the braiding process. This generalization is shown in Fig. 3.9.

3.7 Feasibility estimates

The proposed platform for demonstrating non-Abelian braiding takes advantage of some well-established methods in superconducting qubit experiments. In particular, careful control over the time evolution of the system can reduce diabatic errors and the measurement scheme used

to read out the collective fermionic parity of MZMs can be used to detect and subsequently correct diabatic errors. Moreover, the usual decoherence times, i.e. the relaxation time T_1 and decoherence time T_2, that plague superconducting qubits do not apply to the MZM based qubits and operations considered in this paper, since we simply want the transmon to remain in its ground state. However, the modifications presented here and in Ref. [129] introduce new challenges, which we now address.

The time dependence of the combined MZM-transmon system enters entirely through the magnetic flux threaded through the split Josephson junctions. As mentioned in Section 3.2, setting time derivatives of the Hamiltonian to zero at the beginning and end of the evolution significantly decreases the diabatic error. A benefit of using the transmon architecture is that control over the time evolution of the flux is excellent and current experiments can easily set $\dot{\Phi}(t) = 0$ at the beginning and end of each time step [15, 185].

Transmon experiments do not control the bias flux directly, but rather set the value of a digitally controlled voltage source for an external circuit, which induces a flux through the split Josephson junction via the mutual inductance [155]. Each additional split Josephson junction complicates the experiment due to unwanted cross-talk between the wrong bias circuit and junction. There exist clever schemes to minimize the off-diagonal terms in the mutual inductance matrix through the geometry of the system. It might be possible to achieve the topology of Fig. 3.8 using external circuits. However, doing so while maintaining the ability to independently tune the strength of each junction would undoubtedly be challenging. A possible solution is to use a qubit which relies on voltage rather than magnetic field to tune the ratio of

E_J/E_C [160, 77]. This would eliminate the need for bias circuits while still retaining careful control over the time evolution.

The necessary energy resolution for the top-transmon is $\mathcal{O}(\frac{g^2\delta_+}{\delta\omega^2})$, while for the transmon it is $\mathcal{O}(\frac{g^2}{\delta\omega})$. When operated strictly in the transmon regime, $E_J \gg E_C$, the required resolution for the top-transmon is orders of magnitude larger than for the transmon. However, during measurement the top-transmon is tuned out of the transmon regime, and δ_+ can be comparable to $\delta\omega$. We expect measurement times for the top-transmon to be comparable to those of the transmon.

The hybrid approach for error correction relies on independently tuning the induced charge for each MZM island. Such control can be achieved by gating each island and changing the gate voltage. One can also avoid the additional complication of adding electrostatic gates by using other error correction schemes, such as the dissipation-assisted hybrid protocol described in Section 3.4.2.

3.8 Discussion

With the preceding analysis in hand, we are now in a position to answer the question posed in the title of this paper. As we have shown, diabatic errors occur when anyons are unintentionally created or move in an uncontrolled way. Such errors can be suppressed by making the time dependence of the Hamiltonian as smooth as possible and by coupling to a dissipative bath. They can be further reduced by measuring and correcting for the unwanted creation or motion of anyons, which can be done without measuring the encoded quantum information that we

wish to manipulate. Let us suppose that we can tolerate a probability ε_0 of a diabatic error per braiding step. The value of ε_0 will depend on the task we wish to accomplish and whether or not we hope to carry out a computation without additional error correction. This error probability (assuming, for the moment, that there are no other sources of error, apart from diabatic errors) can be achieved by performing the unitary evolution slowly and smoothly. However, if the time required by this strategy exceeds the time needed for a measurement, then it may be advantageous to utilize a hybrid strategy that involves a faster "nearly adiabatic" evolution together with measurements that detect the occurrence of errors from diabatic transitions.

We assume that the process of nearly adiabatically tuning the Hamiltonian between any two turning points is carried out with the same time t_u. We denote the diabatic transition error probability associated with each segment of nearly adiabatic unitary evolution as $\varepsilon[t_u]$. In the case of no dissipation,

$$\varepsilon[t_u f] = \frac{c[k]}{(\Delta t_u)^{2k+2}}, \quad \text{for} \quad t_u > t_{\text{th}} \tag{3.67}$$

where $t_{\text{th}} = (10c[k])^{\frac{1}{2k+2}}/\Delta$ is the threshold time above which the transition probability is bounded by a power-law, see Fig. 3.2. Recall that Δ is the maximum Coulomb coupling between MZMs on the same island and that the gap separating the ground and first excited state is $\mathcal{O}(\Delta)$. Here k is the number of vanishing time derivatives at the beginning and end of the unitary evolution and $c[k]$ is some k-dependent constant. If we can tolerate an error probability of ε_0 for one-third of the braiding process, the time needed for a braid with unitary evolution is

$$t_{\text{op}} = \frac{3}{\Delta}\left(\frac{c[k]}{\varepsilon_0}\right)^{\frac{1}{2k+2}}. \tag{3.68}$$

For ε_0 very small, this will become a slow process. We could, instead, perform the evolution faster and correct errors using, for instance, the hybrid protocol discussed in Section 3.4.2. There is no benefit to performing the unitary evolution arbitrarily fast, since the likelihood of diabatic errors will be high and several measurements will be necessary. If we perform the unitary evolution much more slowly than the measurement time, t_{meas}, then we fail to take advantage of the benefits of performing measurements. This can be made more quantitative as follows.

Let $t_{\text{op}}/3$ be the total time needed to evolve the system between two turning points (one third of the total time for a braid), including possible diabatic transition error recovery steps. As discussed in Section 3.6.4 this time will be divided between unitary evolution, measurement, and flipping the sign of the couplings by changing the induced charge on the MZM island of interest. We will assume that each segment of nearly adiabatic unitary evolution (from one corner point to the next) takes the same amount of time t_u and that the time needed to flip the sign of the coupling on any given island takes the same amount of time t_{flip}. We also assume that measurement is a relatively slow process, i.e. $t_{\text{meas}} \gg t_u, t_{\text{flip}}$. For the moment we will ignore errors associated with measurement, transitions to the second and third MZM excited states, and flipping the sign of the couplings, we will address these concerns later.

One diabatic transition error recovery step involves the following sequence of processes, to be performed at the desired turning point, following a syndrome measurement of the ancillary pair of MZMs that detected a diabatic transition error: (1) flip the induced charge on the ancillas' island (say island i), (2) near adiabatically tune the Hamiltonian to the previous turning

point, (3) flip the induced charge on island i, (4) near adiabatically tune the Hamiltonian to the desired turning point, and (5) perform a syndrome measurement on the ancillary pair of MZMs. Consequently, the time required to perform one recovery step is

$$t_{\text{rec}} = 2t_u + t_{\text{meas}} + 2t_{\text{flip}}. \tag{3.69}$$

The corresponding probability that process of evolving between two turning points will be completed with n recovery steps (i.e. that the initial near adiabatic evolution and subsequent $n-1$ recovery attempts had a diabatic transition error, but the nth recovery process was successful), for $n \geq 1$, is

$$p_n[t_u] = \varepsilon[t_u]\,[2\varepsilon[t_u](1-\varepsilon[t_u])]^{n-1}\,(1 - 2\varepsilon[t_u] + 2\varepsilon[t_u]^2), \tag{3.70}$$

and, clearly, $p_0 = 1 - \varepsilon[t_u]$. In Eq. (3.70), the first factor of $\varepsilon[t_u]$ is the probability of a diabatic transition error on the initial attempt; each factor of $2\varepsilon[t_u](1-\varepsilon[t_u])$ is the probability of a diabatic transition error occurring on one of the two near adiabatic evolution segments associated with a recovery step; and the final factor of $1 - 2\varepsilon[t_u] + 2\varepsilon[t_u]^2$ is the probability of successfully completing one recovery step without a diabatic transition error (i.e. with either zero or two diabatic transitions occurring during the two near adiabatic evolution segments).

The average number of recovery steps needed to evolve between two turning points without error is thus

$$\langle n[t_u] \rangle = \sum_{n=0}^{\infty} n p_n[t_u] = \frac{\varepsilon[t_u]}{1 - 2\varepsilon[t_u] + 2\varepsilon[t_u]^2}. \tag{3.71}$$

Hence, the average time needed to evolve between two turning points with the diabatic transition errors corrected is

$$\begin{aligned}\frac{\langle t_{\text{op}}[t_u]\rangle}{3} &= t_u + t_{\text{meas}} + \langle n[t_u]\rangle t_{\text{rec}} \\ &= t_u + t_{\text{meas}} + \frac{(2t_u + t_{\text{meas}} + 2t_{\text{flip}})\varepsilon[t_u]}{1 - 2\varepsilon[t_u] + 2\varepsilon[t_u]^2}.\end{aligned} \tag{3.72}$$

This average operation time is minimized by some optimal choice of the time t_u, subject to the constraint that $t_u > t_{\text{th}}$, which is straightforward to compute when the other quantities are specified.

We now apply this to the system discussed in Section 3.6. Ref. [129] estimates $\Delta \sim 10\,\text{GHz}$, for which we find $t_{\text{meas}} \gg 20\,\text{ns}$. We satisfy this inequality by setting $t_{\text{meas}} = 100\,\text{ns}$. We use $c[0] = 2.2$ and $c[1] = 162.5$, obtained from the data shown in Fig. 3.2. As a rough approximation, we set $E_M = 50\,\text{GHz}$ and $t_{\text{flip}} = 10/E_M = .2\,\text{ns}$. In Tables 3.1 and 3.2, we compare the average operation time for a braid with error-correction to the time for a braid with nearly adiabatic unitary evolution and target error probabilities $\varepsilon_0 = 10^{-4}$, 10^{-6}, and 10^{-8}.

We can also consider the effects of dissipation, as discussed in Section 3.2.2. Fitting to the data shown in Fig. 3.2 with system-bath coupling $\lambda = 0.01\Delta$, we see that the error probability for unitary evolution for $k = 0$ is

$$\varepsilon_{k=0}[t_u] = \frac{0.52}{(\Delta t_u)^{1.97}}, \quad \text{for } \varepsilon_{k=0}[t_u] < 10^{-3} \tag{3.73}$$

and for $k = 1$ it is

$$\varepsilon_{k=1}[t_u] = \begin{cases} \frac{162.5}{(\Delta t_u)^4}, & 10^{-2} > \varepsilon_{k=1} > 10^{-5} \\ \frac{0.05}{(\Delta t_u)^{1.95}}, & \varepsilon_{k=1} < 10^{-5} \end{cases} \tag{3.74}$$

Using these expressions, we estimate the braiding times with dissipation for unitary evolution and for the hybrid error correction scheme in Tables 3.1 and 3.2.

k	λ (diss.)	$\langle t_{\text{op}} \rangle$	t_u	$\langle n(t_u) \rangle$
0	0	308 ns	1.7 ns	0.008
1	0	305 ns	1.5 ns	0.004
0	0.1 GHz	308 ns	2.4 ns	0.001
1	0.1 GHz	306 ns	1.5 ns	0.004

Table 3.1: Braiding time using the hybrid protocol for the system discussed in Section 3.6 with Δ=10 GHz and temperature $T = 0.001\Delta$. The columns label: the smoothness of the time evolution of the system Hamiltonian ($k = 0, 1$); the system-bath coupling $\lambda = 0$ (no dissipation) or $\lambda = 0.01\Delta$ (dissipation); the average braiding time, $\langle t_{\text{op}} \rangle$; the corresponding unitary time, t_u; and the average number of recovery steps needed to complete the braid, $\langle n(t_u) \rangle$. The above values assume no measurement error and no error from transitioning to excited states with energy $\mathcal{O}(E_M)$ above the ground state. We use the estimates $t_{\text{flip}} = 0.2$ ns and $t_{\text{meas}} = 100$ ns, and then choose t_u to minimize Eq. (3.72), subject to the constraint that $t_u > t_{\text{th}}$.

k	λ (diss.)	$t_{\text{op}},\ \varepsilon_0 = 10^{-4}$	$t_{\text{op}},\ \varepsilon_0 = 10^{-6}$	$t_{\text{op}},\ \varepsilon_0 = 10^{-8}$
0	0	45 ns	450 ns	4.5 μs
1	0	11 ns	34 ns	110 ns
0	0.1 GHz	23 ns	240 ns	2.5 μs
1	0.1 GHz	11 ns	77 ns	820 ns

Table 3.2: Braiding time using nearly adiabatic unitary evolution for the system discussed in Section 3.6 with Δ=10 GHz and temperature $T = 0.001\Delta$. The first two columns label the smoothness of the time evolution of the system Hamiltonian ($k = 0, 1$) and whether the system-bath coupling is $\lambda = 0$ (no dissipation) or $\lambda = 0.01\Delta$ (dissipation). The third, fourth, and fifth columns list the braiding time to reach a target error probability of $\varepsilon_0 = 10^{-4}$, 10^{-6}, and 10^{-8} respectively, between two turning points. A smaller target error probability increases the corresponding braiding time.

Tables 3.1 and 3.2 give rough estimates of the braiding times for MZMs in a flux-tunable architecture. We see that, if we use an error correcting protocol involving measurements, our braiding operation time is limited by the measurement time. When $t_u > t_{\text{th}}$, the initial syndrome measurement at each turning point has a high probability of finding the desired outcome and projecting the system into its ground state, so we only rarely need to implement the recovery procedure. With error-correction, the times do not depend strongly on k nor on whether the system is coupled to a dissipative bath. For nearly adiabatic unitary evolution, there is a significant improvement in braiding time for $k = 1$ compared to $k = 0$. As discussed in Section 3.2.2, for small error probabilities, dissipation reduces the braiding time for unitary evolution if $k = 0$, but not if $k = 1$. Our analysis suggests that, for a target error probability of $\varepsilon_0 = 10^{-6}$, the braiding time for the hybrid protocol is comparable to the braiding time for unitary evolution when $k = 0$, and is faster when the system is not coupled to a dissipative bath. When $k = 1$, unitary evolution is significantly faster than correcting error through measurement, both with and without a bath. For a target error probability of $\varepsilon_0 = 10^{-8}$, the hybrid protocol is faster than unitary evolution unless $k = 1$ and there is no system-bath coupling. These comparisons neglect measurement error and diabatic transitions to the second and third MZM excited states. Taking into account these errors could shift the crossover point at which the hybrid protocol becomes better than unitary evolution.

The above analysis applies when we restrict our attention to the low energy subspace. Let $\varepsilon_M[t_u]$ be the error probability associated with transitions out of this subspace to excited states of energy $\mathcal{O}(E_M)$, associated with the states supported by the triples of MZMs at T-junction

intersections, whose degeneracies are lifted by Majorana-Josephson coupling. As $E_M \gg \Delta$, $\varepsilon_M[t_u]$ is expected to be much smaller than $\varepsilon[t_u]$. While including $\varepsilon_M[t_u]$ could increase the braiding time for unitary evolution, it will not greatly affect the average braiding time with error-correction (even if $\varepsilon_M[t_u] \approx \varepsilon[t_u]$, $\langle n[t_u] \rangle$ would remain close to zero and the dominant contribution to the braiding time would still be t_{meas}). For our choice of $t_{\text{meas}} = 100\,\text{ns}$, measurement does not distinguish the ground and third excited state, thus such a transition results in an error. Increasing the measurement time would allow us to detect, and correct, such a transition.

The values in Tables 3.1 and 3.2 are subject to change given the experimental implementation. In particular, $\Delta, E_M, t_{\text{meas}}, \lambda$, and $c[k]$ will depend significantly upon system details. (E_M is exponentially sensitive to the separation of MZMs at the center of the T-junction.) We chose $t_{\text{flip}} = 10/E_M$ to justify ignoring errors associated with flipping the sign of the couplings. (Recall that when we exchange the ground state and first excited state, the only transitions that conserve total parity are between states whose energies are separated by a gap $\mathcal{O}(E_M)$.) With more information about the physical system, t_{flip} could be optimized to be as short as possible without inducing diabatic transitions.

Measurement error is another potential issue. Generally, there will be some probability of the measurement projecting the ancillary pair onto an excited state (odd parity), while providing an erroneous readout indicating that the outcome is a ground state (even parity), or vice-versa. Such errors can typically be reduced by repeating the measurement to increase the level of confidence of the measurement. Nonetheless, it is useful to know how small measurement

errors must be in order to safely ignore them in the preceding analysis. Reference [153] shows that we can ignore a measurement error probability of $\varepsilon_{\text{meas}}$ at the nth recovery step, provided that

$$\varepsilon_{\text{meas}} \ll \min_{n\in\mathrm{N}} \left(\varepsilon[t_u], \left(2\varepsilon[t_u](1-\varepsilon[t_u])\right)^{n[t_u]}\right). \tag{3.75}$$

It is important to remember that while braiding MZMs can realize single-qubit Clifford gates, universal quantum computation requires additional gates, such as the two-qubit entangling gate CNOT and the single qubit $\pi/8$ phase gate. There are a number of proposals for how one might implement such additional gates for MZM systems that may be incorporated in the Majorana nanowire (and other) systems considered in this paper [49, 33, 228, 67, 133, 37, 129, 66, 137]. Since these implementations of the additional gates will likely possess undesirable error rates and utilize significantly different methods from those of braiding, they will require the use of different error correction protocols, such as magic-state distillation [47]. We do not focus on this matter here and the errors introduced by these additional (non-braiding) gates are not taken into account in our analysis and Tables 3.1 and 3.2. Ref. [1] discusses milestone experiments leading to MZM based quantum computing, including fusion rule detection, which is simpler to execute than braiding. These experiments are susceptible to the same diabatic errors discussed in the present paper. An interesting future direction is to extend our analysis to the systems discussed in these papers, thereby better understanding the role diabatic errors play in topological quantum computation.

Our measurement-based correction protocol focuses on diabatic transitions from the ground

state to the first excited state of the MZM system. For longer measurement time, it is also possible to detect transitions to the second and third MZM excited states, and one could generalize the hybrid protocol to correct these errors as well. We do not take into account transitions above the superconducting gap. Such excitations are especially dangerous as quasiparticles could braid with the MZMs in an uncontrolled manner. Quasiparticle traps could potentially help with these errors, although perhaps the best strategy is to optimize parameters such that these excitations are extremely rare. As our interest in this paper has been on diabatic effects, we do not address errors arising from thermally-excited quasiparticles. Such errors (analyzed, for instance, in Ref. [203]) can be reduced by maximizing $\beta\Delta$ and, possibly, by variations on the ideas discussed in the present paper.

The hybrid error-correction protocol, introduced in Section 3.4 for MZMs and in Section 3.5 for general non-Abelian anyons, interpolates between braiding via adiabatic tuning of the couplings [7, 252, 129] and measurement-only topological quantum computation (MOTQC) [34, 35]. It uses nearly-adiabatic tuning of the couplings to generate a very high probability of the state being the desired (ground) state at each topological charge/fermion parity measurement step, subject to the constraint that this does not take too long. If measurement returns the excited state, the hybrid scheme is used to converge exponentially to the desired result, albeit with the cost of slowing braiding down to the speed of a measurement, in addition to introducing energy dissipation and heating associated with measurement.

If the braiding operation time $t_{\rm op}$ becomes too long when using nearly adiabatic evolution or our hybrid protocol, one might consider simply using the MOTQC scheme. For the Majorana

network discussed in this paper, we must tune the couplings between subsequent measurements in order to isolate different pairs of MZMs for measurement. This tuning should be done as fast as possible without inducing transitions to higher excited states of energy $\mathcal{O}(E_M)$. Let $t_{\text{tun}} = 10/E_M$ be the required time to tune couplings between subsequent measurements (note that while t_{tun} applies to a different process than t_{flip}, both times are subject to the same constraints). Then the average braiding operation time would be $\langle t_{\text{op}} \rangle_{\text{MOTQC}} = 9t_{\text{meas}} + 6t_{\text{tun}} = 901$ ns for our energy estimates. This is slower than the hybrid protocol for the systems considered in detail in this paper, and hence not the preferred protocol. However, one might envision other system designs for which the MOTQC scheme yields the faster protocol.

In analyzing the diabatic errors in anyon braiding, we have mainly focused on satisfying the lower bound on the operational time. However, as mentioned in the introduction, it is of crucial importance that the braiding time is sufficiently fast that the system does not resolve the ground state degeneracy splitting, which are inevitably present due to nonzero correlation length. The resulting upper bound on braiding time depends on the details of the system. For the system discussed in Section 3.6, the wires hosting MZMs must be sufficiently long compared to the correlation length (coherence length) and we must be able to tune the magnetic fluxes sufficiently close to $\Phi_0/2$. It is worth noting that, to the best of our knowledge, the degeneracy splitting of MZM wires in current experiments is too large for the time estimates given in Tables 3.1 and 3.2. However, the exponential suppression of the degeneracy splitting as a function of L/ξ indicates that only modest increases in the length of the wires and/or the energy gap (which decreases the correlation length) is necessary to obtain an upper time limit

much larger than the braiding times estimated in this paper. For the system of Ref. [5], tripling the length of the longest wire to $4.5\,\mu$m is sufficient.

Chapter 4

Scalable designs for Majorana-based quantum computing

In order to be in control, you have to have a definite plan for at least a reasonable period of time. So how, may I ask, can man be in control if he can't even draw up a plan for a ridiculously short period of time, say, a thousand years, and is, moreover, unable to ensure his own safety for even the next day?

-Mikhail Bulgakov, *The Master and Margarita*

In this chapter, we present designs for scalable Majorana-based quantum computing. The qubits presented here are encoded in aggregates of four or more Majorana zero modes, realized at the ends of topological superconducting wire segments that are assembled into superconducting islands with significant charging energy. Quantum information can be manipulated

according to a measurement-only protocol, which is facilitated by tunable couplings between Majorana zero modes and nearby semiconductor quantum dots. Our proposed architecture designs have the following principal virtues: (1) the magnetic field can be aligned in the direction of all of the topological superconducting wires since they are all parallel; (2) topological T-junctions are not used, obviating possible difficulties in their fabrication and utilization; (3) quasiparticle poisoning is abated by the charging energy; (4) Clifford operations are executed by a relatively standard measurement: detection of corrections to quantum dot energy, charge, or differential capacitance induced by quantum fluctuations; (5) it is compatible with strategies for producing good approximate magic states.

The results contained here were first presented by Torsten Karzig, Christina Knapp, Roman M. Lutchyn, Parsa Bonderson, Matthew B. Hastings, Chetan Nayak, Jason Alicea, Karsten Flensberg, Stephan Plugge, Yuval Oreg, Charles M. Marcus, and Michael H. Freedman in "Scalable Designs for Quasiparticle-Poisoning-Protected Topological Quantum Computation with Majorana Zero Modes," Phys. Rev. B, 95, 235305. Copyright 2017 by the American Physical Society. A subsection of this paper appeared in Chapter 2.

4.1 Introduction

Non-Abelian topological phases of matter provide an attractive platform, in principle, for fault-tolerant quantum computation. However, there are a number of obstacles that must be surmounted in order to make this a reality. (1) A non-Abelian topological phase must be found or engineered. (2) Quasiparticles must be braided in order to manipulate the quantum informa-

tion that is encoded in them; moving individual quasiparticle excitations is a feat that has never been accomplished before, and it would have to be done routinely during the operation of a topological quantum computer. (3) The topological charge of a pair of quasiparticles must be measured in order to determine the result of a calculation. The conceptually simplest way to do this would be with an anyonic interferometry measurement [100, 244, 36, 193, 39, 30], but that requires coherent transport, potentially over long scales; neither an interferometry nor any other measurement has unambiguously measured the topological charge of a pair of quasiparticles. In this chapter, we present a scheme for topological quantum computation that obviates these difficulties.

A path surmounting the first obstacle is to engineer a topological superconducting state supporting MZMs out of semiconductor-superconductor heterostructures [224, 181, 200]. As reviewed in Chapter 2, such phases can be hosted in 1D systems [146, 103, 181, 200], and braiding operations can be implemented in wire networks [7]. There is strong experimental evidence that a topological superconductor has been realized with semiconductor nanowires [190, 220, 79, 65, 74, 95, 5].

The price that is paid in such an approach is that a topological superconductor is not quite a topological phase of matter but, rather, a "fermion parity-protected topological phase" [38] and, therefore, is vulnerable to "quasiparticle poisoning," i.e., to processes that change the number of electrons in the device. However, one can prevent quasiparticle poisoning of MZMs on a superconducting island by incorporating relatively large charging energies that provide a Coulomb blockade for the island, as utilized in the proposals of Refs. [158, 207, 254, 208].

(Charging energy does not protect MZMs from quasiparticle excitations occurring within the device. However, such excitations and the errors they cause are exponentially suppressed by Δ/T for energy gap Δ and temperature T.) We refer to a Coulomb-blockaded superconducting island hosting MZMs as a "MZM island."

A recent experiment, inspired by the theoretical prediction of Ref. [102], reported the first systematic measurement of the ground-state degeneracy splitting for proximitized nanowires in a Coulomb blockade regime and observed that it is exponential in the nanowire length L [5]. The transport measurements of Ref. [5] are in qualitative agreement with theoretical calculations [253]. The combination of material science progress [157, 233], device quality and controllability [5, 114], and theoretical advances involving semiconductor-superconductor heterostructures [24, 6, 165, 241, 75] provides a pathway for topological quantum computation with semiconductor nanowires.

A way to circumvent the second obstacle, i.e., the need to move quasiparticles, is to use a "measurement-only" protocol [34, 35], wherein a sequence of measurements has the same effect as a braiding operation. Such methods eliminate the need to move the computational quasiparticles and, thus, eliminate the need for coherent topological "T-junctions" [7], which may present banal engineering issues such as those identified in Ref. [199].

The remaining obstacle is the measurement of the topological charge of quasiparticle pairs. One might worry that measurements could still involve moving probe quasiparticles through an interferometry loop, thereby reintroducing the second obstacle. However, this concern can be surmounted by taking advantage of the distinction between a fermion parity-protected topolog-

ical phase and a true topological phase (which is a mathematical abstraction that may not quite correspond to any real physical system anyway [38]): topological charge can be manipulated by the process of an electron tunneling into a MZM [96]. As shown in Ref. [102], transport through a pair of MZMs can provide a measurement of their combined topological charge in the presence of a large charging energy.

Majorana-based qubits with four MZMs residing on a Coulomb blockaded island have been studied recently. In particular, Refs. [158, 207] have focused on surface code architectures where the MZM islands form a hexagonal lattice. The large charging energies invoked in these papers distinguishes them from other Majorana surface code proposals in which the charging energies are small [256, 254]. The former surface code approach has the advantage that conductance measurement via interference is naturally built in, with the interfering paths involving co-tunneling through MZM islands. While the surface code aims for fault-tolerant computation, one can also think about a minimal setup in which islands with four MZMs constitute logical qubits, denoted as "Majorana box qubits" in Ref. [208], and measurements are performed by detecting frequency shifts of double dot systems. In that work, a minimal demonstration of the Clifford gates was proposed using four such qubits.

In this chapter, we design a modular system for measurement-only MZM topological quantum computation in which the basic module contains a small network of (4 or 6) MZMs and quantum dots for measurement. [1] Related ideas have appeared in the independent work of Ref. [208], but they are sharpened here by quantum information requirements that lead us to a scalable arrangement with novel features.

[1]The coupling to quantum dots plays a different role here than in Ref. [126], where the dot is a spin qubit.

We analyze five new scalable architectures for Majorana-based quantum computing, each of which overcomes all of the obstacles listed above. Each architecture is centered around a qubit composed of parallel sets of topological superconducting wires. The wires are electrically connected by normal superconductors, so that no individual wire has a charging energy, but the entire qubit is Coulomb blockaded at all times. This fact is an important distinction with respect to the previous Majorana-based quantum computing proposals [7, 121, 133, 37, 226, 129, 66, 1]. Quantum information is manipulated by joint fermion parity measurements on pairs and quartets of MZMs. These measurements allow for intra-qubit braiding operations via the measurement-only protocols, as well as for two-qubit entangling operations. Of our five proposed architectures, three involve six MZMs per superconducting island, which we refer to as "hexons," and two involve four MZMs per island, which we call "tetrons." We evaluate each hexon and tetron design on four axes: (1) quasiparticle poisoning time $\sim$ charging energy E_C; (2) signal visibility $\sim E_C^{-1}$; (3) fabrication simplicity; and (4) computational efficiency.

Due to the exponential suppression of errors, our proposed qubit designs should have sufficiently long coherence times to solve low-depth problems. For long enough computations, the exponentially small errors will eventually become important and must be addressed through some form of error-correction. The computational universality of our proposed qubits allows flexibility in the choice of code, though it would be wise to use codes that take advantage of having high fidelity Clifford gates.

In Section 4.2, we describe one of our designs as an illustrative example of the key concepts utilized in our proposals. In Section 4.3, we explain how the fermion parity of an even number

of MZMs can be measured through their coupling to nearby quantum dots. In Section 4.4, we give a detailed description of all of our topological qubit designs: the two-sided hexon introduced in Chapter 2, as well as one-sided hexons, linear hexons, two-sided tetrons, and linear tetrons. We elucidate the quantum information-theoretic basis for achieving all Clifford operations, i.e., a "Clifford complete" gate set, in a topologically protected manner with these designs. In Section 4.4.3, we compare and contrast the proposed qubit designs using the axes (1)-(4) mentioned above. In Section 4.5, we describe how our proposed architectures support universal quantum computation by using approximate magic state production and distillation. Finally, in Section 4.6, we outline the next experimental steps towards realizing our qubit designs.

4.2 Overview and design example

In this section, we discuss the main principles of the scalable Majorana-based quantum computing architectures presented in this chapter. For concreteness, we focus on a particular example of hexons consisting of six proximitized nanowires. In Section 4.4, we present additional architectures utilizing hexons and tetrons constructed from various numbers of proximitized nanowires.

The main building block of the presented design is a comb-like structure (see Fig. 4.1) consisting of six floating (i.e., not grounded) one-dimensional topological superconductors (1DTSs) of length L. These 1DTSs may be realized, for instance, using InAs wires coated by a superconducting half shell [157]. To form a single island hosting multiple MZMs, the

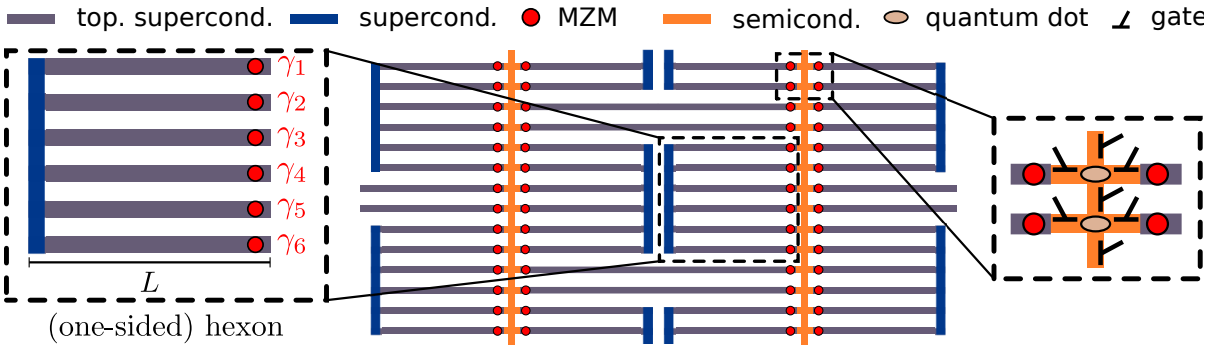

Figure 4.1: An example of a scalable hexon architecture. The minimal building block defining a qubit and an ancilla are one-sided hexons, which are topological Cooper pair boxes containing six MZMs (magnified in the left panel). Note: the illustration is not drawn to scale; in practice, the length L of 1DTS wires is much larger than the correlation length ξ and vertical separation distances between wires are much smaller than ξ. The measurement of joint parities of MZMs becomes possible by selective coupling to quantum dots. The latter are defined and controlled by gates as depicted in the magnification in the right panel. Two-MZM measurements within a hexon and four-MZM measurements involving two hexons (with two MZMs from a given hexon) enable Clifford complete operations on the array of qubits.

1DTSs are connected by a strip of (s-wave) superconductor at one side, which we refer to as the "backbone." Since the superconducting backbone is a conventional (i.e., non-topological) superconductor, the 1DTSs and the magnetic field needed to bring them into the topological phase can all be aligned in the same direction. The vertical distance between neighboring 1DTS is chosen to be shorter than the superconducting coherence length, which will lead to a strong hybridization of the six MZMs located at the backbone side of the 1DTSs. Consequently, there remain only six MZMs in the structure, localized at the non-backbone side. We denote these MZMs by γ_j for $j = 1, \ldots, 6$, which we also use to represent the corresponding Majorana operators. We call this comb-like structure a "one-sided hexon."

The hexon acts as a topological Cooper pair box [28, 8]. If operated away from charge degeneracies, i.e., in Coulomb valleys, the overall parity of the hexon $-i\prod_{j=1}^{6}\gamma_j$ will be fixed

and the charging energy will protect the system from quasiparticle poisoning. A quasiparticle poisoning event would occur if an unpaired fermionic quasiparticle hopped onto or off of the hexon. However, due to the hexon charging energy E_C, such events will be suppressed as $\exp(-E_C/T)$. As such, the hexon has a (nearly) degenerate ground state subspace that is four-dimensional, which we use to encode a logical qubit and an ancilla. A quasiparticle poisoning event would be a "leakage error" in which the system leaves the four-dimensional computation subspace.

One might additionally be concerned about thermally excited quasiparticles within the device. Provided the temperature is much smaller than the energy gap Δ, such excitations and the errors they cause are exponentially suppressed in Δ/T.

In order to avoid errors due to splitting the ground state degeneracies of the MZMs from accruing in the quantum information stored in a hexon, we require two crucial constraints for the one-sided hexons. First, the 1DTSs need to be long enough compared to the effective coherence length ξ within the 1DTSs, i.e., $L \gg \xi$, to suppress the hybridization of the MZMs by a factor of $\exp(-2L/\xi)$. Secondly, we need to suppress the charging energy associated with the mutual capacitance between two 1DTSs within a hexon. Both hybridization of the MZMs and relative charging energies between 1DTSs would result in splitting the degeneracy of the hexon ground states. The relative charging energy decreases exponentially with the number of channels that connect the 1DTSs to the backbone [231]. In the limit of many weak channels (described by a Josephson energy E_J), the relative charging energy E_{C0} is suppressed by a factor $\exp(-\sqrt{8E_J/E_{C0}})$. We assume that a direct connection of the backbone with the

superconducting shell of a nanowire has a large area in units of the Fermi wavelength, i.e., the number of transverse channels in the junction exceeds thousands. Thus, the relative charging energy will be quenched with exponential accuracy so that one can characterize this system as a superconducting island with an overall charging energy E_C. In other words, it is a topological Cooper pair box.

As the superconducting island's charging energy E_C is inversely related to its geometric capacitance, there is a trade-off between using long 1DTSs and maintaining a large charging energy. When the wire length L is much longer than the width w of the island (i.e., the length of the superconducting backbone), the geometric capacitance of the island will approximately depend linearly in L; the dependence of the capacitance on w will be more complicated, but can safely be estimated to be sub-linear. Thus, the charging energy will roughly behave as $1/L$ and there will be an optimal value of L that maximizes the combined protection, i.e., roughly when $E_C/T \approx 2L/\xi$ for the one-sided hexon. Based on estimates from experiments [5], it should not be difficult to reach a regime in which $E_C/T \sim L/\xi \gg 1$.

With the above conditions, dynamical phases and quasiparticle poisoning errors will be strongly suppressed by large exponentials. This opens the path to creating qubits with exceptionally long coherence times. In the next subsection, we discuss how these qubits can be manipulated and combined to a large scale quantum computer.

4.2.1 Single qubit operations

A universal gate set can be generated by the Clifford operations (which can be generated from

the Hadamard gate, Phase gate, and CNOT gate) supplemented by an additional non-Clifford gate. One benefit of Majorana-based quantum computing is that the Clifford operations may be implemented with topological protection, as we now explain for the hexon. We discuss how to implement the (non-Clifford) T gate in Section 4.5.

The hexon can be understood as a standard encoding of a topological qubit in four MZMs combined with an ancillary pair of MZMs. For concreteness, we let the topological qubit be encoded in MZMs γ_1, γ_2, γ_5, and γ_6, which are taken to have total fermion parity even. We can choose the basis states of the topological qubit to be $|0\rangle = |p_{12} = p_{56} = -1\rangle$ and $|1\rangle = |p_{12} = p_{56} = +1\rangle$, where p_{jk} is the eigenvalue of $i\gamma_j\gamma_k$.

The ancillary pair of MZMs γ_3 and γ_4 is thus constrained to have $i\gamma_3\gamma_4 = -1$ in this encoding. The presence of the ancillary pair of MZMs allows us to implement arbitrary braiding operations on the four MZMs of the topological qubit by appropriate measurements [34]. Moreover, we can use measurements to change which MZMs encode the computational qubit, shuttling around the ancillary MZMs via anyonic teleportation. As an example, performing a sequence of parity measurements of $i\gamma_3\gamma_4$, $i\gamma_1\gamma_3$, $i\gamma_2\gamma_3$, and then $i\gamma_3\gamma_4$ generates the same operator obtained by exchanging γ_1 and γ_2 (see Section 4.4.1 for details). In this way, intra-hexon measurements provide a precise way of generating all single-qubit Clifford gates (which can be generated by the Hadamard gate and Phase gate, for example) on the topological qubits.

These operations require us to have the ability to perform a sufficiently diverse set of parity measurements of MZM pairs. Our designs incorporate this via a quantum dot based measurement scheme. Quantum dots can be defined and selectively coupled to MZMs by tuning

depletion gates in a nearby semiconducting wire that is connected to the hexon's MZM side (see Fig. 4.1). Measurements of the parity $i\gamma_j\gamma_k$ can then be done by connecting MZMs γ_j and γ_k to quantum dots in the semiconducting wire. In general, the eigenvalue p_{jk} of $i\gamma_j\gamma_k$ will affect the ground-state energy as well as the average charge and differential capacitance of the quantum dots. This can be used in a variety of schemes to make the desired measurement, as is detailed in Section 4.3.

4.2.2 Entangling operations and full quantum computation

We must entangle different hexons in order to implement quantum operations corresponding to the full set of Clifford gates. Such entangling operations between hexons can be achieved by performing four-MZM measurements, involving two MZMs from each hexon. The latter can also be realized using quantum dots (see Section 4.3 for details). The main idea is to use an interference effect [158, 207] in the hybridization of two quantum dots arranged as in the magnified panel of Fig. 4.1. The pinch-off gates are tuned so that there is no direct connection between the two quantum dots. However, the two dots can hybridize via tunneling in and out of the MZM states of the nearby hexons. Coherently summing amplitudes along the paths through each nearby hexon leads to a detectable dependence of the hybridization energy on the overall parity of the four involved MZMs.

In order to achieve a fully-connected two dimensional graph for the entangling operations, some of the four-MZM measurements must involve MZMs that are separated by distances of approximately $2L$. Measurements involving these longer distances require additional structure

to actualize. For this purpose, additional floating topological superconductors of length $2L$ can act as links to bridge these distances by MZM-mediated coherent electron tunneling [102, 253]. Two such coherent links are placed above and below any superconducting backbone (see Fig. 4.1). The resulting (trivalent) connectivity graph of the hexon qubits is hexagonal.

Due to the freedom of arbitrary MZM exchanges within each hexon, a single entangling operation between adjacent hexon pairs is enough to realize CNOT operations between qubits and therefore make the hexons Clifford complete. The latter can be augmented to full quantum universality if we can also generate approximate magic states. The designs presented here naturally allow us to prepare very precise magic states, which lowers the overhead for magic state distillation (see Section 4.5).

We further note that error correction may be implemented at the software level on the array of hexons, as Clifford complete physical qubits support all stabilizer codes [245].

4.3 Majorana measurements

A key feature of our approach to scalable topological quantum computing is the ability to perform projective measurements of the combined fermionic parity of multiple MZMs. Such measurements are initiated by appropriately tuning gates to couple MZMs to quantum dots, as seen in the magnified right panel of Fig. 2.11. This realizes the devices depicted in Fig. 4.2 with one quantum dot (left panel) or two quantum dots (right panel). The gates control the amplitudes t_j for electrons to tunnel between the MZMs (red) and a quantum dot (light gray). At low temperature $T \ll E_C$, the probability of an excited state with an electron on the island is

exponentially small, as it is proportional to $\exp(-E_C/T)$. The virtual transitions of electrons to the island are state dependent and, therefore, shift the energy levels in a parity-dependent manner. Suitable spectroscopy on the quantum dot system allows measurements of the two-MZM parity (left panel) or of the four-MZM parity (right panel) parity [208].

The amplitude t_j is exponentially suppressed in the tunnel barrier separating γ_j from the quantum dot, and as such may be accurately tuned to zero. Before and after the measurement, all couplings are turned off, leaving the MZM island and the quantum dot with fixed charge. In this decoupled state, environmental noise, which couples to charge, can cause decoherence of states with different occupancy on the quantum dot(s), but has no effect on the MZM island. Thus, unless we are actively performing a measurement, noise cannot measure and collapse the qubit state.

There is a small probability that the final occupancy of the quantum dot(s) after the measurement will be different than before the tunnel couplings were turned on. This probability is suppressed by the charging energy of the MZM island, but it is not zero. If the charge of the quantum dot(s) is different after the measurement than it was before the measurement, then quasiparticle poisoning has occurred (the MZM island was poisoned by the dot(s)). To correct this error, one could repeat the measurement until the final dot occupations are as desired. The chance of such a quasiparticle poisoning event can be reduced by tuning the quantum dot(s) far away from resonance before disconnecting the couplings.

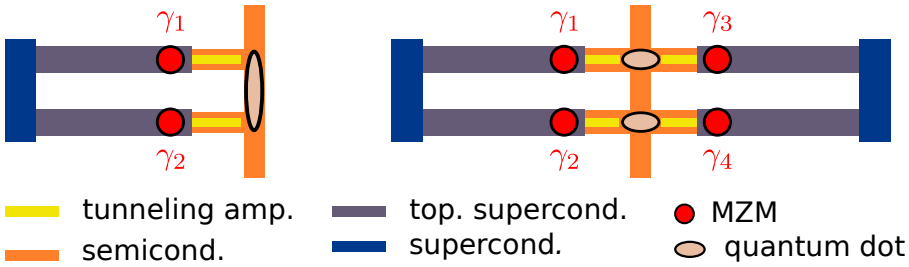

Figure 4.2: Appropriately tuning the gates shown in the magnification of the right of Fig. 2.11 creates the scenarios depicted in the left and right panels here. *Left panel*: A device configuration for measuring the two-MZM parity p_{12} (eigenvalue of $i\gamma_1\gamma_2$). MZMs γ_1 and γ_2 are coupled to a single quantum dot with tunneling amplitudes t_1 and t_2 respectively. *Right panel*: A device configuration for measuring the four-MZM parity $p = p_{12}p_{34}$, where p_{jk} is the eigenvalue of $i\gamma_j\gamma_k$. MZMs γ_1, γ_3 are tunnel coupled to the upper quantum dot, while MZMs γ_2 and γ_4 are tunnel coupled to the lower quantum dot. Both geometries can be modified to measure non-adjacent pairs of MZMs, as demonstrated in Fig. 4.9.

4.3.1 Projective measurement of two-MZM parity

We first discuss the case of two MZMs γ_1 and γ_2 coupled to a single quantum dot as shown in the left panel of Fig. 4.2. While coupling to a single MZM does not provide any information on fermion parity, non-local coupling to two or more MZMs may contain this information [102]. The coupling of quantum dots to MZMs was first discussed in Ref. [96], which considered the case of a grounded superconductor (i.e., $E_C = 0$).

When the tunneling amplitudes are zero, the MZM island and the quantum dot are decoupled. In that case, the Hamiltonian for the MZM island is

$$H_0 = H_{\text{BCS}} + H_C, \tag{4.1}$$

where H_{BCS} is the BCS Hamiltonian for an s-wave superconductor coupled to multiple semiconductor nanowires, and H_C is the charging energy Hamiltonian for the MZM island. In the low-energy approximation when energies are much smaller than the superconducting gap

Δ, the low-energy subspace contains only MZMs. We neglect the length-dependent energy splitting of MZMs, unless otherwise stated. We also assume charging energies of tetrons and hexons are large compared to temperature. The corresponding charging energy Hamiltonian is

$$H_C = E_C \left(\hat{N}_S - N_g \right)^2 . \tag{4.2}$$

The operator $\hat{N}_S$ counts the combined charge of the nanowire-superconductor island in units of the electron charge e and has integer eigenvalues N_S. The induced (dimensionless) charge on the island N_g is controlled by the gate voltage. Henceforth, we consider the limit when the charging energy on the island is large compared to temperature ($E_C \gg T$), so that its charge does not change during the course of a measurement. For simplicity, we will assume that $|N_g| \ll 1$, so that the ground-state configuration has an average charge $\langle \hat{N}_S \rangle = 0$ and energy $E_0 = E_C N_g^2$. For $\Delta \gg E_C$ the two lowest excited states $|N_S = \pm 1\rangle$ have energies $E_1 = E_C \left(1 - N_g\right)^2$ and $E_2 = E_C \left(1 + N_g\right)^2$. Thus, for $E_C \gg T$ the corresponding excitation energies are much larger than the temperature.

We assume that the semiconductor quantum dot is in a few-electron occupancy regime. The corresponding Hamiltonian is given by

$$H_{\text{QD}} = \sum_\alpha h_\alpha f_\alpha^\dagger f_\alpha + \varepsilon_C \left(\hat{n} - n_g \right)^2 , \tag{4.3}$$

where α indexes the electron orbitals of the quantum dot, f_α and $f_\alpha^\dagger$ are the corresponding fermionic annihilation and creation operators, respectively, and $\hat{n} = \sum_\alpha f_\alpha^\dagger f_\alpha$ is the total occupation operator. The h_α are the corresponding orbital energies and ε_C is the charging energy.

Here, we assume that quantum dot is in the spinless regime due to the large magnetic field necessary to drive the semiconductor nanowires into the topological phase [181, 200]. We consider the low temperature limit such that the charging energy ε_C and the level spacing in the dot are much larger than the temperature. The regime of interest is when the quantum dot is tuned to be near the charge-degeneracy point for n and $n+1$ electrons. In this case, one approximates the above Hamiltonian by an effective one corresponding to a single spinless fermion level

$$H_{\text{QD}}^{\text{eff}} = h\hat{n}_f + \varepsilon_C \left(\hat{n}_f - n_g\right)^2, \tag{4.4}$$

where the operator $\hat{n}_f = f^\dagger f$ has integer eigenvalues n_f. The two relevant low-energy states of the dot are defined by $|n_f = 0, 1\rangle$. This approximation is justified as long as the dot charging energy is the largest relevant energy scale in the system, i.e., much larger than the charging energy of the superconducting island, $\varepsilon_C \gg E_C$. The charge-degeneracy point n_g^* is defined by the condition $\epsilon_1(n_g^*) = \epsilon_0(n_g^*)$, where

$$\epsilon_1(n_s) = \varepsilon_C \left(1 - n_g\right)^2 + h, \tag{4.5}$$

$$\epsilon_0(n_s) = \varepsilon_C n_g^2. \tag{4.6}$$

When $T \ll \Delta, E_C$, we can consider the low energy approximation where one writes H_0 in terms of the MZMs on the island. Provided that the tunneling matrix elements between the quantum dot and the MZM island are smaller than the induced superconducting gap in the nanowires and the charging energy, $t_j \ll \Delta, E_C$, one can write the effective tunneling

Hamiltonian [102, 96] as

$$H_{\text{tunn}} = -i\frac{e^{-i\phi/2}}{2}\left(t_1 f^\dagger \gamma_1 + t_2 f^\dagger \gamma_2\right) + \text{h.c.}, \tag{4.7}$$

where t_1 and t_2 correspond to tunneling between the quantum dot and γ_1 and γ_2, respectively, and $e^{i\phi/2}$ is the shift operator which adds an electron to the island $e^{i\phi/2}|N_S\rangle = |N_S + 1\rangle$. Finally, the total Hamiltonian for the coupled system is given by

$$H_{\text{tot}} = H_0 + H_{\text{QD}}^{\text{eff}} + H_{\text{tunn}}. \tag{4.8}$$

The effect of H_{tunn} is to allow fermions to tunnel between the quantum dot and MZM island. We assume that the charging energy on the island is large at all times. Therefore, all electron charging processes are virtual, i.e., any fermion that hops onto the MZM island must hop back to the dot and vice versa. As shown below, such virtual transitions perturb the ground state energies in a parity-dependent manner. Consider first the case where $n_f = 1$ when the tunneling amplitudes are turned off. Turning on the t_j allows a fermion to tunnel from the dot into the MZM and then tunnel back onto the dot through a possibly different MZM. This process mixes the ground state $|N_S = 0\rangle \otimes |n_f = 1\rangle$ with the excited state $|N_S = 1\rangle \otimes |n_f = 0\rangle$, resulting in a shifted ground state energy (to the lowest order in $|t_j|/E_C$)

$$\varepsilon_1^{\text{tot}} = E_C N_g^2 + \epsilon_1 - \frac{|t_1|^2 + |t_2|^2 + ip_{12}\left(t_1^* t_2 - t_1 t_2^*\right)}{4\left(E_C(1 - 2N_g) + \epsilon_0 - \epsilon_1\right)}. \tag{4.9}$$

Here, p_{jk} is the eigenvalue of $i\gamma_j\gamma_k$, the fermion parity of the two MZMs coupled to the quantum dot. In other words, this calculation applies to both $p_{12} = \pm 1$ initial ground states. This parity dependence originates from elastic co-tunneling through the corresponding pair of

MZMs.

Alternatively, if the quantum dot is unoccupied when $t_j = 0$, then when the t_j are turned on, an electron can tunnel from a MZM onto the dot, then tunnel into a (possibly different) MZM, mixing the ground state $|N_S = 0\rangle \otimes |n_f = 0\rangle$ with the excited state $|N_S = -1\rangle \otimes |n_f = 1\rangle$. The corresponding shifted ground state energy is (to lowest order in $|t_j|/E_C$)

$$\varepsilon_0^{\text{tot}} = E_C N_g^2 + \epsilon_0 - \frac{|t_1|^2 + |t_2|^2 - ip_{12}\left(t_1^* t_2 - t_1 t_2^*\right)}{4\left(E_C(1+2N_g) + \epsilon_1 - \epsilon_0\right)}. \tag{4.10}$$

In both Eqs. (4.9) and (4.10), the parity dependence arises from the coupling between the quantum dot and MZMs. Indeed, by setting either t_1 or t_2 to zero one finds a correction to the quantum dot ground-state energy that is independent of p_{12}. At the charge degeneracy point n_g^* of the quantum dot, the parity dependence of $\varepsilon_1^{\text{tot}} - \varepsilon_0^{\text{tot}}$ scales as $\text{Im}[t_1^* t_2/E_C]$.

It is also important to observe that the parity dependence disappears if both t_1 and t_2 are real, even if both quantities are finite. Since time-reversal symmetry is broken, this is not generic. However, for spinless fermions one may introduce an artificial anti-unitary symmetry $\mathcal{T}$ that squares to $+1$ [92]. Since a bilinear coupling between γ_1 and γ_2 is precluded, t_1 and t_2 are necessarily real. Fortunately, $\mathcal{T}$ is most certainly *not* a microscopic symmetry of our setup. However, the parity dependence of the shifted ground state energies may be "accidentally" weak for non-generic tunneling amplitudes. We comment further on this issue in Section 4.6.

4.3.2 Projective measurement of four-MZM parity

In order to describe the device configuration shown in the right panel of Fig. 4.2, the Hamiltonian of Eq. (4.8) is modified to include two superconducting islands (four MZMs) and two

quantum dots. The decoupled MZM island Hamiltonian H_0 becomes a sum of Hamiltonians for the left and right MZM islands (labeled $a = 1$ and 2, respectively). The two islands may have different charging energies and induced charges, so the total (decoupled) charging energy Hamiltonian is the sum of those of the two islands:

$$H_C = \sum_{a=1,2} H_{C,a}, \tag{4.11}$$

$$H_{C,a} = E_{C,a}\left(\hat{N}_{S,a} - N_{g,a}\right)^2. \tag{4.12}$$

For simplicity, we again assume that $|N_{g,a}| \ll 1$ for both islands, so the ground state of the decoupled MZM islands has energy $E_0 = E_{C,1}N_{g,1}^2 + E_{C,2}N_{g,2}^2$. In general, the charging energies and induced charges of the two quantum dots can also be different. For simplicity, we consider the case in which they are the same. The effective Hamiltonian for the two semiconductor QDs may be written as

$$H_{\rm QD}^{\rm eff} = \sum_{a=1,2} h_a \hat{n}_{f,a} + \varepsilon_{C,a}\left(\hat{n}_{f,a} - n_{g,a}\right)^2 + \varepsilon_M\left(\hat{n}_{f,1} - n_{g,1}\right)\left(\hat{n}_{f,2} - n_{g,2}\right). \tag{4.13}$$

The first term in Eq. (4.13) is simply the sum of the effective Hamiltonians of the two decoupled QDs, while the last term describes a mutual charging energy between the two quantum dots. We consider the case when $\varepsilon_M \ll \varepsilon_{C,a}$. The mutual charging energy may be appreciable for the geometry shown in the right panel of Fig. 4.2, but can be neglected in other measurements of the joint parity of four MZMs (e.g., measurements involving MZMs on opposite sides of the two-sided hexon shown in Fig. 4.10). For simplicity, we will henceforth set $h_1 = h_2 \equiv h$ and $\varepsilon_{C,1} = \varepsilon_{C,2} \equiv \varepsilon_C$. We assume that there is no direct tunneling from one dot to the other; the

only way for an electron to tunnel between quantum dots is through a superconducting island.

The tunneling Hamiltonian now involves four MZMs, taking the form

$$H_{\text{tunn}} = -\frac{ie^{-i\phi_1/2}}{2}\left(t_1 f_1^\dagger \gamma_1 + t_2 f_2^\dagger \gamma_2\right) - \frac{e^{-i\phi_2/2}}{2}\left(t_3 f_1^\dagger \gamma_3 + t_4 f_2^\dagger \gamma_4\right) + \text{h.c.}, \tag{4.14}$$

where the upper and lower quantum dots are labeled 1 and 2, respectively, so that f_1, $f_1^\dagger$, f_2, and $f_2^\dagger$ are their corresponding annihilation and creation operators. $e^{-i\frac{\phi_1}{2}}$ and $e^{-i\frac{\phi_2}{2}}$ are the electron shift operators for left and right islands, respectively.

As we saw for two MZMs, nonzero tunneling amplitudes mediate virtual transfer of fermions between the MZM islands and the quantum dot, thereby shifting the spectrum from that of the decoupled system. Crucially, the perturbed energies depend on the joint parity of the two MZM islands $p = p_{12}p_{34}$ and does not depend on p_{12} or p_{34} individually. This dependence can be intuitively understood by considering the tunneling paths a fermion can take: it either travels partway around the loop and then backtracks (thereby only picking factors of p_{jk}^0 or p_{jk}^2, both of which equal one), or it makes a full loop (picking up a factor of $p_{12}p_{34}$). These arguments can be generalized to higher orders in perturbation theory where multiple loops are allowed. The resulting energy shifts only depend on the joint parity in any order of perturbation theory.

More quantitatively, the total Hamiltonian

$$H_{\text{tot}}^{\text{eff}} = H_C + H_{\text{BCS}} + H_{\text{QD}}^{\text{eff}} + H_{\text{tunn}} \tag{4.15}$$

has four low-energy states for given values of p_{12} and p_{34}, which we label $\beta = 0, 1, 2, 3$, with corresponding energies $\varepsilon_\beta^{\text{tot}}$. When $t_j = 0$ and $N_{g,a} = 0$, these four states are those in which the occupancies $(n_{f,1}, n_{f,2})$ of the two dots are $(0,0)$, $(1,0)$, $(0,1)$, and $(1,1)$, and which have

the respective energies ϵ_0, ϵ_1, ϵ_2, and ϵ_3

$$\epsilon_0 = \varepsilon_{C,1} n_{g,1}^2 + \varepsilon_{C,2} n_{g,2}^2 + \varepsilon_M n_{g,1} n_{g,2} \tag{4.16}$$

$$\epsilon_1 = \varepsilon_{C,1} \left(1 - n_{g,1}\right)^2 + h_1 + \varepsilon_{C,2} n_{g,2}^2 - \varepsilon_M (1 - n_{g,1}) n_{g,2} \tag{4.17}$$

$$\epsilon_2 = \varepsilon_{C,1} n_{g,1}^2 + \varepsilon_{C,2} \left(1 - n_{g,2}\right)^2 + h_2 - \varepsilon_M n_{g,1} (1 - n_{g,2}) \tag{4.18}$$

$$\epsilon_3 = \varepsilon_{C,1} \left(1 - n_{g,1}\right)^2 + h_1 + \varepsilon_{C,2} \left(1 - n_{g,2}\right)^2 + h_2 + \varepsilon_M (1 - n_{g,1})(1 - n_{g,2}). \tag{4.19}$$

Consider the case where both islands have equal charging energy, $E_{C,a} = E_C$. When $t_j \neq 0$, the states $\beta = 0$ and 3, corresponding to quantum dot occupancies $(0,0)$ and $(1,1)$, do not hybridize. The tunneling Hamiltonian allows fermions to tunnel into and out of the same MZM, resulting in the perturbed energies given by

$$\varepsilon_0^{\text{tot}} = \epsilon_0 - \frac{1}{4}\left(\frac{|t_1|^2 + |t_3|^2}{E_C + \epsilon_1 - \epsilon_0} + \frac{|t_2|^2 + |t_4|^2}{E_C + \epsilon_2 - \epsilon_0}\right), \tag{4.20}$$

$$\varepsilon_3^{\text{tot}} = \epsilon_3 - \frac{1}{4}\left(\frac{|t_1|^2 + |t_3|^2}{E_C + \epsilon_1 - \epsilon_3} + \frac{|t_2|^2 + |t_4|^2}{E_C + \epsilon_2 - \epsilon_3}\right), \tag{4.21}$$

to leading order in t_j/E_C. These energies are clearly independent of the MZM parities.

In contrast, nonzero t_j hybridizes the $\beta = 1$ and 2 states, corresponding to quantum dot occupancies $(1,0)$ and $(0,1)$. The second order perturbation theory Hamiltonian for these two states can be written as

$$H^{(0)} + H^{(2)} = B_0 1 + B_x \sigma_x + B_y \sigma_y + B_z \sigma_z, \tag{4.22}$$

where the Pauli matrices σ_μ act in the basis of the quantum dot states $(1,0)$ and $(0,1)$. We find

diagonal elements

$$B_0 = \frac{\epsilon_1+\epsilon_2}{2} - \frac{1}{8}\Big(\left(|t_1|^2+|t_3|^2\right)\left(\frac{2E_C+\epsilon_0+\epsilon_3-\epsilon_1-\epsilon_2}{(E_C+\epsilon_0-\epsilon_1)\,(E_C+\epsilon_3-\epsilon_2)}\right) + \left(|t_2|^2+|t_4|^2\right)\left(\frac{2E_C+\epsilon_0+\epsilon_3-\epsilon_1-\epsilon_2}{(E_C+\epsilon_3-\epsilon_1)\,(E_C+\epsilon_0-\epsilon_2)}\right)\Big) \tag{4.23}$$

$$B_z = \frac{\epsilon_1-\epsilon_2}{2} - \frac{1}{8}\Big(\left(|t_1|^2+|t_3|^2\right)\left(\frac{\epsilon_3-\epsilon_2-\epsilon_0+\epsilon_1}{(E_C+\epsilon_0-\epsilon_1)\,(E_C+\epsilon_3-\epsilon_2)}\right) + \left(|t_2|^2+|t_4|^2\right)\left(\frac{\epsilon_0-\epsilon_2-\epsilon_3+\epsilon_1}{(E_C+\epsilon_3-\epsilon_1)\,(E_C+\epsilon_0-\epsilon_2)}\right)\Big) \tag{4.24}$$

and off-diagonal matrix elements

$$B_x = \mathrm{Re}\Big[p_{12}t_1t_2^* + p_{34}t_3t_4^*\Big]\frac{1}{8}\Big(\frac{2E_C+\epsilon_0+\epsilon_3-2\epsilon_2}{(E_C+\epsilon_0-\epsilon_2)\,(E_C+\epsilon_3-\epsilon_2)} + \frac{2E_C+\epsilon_0+\epsilon_3-2\epsilon_1}{(E_C+\epsilon_0-\epsilon_1)\,(E_C+\epsilon_3-\epsilon_1)}\Big) \tag{4.25}$$

$$B_y = \mathrm{Im}\Big[p_{12}t_1t_2^* + p_{34}t_3t_4^*\Big]\frac{1}{8}\Big(\frac{2E_C+\epsilon_0+\epsilon_3-2\epsilon_2}{(E_C+\epsilon_0-\epsilon_2)\,(E_C+\epsilon_3-\epsilon_2)} + \frac{2E_C+\epsilon_0+\epsilon_3-2\epsilon_1}{(E_C+\epsilon_0-\epsilon_1)\,(E_C+\epsilon_3-\epsilon_1)}\Big). \tag{4.26}$$

The latter correspond to elastic co-tunneling processes mediated by different pairs of MZMs.

The energy eigenvalues of Eq. (4.22) are given by

$$\varepsilon_1^{\mathrm{tot}} = B_0 - \sqrt{B_x^2+B_y^2+B_z^2}, \tag{4.27}$$

$$\varepsilon_2^{\mathrm{tot}} = B_0 + \sqrt{B_x^2+B_y^2+B_z^2}. \tag{4.28}$$

Clearly, the parity dependence in these energies comes from $B_x^2+B_y^2$ and results in a term

under the square root in Eqs. (4.27) and (4.28) that is proportional to

$$|p_{12}t_1t_2^* + p_{34}t_3t_4^*|^2 = |t_1|^2|t_2|^2 + |t_3|^2|t_4|^2 + 2p\,\mathrm{Re}\,(t_1t_2^*t_3^*t_4)\,. \tag{4.29}$$

Thus, the only MZM parity dependence of the energies is on the total parity $p = p_{12}p_{34}$ of the four MZMs, arising from fermions tunneling around the entire loop (see Ref. [141] for further details).

In the lower panel of Fig. 4.4, we plot the eigenvalues of Eq. (4.15) as a function of the induced charge $n_{g,1}$ on the top quantum dot. Notice that the parity dependence of $\varepsilon_1^{\mathrm{tot}}$ and $\varepsilon_2^{\mathrm{tot}}$ is strongest for $n_{g,1} = n_{g,2}$, where charge fluctuations are strongest. Experimentally it would therefore be best to tune to a regime where the $(1,0)$ and $(0,1)$ states are resonant (and lower in energy than the $(0,0)$ and $(1,1)$ states). The corresponding stability diagram for the ground state of the decoupled double dot system is shown in the upper panel of Fig. 4.4.

The energy dependence on the four-MZM joint parity p could also be achieved with a single quantum dot. The right panel of Fig. 4.2 can be modified by removing the lower dot and directly coupling MZMs γ_2 and γ_4. Such a system sacrifices some of the tunability of the double quantum dot system and could introduce complications from low-lying excited states in the semiconductor wire segment connecting γ_2 and γ_4. Nonetheless, if a single-dot system were substantially easier to realize, it could prove to be more advantageous to achieve the same projective measurement of four-MZM parity in this way. Similarly, the two-MZM parity measurements of Section 4.3.1 could also be performed using two quantum dots instead of one.

Finally, the above analysis is easily generalized to measure the joint parity of any even number of MZMs. Whenever gate voltages are tuned such that the tunneling connections create

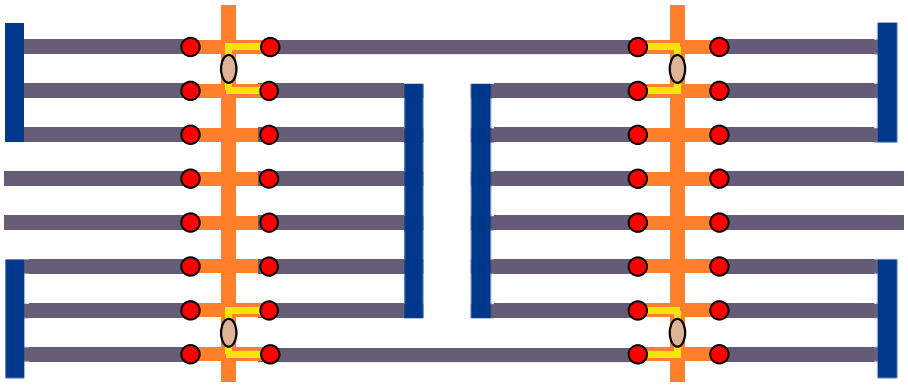

Figure 4.3: An example configuration for a joint parity measurement of 8 MZMs involving two one-sided hexons and two coherent links (using the same legend as Fig. 4.2). Four of the MZMs involved in the measurement are associated with coherent links and are used to facilitate the measurement of the other four MZMs, which are associated to the hexons. The resulting measurement can provide a two-qubit entangling operation on the two hexons.

a single closed loop path for electrons that traverses $2n$ MZMs, the energy of the system will depend on the $2n$-MZM parity. An example configuration for a multiple-MZM measurement using an array of one-sided hexons is shown in Fig. 4.3. In practice, the measurement visibility will decrease with each additional MZM pair, so it is important to utilize measurements involving the smallest number of MZMs possible.

4.3.3 Experimental proposals for MZM parity measurements

The parity-dependent energy shift, discussed in the previous subsections, can be observed using energy level spectroscopy, quantum dot charge, or differential capacitance measurements. We now briefly discuss these different measurements and consider specific proposals which differ in their speed and sensitivity to noise. Each such measurement is designed to project the system to a definite parity state (of two MZMs in Section 4.3.1 and four MZMs in Section 4.3.2). For concreteness, we focus henceforth on the four-MZM case (right panel of Fig. 4.2); the

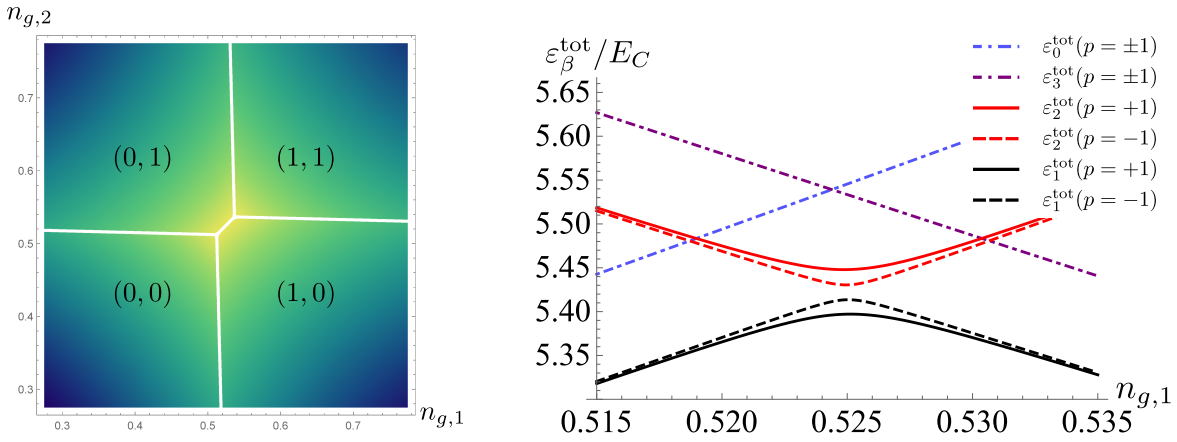

Figure 4.4: Energy as a function of dimensionless induced charges on the quantum dots for the system shown in the right panel of Fig. 4.2. *Left panel*: Stability diagram for the decoupled system ($t_j = 0$) as a function of the occupation numbers $(n_{f,1}, n_{f,2})$ of the double quantum dot system in the ground state. The color scale refers to the ground state energy, whose precise values away from zero (indicated by white) are unimportant for the current discussion. *Right panel*: The four lowest energies $\varepsilon_\beta^{\rm tot}/E_C$ as a function of $n_{g,1}$ for $n_{g,2} = (1 + h/\varepsilon_C)/2$ with tunneling amplitudes $t_1 = 0.1E_C$ and $t_{j\neq 1} = 0.2E_C$. We use the parameter values $N_{g,a} = 0$, $\varepsilon_C = 10E_C$, $h = E_C/2$, and $\varepsilon_M = E_C/2$. For non-vanishing tunneling amplitudes, the quantum dot states $(1, 0)$ and $(0, 1)$ hybridize. The symmetric combination of the $(1, 0)$ and $(0, 1)$ states has energy $\varepsilon_2^{\rm tot}$ (shown in red) and the antisymmetric combination has energy $\varepsilon_1^{\rm tot}$ (shown in black). These energies $\varepsilon_1^{\rm tot}$ and $\varepsilon_2^{\rm tot}$ depend on the joint parity p of the four MZMs; the solid curves correspond to even parity $p = 1$ and dashed curves to odd parity $p = -1$. As our model only considers two quantum dot levels, the states $(0, 0)$ and $(1, 1)$ do not hybridize. These states have corresponding parity-independent energies $\varepsilon_0^{\rm tot}$ (shown as the blue dot-dashed curve) and $\varepsilon_3^{\rm tot}$ (shown as the purple dot-dashed curve), respectively. From the stability diagram (left panel), we see that the mutual charging energy ε_M increases the range of $n_{g,1}$ and $n_{g,2}$ for which the parity-dependent energy $\varepsilon_1^{\rm tot}$ is the ground state.

discussion generalizes straightforwardly to the two-MZM case (left panel of Fig. 4.2).

We assume the double quantum dot system is properly tuned such that the relevant states are those sensitive to the parity of the MZMs, that is, the relevant states have one electron shared between the two quantum dots. Moreover, we focus on the regime in which the system has only weakly occupied excited states, so that the system can be described by the ground state with corresponding energy $\varepsilon_1^{\rm tot}$. When the double dot system is tuned close to resonance,

the gap to the lowest excited state is of the order of $|t|^2/E_C$ when $|t_j| \sim |t|$. In order to have an appreciable difference between the occupation of the ground and excited states, we require that $T \ll |t|^2/E_C$ [2]. Away from resonance, the condition on temperature can be relaxed at the cost of reducing the visibility (see Fig. 4.4). Similarly, finite temperature effects are negligible for single quantum dot measurements in which the first excited state is separated from the ground state by an energy on the order of E_C.

Let us first consider energy level spectroscopy. The dependence of the ground-state energy on parity is shown in Fig. 4.4. One possible spectroscopic measurement is done by coupling the system (MZM island and quantum dots) to a superconducting transmission line resonator. The resonator frequency will have a parity-dependent frequency shift $\Delta\omega$ which can be detected using the reflectometry technique [184]. We find that for the four-MZM device discussed in Section 4.3.2, the frequency shift is given by

$$\Delta\omega \sim \frac{g^2}{4\delta\omega^2}\frac{t^2}{E_C}, \tag{4.30}$$

where g is the coupling between the resonator and the quantum dot and $\delta\omega$ is the detuning, i.e., the frequency difference between $\varepsilon_2^{\rm tot} - \varepsilon_1^{\rm tot}$ at the degeneracy point n_g^* and the resonator frequency. Here, we have assumed that all of the tunneling matrix elements are comparable to t. Using realistic parameters defined in Fig. 4.4, frequency estimates given in Ref. [153], and $E_C = 160$ μeV (see Ref. [5]), we estimate $\Delta\omega \sim 100$ MHz. This frequency shift falls well within the range of transmon sensitivity. Spectroscopy with a transmission line resonator benefits from a fairly short measurement time on the order of 1μs. However, the resonator will

[2] For the parameters of Fig. 4.4, with $E_C = 1$ K, the gap is of the order of 50 mK, which would suffice for typical temperatures $T \sim 20$ mK.

have to operate in large magnetic fields, so one would need to adapt this technology to such conditions.

The main drawback of this proposal is that while this measurement technique is suitable for a small number of qubits, it may become problematic when scaling to a two-dimensional array of qubits. This is because the resonators need to be taken off the plane containing the topological qubits, since there is no room for them in the planar layout shown in Fig. 2.11. Coupling out-of-plane resonators to qubits poses additional experimental challenges.

Another way of performing a joint parity measurement is to detect the average charge on a quantum dot. Indeed, the charge $n_{f,1}$ on the upper dot is related to the energy by

$$\langle n_{f,1} \rangle \approx n_{g,1} - \frac{1}{2\varepsilon_C} \left(\frac{\partial E_{\text{GS}}}{\partial n_{g,1}} - \frac{\varepsilon_M}{2\varepsilon_C} \frac{\partial E_{\text{GS}}}{\partial n_{g,2}} \right), \tag{4.31}$$

where E_{GS} denotes the ground state energy of the system. In this expression, we have neglected $O(\varepsilon_M^2/\varepsilon_C^2)$ terms. The dependence of the average charge on the joint parity of MZMs is shown in Fig. 4.5. Quantum charge fluctuations broaden the step function in a manner that depends on the joint fermion parity of MZMs. Hence, measurement of the charge on the dot allows one to distinguish different parity states. Given that the average charge on the dot can be measured very accurately at low temperatures, i.e., up to roughly $10^{-3}\, e/\sqrt{\tau_{\text{int}}}$ where τ_{int} is the integration time [164, 219, 23] , we believe that our predictions are within experimental reach. Charge measurements are very fast and accurate. This technique is well understood in the semiconductor community and is compatible with large magnetic fields. While the inclusion of SETs in the qubit plane makes the design somewhat more complicated, it does not preclude scaling the system up to a two-dimensional array of qubits.

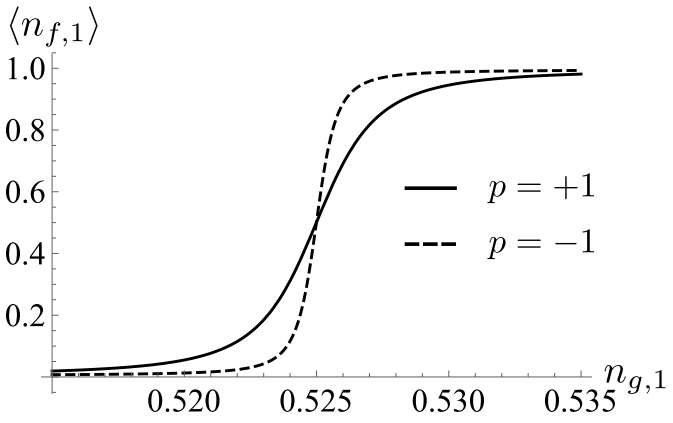

Figure 4.5: Average charge (in units of electron charge) on the upper quantum dot as a function of the dimensionless induced charge $n_{g,1}$ for the system shown in the right panel of Fig. 4.2. We assume the system is in the ground state, and plot the average charge for both even parity (solid curve) and odd parity (dashed curve). We use the parameter values $N_{g,a} = 0$, $\varepsilon_C = 10E_C$, $h = E_C/2$, and $\varepsilon_M = E_C/2$.

Finally, we discuss the third proposal – a differential capacitance (also referred to as the quantum capacitance) measurement [86, 201, 204, 70]. The differential capacitance of the upper quantum dot is given by

$$\frac{C_{\text{diff}}}{C_{\Sigma,D}} = -\left(\frac{C_g}{C_{\Sigma,D}}\right)^2 \frac{\partial(\langle n_{f,1}\rangle - n_{g,1})}{\partial n_{g,1}}, \tag{4.32}$$

where C_g is the capacitance between the gate and the upper quantum dot, and $C_{\Sigma,D} \equiv e^2/2\varepsilon_C$ is the total capacitance of the dot. When the system is tuned close to resonance of the two quantum dots, the energy is sensitive to changes in $n_{g,1}$, making the differential capacitance become appreciable. We can use rf-reflectometry to measure the differential capacitance of the upper quantum dot by coupling the gate voltage $V_{g,1} = en_{g,1}/C_g$ directly to an LC circuit. The circuit's resonant frequency will depend on the differential capacitance, which, in turn, depends on the joint parity of the four MZMs. Thus, the reflection of an rf-signal sent through the circuit can be analyzed to infer the parity state of the system. The frequency of the rf-signal will have

to be properly engineered. If the frequency of the rf-signal is lower than the excitation gap near the resonance (i.e., near $n_{g,1} = n_g^*$, which is the location of the anti-crossing in Fig. 4.4), the system will remain in the ground state, and the differential capacitance will contain information about the ground state curvature at this point. However, if the frequency is too large, the system will undergo a Landau-Zener transition at the resonance (transitioning from one of the lower curves in Fig. 4.4 to one of the upper ones), and the reflected signal will not contain information about the ground state curvature, resulting in a vanishingly small differential capacitance. Since differential capacitance is peaked at the degeneracy point, thermal fluctuations or gate-voltage fluctuations will broaden the signal. In order to suppress the effect of thermal fluctuations, we require that $|t|^2/E_C \gg T$. Provided this broadening is smaller than the parity-dependent differential capacitance difference, the projective measurement can be efficiently performed.

Assuming that the quantum dot charging energy $\varepsilon_C \sim 1 - 10$ K, which corresponds to the total capacitance $C_{\Sigma,D} \sim 10^2 - 10^3$ aF, the change of the differential capacitance for different parity states should be $\delta C_{\text{diff}} \sim 10^2 - 10^3$ aF (see Fig. 4.6). Note that this curve is the derivative of the charge as a function of the $n_{g,1}$ curve shown in Fig. 4.5. That is, it involves the second derivatives (rather than the first derivatives) of the energy with respect to $n_{g,1}$ and $n_{g,2}$. The curves in Fig. 4.6 are peaked where the curves in Fig. 4.5 are steepest. Reflectometry experiments in quantum dot systems have measured differential capacitances of the order of 10 aF in 40 μs [70]. Therefore, we believe that the joint parity state should be measurable through the differential capacitance even when the tunnel couplings are not optimized. The gates needed for the reflectometry measurement are already necessary in the system in order to

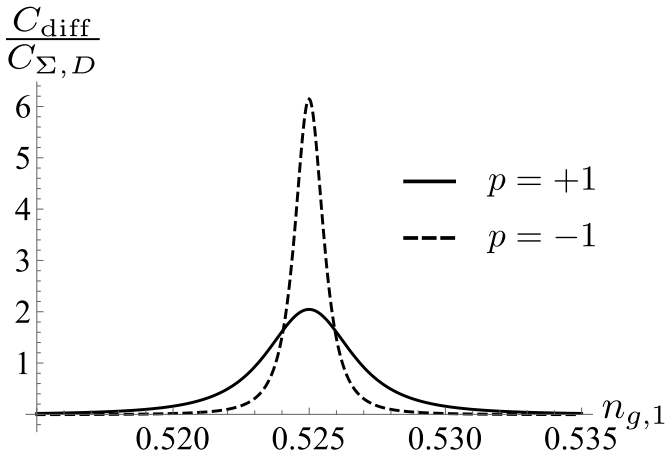

Figure 4.6: Differential capacitance of the ground state $C_{\rm diff}$ (in units of $C_{\Sigma,D}$) as a function of the dimensionless induced charge $n_{g,1}$ for the system shown in the right panel of Fig. 4.2. Both even parity (solid curve) and odd parity (dashed curve) are shown. We use the parameter values $N_{g,a} = 0$, $\varepsilon_C = 10E_C$, $h = E_C/2$, $\varepsilon_M = E_C/2$, and $C_g/C_{\Sigma,D} = 0.1$.

define the quantum dots (see Fig. 2.11), and the LC circuits are can be moved off the plane of the MZM islands.

Both charge-sensing and reflectometry detection of differential capacitance have the attractive feature of being measurements of ground state properties. Up to exponentially small thermal corrections, there is no decoherence in the ground state; as such, the visibility of these measurements will not decrease significantly over time.

4.4 Clifford-complete Majorana architectures

We now show how the projective measurements of the previous section may be used in combination with MZM-based qubits to implement the complete set of multi-qubit Clifford gates in a topologically protected manner. All of our designs utilize measurement-based braiding, reviewed in Chapter 2. We show here that the allowed set of measurements for each design is

sufficient to implement Clifford-complete gates. The next section will explain how the designs can be supplemented with magic state distillation to support universal quantum computation.

4.4.1 Hexon architectures

In this section, we describe the three different hexon architectures. Six is the smallest number of MZMs that supports the combination of one computational qubit (encoded in four of the MZMs) and one ancillary pair of MZMs. This combination is particularly useful because the presence of the ancillary pair makes it possible to generate the braiding transformations of the topological qubit without physically transporting the MZMs. That is, sequences of topological charge measurements can generate the braiding transformations on the qubit states encoded in the MZMs [34, 35]. The topological charge of an even number of MZMs is their joint electron number parity. In this chapter, we focus on measurement-based protocols. However, the braiding transformations can equivalently be performed using similar methods that instead utilize adiabatic tuning of couplings between MZMs [32] or hybrid protocols that use both nearly-adiabatic tuning and measurement [153]. Furthermore, an entangling gate can be implemented with the addition of a joint parity measurement of four MZMs from neighboring hexons, two MZMs from each hexon. Thus, by using the hexon together with the ability to perform joint parity measurements, one generates all multi-qubit Clifford gates with topological protection, while simultaneously protecting the qubit from quasiparticle poisoning errors.

Quantum information basics

The full set of single-qubit Clifford gates can be generated on the computational qubit encoded in a single hexon given an appropriate minimal set of joint parity measurements of pairs of MZMs. We can diagrammatically represent the topological state of a hexon as shown in Fig. 5.1. We label the MZMs γ_j with $j = 1, \ldots, 6$ from left to right. The diagram may be interpreted as follows: The center two MZMs γ_3 and γ_4, forming the ancillary pair, fuse to even fermion parity ($p_{34} = -1$). The left-most and the right-most pairs of MZMs, γ_1 and γ_2, and γ_5 and γ_6, respectively, forming the computational qubit, have the same fusion channel $a = 0$ (even fermion parity) or 1 (odd fermion parity). That is, the fusion channel a labels the qubit basis states

$$|0\rangle = |p_{12} = p_{56} = -1\rangle \tag{4.33}$$
$$|1\rangle = |p_{12} = p_{56} = +1\rangle. \tag{4.34}$$

The total fusion channel of the four MZMs forming the computational qubit is even fermion parity ($p_{12}p_{56} = 1$).

In Section 4.3.3, we explained how joint fermion parity measurements may be implemented using dispersive transmon measurements, charge-sensing, or reflectometry. While the outcomes of quantum measurements are inherently probabilistic, the forced-measurement protocol [34] reviewed in Chapter 2 and utilized in Chapter 3 can again be applied here to obtain the desired measurement outcome of a particular step of the measurement-only protocol. This is a repeat-until-success protocol involving alternating measurements between the pair of MZMs that is to become ancillary and the pair that was ancillary, until the desired outcome is achieved.

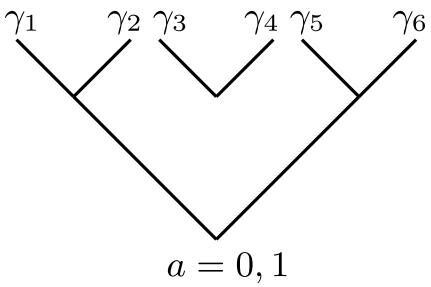

Figure 4.7: Diagrammatic representation of the topological states (degenerate ground states) of a hexon. The center two MZMs γ_3 and γ_4 fuse to even fermion parity, forming the ancillary pair of MZMs. The left and right pairs of MZMs both fuse to $a = 0$ or 1, which correspond to even or odd fermion parity, respectively. These outer pairs of MZMs form the computational qubit. The fusion channel a labels the qubit basis state. See Appendix A for a review of diagrammatic anyon models.

As such, the encoded computational state information is preserved and this allows us to think in terms of projectors, rather than projective measurements.

Let $\Pi_0^{(jk)} = \frac{1-i\gamma_j\gamma_k}{2}$ project MZMs j and k to the vacuum (even fermion parity) channel. Braiding operations can be implemented through the application of a series of such projectors. For instance, the following sequence of projections generates the braiding transformation corresponding to exchanging the first and second MZMs

$$\Pi_0^{(34)}\Pi_0^{(13)}\Pi_0^{(23)}\Pi_0^{(34)} \propto R^{(12)} \otimes \Pi_0^{(34)}, \tag{4.35}$$

where $R^{(12)} \equiv (1 + \gamma_1\gamma_2)/\sqrt{2}$ is the braiding transformation for exchanging MZMs 1 and 2. Whether the operator $R^{(12)}$ describes a clockwise or counterclockwise exchange of the MZMs is a matter of convention since the γ_i operators can be changed by a sign via a gauge transformation. Here, we define it as a counterclockwise exchange as diagrammatically represented in Fig. 4.8. This choice determines whether the projector $\Pi_0^{(13)}$ is interpreted in the diagrammatic representation as an over-crossing or under-crossing with respect to the γ_2 charge line.

We note that the above convention should be fixed with respect to a particular measurement

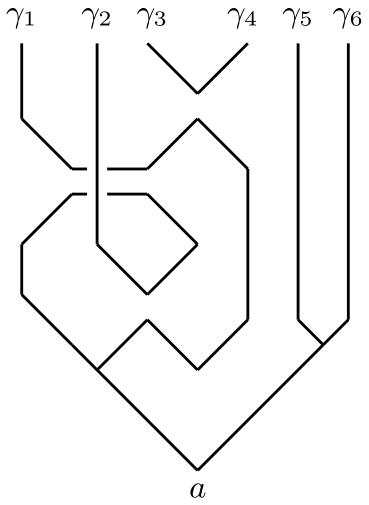

Figure 4.8: Diagrammatic representation of $\Pi_0^{(34)}\Pi_0^{(13)}\Pi_0^{(23)}\Pi_0^{(34)}$ applied to the topological state of a hexon qubit. Pairs of MZMs are projected to the vacuum (even fermion parity) fusion channel to perform anyonic teleportations on the topological state space of the MZMs. The series of projections has the same effect as exchanging the positions of MZMs 1 and 2, i.e., it generates the braiding operator $R^{(12)}$. This provides a diagrammatic proof of Eq. (4.35), as originally given in Ref. [34]. See Appendix A for a review of diagrammatic anyon models.

setup (defined by the complex couplings t_j of MZMs to quantum dots). The effect of a change of the measurement setup during the calculation (e.g., by deciding to measure a certain pair of MZMs differently than in the initial definition) can be tracked by a bookkeeping of phase changes [7, 101, 116].

While Eq. (4.35) has the elegant diagrammatic representation shown in Fig. 4.8, which makes the relation to braiding apparent, it can also be derived explicitly in terms of Majorana operators, as was done in Eq. (2.36).

A sufficient gate set for generating all single-qubit Clifford gates is given by the two (intra-hexon) braiding transformations, $R^{(12)}$ and $R^{(25)}$, which, up to an overall phase, respectively correspond to the computational gates

$$R^{(12)} = \begin{pmatrix} 1 & 0 \\ 0 & -i \end{pmatrix}, \tag{4.36}$$

$$R^{(25)} = \frac{1}{\sqrt{2}} \begin{pmatrix} 1 & i \\ i & 1 \end{pmatrix}, \tag{4.37}$$

using the qubit basis. Note that the Hadamard gate is given by $H = R^{(12)} R^{(25)} R^{(12)}$.

The braiding transformation $R^{(25)}$ may be implemented using the following sequence of projections

$$\Pi_0^{(34)} \Pi_0^{(35)} \Pi_0^{(23)} \Pi_0^{(34)} \propto R^{(25)} \otimes \Pi_0^{(34)}. \tag{4.38}$$

In order to have a multi-qubit Clifford complete gate set, we only need to add the ability to perform an entangling two-qubit Clifford gate between neighboring computational qubits. Similarly labeling the MZMs of a second hexon by $j = 7, \ldots, 12$, we find that the following sequence of projective parity measurements on two and four MZMs in two hexons

$$\Pi_0^{(34)} \Pi_0^{(35)} \Pi_0^{(5678)} \Pi_0^{(45)} \Pi_0^{(34)} \propto W^{(5678)} \otimes \Pi_0^{(34)}, \tag{4.39}$$

generates $W^{(5678)} \equiv \left(1 + i\gamma_5\gamma_6\gamma_7\gamma_8\right)/\sqrt{2}$. In terms of the topological qubit basis states of the two hexons, this yields the two-qubit entangling Clifford gate

$$W = \begin{pmatrix} 1 & 0 & 0 & 0 \\ 0 & i & 0 & 0 \\ 0 & 0 & i & 0 \\ 0 & 0 & 0 & 1 \end{pmatrix}, \tag{4.40}$$

up to an overall phase [141]. Note that the controlled-Z gate is given by $C(Z) = R^{(12)} R^{(78)} W^{(5678)}$.

We emphasize that this two-hexon operation respects the fermion parity of each hexon separately, so it is compatible with the protection from quasiparticle poisoning afforded by the Coulomb charging energy on each superconducting island. We also note that, as long as one is able to perform the appropriate measurements of MZMs, one ancillary pair of MZMs on an island is sufficient for implementing entangling gates between two computational qubits on separate islands (i.e., between two hexon qubits), without the need of extra ancillary MZMs. In the above example, the only ancillary pair needed was MZMs 3 and 4.

Taken together, Eqs. (4.35), (4.38), and (4.39) reveal a sufficient set of measurements that allow us to generate all multi-qubit Clifford gates. While the operational efficiency may be improved if we are able to perform measurements on additional groups of MZMs, practical constraints may limit which groups of MZMs we can jointly measure, as we will discuss below. In our proposed hexon architectures, we find that we are always able to perform measurements that are Clifford complete.

The three different hexon architectures that are described in the following subsections support several additional operations that make computations more efficient. For instance, it is convenient to be able to shuttle the computational MZMs, so that they are adjacent to each other. This shuttling can be achieved with a series of projective fermion parity measurements of pairs of MZMs [141]. From the Gottesman-Knill theorem, we know that Clifford operations can be efficiently modeled on a classical computer. This can be used to transfer some of the computation from quantum operations, such as those described above, to classical simulation, by appropriately keeping track of which gates have been performed. These "Pauli frame

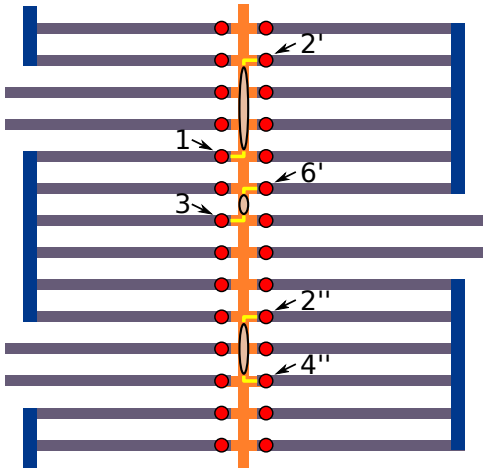

Figure 4.9: An example generalizing the measurements of MZMs from Fig. 4.2 (using the same legend). The upper region shows a four-MZM measurement of the joint parity operator $-\gamma_1\gamma_3\gamma_{2'}\gamma_{6'}$. The lower region shows a two-MZM measurement of the parity operator $i\gamma_{2''}\gamma_{4''}$. The quantum dots (gray ellipses) and their couplings (yellow lines) to MZMs are defined by appropriately tuning a set of underlying gates (see Fig. 4.1). Note: the illustration is not drawn to scale. In practice, the length (horizontal direction on the figure) is much larger than the width $L \gg w$, so as to simultaneously optimize topological protection due to the length of the 1DTSs and suppression of QPP error rates by large charging energies. As a practical constraint, in order for the quantum dots connecting MZMs to remain coherent, the vertical separation of the MZMs connected to the same quantum dot must be shorter than the effective coherence length of that quantum dot. The same principles apply to subsequent figures.

changes" are discussed in further detail for the tetron architectures in Section 4.4.2.

One-sided Hexon

The main operational principles of one-sided hexon architectures are discussed in Section 4.2. Here, we provide further details. Figure 4.9 gives examples of defining connections and quantum dots in the semiconducting structure that is coupled to MZMs for possible two-MZM measurements and four-MZM measurements. With obvious generalizations of the depicted two-MZM measurement, it is possible to measure the parity of an arbitrary pair of MZMs inside a hexon. Together with a set of four-MZM measurements between neighboring hexons,

this design allows for more than enough measurements to achieve Clifford completeness (see Section 4.4.1).

Measurement of the joint parity of vertically-separated MZMs places a practical constraint on the width w of the one-sided hexon (i.e., the length of the the backbone). A quantum dot coupled to the top and bottom MZMs of a given hexon must remain coherent for the measurement to be successful. Thus, the width of the one-sided hexon must be smaller than the effective coherence length of the quantum dots. Furthermore, as discussed in Section 4.2, simultaneously optimizing charging energy and suppressing hybridization of the computational MZMs (i.e., $L \gg \xi$) implies that it is beneficial to design the one-sided hexon so that it is much longer than it is wide ($L \gg w$). The same two principles apply to all qubit designs presented in this paper. For ease of illustrating the important features of the qubit designs, the corresponding figures are not drawn to scale.

The one-sided hexon has an additional constraint on the width compared to the alternative hexon designs presented in the following sections: the 1DTSs should have vertical separation less than ξ in order to strongly hybridize the MZMs at the backbone side of the device. When this condition is satisfied, the one-sided hexon provides topological protection corresponding to MZM separation distances of $2L$ for 1DTSs of length L. This property should also enable the one-sided hexon design to realize a better optimal combination of topological protection and protection from QPP granted by the charging energy. As discussed in Section 4.2, we roughly expect the charging energy of a hexon to have $1/L$ dependence for $L \gg w$. Garnering topological protection for MZM separations of $2L$ makes it more endurable to decrease L for

the trade-off of increasing the charging energy and its corresponding QPP protection. Another potential trade-off involved in decreasing L is a reduced visibility for MZM parity measurements. This is because the MZM parity dependent terms in the shifted ground state energies of the hexon coupled to quantum dots depend inversely on excited state energies that increase as L decreases, see e.g., Eqs. (4.9) and (4.10).

A possible challenge for one-sided hexons could arise if the energy splitting due to hybridization of the MZMs at the backbone side of the wires is small for some reason. When the device has the $\mathcal{T}^2 = +1$ symmetry mentioned at the end of Section 4.3.1, these energy splittings will vanish. Generically, this symmetry is not present, but it can occur when the cubic Rashba couplings vanish and the Zeeman field is perfectly aligned with the wires. If the symmetry is only weakly broken, then some of these energy splittings will be small. When the energy splittings are smaller than the temperature, there will be fluctuating low energy degrees of freedom in the superconducting backbone. For the purpose of protecting the information stored in MZMs at the non-backbone side of the hexon, the relevant length scale for topological protection is then reduced from $2L$ to L, the distance separating the MZMs from the backbone. Similar arguments would apply for low energy states induced by disorder at the backbone-1DTS interface. We briefly return to this issue in Section 4.6.

Two-sided hexon

A two-sided hexon consists of three 1DTSs joined by a superconducting backbone, as depicted schematically in the magnification of Fig. 4.10. In contrast to the one-sided hexon, the backbone is located far away from the MZMs at the ends of the 1DTS. Similar to the one-sided

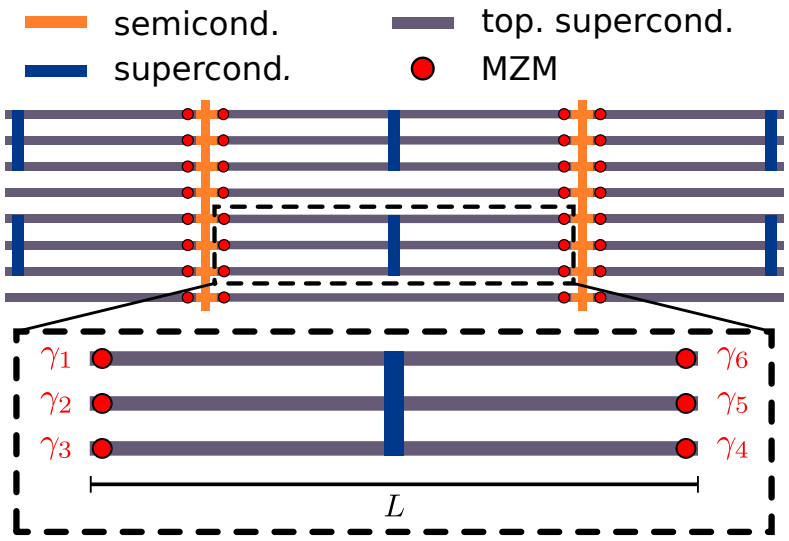

Figure 4.10: A two-sided hexon architecture. Note: the illustration is not drawn to scale for the same reason as Fig. 4.9. The magnification shows a single two-sided hexon. Additional topological superconducting links and semiconducting structures allow appropriate measurements to manipulate and entangle two-sided hexons.

hexon, it is straightforward to measure the parity of any pair of the three MZMs at a given side (left or right) of the two-sided hexon. However, achieving single qubit Clifford completeness requires the ability to measure the parity for at least two distinct pairings of MZMs involving one MZM from each side of the hexon. For example, enumerating the MZMs 1-6 as shown in Fig. 4.10, we see that Eqs. (4.35) and (4.38) utilize the measurements $\Pi_0^{(34)}$ and $\Pi_0^{(35)}$. Due to the large distance L between the MZMs on the left and right sides of the hexon, such measurements require long coherent links between both sides. These can be provided by floating topological superconductors, as in the case of the inter-hexon links in the one-sided design. Due to the connectivity of all the MZMs to the semiconducting structure at each corresponding side of the two-sided hexon, adding a single link of length L to each hexon is sufficient to perform arbitrary two-MZM measurements within the hexon.

Entangling four-MZM measurements between horizontally adjacent two-sided hexons can be implemented in a manner similar to those in the one-sided hexon case (cf. Fig. 4.9). For vertically adjacent two-sided hexons, entangling operations could be performed by defining a quantum dot in each of the semiconducting structures to the left and to the right of the hexons and connecting each dot to each of the two hexons. To avoid unwanted two-MZM measurements, each dot at the left side should have exactly one connection to the left side of each of the hexons involved, and similarly each dot at the right side should have exactly one connection to the right side of each hexon.

The main differences from the one-sided hexon designs are that the connectivity graph of the hexon qubits (linking pairs that can be directly acted on by entangling operators) is now rectangular (4-valent), rather than hexagonal, and that the relevant distance for MZM hybridization is L, rather than $2L$. In order to attain the same level of topological protection, two-sided hexons will generally be more elongated than their one-sided counterparts. We therefore expect the two-sided hexons to have a smaller charging energy (roughly half as large) than the one-sided hexons, for the same level of topological protection. Note that the presence of accidental low energy states, e.g., due to disorder, at the backbone-1DTS interfaces might further reduce the length scale of the topological protection to $L/2$.

Linear hexon

A linear hexon consists of a single 1DTS wire of length L, where two segments of length ℓ_c are tuned to be in a normal superconducting state (for example, by gating), leaving three topological segments of length ℓ_t. This is depicted schematically in the magnification in Fig. 4.11.

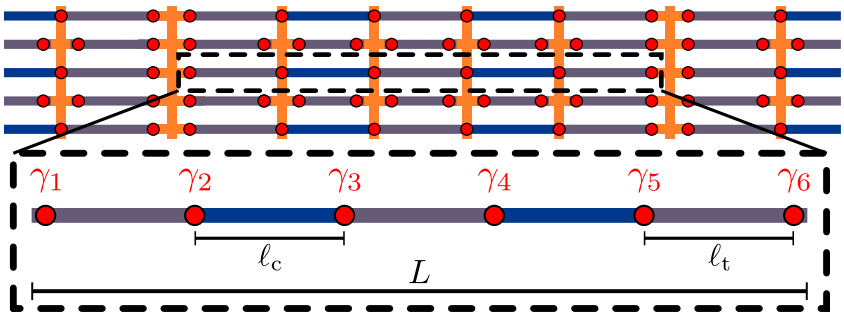

Figure 4.11: A linear hexon architecture. Note: the figure is not drawn to scale for the same reason as in Fig. 4.9. The length ℓ_c of the non-topological segments is much larger than the corresponding correlation length ξ_c of the non-topological regions and the length ℓ_t of the topological segments is much larger than the correlation length ξ of the topological regions. The legend used is the same as in Fig. 4.10. The magnification shows a single linear hexon. Additional topological superconducting links and semiconducting structures allow appropriate measurements to manipulate and entangle linear hexons.

Since topological regions are joined by the same superconducting shell, this construction does not require additional superconducting backbones to define an island hosting six MZMs. This simplifies the fabrication of linear hexons. On the other hand, no pairs of MZMs within a single linear hexon can be simultaneously connected to a single quantum dot. As such, this design requires a more elaborate measurement apparatus to enable measurements within a hexon. As in the other hexon designs, we envision floating topological superconductors as coherent links that can bridge longer distances. Each MZM measurement in a linear hexon array involves a combination of such links and quantum dots.

We arrange the hexons in a rectangular array. Between each vertical row of hexons, we arrange a vertical row of coherent links, where five links are used to span the length of one hexon. Quantum dots exist in the orange regions of Fig. 4.11 and can be controlled by gates. The use of quantum dots is completely analogous to those depicted in Fig. 4.9. The dots can be tunably coupled to any adjacent MZM independently. In this way, any pair of MZMs connected by

an orange region can be simultaneously coupled to a quantum dot. Two-MZM measurements within a given hexon are performed using the coherent links spanning that hexon. It is possible to perform all two-MZM measurements within a hexon, which grants single-qubit Clifford completeness.

Entangling operations on vertically-adjacent linear hexons also works similar to the examples depicted in Fig. 4.9. As discussed in Section 4.4.1, there will be a maximum vertical distance between MZMs that can be simultaneously coupled to a given quantum dot. We assume this distance allows the dots to vertically reach at least two rows apart (i.e., at least between neighboring rows of hexons) in either direction. A greater reach can reduce the need for some operations, such as Swap gates, but is not necessary to achieve Clifford completeness.

Entangling operations on horizontally-adjacent linear hexons require the use of links to facilitate coherent transport between distant MZMs. In principle, the linear hexon design allows the joint measurement of any four MZMs within a given horizontal row of hexons, where two of the measured MZMs belong to one hexon and two belong to another hexon, by using multiple coherent links to couple distant pairs of MZMs. However, practical constraints of the measurement visibility will limit the number of links that can be used in a given measurement. Fortunately, Clifford completeness can be achieved with measurements that require at most two links per measurement.

In order to attain good topological protection, both ℓ_c and ℓ_t should be much longer than the corresponding coherence lengths (ξ_c and ξ) in the conventional and topological superconducting regions. Assuming similar length scales for the latter, the relevant scale of the topological

protection is given by $L/5$ in terms of the length of the parent 1DTS. Linear hexon designs therefore require much larger L as compared to the other hexon designs. We expect this also leads to the smallest hexon charging energy (and, hence, the worst quasiparticle poisoning protection) of the three designs.

4.4.2 Tetron architectures

In this section, we describe the architectures of tetrons, which are topological qubits composed of four MZMs, examples of which are shown in Figs. 4.13 and 4.14. Four is the smallest number of MZMs for which a sector of fixed total fermion parity supports a qubit, i.e., a two-dimensional Hilbert space. The absence of the extra ancillary pair of MZMs that were present in the hexon designs results in two important differences. The first is that we have only two main tetron designs; the tetron analog of the one-sided hexon design cannot be scaled into a two-dimensional array, as each qubit can only connect to its vertically adjacent neighbors. The second difference is that we are not able to generate topologically protected single qubit Clifford gates via operations acting on only one tetron. Instead, the Clifford gates are generated either by joint parity measurements on a pair of tetron qubits or by "Pauli frame changes." In the following section, we show how to perform the desired gates using a limited set of measurements; in subsequent sections, we detail various designs, some of which will allow more variety in the possible measurement operations. The more limited set of operations will require a more complicated construction of the Clifford gates requiring additional resources and operations, so there is a trade-off to minimizing the number of different measurements

implemented.

Quantum information basics

Consider a system of qubits arranged in a plane in a square lattice, with each qubit labeled by its integer horizontal and vertical coordinates in the lattice. Assume that one has the ability to make a limited set of measurements that we call the elementary operations: between any pair of qubits j and k separated by a displacement $(0, \pm 1)$, one can make measurements of the operators Y_jY_k, Z_jZ_k, X_jX_k, X_jZ_k, and Z_jX_k; between any pair of qubits i and j separated by a displacement $(\pm 1, 0)$, one can make measurements of either the operator Z_jZ_k or Y_jY_k (either one suffices). Assume also that we can make single qubit measurements of the operators X_j, Y_k, and Z_l.

We first explain how this set of measurements provides a Clifford complete set of operations for this system, up to Pauli frame changes. Subsequently, we explain how a smaller set of measurements may generate Cilfford completeness by creating "standards," which removes the need for the single qubit measurements and the vertical Y_jY_k measurements. In a final reduction, we show that Clifford completeness may be attained even if the only available operations are vertical X_jX_k measurements and horizontal Z_jZ_k measurements. In the basic architectures utilizing these methods, we break the qubits into a "checkerboard" arrangement, using one color as data qubits and one as ancillary qubits. That is, we designate a qubit as a data qubit when the sum of its coordinates is even, and as an ancillary qubit when the sum of its coordinates is odd.

The available measurements described in this section differ by a notational choice from

those described in later sections by a permutation of the X, Y, and Z operators, which amounts to a "Pauli frame change." The reason is that, here, X and Z are a natural pair of measurements to use to build CNOT gates.

Pauli Frame Changes— Pauli frame changes [154] refers to the idea of not performing certain single qubit Clifford gates such as X, Z, and H in a quantum circuit, but instead modifying subsequent measurements accordingly. The idea is that, given a sequence composed of single qubit operators X, Z, and H, and single-qubit Pauli measurements, we classically track the total single qubit operation and perform the appropriately conjugated measurements. Thus, for a sequence such as: measure Z_jZ_k, apply H_k, measure Z_kZ_l, apply X_k, and measure Z_jZ_k, we commute the operators X and H through the measurements by appropriately changing what measurements we perform. Using $Z_kZ_lH_k = H_kX_kZ_l$ and $Z_jZ_kX_kH_k = -X_kH_kZ_jX_k$, we find that this sequence of operations is equivalent to the sequence: measure Z_jZ_k, measure X_kZ_l, measure $-Z_jX_k$, and apply X_kH_k. The final single qubit Clifford gates do not need to be performed if they follow all measurements in the circuit.

One can also commute the single qubit Clifford gates through CNOT gates. Since magic state injection is performed using CNOT gates, single qubit Clifford gates are not necessary even when the circuit includes T gates, where

$$T \equiv \begin{pmatrix} 1 & 0 \\ 0 & e^{i\pi/4} \end{pmatrix}. \tag{4.41}$$

The effect of Pauli frame changes is to permute the set of two-qubit measurements. This may change the set of available measurements if the set of elementary operations does not

include all two-qubit measurements. For this reason, we will avoid Pauli frame changes corresponding to commuting the Clifford phase gate

$$S \equiv \begin{pmatrix} 1 & 0 \\ 0 & i \end{pmatrix} \tag{4.42}$$

through other operations. This allows the set of available vertical measurements needed to remain fixed throughout the computation.

As we describe specific operations that we build out of the elementary measurements, we will sometimes say that we can perform an operation "up to $\{X, Z, H\}$" or "up to $\{X, Z\}$," describing the possible frame change on the qubits. The particular frame change that is implemented is determined by the measurement outcomes. An operation up to $\{X, Z\}$ may map $Z \to \pm Z$ and $X \to \pm X$ (with the mapping on Y determined by the mapping of X and Z). An operation up to $\{X, Z, H\}$ may additionally map $Z \to \pm X$ and $X \to \pm Z$.

Vertical Teleportation— Using measurements $X_k X_l$ and $Z_k Z_l$ between a pair of qubits with displacement $(0, \pm 1)$, one can create an EPR pair of the qubits k and l. A further pair of measurements $X_j X_k$ and $Z_j Z_k$ will teleport the state of qubit j to qubit l. This teleportation is up to $\{X, Z\}$ on qubit l.

Vertical CNOT and Swap— We can also apply a CNOT gate, up to $\{X, Z\}$, on two qubits separated by $(0, \pm 2)$, e.g., two data qubits separated vertically by one ancillary qubit in between them. For this, we can use the left circuit of Fig. 4.12 (this circuit is the same as in Fig. 2 of Ref. [270]), where the control, ancillary, and target qubits are labeled C, A, and T, respectively. Qubit A is initialized in an eigenstate of Z. We take qubits C and T to be on the even sublattice, separated in the vertical direction with A the ancillary qubit in between them. This circuit gives

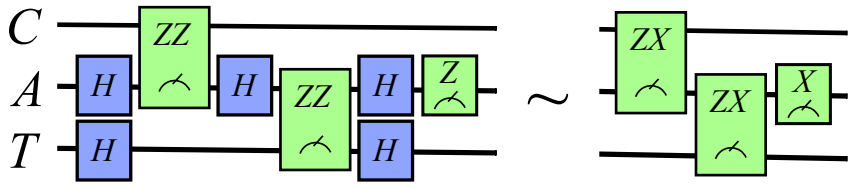

Figure 4.12: Two equivalent circuits implementing the CNOT gate. The control, ancillary, and target qubits are labeled C, A, and T, respectively. Gates labeled H are Hadamard gates, the other boxes correspond to one and two qubit measurements as indicated by the corresponding Pauli operators. The left circuit implements a CNOT up to $\{X, Z\}$ on qubits C and T. As explained in text, the Hadamard operators can be commuted through to yield the simplified circuit shown on the right, up to $\{X, Z, H\}$.

a CNOT up to $\{X, Z\}$ on qubits C and T.

The Hadamard operators in this circuit can be commuted through the measurements to the end of the circuit, resulting in the CNOT gate up to $\{X, Z, H\}$. The resulting sequence of operations in the simplified circuit is: measure $Z_C X_A$, measure $Z_A X_T$, and measure X_A.

The ability to perform CNOT gates in both directions on a pair of qubits allows one to Swap the pair of qubits (through the application of three alternating CNOT gates). This allows arbitrary motion of the data qubits in the vertical direction.

Hadamard Gate Without Pauli Frame Change and Single Qubit X Measurement— The method of Pauli frame changes above is the most efficient method to implement a single qubit Clifford gate, as no actual operations need to be performed on the qubits. However, switching between different Pauli frames may change the set of available operations. The Hadamard gate does not affect the set of available operations in the vertical direction. Thus, if we only consider vertical measurements, we can perform Hadamard gates by frame changes. However, suppose that we wish to perform a Hadamard gate followed by a measurement of $Z_j Z_k$ of qubits separated by $(\pm 1, 0)$. In this case, the new frame requires a measurement of $Z_j X_k$,

which is not an elementary operation for those qubits.

In order to overcome this, we show how to perform a Hadamard gate while only utilizing Pauli frame changes that are up to $\{X, Z\}$, as such Pauli frame changes will leave the set of available horizontal operations unchanged. Let Swap_{jk} swap qubits j and k. Consider the operation

$$U = \text{Swap}_{jl} H_l \text{Swap}_{jl} H_l, \tag{4.43}$$

for a pair of data qubits j and l that are separated by $(0, \pm 2)$ (i.e., vertically nearest-neighbor data qubits with one ancillary qubit in between them). Our implementation of Swap_{jl} is up to $\{X, Z\}$. Since H_l appears twice in this operation, the net frame change in performing U is still up to $\{X, Z\}$; that is, it will not interchange $X_k \leftrightarrow Z_k$. As an operator, $U = H_j H_l$ applies the Hadamard gate to each of the two qubits.

An alternative way to implement a Hadamard gate is to use the following variant of the vertical teleportation protocol. Use measurements $X_k Z_l$ and $Z_k X_l$ between a pair of qubits separated by $(0, \pm 1)$, e.g., one data qubit and one ancillary qubit, to create an EPR pair up to the Hadamard gate on l. Then measure $X_j X_k$ and $Z_j Z_k$ to teleport the state of qubit j to qubit l while performing a Hadamard on the encoded state. Since teleportation may be used to route qubits, this allows the Hadamard gate to be performed "for free" at the same time as a teleportation.

Horizontal CNOT and Swap— Using the method described above to generate a Hadamard gate without frame change, the horizontal measurements of $Z_j Z_k$ can be conjugated to become measurements of $Z_j X_k$ or $X_j X_k$. We thereby obtain a CNOT gate acting on a pair of qubits

separated by $(\pm 2, 0)$ by using only $Z_j Z_k$ measurements horizontally. If instead we have only $Y_j Y_k$ measurements horizontally, we can use an S gate (which we explain how to implement below) to conjugate them to become measurements of $X_j X_k$. Since a Swap is generated from three alternating CNOT gates, we now have the ability to perform horizontal Swaps of second nearest neighbor pairs of qubits, using the intermediate qubit as an ancillary qubit to facilitate the operation.

S gate— An S gate can be implemented without frame change by utilizing state injection of a $+1$ eigenstate of Y. Such a state can be produced by measuring a single qubit Y operator.

Note that instead of implementing a standard state injection using unitary gates (e.g., a CNOT gate), a measurement-based injection is more tailored for our architectures. In particular, a shorter circuit for implementing an S gate (up to Z gates on the source) is given by the sequence of operations: prepare an ancillary qubit in the $+1$ eigenstate of Y, measure the operator ZX, where Z is on the data qubit and X is on the ancillary qubit, and then measure Z on the ancillary qubit.

$Y_j Y_k$ Measurement— We can measure $Y_j Y_k$ between any pair of qubits j and k that are separated by $(0, \pm 2)$ using only the other elementary operations, through the following sequence: apply a CNOT gate from j to k, apply a Hadamard gate on qubit j, apply a CNOT gate from j to k, measure Z_k, apply a CNOT gate from j to k, apply a Hadamard gate on qubit j, and apply a CNOT gate from j to k. One may verify that the result of this sequence of operations is equal to a measurement of $-Y_j Y_k$.

Living without Single-Qubit Measurements: Using "Standards"— If it is not possible to

perform single-qubit measurements, but only two-qubit measurements, it is still possible to generate a Clifford complete set of operations. By measuring X_jX_k, Y_jY_k, or Z_jZ_k, a qubit state that is an eigenvector of X, Y, or Z can be copied indefinitely. We call such a qubit a "standard."

To achieve Clifford completeness without single-qubit measurements, we store standards in every data qubit with odd horizontal coordinate. The data qubits now have coordinates $(2n, 2m)$ in the lattice, for $n, m \in \mathrm{Z}$ (i.e., there are now three ancillary qubits per data qubit). With this arrangement, one can perform single qubit measurements on qubits with even horizontal coordinate. In fact, which eigenstate of X, Y, or Z we choose for the standard is arbitrary, as the choice has no effect on measurements, when restricting to Clifford operations. If magic state injection is performed, the choice of eigenstate used for the Y standard becomes important. In this case, magic state injection can be used to identify the choice of Y standard (see the discussion on page 38 of Ref. [212]).

Restricted Two-Qubit Operations— Now suppose that we can measure X_j or Z_j on any single qubit, but we can only perform the limited set of two-qubit measurements: Z_jZ_k between a pair of vertically-separated qubits and X_jX_k between a pair of horizontally-separated qubits. This is still sufficient to build a universal quantum computer if we can produce an approximate magic state. While this is not likely to be a practical architecture and all architectures we describe have more than this set of measurements, it is interesting that this restricted set of operations remains universal. The following discussion of operations will be up to $\{X, Z\}$.

Using the same circuit shown in Fig. 4.12, we can perform a CNOT between two qubits

separated by a displacement $(\pm 1, \pm 1)$. For example, to generate a CNOT gate with the $(0, 0)$ qubit as the control and the $(1, 1)$ qubit as the target, we use the following sequence: prepare the ancillary qubit A in an X eigenstate, measure $Z_C Z_A$, and measure $X_A X_T$. Given the ability to perform CNOT gates, we can perform Swap. In the above example, the $(1, 1)$ qubit is a standard. Applying multiple Swap operations allows the data qubits to move arbitrarily within the data qubit sublattice while leaving the standards intact.

However, we do not yet have the ability to perform the full Pauli group with this restricted set, since we do not have the ability to perform the Hadamard gate. These gates cannot be implemented through Pauli frame changes as we have a smaller set of elementary operations. Suppose, however, that we could produce many Y standards, either $Y = +1$ or $Y = -1$ eigenstates. Using this Y standard and state injection, we can perform an S gate. Once we have an S gate, we can also measure $Y_j X_k$, $X_j Y_k$, and $Y_j Y_k$ between any two horizontally separated qubits. Thus, we have the ability to perform all the elementary operations described at the beginning of this section, but with Y and Z operators interchanged and horizontal and vertical directions interchanged. We therefore have operations that are Clifford complete up to $\{X, Z\}$.

If we can produce approximate Y standards, we can distill them using methods similar to, but simpler than the methods of Ref. [46]. For this, we can use any CSS code that allows transversal S gates, such as the 7-qubit code [111]. Using a CSS code allows us to check the stabilizers of the code using only CNOT gates and measurement and preparation of qubits in Z and X eigenstates. We note that we can generate Y standards, for example, if we can

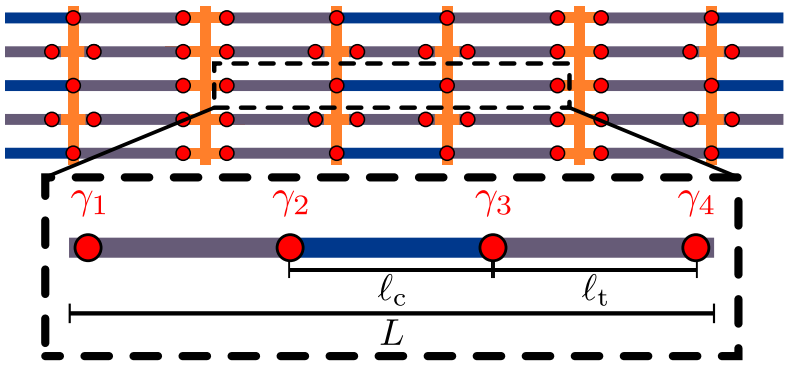

Figure 4.13: A linear tetron architecture. Note: the illustration is not drawn to scale for the same reason as in Fig. 4.9. The length ℓ_c of the non-topological segments is much larger than the corresponding correlation length ξ_c of the non-topological regions and the length ℓ_t of the topological segments is much larger than the correlation length ξ of the topological regions. The legend used is the same as in Fig. 4.10. The magnification shows a single linear tetron. Additional topological superconducting links (gray) and semiconducting structures (orange) allow appropriate measurements to manipulate and entangle linear tetrons.

generate an approximate S gate. Of course, if we can generate approximate T gates, then we can produce approximate $S = T^2$ gates. Similarly, if we can produce approximate magic states, we can use them to produce approximate Y standards.

Linear tetron

A linear tetron consists of a single 1DTS wire in which a middle segment of length ℓ_c has been tuned to be in a normal superconducting state (for example, by gating), leaving two topological segments of length ℓ_t. This is depicted schematically in the magnification in Fig. 4.13. As a result, there are four MZMs, one at each end of the wire and one at each of the two boundaries between topological and normal superconducting regions. The linear tetron is, in some sense, the simplest of our qubit designs. However, this simplicity of the single qubit is somewhat offset by the complexity of the associated measurement apparatus, i.e., the array of quantum

dots and floating topological superconductor links that are needed for measurements, which we now describe (see Fig. 4.13).

We arrange the tetrons in a rectangular array. Between each vertical row of tetrons, we arrange a vertical row of coherent links, where three links are used to span the length of one tetron. These links can be provided by floating topological superconductors, as in the case of the linear hexon. Measurements of linear tetrons are done in a similar manner to measurements of linear hexons. Any pair of MZMs connected by an orange region of Fig. 4.13 can be simultaneously coupled to a quantum dot. As discussed in Section 4.4.1, there will be a maximum vertical distance between MZMs that can be simultaneously coupled to a given quantum dot. We assume this distance allows quantum dots to span the separation between neighboring rows of hexons. This is sufficient to perform the measurements used in the protocols of Section 4.4.2. Just as for linear hexons, a greater reach can reduce the need for some operations.

Let us label the MZMs on a given tetron as γ_1, γ_2, γ_3, and γ_4, from left to right. We required the total fermion parity of a tetron to be even (e.g., by using charging energy), $p_{12}p_{34} = 1$. The qubit basis states are then defined to be

$$|0\rangle = |p_{12} = p_{34} = -1\rangle \tag{4.44}$$
$$|1\rangle = |p_{12} = p_{34} = +1\rangle. \tag{4.45}$$

The Pauli operators on the qubit are represented in terms of MZM operators as

$$X = i\gamma_2\gamma_3 = i\gamma_1\gamma_4, \tag{4.46}$$
$$Y = i\gamma_1\gamma_3 = -i\gamma_2\gamma_4, \tag{4.47}$$
$$Z = i\gamma_1\gamma_2 = i\gamma_3\gamma_4, \tag{4.48}$$

up to an overall phase.

In order to distinguish different tetrons, we label each tetron and its operators by its (integer-valued) coordinate (j, k) in the two-dimensional array.

Measurements of $Z^{(j,k)}Z^{(j,k+1)}$, $X^{(j,k)}X^{(j,k+1)}$, and $Y^{(j,k)}Y^{(j,k+1)}$ between vertically-neighboring tetrons can be performed by turning on the couplings of the corresponding MZMs to the adjacent quantum dots located between the two tetrons, and then probing these quantum dots by measuring the shift of the capacitance or charge, as discussed in Section 4.3.3. More specifically, quantum dots connecting MZMs of vertically-neighboring tetrons can be directly coupled to the pairs $\gamma_i^{(j,k)}$ and $\gamma_i^{(j,k+1)}$ for $i = 1, 2, 3, 4$. By turning on two such pairs of couplings, we can measure the claimed two-qubit operators.

Measurements of $Z^{(j,k)}Z^{(j+1,k)}$ between horizontally-neighboring tetrons further require the use of links to facilitate coherent transport between distant MZMs. In some cases, we need to use multiple links in order to couple more distant MZMs, as discussed for the linear hexon design in Section 4.4.1. To be more specific, a quantum dot that sits between two horizontally-neighboring tetrons at (j, k) and $(j + 1, k)$ can be directly coupled to both $\gamma_4^{(j,k)}$ and $\gamma_1^{(j+1,k)}$. Using the combination of two coherent links and three quantum dots, we can couple this unit to both $\gamma_3^{(j,k)}$ and $\gamma_2^{(j+1,k)}$. We can think of this combination of coherent links and dots as an effective quantum dot, to relate to the measurement discussion of Section 4.3.2. The "quantum dot" energy levels now depend on the joint parity $p = p_{(j,k)}p_{(j+1,k)}$, which is the eigenvalue of the operator $Z^{(j,k)}Z^{(j+1,k)} = -\gamma_3^{(j,k)}\gamma_4^{(j,k)}\gamma_1^{(j+1,k)}\gamma_2^{(j+1,k)}$.

In this way, we can perform all the two-qubit measurements assumed in the previous sec-

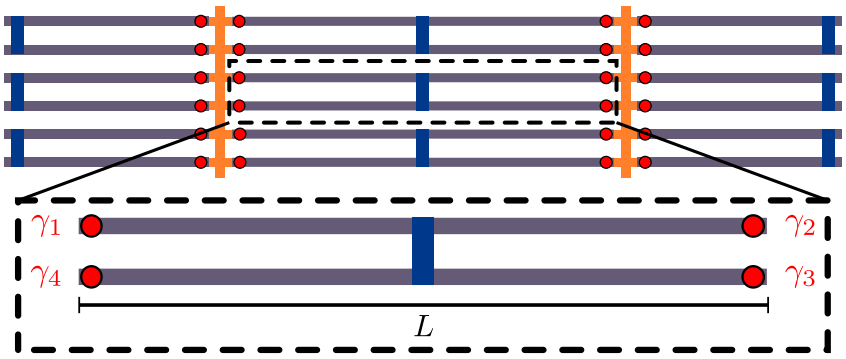

Figure 4.14: A two-sided tetron architecture. Note: the illustration is not drawn to scale for the same reason as in Fig. 4.9. The legend used is the same as in Fig. 4.10. The magnification shows a single two-sided tetron. Additional topological superconducting links and semiconducting structures allow appropriate measurements to manipulate and entangle two-sided tetrons.

tion. These two-qubit measurements are sufficient for Clifford-complete operations, as described in Section 4.4.2. However, similar to the case of linear hexons, we can also perform single qubit measurements and other two-qubit (entangling) measurements by using the links to facilitate coherent transport across longer distances. For example, an effective quantum dot (composed of links and quantum dots) can be coupled to any two different MZMs from the same tetron, so that the dot's energy levels depend on the parity of these two MZM operators, in other words, on the eigenvalue of the corresponding Pauli operator.

Two-Sided tetron

A two-sided tetron consists of two 1DTSs joined by a superconducting backbone, as depicted schematically in the magnification in Fig. 4.14. The backbone is located in the middle of the wires, far away from any of the four MZMs at the ends of the 1DTSs. This design facilitates joint measurements between horizontally-neighboring tetrons and somewhat complicated

measurements between vertically-neighboring tetrons, which are analogous to those depicted in Fig. 4.9 for hexons. One could include links to increase the variety of operations, but it is instructive to consider the architecture design with no links.

Let us label the MZMs of a two-sided tetron as γ_1, γ_2, γ_3, and γ_4, in clockwise order starting from the upper left.

A joint Pauli operator on horizontally-neighboring tetrons can be measured if one quantum dot is coupled to $\gamma_2^{(j,k)}$ and $\gamma_1^{(j+1,k)}$ and a second quantum dot is coupled to $\gamma_3^{(j,k)}$ and $\gamma_4^{(j+1,k)}$. This coupling configuration allows for a measurement of $X^{(j,k)}X^{(j+1,k)} = -\gamma_2^{(j,k)}\gamma_3^{(j,k)}\gamma_1^{(j+1,k)}\gamma_4^{(j+1,k)}$.

The simplest measurement of vertically-neighboring tetrons is given by coupling one quantum dot to $\gamma_1^{(j,k)}$ and $\gamma_4^{(j,k+1)}$ and a second quantum dot to $\gamma_2^{(j,k)}$ and $\gamma_3^{(j,k+1)}$. This coupling configuration allows for a measurement of $Z^{(j,k)}Z^{(j+1,k)} = -\gamma_1^{(j,k)}\gamma_2^{(j,k)}\gamma_3^{(j,k+1)}\gamma_4^{(j,k+1)}$.

Using the semiconductor wires (orange in Fig. 4.14), we can perform additional measurements that require coupling MZMs over a slightly more extended range. The length scale of the quantum dots constrains the distance over which a measurement may be performed, see the discussion in Section 4.4.1. For example, we can couple one quantum dot to $\gamma_1^{(j,k)}$ and $\gamma_4^{(j,k+1)}$ and instead couple the second quantum dot to $\gamma_3^{(j,k)}$ and $\gamma_3^{(j,k+1)}$. This coupling configuration allows for a measurement of $Y^{(j,k)}Z^{(j+1,k)} = -\gamma_1^{(j,k)}\gamma_3^{(j,k)}\gamma_3^{(j,k+1)}\gamma_4^{(j,k+1)}$. The other two-qubit joint Pauli measurements of vertically-neighboring tetrons can be similarly implemented.

The only single-qubit measurement that is possible in this architecture (without introducing links) is a measurement of X, which can be implemented by coupling a quantum dot to $\gamma_1^{(j,k)}$ and $\gamma_4^{(j,k)}$ or to $\gamma_2^{(j,k)}$ and $\gamma_3^{(j,k)}$. As described in Section 4.4.2, if we only have this restricted

set of measurements, we can still achieve Clifford complete operations through the use of "standards."

As in the other architectures, we can increase the set of possible operations by introducing horizontal links provided by floating topological superconductors, that facilitate coherent transport across the length of the hexons. In particular, this enables measurement of all single-qubit Pauli operators measurements. Such structures were previously considered in Ref. [208].

4.4.3 Design summary

The different hexon and tetron architectures presented in this chapter have different advantages and challenges. A priori, it is difficult to make quantitative performance estimates and rankings between the designs. In this section, we summarize the common principles that apply to all the presented designs, as well as their differences.

Common design principles

The common design principles we used to protect the encoded quantum information are [3]: (1) magnetic field alignment in the direction of the 1DTSs to maximize the gap; (2) avoiding the use of topological T-junctions to avoid low energy modes close to the MZMs; (3) finite charging energy of the individual qubit units (hexons or tetrons) to suppress quasiparticle poisoning at low temperature; (4) long 1DTSs to suppress hybridization of the computational MZMs; and

[3]Note that we also avoided using tunable Josephson junctions in our designs. Tunable Josephson junctions provide the ability to cut and reconnect the superconducting backbone of the designs, which allows for additional flexibility in coupling distant MZMs. In order to reach both regimes of coupled and fully decoupled MZMs, the Josephson junction would need to be tunable over a wide range $E_J \sim E_C \ldots E_J \gg E_C$, which might be difficult in practice.

(5) the ability to perform a sufficient set of measurements to achieve a topologically protected Clifford complete gate set.

Design principles (1)-(5) lead to exponential suppression of errors in the qubit architectures. More explicitly, error rates from quasiparticle poisoning and thermally excited quasiparticles are exponentially suppressed by the ratios E_C/T and Δ/T, respectively. Errors due to MZM hybridization are exponentially small in L/ξ. Furthermore, the fidelity of manipulating quantum information in the presented measurement-based scheme scales exponentially with the integration time of the measurement [4].

Design Differences

We qualitatively compare the different designs using the four axes mentioned in the introduction: (1) quasiparticle poisoning time, (2) signal visibility, (3) fabrication simplicity, and (4) computational efficiency.

(1) The larger the charging energy E_C of each individual qubit unit (hexon or tetron), the stronger the suppression of quasiparticle poisoning. As discussed in Section 4.2, when the length L of a qubit unit (along the direction of the 1DTS wires) is much larger than its width w, we expect the geometric capacitance of a qubit unit to depend roughly linearly on L and sub-linearly on w. Thus, there is a trade-off between shorter L, which provides better protection against quasiparticle poisoning, and longer L, which provides better protection against hybridization of the MZMs. The maximum combined protection is achieved at some optimal

[4]The fidelity of manipulating quantum information in a measurement-only protocol is set by the experimental certainty for distinguishing between two measurement outcomes.

value of L, where the corresponding error rates are equal. This is roughly when $E_C/T \approx L_{\rm h}/\xi$, where $L_{\rm h}$ is the effective distance between MZMs. For the one-sided hexons, two-sided hexons, linear hexons, linear tetrons, and two-sided tetrons, we roughly have $L_{\rm h} \approx 2L$, L, $L/5$, $L/3$, and L. Assuming that the correlation length ξ and the w dependence of E_C is approximately the same for all the qubit designs, we rank their relative error protection (combined protection from quasiparticle poisoning and MZM hybridization) from largest to smallest as: one-sided hexons, two-sided tetrons, two-sided hexons, linear tetrons, and linear hexons. Note that this ordering assumes that there are no low energy states from weakly hybridized MZMs at the superconducting backbone of the one-sided hexons. When this assumption is not valid, $L_{\rm h} \approx L$ for the one-sided hexons, and so its ranking will drop to below the two-sided hexons.

(2) Since the MZM measurements rely on fermion parity dependent energies of the system when MZMs are coupled to quantum dots, the visibility of such measurements will be lower when the charging energy E_C is larger [see (1)]. This is because the parity dependent terms in these energies depend inversely (to lowest order in perturbation theory) on excited state energies that are of the order of the charging energy. This effect can be compensated to some degree by increasing the tunneling amplitudes t_j. Another aspect that influences the visibility is the separation distance between the MZMs being measured. Longer distance measurements require more coherent links, which will decrease visibility. In this regard, the linear hexons and tetrons require more coherent links than the other designs. It is difficult to precisely estimate the effects of all these factors on the visibility in order to produce a meaningful ranking of designs.

(3) The simplicity of fabricating different designs will ultimately be decided experimentally. Here, we mention qualitative differences in the fabrication of the designs. While it is clear that fabricating a tetron is slightly easier than fabricating a corresponding hexon, we do not expect qualitative differences in the fabrication difficulty and focus on hexons in the following discussion. One important challenge for the one-sided and two-sided hexons will be the deposition of the superconducting backbone, as this must be done without disturbing the underlying 1TDSs too much. Attaining the larger charging energy of the one-sided hexon additionally requires sufficient hybridization of the MZMs in the superconducting backbone. The linear hexons have the advantage of not requiring any such superconducting backbones. The drawback is the presence of more coherent links and the requirement of tuning larger regions of the 1DTS out of the topological regime.

(4) Hexons are computationally more efficient than tetrons. With six MZMs for each qubit, it is possible to do all single qubit Clifford operations within a hexon. Furthermore, adjacent qubits may be entangled without any additional ancillary hexons. In contrast, even in the most efficient tetron design, roughly half of the tetrons are required to be ancillary in order to provide the full set of Clifford gates, thus requiring a total of eight MZMs for each qubit. The computational efficiency is further reduced when limiting the number of allowed single qubit Pauli measurements, as in the case of the two-sided tetron without coherent links. Clever algorithms using standards (described in Section 4.4.2) still allow realization of all Clifford operations. However, the computational efficiency is reduced, since this scheme requires 3/4 of the tetrons to be ancillary (as one fourth of the tetrons are used to encode standards), leaving

only one fourth as computational data qubits. On top of the increased hardware requirements, the preparation and distribution of appropriate standards requires additional applications of gate operations.

4.5 Universal quantum computing

4.5.1 T gate

Nearly all of our discussion so far has focused on achieving topologically protected Clifford complete operations via an adaptive sequence of measurements. However, as reviewed in Chapter 2, in order for the designs presented here to support universal quantum computation, we need the addition of a non-Clifford gate. We now describe how this can be achieved by using a more elaborate classical control protocol than is required to implement the Clifford complete operations.

We focus on implementing a T gate using magic state distillation (see Chapter 2 for a review). For the five planar design layouts that we have presented, magic state distillation may be efficiently synthesized using the combinations of measurements that each layout permits (see Section 4.4). This is a concrete implementation of measurement-only quantum computation as described in Refs. [34], [32]. In the case of the tetron designs, Clifford completeness requires at least half of the tetrons to be ancillary (more if links are not used). In all our designs, an additional portion of the hexon or tetron qubits will need to be dedicated to the preparation of approximate magic states.

The same classical control electronics used to produce Clifford operations can instead produce approximate magic states following the approach described in Ref. [142]. This protocol is an extension and combination of two antecedents: an adiabatic protocol which produces high fidelity magic states via a dynamic decoupling that exploits topologically protected regions of the single qubit Bloch sphere [137], and a hybrid adiabatic-measurement protocol that utilizes measurement to suppress diabatic errors [153].

As described in Ref. [137], a MZM based qubit state adiabatically evolved around a closed loop in the Bloch sphere picks up a relative phase of α between the even and odd fermion parity sectors, where α is the solid angle enclosed by the loop, i.e., the geometric phase. This evolution is performed by changing couplings to ancillary MZMs. Because MZM couplings drop off exponentially in system parameters, combinations in which one (or two) couplings are zero constitute topologically protected great circle paths on the Bloch sphere (formed by the boundaries of octants of the sphere). It is the protected nature of these paths, specifically the closed path enclosing one octant of the Bloch sphere, that leads to the topologically protected phase gate S, for which $\alpha = \pi/2$. Producing the T gate with $\alpha = \pi/4$ is not protected, but one may cancel low-frequency errors by defining a particular loop contour c on the Bloch sphere. This contour is "snake-like," consisting of different vertical sweeps from the north pole to the equator, some partial evolution along the equator, and sweeps back to the north pole (see Fig. 4 in Ref. [137]). Optimal cancellation is achieved by selecting Chebyshev roots as turning points along the equator.

One may adapt this idea to a measurement-based scheme in the same spirit as measurement-

only topological quantum computation [34, 35], in which the unitary gate implemented by an elementary braid exchange is instead implemented by a composition of measurements, each incorporating one fixed anyon of an ancillary pair. In the present context, a similar sequence of measurements that now project on the turning points of c can produce the same relative phase between the different qubit states as the earlier adiabatic protocol [137]. This yields a measurement-based implementation of the T gate. As in earlier measurement-only schemes, recovery from unwanted measurement outcomes must be addressed. In the case of hexons, one may use the incorporated ancillary MZMs for this recovery. In the case of tetrons, one must instead utilize one of the nearby ancillary tetrons.

Whereas all measurements used in our constructions of Clifford gates involved creating a single closed loop through MZM islands and quantum dot tunnel junctions, in order to create the projections required to simulate adiabatic evolution along the Bloch sphere contour c, this is not sufficient. Just as c explores along the $X - Y$ equator, we will need to simultaneously turn on tunneling at the junctions used to implement an X measurement and the junctions used to implement a Y measurement. Moving along this equator corresponds to tuning the relative tunneling amplitudes between these two sets of junctions. Tuning these ratios will require uniformity of manufacture and careful calibration of each junction, but given the mathematical ability of dynamic decoupling to remove low frequency errors, we have some confidence in this procedure, at least to generate magic states accurate enough for distillation.

4.5.2 Quantum error correction

Combining the topologically protected implementation of the Clifford gates with the ability to produce and distill magic states, we expect the architectures proposed in Section 4.4 can lead to a high fidelity quantum computer that allows for many gate operations before decohering. For low-depth quantum computing (with magic state distillation), this approach might even be sufficient without quantum error correction [188]. Large-scale quantum computing, however, will still require embedding the presented architectures into an error correcting superstructure. We note that, since our designs allow for a complete set of high fidelity Clifford operations, any error correcting stabilizer code can be implemented on a software basis without changing the presented designs. Finding an optimized hardware for error correction is an interesting subject for future research.

4.6 Conclusions and near-term directions

Experimental explorations of MZMs in nanowire devices have evolved to an impressive degree over the past few years, with synergistic breakthroughs on the fabrication and characterization fronts [190, 220, 79, 65, 74, 95, 57, 125, 157, 5, 114]. In parallel, new theory insights have emerged that appear auspicious for eventual quantum computing applications. Notable examples include anticipation of the virtues of charging energy, both for protecting quantum information and facilitating Majorana measurements [102, 158, 207, 254, 208]; measurement-only topological quantum computation [34, 35]; improved modeling of microscopic details of Majorana systems [199, 239, 210, 215, 240, 237, 259, 268, 69]; a quantitative understand-

ing of braiding "speed limits" [140, 229, 139, 138] and the role of measurement in saturating them [153]; and improved methods of producing phase gates which, together with topologically protected operations, enable computational universality [137].

In this chapter, we have considered these new theoretical developments in the context of realistic experimental implementations in order to design scalable MZM-based quantum computing architectures with a variety of possible modules. All of our designs feature (i) parallel topological wires connected into units with appreciable charging energy and (ii) common measurement-based approaches that use proximate quantum dots and/or interferometry to enact all operations necessary for achieving fault-tolerant universal quantum computation. These architectures display some similarities to the surface-code setups introduced recently in Refs. [246, 158, 207], but seek to leverage the topological quantum information processing afforded by MZMs, rather than pursuing active error correction. Our study is instead closer in spirit to the parallel works of Refs. [254, 208], but goes beyond these works in designing two-dimensional arrays, rather than few-qubit arrangements.

While we primarily focused on issues pertinent for long-term circuit designs, there are many interesting shorter-term goals for investigating the basic operating principles in relatively simple setups. Demonstrating the ability to perform fermion parity measurements of MZMs presents one notable target given the prominence of measurements in our proposed schemes. In this regard, it is worth commenting that relying only on parallel topological wires entails a potential challenge: the measurement visibility for certain MZM pairs within a given unit can be "accidentally" low, as discussed in Section 4.3.1. We stress, however, that many factors (e.g.,

higher-order band structure corrections, orbital magnetic field effects, or additional spin-orbit couplings) are expected to alleviate this issue. Optimizing the visibility for such cases poses a worthwhile problem both for theory and experiment. Other measurement issues also warrant further attention. Contrary to the topological qubits themselves, interferometric measurements are not immune to dephasing, which can hamper visibility. It is important to establish the length scales over which 1DTSs can serve as effective coherent links, the time scales required to perform a measurement, and the length and time scales over which we can resolve the state of MZMs coupled through intervening quantum dots.

These measurement-centric issues can be addressed in the framework of experiments relevant for quantum information. We partition these experiments into groups involving progressively more complex device geometries:

Two separate floating 1DTSs. In order to test the length scales over which floating 1DTSs can be used as coherent links, a device with two floating nanowires, as shown in Fig. 4.15(a), could be used to realize an interference experiment that is conceptually similar to the proposal in Ref. [102]. Two 1DTSs act as the arms of an Aharonov-Bohm interferometer. If coherence is maintained, the tunneling between a quantum dot on the left and one on the right is modulated by the enclosed flux. Although this device cannot access properties of topological qubits, since the MZM parities are fixed by the individual 1DTSs' charging energies, such an experiment is a crucial test of the concept of using floating 1DTSs as coherent links. Moreover, such a system can provide strong evidence for topological superconductivity by observing π shifts in the interference pattern when the dimensionless gate voltage applied to one 1DTS changes by

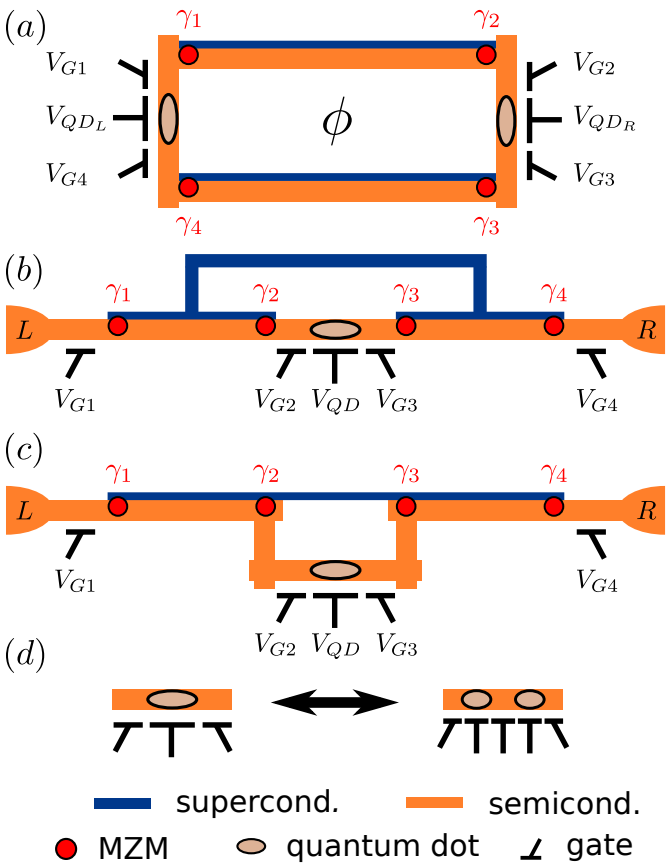

Figure 4.15: Examples of designs for experiments that demonstrate some of the basic operating principles in our scalable quantum computing architectures. (a) Experimental test of long distance coherent transport through floating 1DTSs. Two long wires are coated with a superconductor and tuned into the topological regime. If single electron transport is coherent, the hybridization of left and right quantum dots should show Aharonov-Bohm oscillations when changing the enclosed flux ϕ. (b) and (c) Experimental test of quasiparticle poisoning rate, MZM hybridization, and measurement functionality of a topological qubit. These single tetron configurations contain the minimal structure for a topological qubit. The left and right leads can be used to first tune the system into the topological regime by checking for zero bias peaks associated with γ_1 and γ_4. The central dot allows one to measure $i\gamma_2\gamma_3$, e.g., using charge sensing. The apparatuses shown in (b) and (c) differ in fabrication details. In (b) the quantum dot is defined on the same nanowire as the MZMs in a region where the superconducting shell was etched away. A superconducting bridge joins the two superconducting shells. In (c) no superconducting bridge is needed. A non-topological region between γ_2 and γ_3 is created by etching away the semiconducting part of the nanowire, or possibly by gating. The quantum dot is defined in a nearby nanowire connected to the 1DTS composed of four joined wires [13]. Note that the distance between γ_2 and γ_3 has to be much larger than the superconducting coherence length. (d) For enhanced measurement flexibility, additional gates allow one to replace single dot configurations by double dot configurations.

1 (indicating the parity of the 1DTS has flipped).

Single tetron. A device with four MZMs on a single superconducting island with charging energy, i.e., a tetron, features the minimal number of MZMs that yields a ground-state degeneracy and constitutes a single topological qubit. Figs. 4.15(b) and (c) show devices designed for first-generation experiments. A wealth of information can already be gleaned from such systems. For example, one can partly characterize the qubit's stability by continuously measuring the parity of a given MZM pair. In the devices shown in Figs. 4.15(b) and (c), the parity $i\gamma_2\gamma_3$ can be measured via the central quantum dot. quasiparticle poisoning events would manifest as telegraph noise in the signal of such a continuous measurement, provided subsequent instances of quasiparticle poisoning events are separated by sufficiently long times. The extracted parity lifetimes would help quantify the suppression of quasiparticle poisoning events by charging energy, as well as limitations from thermally-excited or non-equilibrium excited quasiparticles within a tetron. In the regime of very small quasiparticle poisoning rates, the central quantum dot allows us to quantify the hybridization between MZM pairs.

A measurement of $i\gamma_2\gamma_3$ initializes the qubit in an X eigenstate. After performing such a measurement and turning off the couplings to the quantum dot, hybridization due to tunneling between γ_1 and γ_2 or between γ_3 and γ_4 will split the ground state degeneracy, acting as a perturbation to the Hamiltonian proportional to Z. Thus, the probability distribution of outcomes for subsequent measurements of $i\gamma_2\gamma_3$ will reveal this energy splitting by varying the intermittent time intervals between measurements. If the quantum dot in the middle is replaced by two quantum dots, as depicted in Fig. 4.15(d), we will have more flexibility in performing

the measurement. For instance, it will be possible to turn on the couplings of the MZMs to the quantum dots for a very short time interval and then subsequently measure their effect on the double dot system over a longer time interval.

By adapting the protocols from Ref. [1], tetrons can be used to detect the nontrivial fusion rules of MZMs. The implementation is especially straightforward if the setup allows the individual measurements of both $i\gamma_1\gamma_2$ and $i\gamma_2\gamma_3$ (this would be the case for either of the tetron designs of Sec. 4.4.2). A measurement-only approach to fusion-rule detection can then be viewed as follows. Measurement $i\gamma_1\gamma_2$ projects onto a particular fusion channel, initializing the topological qubit in a fixed direction of the Bloch sphere. Subsequently measuring $i\gamma_2\gamma_3$ then projects the topological qubit onto an axis of the Bloch sphere rotated from the previous state's direction by $\pi/2$. This should yield equal probability of the two possible measurement outcomes, reflecting the two accessible fusion channels.

In principle, it is also possible to detect fusion rules in the devices show in Figs. 4.15(b) and (c), provided one can control the coupling between MZMs γ_1 and γ_2 or between γ_3 and γ_4, for example by tuning the topological gap via the external magnetic field. Once the coupling becomes appreciable, the environment will relax the system to the ground state, effectively performing the projection into a fixed fusion channel.

Finally, these devices allow one to implement an approximate T gate. With a well-timed pulse changing $V_{G,2}, V_{Q,D}$, and $V_{G,3}$, γ_2 and γ_3 can be coupled temporarily such that the dynamical phase accrued by the state of the system is $\frac{\pi}{8}p_{23}$.

Single hexon. Adding two more MZMs to the above module, i.e., building a hexon, pro-

vides the minimal architecture to test the measurement-only implementation of braiding transformations, as explained in Section 4.4.1. Moreover, this setup allows for more advanced approaches to implementing T gates [137].

Two tetrons. The final basic operation needed for quantum computing, namely four-MZM measurement, can be demonstrated with two tetrons each realizing a single topological qubit. Experimental validation requires some care to ensure that the implementation of the measurement does not unintentionally probe the state of any MZM pairs within the quartet of MZMs whose joint parity is being measured. For example, suppose that we wish to measure $-\gamma_1^{(1)}\gamma_2^{(1)}\gamma_1^{(2)}\gamma_2^{(2)} = Z^{(1)}Z^{(2)}$, but inadvertently project onto an eigenstate of $i\gamma_1^{(1)}\gamma_2^{(1)} = Z^{(1)}$ in the process. This error can be detected by initializing the system in the state $\frac{1}{2}\left(|0\rangle + |1\rangle\right)\left(|0\rangle + |1\rangle\right)$, performing the measurement (intended to be) of $Z^{(1)}Z^{(2)}$, and then performing a measurement of $Z^{(1)}$. If the final measurement does not yield both possible outcomes with equal probability, then it indicates that the measurements are not performing as intended. A battery of similar tests may be used to more precisely characterize errors in the measurements.

Together, these experiments test much of the physics underlying our scalable designs. Outcomes of even the simplest tests should discriminate among the various possible qubit designs that we proposed and inform inevitable refinements. Yet another issue that should factor into eventual designs is circuit calibration, in the sense of ensuring that each individual 1DTS wire resides in its topological phase for systems supporting a large number of qubits. One could, of course, view successful implementation of the preceding experiments as calibration, though coarser methods that merely indicate the presence of MZMs, rather than information about their

quantum states, are clearly desirable. We expect that the interferometric measurements involving quantum dots, which we invoked for computation, also suffice for this purpose, though detailed studies would be certainly be useful.

A further research topic is to understand how much advantage can be gained by using architectures that allow more general measurements. Even using only a fairly limited set of two-qubit measurements, we were able to generate universal Clifford operations. However, more general measurements simplify the implementation of certain computational operations and, thus, might allow quantum algorithms to be implemented using fewer measurements in total. This leads to a trade-off worth investigating further.

Finally, we note that tailored algorithms for our measurement-based architectures can significantly increase the efficiency of our designs. Efficient algorithms will, in general, differ from the standard literature, which usually relies on a set of unitary Clifford gates and single-qubit measurements. For example, instead of using several CNOT gates for state injection or swap operations, where each CNOT gate requires a set of single-qubit and multi-qubit measurements, it will be more efficient to directly perform the desired operation without using CNOT gates (see the example in Sec. 4.4.2 – *S gate*). The search for such tailored algorithms will be an important subject of future research.

Chapter 5

Dephasing of Majorana-based qubits

I did know once, only I've sort of forgotten.

-A.A. Milne, *Winnie the Pooh*

In this chapter, we analyze charging-energy-protected Majorana-based qubits, focusing on the residual dephasing that is present when the distance between Majorana zero modes (MZMs) is insufficient for full topological protection. We argue that the leading source of dephasing is $1/f$ charge noise. This noise affects the qubit as a result of the hybridization energy and charge distribution associated with weakly-overlapping MZMs, which we calculate using a charge-conserving formalism. We estimate the coherence time to be hundreds of nanoseconds for Majorana-based qubits whose MZM separation is $L \sim 5\xi$ (with ξ being the coherence length). The coherence time grows exponentially with MZM separation and eventually becomes temperature-limited for $L/\xi \sim 30$.

This chapter previously appeared as "Dephasing of Majorana-based qubits" by Christina Knapp, Torsten Karzig, Roman Lutchyn, and Chetan Nayak in Phys. Rev. B 97, 125404.

5.1 Introduction

Topological phases offer the promise of qubits that are insensitive to local sources of noise, provided that the relevant distance and time scales are sufficiently large [147, 193]. When qubit operations are done too rapidly, however, diabatic errors can occur [59, 140, 229, 153]. Furthermore, as the separation between topological excitations is decreased, eventually approaching and then falling below the coherence length, topological qubits evolve smoothly into more conventional (local) qubits and are susceptible to the same noise sources [216, 108, 51]. At present, the most promising approach to topological quantum computing encodes the qubit in the joint parity state of Majorana zero modes (MZMs), exotic defects of topological superconductors that obey non-Abelian statistics [218, 146, 6]. A one-dimensional topological superconductor can be engineered out of a semiconductor nanowire with strong spin orbit coupling, proximitized by an s-wave superconductor and subjected to a magnetic field [224, 181, 200]. Motivated by the strong experimental evidence for the observation of MZMs in such systems [190, 220, 79, 65, 74, 95, 5, 274, 179], there is a growing interest in moving beyond detection of MZMs to their application in topological quantum computing [1, 179]. In particular, recent theoretical work has proposed qubits comprised of four or six MZMs on an island with substantial charging energy [207, 141]. In this chapter, we analyze the dephasing of such

qubits that occurs when two of the MZMs on such an island approach each other.

The MZM qubits of the previous chapter [207, 141] have a fixed electric charge, which protects them from poisoning by excited quasiparticles originating elsewhere in the device. However, they are still vulnerable to two types of errors. (1) An excited fermionic quasiparticle on the island can be absorbed or emitted by a MZM. If this happens once, it takes the qubit out of the computational subspace; if it happens twice, it causes a bit or phase error, depending on which two MZMs are affected. (2) When the separation between MZMs is not large compared to the coherence length, the overlap between MZMs causes a redistribution of the electric charge in the island. The resulting charge distribution (which will, in general, have a non-vanishing line dipole moment between the semiconductor and superconductor) couples to phonons and the electrostatic environment of the island. These low-energy degrees of freedom cause the qubit to decohere.

In this chapter, we give quantitative estimates for both types of errors mentioned in the previous paragraph. Type (1) depends on the density of excitations, and therefore is small when this density is small. In thermal equilibrium, these errors are exponentially suppressed in the product of the gap Δ and the inverse temperature β. The main focus of the chapter is to quantify type (2) errors by computing the hybridization energy and charge distribution associated with MZMs using a charge-conserving formalism. We show how a dipole moment develops between a semiconductor nanowire and its superconducting shell. This dipole formation is analogous to the situation that occurs in a double quantum dot charge qubit, except that the transferred charge is much less than the charge of an electron. We give quantitative estimates

of the resulting dephasing using measurements of the electrostatic noise spectrum in similar devices and the electron-phonon coupling and phonon spectrum of InAs. Very similar physics applies to the measurement process proposed in Ref. [141]: when a quantum dot is coupled to a MZM, a dipole moment develops between the quantum dot and the qubit. We report the corresponding dephasing times which quantify how fast the environment reads out the parity of a pair of MZMs during the measurement process.

The remainder of this chapter is organized as follows. In Section 5.2, we develop the basic setup of the qubit-environment coupling. In Section 5.3, we calculate the hybridization energy and charge distribution associated with the overlap of a pair of MZMs. We estimate qubit dephasing times due to several different noise sources in Section 5.4. In Section 5.5, we discuss additional effects of charge noise on the qubit system. We conclude in Section 6.6.

5.2 Basic setup

Consider a two-level system with density matrix $\rho(t)$, described by a Hamiltonian $H_S = \Omega\sigma^z$. We assume that the system interacts weakly with its environment, described by a Hamiltonian H_E, and that the environment is in thermal equilibrium at inverse temperature β. The density matrix $\rho(t)$ undergoes a particularly simple time evolution when the system-environment interaction is diagonal in the system's energy basis,

$$H_{\text{SE}} = \frac{a_z}{2}\sigma^z \otimes \Phi, \tag{5.1}$$

where Φ acts on the environment degrees of freedom. The diagonal elements of $\rho(t)$ have constant magnitude and the off-diagonal elements decay according to [73]

$$|\rho_{01}(t)| = e^{-B^2(t)}|\rho_{01}(0)|, \tag{5.2}$$

where

$$B^2(t) \equiv a_z^2 \int_0^\infty d\omega\, S(\omega)\, \frac{\sin^2(\omega t/2)}{(\omega/2)^2}. \tag{5.3}$$

Here, the noise spectral function of Φ is given by

$$S(\omega) \equiv \int_{-\infty}^{\infty} dt\, \frac{e^{i\omega t}}{2\pi} \left(\frac{\langle \Phi(t)\Phi(0)\rangle + \langle \Phi(0)\Phi(t)\rangle}{2} \right) \tag{5.4}$$

where $\langle \Phi(t)\Phi(0)\rangle \equiv \text{tr}\left(e^{-\beta H_{\text{E}}}\Phi(t)\Phi(0)\right)$.

We use Eq. (5.3) to analyze dephasing times for the tetrons presented in the previous chapter. In Fig. 5.1, we depict two possible geometries of such qubits. The common elements of both geometries are: two topological sections built from a semiconductor wire (light orange) proximitized by a superconductor (dark blue), connected by a trivial s-wave superconductor [labeled (s)] to form a Coulomb-blockaded superconducting island hosting four MZMs. We call the trivial superconducting region the "backbone." The qubit is encoded according to $\sigma^z \equiv i\gamma_1\gamma_2$ (note that in the ground state, $i\gamma_1\gamma_2 = i\gamma_3\gamma_4$). The main difference between the two geometries is that the upper design (a) requires at least two semiconducting nanowires while the lower design (b) can be realized with a single nanowire and a loop-shaped backbone.

We consider the limit in which the energy gap in the superconducting backbone is much larger than in the topological sections. Then, the amplitude for a fermion to tunnel from γ_1 or γ_2 to γ_3 or γ_4 will be very small. The dominant error mechanism will be dephasing from the

coupling of the electromagnetic environment to the charge shared by γ_1 and γ_2 (and shared by γ_3 and γ_4). This assumption simplifies our calculations, but does not change our main results.

The qubit states stored in $i\gamma_1\gamma_2$ are slightly split in energy by ε_{hyb}, resulting from overlap of the MZM wavefunctions. This hybridization energy fluctuates with the electromagnetic environment, resulting in the dephasing of the qubit. The qubit-environment coupling can be modeled by the simple Taylor expansion:

$$H_{\text{MZM-E}} = \frac{1}{2}\left(\frac{\partial\varepsilon_{\text{hyb}}}{\partial E_z}\right) i\gamma_1\gamma_2 \otimes \delta E_z(t) \tag{5.5}$$

where E_z is the electric field component perpendicular to the semiconductor-superconductor interface, as shown in Fig. 5.1. This interaction can equivalently be understood as the electrostatic environment coupling to the dipole moment

$$\vec{p}_{\text{top}} = \frac{\partial\varepsilon_{\text{hyb}}}{\partial E_z}\hat{z}, \tag{5.6}$$

whose sign depends on the parity of MZMs γ_1 and γ_2. We calculate the hybridization energy and the charge distribution in the topological wire leading to this dipole moment in Section 5.3.

For both qubit designs shown in Fig. 5.1, a measurement is performed by coupling two of the MZMs to an auxiliary quantum dot (yellow) as described in the previous chapter [141]. This coupling can be achieved by lowering tunnel barriers (not shown) in the semiconducting region neighboring MZMs γ_2 and γ_3, so that an electron can tunnel into MZM γ_j with amplitude t_j. We always work in the weak coupling limit, $|t_j| \ll E_C$, where E_C is the charging energy of the MZM island. When the combined MZM qubit-quantum dot system is in its ground state, the charge distribution on the quantum dot becomes parity-dependent [141]. Measuring the

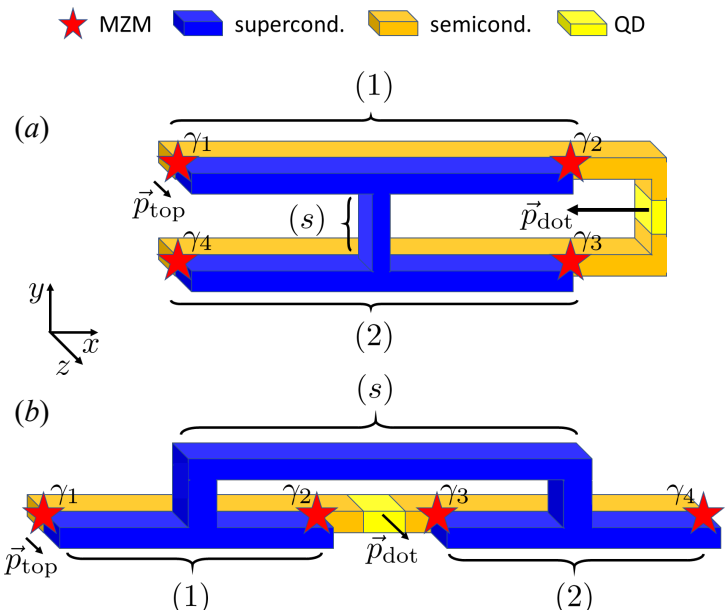

Figure 5.1: Two charge-protected MZM qubit geometries: (a) Two-sided tetron and (b) loop qubit. Each design has two topological sections, labeled (1) and (2), consisting of a semiconducting nanowire (orange) proximitized by a superconducting wire (blue), and tuned into the topological phase so that MZMs (red stars) are localized at either end. The two topological sections are connected by a trivial superconductor, the "superconducting backbone," labeled by (s). The superconducting backbone ensures that the device acts as a single superconducting island, thereby allowing superpositions of all (total fermion parity even) MZM states. When the superconducting island has appreciable charging energy, extrinsic quasiparticle poisoning is strongly suppressed, hence the designation that these are "charging-energy protected MZM qubits." MZMs belonging to the same wire (γ_1 and γ_2 or γ_3 and γ_4) will slightly overlap, resulting in a relative charge distribution between the semiconductor and superconductor in the topological sections. This charge buildup results in a dipole moment, $\vec{p}_{\text{top}}$, oriented perpendicular to the semiconductor/superconductor interface. Provided the lengths of the topological wires are equivalent in the two designs, $\vec{p}_{\text{top}}$ will be the same. A measurement of the fermion parity $i\gamma_2\gamma_3$ is performed by tunnel coupling MZMs 2 and 3 to an auxiliary quantum dot (yellow), located in the semiconducting region connecting wires (1) and (2). The qubit-quantum dot system also forms a dipole moment, $\vec{p}_{\text{dot}}$, whose magnitude and direction depends on the device geometry. We assume an essentially vanishing screening length so that the displacement vector entering $\vec{p}_{\text{dot}}$ points from the quantum dot to the surface of the superconductor: note that this results in $\vec{p}_{\text{top}}$ and $\vec{p}_{\text{dot}}$ being parallel in (b), provided topological sections (1) and (2) are equidistant from the quantum dot. Coupling of $\vec{p}_{\text{top}}$ to the environment sets the dephasing time of the qubit; coupling of $\vec{p}_{\text{dot}}$ to the environment sets how fast the environment measures $i\gamma_2\gamma_3$.

quantum dot charge thus allows one to infer the MZM parity.

When the system is tuned into a measurement configuration with a single electron able to tunnel between the quantum dot and MZM qubit, another dipole moment emerges. In the weak coupling limit, when the quantum dot and MZM qubit are off-resonant, the dipole moment is (up to corrections of order $|t_j|^2/E_C^2$)

$$\vec{p}_{\text{dot}} = e\vec{d}\tau^z, \tag{5.7}$$

where $\vec{d}$ is a displacement vector from the quantum dot to the surface of the superconductor (we assume an essentially vanishing screening length) and $\tau^z = +1$ if the electron is on the quantum dot and -1 if the electron is on the qubit. The qubit-dot dipole moment will couple to electromagnetic noise via

$$H_{\text{QD-E}} = \frac{1}{2}\vec{p}_{\text{dot}} \otimes \delta\vec{E}(t). \tag{5.8}$$

Unlike the case of the qubit, which we want to be able to stay in a superposition for extended times, a successful measurement relies on collapsing the quantum mechanical state of the MZM island-quantum dot system. The corresponding dephasing time therefore quantifies how fast the environment measures the MZM parity p_{23}. Moreover, if the combined MZM island-quantum dot system populates the charge excited state during the initialization process, a short relaxation time can help to quickly return the system to its ground state.

Noise in the electromagnetic environment is given by

$$S_E(\omega) = \int dt \frac{e^{i\omega t}}{2\pi} \left(\frac{\langle \delta E_z(t)\delta E_z(0)\rangle + \langle \delta E_z(0)\delta E_z(t)\rangle}{2} \right), \tag{5.9}$$

and is generally believed to be due to slow fluctuations of two level states in the environment [202, 73]. We do not have a microscopic model of these processes, so we extract the

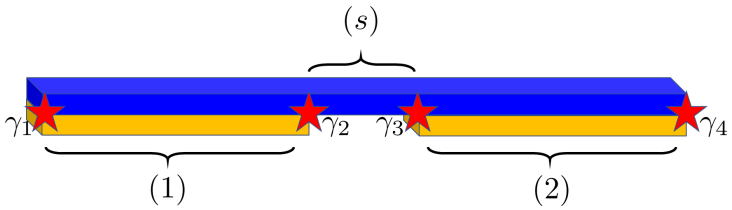

Figure 5.2: Relevant geometry for the charge distribution calculation in Section 5.3 with the same legend as in Fig. 5.1. Analogously to the qubit designs, there are two topological segments (each hosting a MZM at either end) of length L, and a trivial superconducting region labeled (s) of length ℓ.

low-frequency form of these fluctuations, which are assumed to have a $1/f$ frequency dependence, from experiments on similar devices [192, 205, 204, 84, 234]:

$$S_E(\omega) = \frac{\alpha_E}{\omega}. \tag{5.10}$$

Other noise sources affecting the MZM qubit are coupling to phonons and finite temperature excitations of quasiparticles in the superconductor. The former couples to the charge distribution in the MZM qubit in much the same way as $1/f$ charge noise, but is predicted to have a smaller effect that becomes negligible when the wires are sufficiently long, see Section 5.4 [151]. Conversely, thermally-excited quasiparticles only become a relevant noise source compared to $1/f$ charge noise when the wire is sufficiently long such that $e^{L/\xi} \gtrsim e^{\beta\Delta}$, see Section 5.4 [151].

5.3 Hybridization energy and charge distribution in MZM qubits

In this section, we calculate the hybridization energy and the charge distribution resulting from the overlap between the MZMs γ_1 and γ_2 (or equivalently between γ_3 and γ_4) in Fig. 5.2. We expect the essential physics of this simplified geometry to be the same as that of the MZM qubits shown in Fig. 5.1 when the qubit is idle (i.e., the auxiliary quantum dot is disconnected from the superconducting islands). In order to avoid subtleties in the interpretation of the charge distribution calculated with BCS mean-field theory, we will use the explicitly charge-conserving formalism of Refs. [227, 93, 62]. We compare our results with previous studies of the hybridization energy [61, 60] and charge distribution [25, 170, 83] at the end of each subsection.

We model the topological segment (j) of the device shown in Fig. 5.2 as a one-dimensional spinless semiconducting wire in contact with a quasi-one-dimensional algebraically-ordered superconductor. This model allows us to set up a controlled theory to study how phase fluctuations couple to MZMs, and ultimately to extract how the energy splitting and charge distribution depend on the fermion parity. Electron operators in the semiconductor can be bosonized as

$$\psi_r^{(j)}(x) \sim e^{-i(r\phi_j(x)-\theta_j(x))}, \tag{5.11}$$

where $r = \pm 1$ for right or left-movers. The superconductor electron operators are described

in terms of spin (σ) and charge (ρ) modes

$$\psi_{r,\sigma}(x) \sim e^{-\frac{i}{\sqrt{2}}(r\phi_\rho(x)-\theta_\rho(x)+\sigma(r\phi_\sigma(x)-\theta_\sigma(x)))}, \tag{5.12}$$

where $\sigma = \pm 1$ for up or down spins and $r = \pm$ corresponds to right and left movers. The fields $\phi_\alpha(x),\ \theta_\beta(x')$ satisfy the usual commutation relations

$$[\partial_x \phi_\alpha(x), \theta_\beta(x')] = i\pi\delta(x-x')\delta_{\alpha\beta}, \tag{5.13}$$

for $\alpha, \beta \in \{1, 2, \rho, \sigma\}$.

The above definitions yield the bosonized effective Lagrangian introduced in Ref. [93],

$$\mathcal{L} = \mathcal{L}^{(1)} + \mathcal{L}^{(2)} + \mathcal{L}^{(s)}, \tag{5.14}$$

where the trivial superconducting backbone is described by

$$\mathcal{L}^{(s)} = \frac{1}{2\pi}\int_L^{L+\ell} dx\Big\{ -2i\left(\partial_\tau\theta_\rho\right)\left(\partial_x\phi_\rho\right) + K_\rho v_\rho \left(\partial_x\theta_\rho\right)^2 + \frac{v_\rho}{K_\rho}\left(\partial_x\phi_\rho - k_F^{(\rho)}\right)^2\Big\}, \tag{5.15}$$

and the topological sections are described by

$$\begin{aligned}\mathcal{L}^{(1)} = \frac{1}{2\pi}\int_0^{L} dx\Big\{ & -2i\left(\partial_\tau\theta_1\right)\left(\partial_x\phi_1\right) + Kv\left(\partial_x\theta_1\right)^2 + \frac{v}{K}\left(\partial_x\phi_1 - k_F\right)^2 \\ & -2i\left(\partial_\tau\theta_\rho\right)\left(\partial_x\phi_\rho\right) + K_\rho v_\rho\left(\partial_x\theta_\rho\right)^2 + \frac{v_\rho}{K_\rho}\left(\partial_x\phi_\rho - k_F^{(\rho)}\right)^2 \\ & -\frac{\Delta_P}{a}\cos\left(\sqrt{2}\theta_\rho - 2\theta_1\right)\Big\}\end{aligned} \tag{5.16}$$

$$\mathcal{L}^{(2)} = \int_{L+\ell}^{2L+\ell} dx\Big\{(1) \leftrightarrow (2)\Big\}. \tag{5.17}$$

The Luttinger parameter and Fermi velocity are K and v, respectively, for the semiconducting wires, and K_ρ and v_ρ for the superconductor's charge mode. The pairing term, $\frac{\Delta_P}{2\pi a}\cos(\sqrt{2}\theta_\rho -$

$2\theta_j$), emerges from integrating out the gapped spin degrees of freedom in the s-wave superconductor [93]. Here, Δ_P and a are the Cooper-pair-hopping amplitude and the theory's short distance cutoff, respectively.

As follows from Eqs. (5.11) and (5.12), the fields $\partial_x \phi_{\rho/j}$ represent the total particle number in the superconductor and semiconductors, respectively. These field definitions lead to periodic boundary conditions, thereby simplifying the instanton calculation of the hybridization energy below (by avoiding twisted boundary conditions due to phases of the form $\exp\{ik_F L\}$). As such, the density of the wires is fixed explicitly in the Hamiltonian by including shifts of $\partial_x \phi_j$ by k_F, and of $\partial_x \phi_\rho$ by $k_F^{(\rho)}$.

In order to obtain low-energy effective description, we first run the renormalization group (RG) procedure. The superconducting pairing term is relevant and flows to strong coupling according to

$$\frac{dy}{dl} = \left(2 - \frac{1}{2K_\rho} - \frac{1}{K}\right) y, \tag{5.18}$$

where $y = \Delta_P a/\tilde{v}$, the length scale l is defined in terms of the short distance cutoff a_0 as $l = \log(a/a_0)$. We define the coherence length ξ as the length scale for which $y(l) = 1$, implying

$$\xi = a_0 \left(\frac{\tilde{v}}{\Delta_P a_0}\right)^{\left(2-(2K_\rho)^{-1}-(K)^{-1}\right)^{-1}}, \tag{5.19}$$

where the effective Fermi velocity is given by

$$\tilde{v} = v_\rho/2K_\rho + v/K. \tag{5.20}$$

In the following, we will work in the strong-coupling limit, for which the RG is carried out until the short distance cutoff $a \to \xi$. We take the mean field limit of this model to be when the velocities v and v_ρ are unchanged, the semiconductor is non-interacting ($K \to 1$), and the superconductor has an infinite number of channels ($K_\rho \to \infty$) [171, 88]. Taking this limit, we recover the mean field expressions: $\tilde{v} \to v$ and $\xi_{\text{MF}} \equiv \xi(K_\rho, K=1)|_{K_\rho \to \infty} = v/\Delta_P$.

At this scale ($a \to \xi$), one can neglect spatial fluctuations of the fields $\theta_{j/\rho}$ and take into account only uniform temporally-fluctuating modes. Integrating out the $\phi_{j/\rho}$ fields, we have

$$\begin{aligned}\mathcal{L}^{(j)} = \frac{L}{2\pi}\Big\{ &\frac{K}{v}\left(\partial_\tau \theta_j - i\frac{v}{K}k_F\right)^2 + \frac{K_\rho}{v_\rho}\left(\partial_\tau \theta_\rho - i\frac{v_\rho}{K_\rho}k_F^{(\rho)}\right)^2 \\ &- \frac{\Delta_P}{\xi}\cos\left(\sqrt{2}\theta_\rho - 2\theta_j\right)\Big\}.\end{aligned} \tag{5.21}$$

For the topological wire (j), we define average and difference fields between the nanowire and superconducting shell to be

$$\theta_j^+ = \frac{1}{2}\left(\frac{1}{\sqrt{2}}\theta_\rho + \theta_j\right) \tag{5.22}$$

$$\theta_j^- = \frac{1}{\sqrt{2}}\theta_\rho - \theta_j. \tag{5.23}$$

In terms of these fields, Eq. (5.21) becomes

$$\begin{aligned}\mathcal{L}^{(j)} = \frac{L}{2\pi}\Big\{ &\frac{1}{2}\left[\frac{K_\rho}{v_\rho} + \frac{K}{2v}\right]\left[4\left(\partial_\tau \theta_j^+\right)^2 + \left(\partial_\tau \theta_j^-\right)^2\right] \\ &+ 2\left[\frac{K_\rho}{v_\rho} - \frac{K}{2v}\right]\left(\partial_\tau \theta_j^+\right)\left(\partial_\tau \theta_j^-\right) - \frac{\Delta_P}{\xi}\cos\left(2\theta_j^-\right) \\ &- 2i\left(\sqrt{2}k_F^{(\rho)} + k_F\right)\partial_\tau \theta_j^+ - i\left(\sqrt{2}k_F^{(\rho)} - k_F\right)\partial_\tau \theta_j^-\Big\}.\end{aligned} \tag{5.24}$$

Integrating out the quadratic fields θ_j^+ results in the effective action for θ_j^-:

$$S_{\text{eff}} = \frac{L}{2\pi} \int d\tau \left\{ \frac{1}{\tilde{v}} \left(\partial_\tau \theta_j^- + i\mu_- \right)^2 - \frac{\Delta_P}{\xi} \cos\left(2\theta_j^-\right) \right\}, \tag{5.25}$$

where

$$\mu_- \equiv \frac{v}{K} k_F - \frac{v_\rho}{\sqrt{2} K_\rho} k_F^{(\rho)}. \tag{5.26}$$

The quantity μ_- can be understood as the Fermi energy of the semiconductor measured relative to the Fermi energy of the superconductor, we will henceforth refer to this as the relative Fermi energy. We comment below on the role of μ_- in the dephasing of the topological qubit. In the mean field limit, the superconductor's Fermi energy is fixed; as such μ_- is only determined by the Fermi energy of the semiconductor. Recall that we are working in the limit that the gap in the (trivial) superconducting backbone is much larger than the gap in the topological sections of the qubit, so that fermion tunneling between the regions (1) and (2) is strongly suppressed. For this reason, we have dropped an interwire coupling term, $\delta S^{(12)} \propto \int d\tau_1 d\tau_2 \partial_{\tau_1} \theta_1^-(\tau_1) \partial_{\tau_2} \theta_2^-(\tau_2)$, which we do not expect to qualitatively change our results.

The two ground states of the system are $(\theta_1^-, \theta_2^-) = (0,0)$ or $(0,\pi)$. The states (π,π) and $(\pi,0)$ are equivalent to, respectively, $(0,0)$ or $(0,\pi)$. As discussed in Ref. [93], symmetric and antisymmetric superpositions of the two ground state configurations of (θ_1^-, θ_2^-) are associated with even and odd fermion parity in the two topological wires. Therefore, all information about the topological qubit (i.e., the MZM parity) is contained in the configuration of the θ_j^- fields.

The splitting between the two ground states can be obtained from an instanton calculation in which θ_1^- winds by π while θ_2^- remains unchanged, or vice versa. The two key features for the present purposes are: (1) an instanton event takes the system between the two fermion parity states, as such the resulting degeneracy splitting can be associated with the MZM hybridization energy; and (2) there is a relative charge density buildup associated with this instanton and, therefore, with the MZM parity state.

5.3.1 MZM hybridization energy

In an instanton/anti-instanton solution, $\theta_j^-(\tau)$ interpolates between $\theta_j^-(-\infty) = 0$ and $\theta_j^-(\infty) = \pm\pi$, e.g.,

$$\theta_1^-(\tau) = \pm\frac{\pi}{2}\left(1 + \tanh\left[\sqrt{\frac{\Delta_P\tilde{v}}{\xi}}(\tau - \tau_0)\right]\right). \tag{5.27}$$

There are similar instantons in which the phase winds on the other topological segment. We neglect multi-instanton solutions, since they have larger action and are, therefore, exponentially suppressed compared to the single instanton/anti-instanton solutions. There is a one-parameter family of such instanton/anti-instanton solutions, parameterized by the mid-point in imaginary time of the instanton, τ_0. We must average over τ_0 to include the effect of the entire family. Instantons and anti-instantons contribute with opposite phases (due to the μ_- term in the action) and have opposite charge [due to the $\pm$ sign in Eq. (5.27)].

The instanton calculation results in the following expression for the degeneracy splitting:

$$\varepsilon_{\text{hyb}} = A\cos\left(\frac{L\mu_-}{\tilde{v}}\right)\exp\left\{-\frac{L}{\xi_{\text{MF}}}f(K_\rho, K)\right\}, \tag{5.28}$$

where the dimensionless function in the exponent is $f(K_\rho, K) = \frac{2\sqrt{2}}{\pi}\sqrt{\frac{\xi_{\rm MF}}{\xi}}$. Up to numerical prefactors of order one, the constant A is given by the attempt frequency $A = \sqrt{\Delta_P \tilde{v}/\xi}$. Equation (5.28) is one of our main results of this section and, to our knowledge, the first reporting of the hybridization energy in a charge conserving formalism that captures both the oscillatory dependence and exponential suppression of the degeneracy splitting with length. In the mean field limit (i.e. $K_\rho \to \infty$, $v_\rho = \text{const}$), $\varepsilon_{\rm hyb}^{\rm MF} \sim \cos(k_F L) \exp\left\{-\frac{2\sqrt{2}L}{\pi\xi_{\rm MF}}\right\}$, which agrees with previous mean field calculations of the degeneracy splitting in a topological superconductor [61, 60].

5.3.2 Charge distribution

To calculate the charge distribution associated with the MZMs, we first consider the charge densities in one of the semiconducting wires $\langle\rho_j\rangle = \frac{1}{\pi}\frac{K}{v}\langle\partial_t\theta_j\rangle$ and the neighboring region of the trivial superconductor $\langle\rho_\rho\rangle = \frac{\sqrt{2}}{\pi}\frac{K_\rho}{v_\rho}\langle\partial_t\theta_\rho\rangle$. In terms of θ^- fields, one finds

$$\langle\rho_j\rangle = -\frac{1}{\pi\tilde{v}}\langle\partial_t\theta_j^-\rangle + \frac{Kv_\rho}{\pi}\left(\frac{\sqrt{2}k_F^{(\rho)} + k_F}{2K_\rho v + v_\rho K}\right) \tag{5.29}$$

$$\langle\rho_\rho\rangle = +\frac{1}{\pi\tilde{v}}\langle\partial_t\theta_j^-\rangle + \frac{2K_\rho v}{\pi}\left(\frac{\sqrt{2}k_F^{(\rho)} + k_F}{2K_\rho v + v_\rho K}\right). \tag{5.30}$$

Only the first term on the right side of Eqs. (5.29) and (5.30) depends on the field configuration of θ_j^- and thus on the fermion parity of wire (j). As one can see, the total charge expectation value of the system, $\langle\rho_j\rangle + \langle\rho_\rho\rangle$ is independent of the θ_j^- field and, thus, does not encode any topological information. Instead, the MZM parity is encoded in a line dipole moment forming between the semiconductor and superconductor. Only environmental degrees of freedom that

resolve the charge separation of this dipole moment couple to the MZM charge distribution. We comment on the relevant distance scale for this dipole moment at the end of this section.

Equations (5.29) and (5.30) hold even if we extend the trivial superconducting region to infinity, corresponding to a grounded superconductor. In the model presented in Ref. [227], the topological wire is an intrinsic p-wave superconductor with an odd number of channels. The role played here by the semiconductor and superconductor is instead played by different channels. As the corresponding wavefunctions will have different transverse profiles, the MZM overlap will result in some multipole charge distribution.

More explicitly, using the expression given in Eq. (5.27) for the instanton contribution to θ_1^-, we can calculate the MZM parity-dependent relative charge density $\langle \rho_- \rangle = \frac{1}{\pi \tilde{v}} \langle \partial_t \theta_1^- \rangle$. Approximating this charge as uniformly spread over the length of the topological section, we find

$$\frac{\Delta Q_{\text{MZM}}}{e} = -\frac{L}{\sqrt{\xi_{\text{MF}} \xi}} \sin\left(\frac{L\mu_-}{\tilde{v}}\right) \exp\left\{-\frac{L}{\xi_{\text{MF}}} f\left(K_\rho, K\right)\right\}. \tag{5.31}$$

Ultimately, we are interested in how the charge distribution associated with the MZMs couples to charge noise in the topological qubit's environment. We expect electric field fluctuations to vary the parameters of the semiconductor (k_F, v) relative to those of the superconductor ($k_F^{(\rho)}$, v_ρ), resulting in noise in the relative Fermi energy μ_-. One can verify that $\Delta Q_{\text{MZM}}/e = \partial_{\mu_-} \varepsilon_{\text{hyb}}$; combining this expression with Eq. (5.6) we have

$$\vec{p}_{\text{top}} = \Delta Q_{\text{MZM}} \frac{\partial \mu_-}{\partial E_z} \hat{z}. \tag{5.32}$$

Importantly, we see that charge noise only couples to the topological qubit through the relative Fermi energy μ_- between the semiconductor and superconductor; total charge does not

couple to the qubit state. Note that in the above argument we have assumed that ξ and ξ_{MF} are parameters independent of μ_-. Since the leading order μ_--dependence of Δ_P and v tends to cancel in ratios v/Δ_P, charge fluctuations predominantly couple to the prefactor rather than the exponential of the hybridization energy in Eq. (5.28). More explicitly, on the mean-field level we can express parameters v and Δ_P as

$$v = k_F \left(\frac{1}{m} - \frac{\alpha^2}{\sqrt{V_Z^2 + \alpha^2 k_F^2}} \right) \quad \Delta_P = \frac{\alpha k_F \Delta_0}{\sqrt{V_Z^2 + \alpha^2 k_F^2}} \,. \tag{5.33}$$

Here, m, α, k_F are, respectively, the effective mass, spin orbit coupling and Fermi momentum of the band that hosts the MZMs. For the p-wave gap we assume that the system is well inside the topological regime with Zeeman energy $V_Z \gg \Delta_P$. Δ_0 denotes the induced s-wave pairing.

Since the chemical potential of the superconductor will not be affected by charge fluctuations we can set $\partial_{\mu_-} = \tilde{v}^{-1} \partial_{k_F}$. Using Eq. (5.33) the derivative $\partial_{\mu_-} \varepsilon_{\text{hyb}}$ now has three contributions. (1) The derivative of the attempt frequency is of the order $\partial_{\mu_-} \Delta_P$ and yields a contribution $Q^{(1)}_{\text{MZM}}$ which is bounded by $\varepsilon_{\text{hyb}}/\varepsilon_F$, with ε_F being the Fermi energy of the band. (2) The contribution from the derivative of the cosine that was used for Eq. (5.31) is $Q^{(2)}_{\text{MZM}} \sim \varepsilon_{\text{hyb}}/\delta$, where $\delta = v/L$ is the level spacing. (3) The derivative of the exponent contributes as $Q^{(3)}_{\text{MZM}} \sim (\varepsilon_{\text{hyb}}/\delta) \partial_{k_F} \xi^{-1}$. Since the leading order dependence of v and Δ_P on k_F cancels in $\xi = v/\Delta_P$, we find $\partial_{k_F} \xi^{-1} \sim \Delta_P/\varepsilon_F$. We therefore conclude that unless the system is close to the fine-tuned point $\sin(\mu_-/\delta) = 0$, the relevant charge dipole can be estimated by $Q^{(2)}_{\text{MZM}}$ as stated in Eq. (5.31).

From Eq. (5.30), we see that including superconducting fluctuations was essential to observing the formation of a parity-dependent line dipole moment between the semiconductor

and superconductor. We now compare our results with the ones obtained using the BCS mean-field approximation, where superconducting fluctuations are not considered. Previous calculations using BCS mean-field theory concluded that there is a parity-dependent charge correction in the semiconductor only. Indeed, in the mean-field limit of our charge conserving formalism, our expression for ΔQ_{MZM} agrees with the BCS mean-field theory expressions in Refs. [25, 170, 83]. However, the latter-two papers do not take into account the screening of charge by the superconducting condensate, which exactly cancels the semiconducting contribution so that the total charge is independent of θ_j^-. Thus, noise that couples to the total charge of the island does not contribute to dephasing of the topological qubit. Instead, we find that fluctuations in the electric field that couples to the line dipole moment at the superconductor-semiconductor interface contribute to dephasing. Previously, based on BCS mean-field theory calculations, ΔQ_{MZM} was either thought to be an absolute line charge [170, 83], or the relevant distance scale entering the line dipole moment was assumed to be on the order of the semiconducting wire's diameter, w [25]. Although our calculation does not include an estimation of the relevant length scale separating the charge in the semiconductor and superconductor, simulations of Al-InAs nanowires [9] indicate that there is an accumulation layer at the superconductor-semiconductor interface, resulting in a suppression of the dipole moment found in Ref. [25] by at least a factor of $r/w \sim 0.1$, where r is the separation between the semiconductor and superconductor wavefunctions. We therefore do not expect the charge ΔQ_{MZM} to be observable via charge sensing for wires satisfying $L/\xi > 5$, as was suggested in Refs. [170] and [25]. The combination of the MZM charge distribution being interpreted as

a dipole moment, and the concentration of the charge near the interface, suppresses the image charge effect discussed in Ref. [83] by a factor of $(r/w)^2$. As such, detecting the dielectric screening of the charge buildup in the topological wire is beyond current experimental reach.

5.4 Dephasing of MZM qubits

We now use the charge distribution ΔQ_{MZM} derived in the previous section to calculate the dephasing time of a topological qubit. We define the *pure dephasing time*, T_2^*, of the qubit to be the time scale over which off-diagonal elements of the qubit density matrix decay: $B^2(T_2^*) = 1$, where $B^2(t)$ is given in Eqs. (5.2) and (5.3). All qubit operations must occur on a faster time scale than the dephasing time, thus understanding the behavior of T_2^* is critical for designing and building a working qubit.

Note that topological qubits are special in the sense that ideally there is no energy splitting between the two qubit states, thus which processes we call dephasing and which we call relaxation amounts to a choice of basis. We start by choosing the z-basis of the qubit as the parity of $i\gamma_1\gamma_2$ and neglect fermion tunneling between the two topological wires, thus reducing the problem to pure dephasing. We comment on relaxation processes at the end of this section.

The dephasing processes considered in this section are noise in the electromagnetic environment (E), coupling to phonons (ph), and finite temperature excitations (β). We make the approximation that all noise sources are independent and write the dephasing exponent as a sum of the dephasing exponents from each noise source:

$$B^2(t) = B_E^2(t) + B_{\text{ph}}^2(t) + B_\beta^2(t). \tag{5.34}$$

L/ξ	5	10	20	30*
$T^*_{2,E}$	600 ns	30 μs	100 ms	10 min
$T^*_{2,\beta}$	20 s	20 s	20 s	20 s
T^*_2	200 ns	30 μs	100 ms	20 s

Table 5.1: Dephasing times for the parameters of bulk InAs evaluated at different values of L/ξ for different noise sources. The first row is the pure dephasing time due solely to $1/f$ charge noise, $T^*_{2,E}$, which grows exponentially with wire length, see Eq. (5.38). The second row is the pure dephasing time due solely to thermally-excited quasiparticles in the superconductor, $T^*_{2,\beta}$, which is independent of L/ξ in thermal equilibrium. The latter only becomes relevant for long wires. The last row is the pure dephasing time due to all three noise sources discussed in Section 5.4. We do not define a dephasing time due solely to coupling to phonons as $B^2_{\text{ph}}(t) < 1$ for experimentally reasonable time scales; coupling to phonons shifts the dephasing time for short wires, $L/\xi = 5$, but has negligible effect for longer wires. The time estimates in the table do not take into account corrections due to disorder or non-equilibrium quasiparticles in the superconductor. The asterisk on the last column, $L/\xi \sim 30$ indicates that these corrections are likely to become important once the dephasing time estimate from intrinsic physics of the qubit (finite size effects, phonons, thermal quasiparticle excitations) has reached the order of tens of seconds.

We do not take into account disorder in our estimates of the different dephasing processes. Our results therefore represent the unavoidable intrinsic dephasing that is left even if growth and fabrication of the qubits is optimized. Given that topological qubits will likely be built from epitaxially grown nanowires with clean semiconductor-superconductor interfaces [179], we expect that our estimates provide a good guideline for realistic dephasing times.

5.4.1 $1/f$ noise

We begin by considering the effect of the electromagnetic environment on the qubit. From Eqs. (5.5) and (5.6), we see that Eq. (5.2) becomes

$$B^2_E(t) = |\vec{p}_{\text{top}}|^2 \int_{1/t}^{\infty} d\omega \frac{\alpha_E}{\omega} \frac{\sin^2(\omega t/2)}{(\omega/2)^2}, \tag{5.35}$$

where we have used Eq. (5.10) for the spectral function. This expression is weakly dependent on the lower frequency cutoff, which we have approximated as $1/t$; essentially this choice of cutoff frequency amounts to only considering the noise remaining after a "charge echo pulse" [192]. Solving for $B_E^2(T_{2,E}^*) = 1$, we find

$$T_{2,E}^* = \left(|\vec{p}_{\text{top}}|\sqrt{\alpha_E \kappa}\right)^{-1}, \tag{5.36}$$

where $\kappa \equiv 1 - \cos[1] + \sin[1] - \text{Ci}[1] \approx 0.96$.[1] We make the approximation that electric field can be related to the gate voltage (assumed to be applied directly at the side of the wire opposite to the superconducting shell) by $E_z w = V_g$, where w is the diameter of the topological wire [2]. We can then write the topological dipole moment as

$$\vec{p}_{\text{top}} \sim \Delta Q_{\text{MZM}} \left(\frac{\partial \mu_-}{\partial V_g} w\right) \hat{z}. \tag{5.37}$$

Plugging Eq. (5.31) into Eqs. (5.36) and (5.37), we see that if $\xi \approx \xi_{\text{MF}}$, the pure dephasing time grows with L/ξ as

$$T_{2,E}^* = c \frac{\xi}{L} \exp\left\{\frac{2\sqrt{2}}{\pi} \frac{L}{\xi}\right\}, \tag{5.38}$$

where $c = \left(w(\partial_{V_g}\mu_-)\sqrt{\alpha_E \kappa}\right)^{-1}$. Simulation of a mean field InAs nanowire with radius $w = 60$ nm, proximity-coupled to an Al superconducting shell estimates the relative Fermi energy to change with gate voltage as $\partial_{V_g}\mu_- \sim 0.1$ [9]. Making the approximation that electric field noise will be similar to the values reported in Refs. [205, 204, 84, 234], we set $\alpha_E = 10$ (V/m)^2, resulting in $c \approx 40$ ns [151]. Our estimates for the dephasing time for different

[1] Ci$[x]$ is the cosine integral function, defined by $\int_x^\infty dx \cos(x)/x$.

[2] This approximation makes the assumption that the superconductor screens the electric field, so that fluctuations in the electric field can only vary over the diameter of the semiconducting wire

values of L/ξ are reported in Table 5.1. The dephasing times for long wires are predicted to be orders of magnitude larger than dephasing times of conventional charge qubits precisely because ΔQ_{MZM} is a small fraction of an electron charge.

5.4.2 Phonons

In addition to $1/f$ charge noise, we can also consider dephasing from phonons coupling to the charge distribution in the MZM qubit. For the sake of concreteness, we will focus on InAs devices. We neglect phonons in the superconductor, which are expected to have a subleading contribution. The phonon spectrum and electron-phonon coupling are reasonably well-understood in bulk InAs, which will allow us to place an upper bound on the dephasing due to phonons, since the device geometry may place further restrictions on the phonon spectrum. The qubit dephasing from phonons results from the interactions

$$H_{\text{MZM-ph}} = i\gamma_1\gamma_2 \int \frac{d^3q}{(2\pi)^3} \rho_{\text{MZM}}(-q) \left[Diq_j u_j(q) + eh_{14} \sum_\lambda M_\lambda(q) \epsilon_j^\lambda(q) u_j(q) \right], \tag{5.39}$$

where $u_j(q)$ is the Fourier transform of the displacement in the jth direction, $D = 5.1$ eV is the conduction band deformation potential of InAs [260] and $h_{14} = 3.5 \times 10^6$ V/cm is its piezoelectric coupling [183]. Note that as InAs is electron-doped we do not need to consider the valence band deformation potential. The form factor $M_\lambda(q)$ depends on the nanowire or quantum well geometry and is bounded from above by one; ϵ_j^λ are the polarization vectors. This coupling is also of the form of Eq. (5.1), where now $\sigma = i\gamma_1\gamma_2$ and the environment operator Φ is dependent on the charge distribution $\rho_{\text{MZM}}(q)$ associated with overlapping MZMs.

The noise due to phonons coupling to the MZM charge distribution is

$$a_z^2 S_{\text{ph}}(\omega) = \int \frac{d^3q}{(2\pi)^3} |\rho_{\text{MZM}}(q)|^2 \left\langle u_i(-q,-\omega) u_j(q,\omega) \right) \big\rangle \times \Big[D^2 q^2 \delta_{ij} + (e h_{14})^2 \sum_{\lambda,\lambda'} M_\lambda(-q) M_{\lambda'}(q) \epsilon_i^\lambda(-q) \epsilon_j^{\lambda'}(q) \Big]. \quad (5.40)$$

The correlation function $\langle u_i(-q,-\omega) u_j(q,\omega) \rangle$ is obtained from the fluctuation-dissipation theorem,

$$\langle u_i(-q,-\omega) u_j(q,\omega) \rangle = \chi_{ij}(q,\omega)(1 - e^{-\beta\omega})^{-1}, \quad (5.41)$$

where

$$\chi_{ij}(q,\omega) = \delta_{ij}\, \delta(\omega^2 - v_l^2 q^2)/\rho + (\delta_{ij} - q_i q_j/q^2)\, \delta(\omega^2 - v_t^2 q^2)/\rho. \quad (5.42)$$

The longitudinal and transverse phonon velocities are $v_l \approx 4.7$ km/s and $v_t \approx 3.3$ km/s, respectively. The density of InAs is $\rho \approx 5.7$ g/cm^3.

We approximate the charge density in the semiconducting nanowire ρ_{MZM} as

$$\rho_{\text{MZM}}(\mathbf{x}) = \frac{Q_{\text{MZM}}}{e} \frac{\delta(x)\delta(y)}{L}, \quad (5.43)$$

with Fourier transform

$$\rho_{\text{MZM}}(\mathbf{q}) = \frac{\Delta Q_{\text{MZM}}}{e} \text{sinc}\,(q_x L)\,. \quad (5.44)$$

We are interested in an upper bound on the dephasing from phonons, so we approximate $\text{sinc}(q_x L)$ by 1. Thus the coupling constant a_z can be identified as the dimensionless charge Q_{MZM}/e. We ignore the difference between longitudinal and transverse phonon velocities and

replace v_l and v_t by their average, $v = 4$ km/s. Then, the spectral function of phonons coupled to the MZMs can be bounded by the expression

$$S_{\text{ph}}(\omega) = \left[D^2 \frac{\omega^2}{v^2} + (eh_{14})^2 M_{ii} \right] \frac{1}{\rho} \frac{1}{(2\pi)^2} \frac{\omega}{v^3} \left(1 - e^{-\beta\omega}\right)^{-1}, \tag{5.45}$$

where we have written the form factor-dependent sum in Eq. (5.40) as M_{ij}. Then, dephasing from phonons is described by

$$B^2_{\text{ph}}(t) = \int_0^{\omega_D} d\omega \frac{\Delta Q^2_{\text{MZM}}}{e^2} S_{\text{ph}}(\omega) \frac{\sin^2(\omega t/2)}{(\omega/2)^2} \tag{5.46}$$

$$= \frac{\Delta Q^2_{\text{MZM}}}{(2\pi)^2 e^2 v^5 \rho} (1 - e^{-\beta\omega})^{-1} \Big(D^2 \frac{\left[2 + (\omega_D t)^2 - 2\cos(\omega_D t) - 2\omega_D t \sin(\omega_D t)\right]}{t^2} + 2v^2 (eh_{14})^2 M_{ii} \left[\gamma - \text{Ci}(\omega_D t) + \log(\omega_D t)\right] \Big), \tag{5.47}$$

where the Debye frequency in InAs is $\omega_D = 3.3$ THz. In the zero temperature, long time limit, $B^2_{\text{ph}}(t)$ grows in time as a logarithm,

$$B^2_{\text{ph}}(t \to \infty) = \frac{\Delta Q^2_{\text{MZM}}}{(2\pi)^2 e^2 v^5 \rho} \left(D^2 \omega_D^2 + 2(eh_{14})^2 M_{ii} v^2 [\gamma + \log(\omega_D t)] \right). \tag{5.48}$$

Using the upper bound $M_{ii} = 3$, the above expression for the parameters of InAs is roughly

$$B^2_{\text{ph}}(t \to \infty) \approx e^{-\frac{4\sqrt{2}}{\pi}\frac{L}{\xi}} \left(\frac{L}{\xi}\right)^2 (300 + 0.1 \log[t(1\text{ Hz})]). \tag{5.49}$$

The logarithmic term only becomes important on astronomically-long time scales. Thus, for any reasonable time scales, coupling to phonons only contributes to the MZM qubit dephasing when the constant term is of order one, i.e., $L/\xi \lesssim 6.5$. For longer wires, coupling of the MZM qubit to phonons has a negligible effect on the dephasing time.

5.4.3 Thermally excited quasiparticles

Yet another source of qubit dephasing is finite temperature excitations of quasiparticles in the superconductor. In contrast to the discussion in the previous section where phonons couple to the exponentially-small dipole moment $\vec{p}_{\text{top}}$, at finite temperature phonons can also lead to dephasing that is not exponentially suppressed in L/ξ. Here we consider the emission of a quasiparticle from the MZMs into the continuum by absorbing a phonon from the finite-temperature bath. Such a process would takes the qubit outside of its Hilbert space and would contribute to dephasing. The corresponding timescales $T^*_{2,\beta}$ will in general be exponential in the ratio of the topological superconducting gap to the temperature, $\beta\Delta$.

Consider first the effect of phonons in InAs. The relevant part of the electron-phonon Hamiltonian that describes excitations of a MZM γ to the continuum modes c_k (with energy $\varepsilon_k > \Delta$) is

$$H_{\text{ex,ph}} = \int \frac{d^3q}{(2\pi)^3} \sum_k m_k(-q)(c_k^\dagger + c_k)\gamma\phi_{\text{ph}}(q)\,. \tag{5.50}$$

Here $m_k(-q) = \int d^3x \psi_k^*(\mathbf{x})\psi_0(\mathbf{x})\exp(-i\mathbf{q}\mathbf{x})$ is the matrix element in terms of the (3D) wave-function of the excited quasiparticle $\psi_k(\mathbf{x})$ and MZM $\psi_0(\mathbf{x})$ respectively. From Eq. (5.39), we have $\phi_{\text{ph}}(q) = \left[Diq_j u_j(q) + eh_{14}\sum_\lambda M_\lambda(q)\epsilon_j^\lambda(q)u_j(q)\right]$. To estimate an upper bound on the excitation rate, we assume $m_k(q) = m_k \sim \sqrt{\xi/L}$. The golden rule expression for the rate of exciting a quasiparticle c_k then takes the form

$$\Gamma_{\gamma\to c_k} = |m_k|^2 \int dt e^{-i\varepsilon_k t}\langle\Phi_{\text{ph}}(t)\Phi_{\text{ph}}(0)\rangle \tag{5.51}$$

where $\Phi_{\text{ph}} = \int d^3q\phi_{\text{ph}}(q)$. One can estimate $\Gamma_{\gamma\to c_k}$ using the phonon spectral function

$S_{\text{ph}}(-\varepsilon_k \approx -\Delta)$ of Eq. (5.45) where the appropriate coupling constant is now m_k. Summing over all possible excited quasiparticles (assuming a BCS-like density of states) yields

$$T_{2,\beta}^{*-1} = \sqrt{\frac{\pi}{2\Delta\beta}} S_{\text{ph}}(-\Delta)\,. \tag{5.52}$$

Using the values of the previous section and $\Delta = 1\text{K}$, $\beta^{-1} = 50\text{mK}$ we find

$$T_{2,\beta}^{*} = \tau_0 \text{exp}\left\{\beta\Delta\right\}. \tag{5.53}$$

with $\tau_0 \sim 50\text{ns}$.

At low enough temperatures, the superconductor may not reach thermal equilibrium. In the presence of a larger-than-thermal density of non-equilibrium quasiparticles, the dominant dephasing process is due to quasiparticle relaxation into the MZMs $T_{2,\text{neq}}^{*-1} = \sum_k n_k \Gamma_{c_k \to \gamma}$ with n_k denoting the occupation of the kth quasiparticle and $\Gamma_{c_k\to\gamma} = |m_k|^2 S_{\text{ph}}(\varepsilon_k \approx \Delta)$. Using the same assumptions as above we find

$$T_{2,\text{neq}}^{*-1} = \xi n_{\text{qp}} S_{\text{ph}}(\Delta), \tag{5.54}$$

where $n_{\text{qp}} = \frac{1}{L}\sum_k n_k$ is the density of above-gap quasiparticles in the system. Since the phonon bath is in thermal equilibrium $S_{\text{ph}}(\Delta)/S_{\text{ph}}(-\Delta) = \exp(\beta\Delta)$ and we can therefore extend Eq. (5.53) the regime of non-equilibrium quasiparticles by identifying $\sqrt{\pi/(2\Delta\beta)}\exp(-\beta\Delta)$ $\to \xi n_{\text{qp}}$. Given the small size of the superconducting shell, we expect $\xi n_{\text{qp}} \ll 1$ which still leads to long dephasing times. The concentration of nonequilibrium quasiparticles is highly system dependent and in most cases can be avoided by properly shielding the superconductor from extrinsic excitations; as such we do not attempt to estimate the correction to the finite temperature dephasing times from nonequilibrium effects here.

So far we have assumed that most of the MZM wavefunction weight is in the semiconduc-

tor and thus have not considered the contribution of phonons in the superconductor. In the case when the tunneling rate between the superconductor and semiconductor is large (i.e. strong tunneling regime), transitions due to phonons in the superconductor might become important. One can estimate the corresponding rate for Aluminum using $\tau_0^{(\mathrm{Al})} \sim 100 - 500$ns [180] and the corresponding value for $\Delta^{(\mathrm{Al})}$. Since Aluminum has weak electron-phonon coupling with $\tau_0^{(\mathrm{Al})} > \tau_0$ as well as $\Delta^{(\mathrm{Al})} > \Delta$, we expect that the excitation rate is determined by the semiconductor contribution. One can estimate an upper bound for $T_{2,\beta}^{-1}$ by assuming that most of the MZM wavefunction resides in InAs. The resulting time scale $T_{2,\beta}$ is ~ 20s, see Table 5.1.

5.4.4 Discussion

Finally, we note that throughout we assumed the limit of large charging-energy protection and thus neglected extrinsic quasiparticle poisoning as a noise source. The latter could take the qubit from its ground state subspace with total fermion parity even, to an excited state subspace with total fermion parity odd. Extrinsic quasiparticle poisoning is exponentially suppressed in the ratio of charging energy to temperature, $\sim \exp\{-\beta E_C\}$, and can be ignored provided $E_C/T \gg 1$. Note that the charging energy decreases with qubit size ($E_C \sim L^{-1}$ for nearly-linear qubits), thus we need to use suitably designed qubits to justify ignoring this contribution to the dephasing.

In the above discussion we focused on a situation for which the qubits are susceptible to dephasing, but not to relaxation. If we include interwire fermion tunneling, MZMs γ_i and γ_j will in general be coupled by some hybridization energy ε_{ij} and the same noise sources

responsible for dephasing will cause the qubit to relax to its absolute ground state. The time scale of this relaxation is roughly given by $T_1 \sim (\pi\alpha_E|\varepsilon_{23} + i\varepsilon_{24}|^2/\varepsilon_{12})^{-1}$, see Section 5.7, which is longer than the dephasing time provided $\varepsilon_{12} > \varepsilon_{23}, \varepsilon_{24}$.

5.5 Other effects of charge noise on the MZM qubit system

Both $1/f$ charge noise and phonons couple to the qubit via a relative charge buildup between the semiconducting and superconducting wires forming in the topological sections of the qubit. This charge is exponentially suppressed in L/ξ, thus in the ideal limit of infinitely separated MZMs, the qubit would be immune to such noise sources. Essentially, finite-sized wires turn the MZM qubit into charge qubits, albeit with a much weaker coupling to the environment because ΔQ_{MZM} is only a small fraction of an electron charge. As such, the dephasing times predicted in Table 5.1 are orders of magnitude larger than typical nanosecond-scale dephasing times for conventional charge qubits [192, 204, 202].

In addition to setting the qubit coherence times T_1 and T_2^*, one might wonder whether $1/f$ charge noise could resolve the discrepancy between the predicted oscillatory behavior of the MZM hybridization energy ε_{hyb}, see Eq. (5.28) and Refs. [210, 76, 170, 215, 25], and either the lack of oscillations [190, 79, 65, 114] or the decay of oscillations with magnetic field [5] observed in Majorana nanowire experiments. This discrepancy has been the subject of many studies [83, 64, 177, 178], but has not yet been resolved. If Eq. (5.28) is subject to a fluctuating electric field, the argument of the cosine can be expanded as a constant plus a fluctuating piece,

$$\frac{L\mu_-}{\tilde{v}} \sim \frac{L\bar{\mu}_-}{\tilde{v}} + \left(\frac{L}{\tilde{v}}\frac{\partial\mu_-}{\partial V_g}w\right)\delta E_z, \tag{5.55}$$

where we have written the average relative Fermi energy of the topological wire as $\bar{\mu}_-$ and made the same approximation as before that $E_z w = V_g$. The second term must be of order π to wash out the cosine oscillations. For $L = 1$ μm, $\tilde{v} \sim 10^5$ m/s, $\delta E_z \sim \sqrt{10}$ V/m, and the parameter values used in Section 5.4, the second term is too small by a factor of 10^{-4}. We thus do not believe that charge noise can explain the lack of oscillations in present-day experiments.

Lastly, we note that $1/f$ charge noise will also couple to the MZM qubit when it is tuned into a measurement configuration involving the auxiliary quantum dot in Fig. 5.1. An electron hopping between the quantum dot and superconducting island forming the MZM qubit will have a corresponding dipole moment $\vec{p}_{\text{dot}} = q_{\text{dot}}\vec{d}$, which couples to $1/f$ charge noise in the same manner as does the topological dipole moment $\vec{p}_{\text{top}}$. The two-level MZM island-quantum dot system dephases on a time scale

$$\tau_2^* \sim \left(|\vec{p}_{\text{dot}}|\sqrt{\alpha_E \kappa}\right)^{-1}. \tag{5.56}$$

Furthermore, since the system-environment Hamiltonian will not be diagonal in the system's energy basis, the dot-MZM island system will relax to its ground state on a time scale set by the MZM island charging energy E_C and the parity-dependent tunneling amplitude $\tilde{t}$ between the quantum dot and MZM island:

$$\tau_1 \sim \left(\frac{4|\tilde{t}|^2}{E_C^2}|\vec{p}_{\text{dot}}|^2\frac{\pi\alpha_E}{E_C}\right)^{-1}. \tag{5.57}$$

Equations (5.56) and (8.10) are found by expanding the Hamiltonian of Eq. (5.8) in the energy basis of the tunnel-coupled MZM island, quantum dot system, and comparing to the coherence times expressions derived in Section 5.7. For $|\tilde{t}|/E_C \sim 0.1$, $E_C \sim 1$ K, and $d \sim 100$ nm, $\tau_1 \sim 5$ μs and $\tau_2^* \sim 2$ ns. Conversely to the dephasing time T_2^* of the MZM qubit, which

we want to be as long as possible, it is beneficial for τ_1 and τ_2^* to be short. The time τ_2^* quantifies how quickly the environment collapses the state during a measurement. Taking into account the measurement apparatus this time scale will be even shorter. Since the MZM parity measurement relies on the dot-MZM island system being in its ground state, τ_1 effectively sets a lower bound on the measurement time if in the initialization of the measurement the charge-excited state of the system is significantly populated.

5.6 Conclusions

In this chapter, we investigated intrinsic contributions to dephasing of charge-protected Majorana-based qubits built from topological superconducting nanowires, shown in Fig. 5.1. We calculated the hybridization energy between two MZMs in a charge-conserving formalism, demonstrating that the oscillatory behavior depends on the relative Fermi energy between the semiconductor and superconductor comprising the topological nanowire. Furthermore, we found the charge distribution resulting from the MZM overlap is a dipole moment between the line charges in the semiconductor and superconductor; the relevant length scale entering into this dipole moment is anticipated to be much smaller than the wire radius due to an accumulation layer at the semiconductor-superconductor interface. Thus, our findings indicate that experimental detection of the charge distribution due to the MZM overlap requires much greater sensitivity than was previously suggested [170, 25, 83].

By estimating the electrostatic environment to be similar to that in experiments on related devices [192, 205, 204, 84, 234], we calculated dephasing times due to $1/f$ charge noise cou-

pling to the dipole moment discussed in the previous paragraph. We reported these dephasing times in Table 5.1 for different values of MZM separation. By comparing dephasing from $1/f$ charge noise to dephasing from the dipole moment coupling to phonons and from thermally-excited quasiparticles in the superconductor, we expect that $1/f$ charge noise will be the dominant noise source for charge-protected MZM qubits. We neglected extrinsic contributions to the dephasing times, such as disorder in the superconductor, which are beyond the scope of this chapter. We also find that during a measurement of the qubits in Fig. 5.1, $1/f$ charge noise couples to a dipole moment formed between the MZM island and the auxiliary quantum dot. The coherence times associated with the combined quantum dot-MZM island system describe how quickly the environment measures the MZM parity.

Our results have important implications for future experiments on Majorana-based qubits. In particular, in order to observe Rabi oscillations in either of the qubit designs shown in Fig. 5.1, for instance by coupling MZMs γ_2 and γ_3 for a fixed amount of time, it is necessary that the energy splitting satisfies $\varepsilon_{23}T_2^* > 1$ so that multiple oscillations may be observed before the qubit dephases. For $L/\xi = 5$, our estimate of $T_2^* \sim 200$ ns suggests that ε_{23} must be greater than 5 MHz.

5.7 Master equation derivation

In this appendix, we derive explicit expressions for the pure dephasing time T_2^* and the relaxation time T_1. We begin by assuming that a system, with density matrix $\rho(t)$ has a weak interaction with the environment so that the Hamiltonian $H_{SE} = \frac{\sigma}{2} \otimes \Phi$ can be treated pertur-

batively. We further assume the environment is in thermal equilibrium, described by density matrix ρ_E. The interaction picture Heisenberg equation to second order in H_{SE} is

$$\dot{\rho}^I(t) = -\int_0^t dt' \mathrm{Tr}_E \left(\left[H_{SE}(t), \left[H_{SE}(t'), \rho^I(t') \otimes \rho_E \right] \right] \right). \tag{5.58}$$

We can expand the double commutator and trace over the environmental degrees of freedom, yielding

$$\begin{aligned} -\dot{\rho}^I(t) = \frac{1}{4}\int_0^t dt' \Big\{ & \langle \Phi(t)\Phi(t') \rangle \left(\sigma(t)\sigma(t')\rho^I(t') - \sigma(t')\rho^I(t')\sigma(t) \right) \\ & + \langle \Phi(t')\Phi(t) \rangle \left(\rho^I(t')\sigma(t')\sigma(t) - \sigma(t)\rho^I(t')\sigma(t') \right) \Big\}. \end{aligned} \tag{5.59}$$

We have written $\langle \Phi(t)\Phi(t') \rangle = \mathrm{tr}_E \{ \Phi(t)\Phi(t')\rho_E \}$. Provided the correlation time of the environment is short, we can approximate $\rho^I(t') \approx \rho^I(t)$, and extend the lower limit of integration to $-\infty$:

$$\begin{aligned} \dot{\rho}^I(t) = \frac{1}{4}\int_{-\infty}^t dt' \Big\{ & \langle \Phi(t)\Phi(t') \rangle \left(\sigma(t)\sigma(t')\rho^I(t) - \sigma(t')\rho^I(t)\sigma(t) \right) \\ & + \langle \Phi(t')\Phi(t) \rangle \left(\rho^I(t)\sigma(t')\sigma(t) - \sigma(t)\rho^I(t)\sigma(t') \right) \Big\}. \end{aligned} \tag{5.60}$$

Finally, we change variables so that $t' \to t - t'$ and rewrite our equation in the Schrödinger picture. Denote the energy basis of the system Hamiltonian by $\{|m\rangle\}$ such that $H_S|m\rangle =$

$\varepsilon_m|m\rangle$. Inserting resolutions of identity and writing $\Delta_{mn} \equiv \varepsilon_m - \varepsilon_n$ we have

$$\begin{aligned}
&\dot{\rho}_{sr}(t) + i\,(E_s - E_r)\rho_{sr}(t) \\
&= -\frac{1}{4}\sum_{mn}\int_0^\infty dt' \Big(\langle \Phi(t')\Phi(0)\rangle \left[e^{-i\Delta_{mn}t'}\sigma_{sm}\sigma_{mn}\rho_{nr}(t) - e^{-i\Delta_{sm}t'}\sigma_{sm}\rho_{mn}(t)\sigma_{nr} \right] \\
&\qquad\qquad + \langle \Phi(0)\Phi(t')\rangle \left[e^{-i\Delta_{mn}t'}\rho_{sm}(t)\sigma_{mn}\sigma_{nr} - e^{-i\Delta_{nr}t'}\sigma_{sm}\rho_{mn}(t)\sigma_{nr} \right] \Big).
\end{aligned} \tag{5.61}$$

The master equation given in Eq. (5.61) is generally hard to solve. We focus on the special case for which we can expand σ in terms of Pauli matrices, $\sigma = \sum_j a_j \sigma^j$ with $a_z \gg |a_x + i a_y|$. When considering the pure dephasing time, we restore the original upper limit of integration to t rather than $+\infty$. Then, we can approximate the equation for the off-diagonal density matrix elements as

$$\dot{\rho}_{01}(t) - i\Delta_{10}\rho_{01}(t) = -\rho_{01}(t)\frac{a_z^2}{2}\int_0^t dt' \left(\langle \Phi(t')\Phi(0)\rangle + \langle \Phi(0)\Phi(t')\rangle \right). \tag{5.62}$$

We are generally interested in understanding how the magnitude of the off-diagonal elements decay, given by

$$\frac{d}{dt}|\rho_{01}(t)| = \frac{d}{dt}\sqrt{\rho_{01}(t)\rho_{10}(t)} = -|\rho_{01}(t)|\frac{a_z^2}{2}\int_0^t dt' \left(\langle \Phi(t')\Phi(0)\rangle + \langle \Phi(0)\Phi(t')\rangle \right). \tag{5.63}$$

We define the spectral function by Eq. (5.4), which may be equivalently written as

$$\langle \Phi(t)\Phi(0)\rangle + \langle \Phi(0)\Phi(t)\rangle = 4\int_0^\infty d\omega \cos(\omega t) S_\Phi(\omega). \tag{5.64}$$

Then, our expression for the off-diagonal density matrix elements becomes

$$\frac{d}{dt}|\rho_{01}(t)| = -|\rho_{01}(t)|2a_z^2\int_0^\infty d\omega\frac{\sin(\omega t)}{\omega}S_\Phi(\omega). \tag{5.65}$$

Integrating both sides results in Eqs. (5.2) and (5.3).

The pure dephasing time is defined by $B^2(T_2^*) = 1$. In the case of $1/f$ charge noise,

$$1 = a_z^2\alpha_E\int_{2\pi/T_2^*}^\infty d\omega\frac{\sin^2(\omega T_2^*/2)}{\omega(\omega/2)^2} = \left(T_2^*\right)^2 a_z^2\alpha_E\kappa, \tag{5.66}$$

where $\kappa = 1 - \cos(1) + \sin(1) - \text{Ci}(1) \approx 0.96$.

The relaxation time is the time scale on which the diagonal density matrix element $\rho_{11}(t)$ decays. If we assume $T_1 \gg T_2^*$, then we can consider Eq. (5.61) on time scales for which the off-diagonal density matrix elements are negligible:

$$\begin{aligned}\dot{\rho}_{11}(t) = &-\rho_{11}(t)\frac{|a_x+ia_y|^2}{4}\int_0^\infty dt'\left(\langle\Phi(t')\Phi(0)\rangle e^{-i\Delta_{01}t'} + \langle\Phi(0)\Phi(t')\rangle e^{-i\Delta_{10}t'}\right)\\ &+\rho_{00}(t)\frac{|a_x+ia_y|^2}{4}\int_0^\infty dt'\left(\langle\Phi(t')\Phi(0)\rangle e^{-i\Delta_{10}t'} + \langle\Phi(0)\Phi(t')\rangle e^{-i\Delta_{01}t'}\right).\end{aligned} \tag{5.67}$$

Noting that $\rho_{00}(t) = 1 - \rho_{11}(t)$, we can rewrite the above as

$$\begin{aligned}\dot{\rho}_{11}(t) = &-\rho_{11}(t)\frac{|a_x+ia_y|^2}{4}\int_0^\infty dt' 2\cos\left(\Delta_{10}t'\right)\left(\langle\Phi(t')\Phi(0)\rangle + \langle\Phi(0)\Phi(t')\rangle\right)\\ &+\frac{|a_x+ia_y|^2}{4}\int_0^\infty dt'\left(\langle\Phi(t')\Phi(0)\rangle e^{-i\Delta_{10}t'} + \langle\Phi(0)\Phi(t')\rangle e^{-i\Delta_{01}t'}\right).\end{aligned} \tag{5.68}$$

The last line just provides a constant term. Plugging the spectral function into the first line, we find that the diagonal density matrix element decays as

$$\rho_{11}(t) = \rho_{11}(0)\text{exp}\left(-\pi|a_x+ia_y|^2 S_\Phi(\Delta_{10})t\right). \tag{5.69}$$

Defining the relaxation time to be the value of t for which the argument of the exponent equals

-1, we have

$$(T_1)^{-1} = \pi |a_x + i a_y|^2 S_\Phi (\Delta_{10}) . \tag{5.70}$$

Chapter 6

Modeling noise and error correction for Majorana-based quantum computing

I am perfectly convinced by it that Mr. Darcy has no defect. He owns it himself without disguise.

-Jane Austen, *Pride and Prejudice*

Majorana-based quantum computing seeks to use the non-local nature of Majorana zero modes to store and manipulate quantum information in a topologically protected way. While noise is anticipated to be significantly suppressed in such systems, finite temperature and system size result in residual errors. In this work, we connect the underlying physical error processes in Majorana-based systems to the noise models used in a fault tolerance analysis. Standard qubit-based noise models built from Pauli operators do not capture leading order noise

processes arising from quasiparticle poisoning events, thus it is not obvious *a priori* that such noise models can be usefully applied to a Majorana-based system. We develop stochastic Majorana noise models that are generalizations of the standard qubit-based models and connect the error probabilities defining these models to parameters of the physical system. Using these models, we compute pseudo-thresholds for the $d = 5$ Bacon-Shor subsystem code. Our results emphasize the importance of correlated errors induced in multi-qubit measurements. Moreover, we find that for sufficiently fast quasiparticle relaxation the errors are well described by Pauli operators. This work bridges the divide between physical errors in Majorana-based quantum computing architectures and the significance of these errors in a quantum error correcting code.

The results presented here were previously published in "Modeling Noise and Error Correction for Majorana-based Quantum Computing" by Christina Knapp, Michael Beverland, Dmitry I. Pikulin, and Torsten Karzig, Quantum 2, 88 (2018).

6.1 Introduction

As we have explored through the previous chapters of this thesis, topological phases of matter provide an attractive approach for fault-tolerant quantum computation and Majorana zero modes (MZMs) are at present the most promising platform. The motivation for using these exotic topological defects to encode a qubit state is that information can be stored non-locally such that it is protected from a noisy local environment. However, physical realities such as finite temperatures, energy gaps, and system sizes mean that a topological qubit will still be

exposed to errors, just at a significantly reduced error rate.

In addition to lower error rates, Majorana-based qubits are distinct from more conventional qubits in that phase and bit-flip errors arise from the same physical processes. To understand this point, recall that quantum information is encoded in the joint parity of a pair of MZMs. Application of one of the corresponding Majorana operators to the qubit state flips the fermion parity. When using a modular approach with four MZMs per qubit, such as the charging-energy protected qubits presented in Chapter 4 and discussed in Chapter 5, there is a basis choice in how to encode the qubit state. That is, we could pair γ_1 with γ_2 and γ_3 with γ_4, but an equally valid choice would be γ_1 with γ_3 and γ_2 with γ_4. Therefore, unlike other qubit schemes, phase errors and bit-flip errors result from the same physical processes (e.g., for one encoding choice, $\gamma_1\gamma_3$ flips the qubit state, while for the other it results in a phase error). Physically, errors described by Majorana operators are due to, for instance, thermally excited quasiparticles, finite hybridization of MZMs, or external quasiparticle poisoning of the island. In the absence of non-equilibrium noise sources, these errors will generally be exponentially suppressed in ratios involving the physical parameters of the system that are expected to be large, but cannot be made arbitrarily small for practical reasons [108, 51, 216, 186, 128, 203, 131, 151].

The small error rates discussed above set an upper bound on the qubit lifetime. In order to store information for a longer time, it is necessary to perform quantum error correction on the system. For a given quantum error correcting code, if the error rate is below a particular value, known as the code's pseudo-threshold, the qubit's lifetime is increased. Studying the effectiveness of quantum error correcting codes for Majorana-based systems is

a relatively recent and important development in the field of topological quantum computation [48, 246, 50, 256, 168, 254, 158, 207, 167, 175, 174, 122, 255, 176]. Thus far, the majority of studies (with the exceptions of Refs. [48, 50, 122, 255]) have assumed qubit-based noise models, which approximate noise in the system by Pauli errors and measurement bit-flips. For a MZM system, errors are naturally modeled by products of Majorana operators. Some of the most important types of errors (*e.g.*, quasiparticle poisoning [108, 51, 216]) involve an odd number of Majorana operators, which take the system out of the computational subspace and are therefore not described by Pauli operators. Thus, unless the effect of these errors can be captured with measurement bit-flips, the noise affecting a MZM system is outside the scope of a qubit-based noise model.

The purpose of this chapter is to connect the underlying physical error processes in a Majorana-based quantum computing architecture to a noise model that can be used to analyze fault tolerance of the system. To this end, we develop stochastic Majorana noise models from physical considerations of the tetron, proposed in Chapter 4 and analyzed in Chapter 5, and discuss the parameters that control the probabilities of applying different products of Majorana operators and the probability of measurement bit-flips. These noise models reduce to qubit-based noise models when the probabilities of an odd number of Majorana operators being applied is set to zero. By analyzing these noise models for a small Bacon-Shor subsystem code [12, 156, 235], we find that correlated errors induced through multi-qubit measurements are most problematic for fault tolerance, and therefore, would be most important to minimize in a Majorana-based quantum computing architecture. We find that for charging-energy-protected

MZM qubits [208, 141], the pseudo-threshold values calculated with a Majorana noise model are well approximated by a qubit-based noise model for finite, but sufficiently small, odd-Majorana error probabilities. More generally, our work provides and exemplifies a framework for analyzing Majorana-based error correction that can be extended to other physical MZM architectures.

6.2 Stochastic Majorana noise models

In this section, we develop stochastic Majorana noise models analogous to the standard qubit-based noise models. There are several motivations for tailoring a noise model to a system of MZMs. (1) In general, the physical sources of errors are best understood in terms of interactions of the environment with the MZMs; a Majorana noise model is therefore more transparently connected to the physical system, affords a more precise description of the noise that can lead to more realistic quantum error correction simulations, and can be applied independently of the encoding of quantum information. (2) Majorana-based quantum computing architectures do not necessarily group MZMs into qubits; as such, noise models that describe environmental effects as qubit errors are not applicable to all MZM systems. For instance, a Majorana fermion code [48, 122, 255] could not be fully analyzed with a qubit noise model. (3) Even when MZMs are arranged into qubits, some of the most common types of errors take the system out of the computational subspace (*e.g.*, quasiparticle poisoning [108, 51, 216]), and are therefore not captured by the probabilistic application of Pauli errors.

Throughout this paper, we consider a set of $2n$ Majorana zero modes (MZMs), with corre-

sponding operators $\gamma_1, \gamma_2, \ldots \gamma_{2n}$. Noise models discretize time into *time steps*. In a stochastic Majorana noise model, after a time step τ, a probabilistically generated string of Majorana operators, $\gamma_1^{a_1} \ldots \gamma_{2n}^{a_{2n}}$, for $\vec{a} \in \{0,1\}^{2n}$, is applied to the state ρ_{M} of the MZM subsystem. Additionally, the noise models allow for measurement errors that modify the binary vector $\vec{m} = (m_1, \ldots, m_N)$ of the time step's N measurement outcomes by bitwise addition of the probabilistically generated vector $\vec{b} = (b_1, \ldots, b_N)$, for $\vec{m}, \vec{b} \in \{0,1\}^N$. The noise model only tracks operators applied to either the MZM subsystem or the measurement outcomes. Considering operators acting on the full system (*i.e.*, MZM subsystem and its environment) enables us to identify which operators to include in the noise model.

More explicitly, when the full system (MZMs plus environment) begins in a product state $\rho_{\mathrm{M}} \otimes |e_0\rangle\langle e_0|$, the time-evolved projected density matrix can be written as [198]

$$\sum_j \langle e_j | U \left[\rho_{\mathrm{M}} \otimes |e_0\rangle\langle e_0| \right] U^\dagger | e_j \rangle = \sum_j \varepsilon_j \rho_{\mathrm{M}} \varepsilon_j^\dagger, \tag{6.1}$$

where U denotes the unitary evolution and $\varepsilon_j \equiv \langle e_j | U | e_0 \rangle$ is the projection of the environmental noise processes onto the MZM subsystem. The operator ε_j is therefore some combination of Majorana operators:

$$\varepsilon_j = \sum_{\vec{a}} O_{\vec{a}}^j = \sum_{\vec{a}} o^j_{a_1 \ldots a_{2n}} (\gamma_1)^{a_1} \ldots (\gamma_{2n})^{a_{2n}}. \tag{6.2}$$

Instead of considering the density matrix ρ_{M}, Eq. (6.1) can equivalently be seen as a quantum

trajectory where during the time step the pure state $|\psi\rangle_{\mathrm{M}}$ transforms as

$$|\psi\rangle_{\mathrm{M}} \xrightarrow{\tau} \sum_{\vec{a}} O_{\vec{a}}^{j} |\psi\rangle_{\mathrm{M}} \tag{6.3}$$

with some probability P_j. Noise described by Eq. (6.3) depends on the 2^n coefficients $o^l_{a_1 \ldots a_{2n}}$, which renders numerical simulations of large systems intractable.

Fortunately, Eq. (6.3) can be greatly simplified by noting that decoherence processes such as energy relaxation and phonons will destroy the coherence between different products of Majorana operators. In other words, local noise processes do not result in superpositions of products of Majorana operators (as opposed to non-local operations on the computational state that allow coherent superpositions of Majorana operators to be maintained over long time periods). Moreover, error correction itself separates many of the linear combinations in Eq. (6.3) [198]. Given these considerations, we can replace the intractable model of Eq. (6.3) with a simpler, stochastic Majorana noise model. Then each time step gives:

$$|\psi\rangle_{\mathrm{M}} \xrightarrow{\tau} (\gamma_1)^{a_1} \ldots (\gamma_{2n})^{a_{2n}} |\psi\rangle_{\mathrm{M}} \tag{6.4}$$

$$\vec{m} \xrightarrow{\tau} \vec{m} \oplus \vec{b}, \tag{6.5}$$

with some probability $\Pr(\vec{a}, \vec{b})$. The order of Majorana operators in Eq. (6.4) is unimportant as it only contributes to the overall phase of the error operator.

The noise described by Eq. (6.4) is unitary, and thus does not include an amplitude damping channel or an erasure channel. This is not necessarily a crucial limitation since a pessimistic

estimate can be obtained by sufficiently strong noise that randomly flips the qubits. This is the standard approach for the qubit-based noise models reviewed in the next section. As a consequence, however, the latter fails to take into account the relaxation time T_1 characterizing the timescale during which the system relaxes to the lower-energy qubit state. In a MZM system, there is no such time scale, since in practice the temperature is larger than the degeneracy splitting of the qubit states. Thus, the assumption that noise has unit amplitude provides a more accurate description of the physical noise processes for Majorana-based qubits.

The content of different stochastic models is contained entirely in the probability distribution $\{\Pr(\vec{a}, \vec{b})\}$. Given this distribution, the errors in the system propagate classically and can be efficiently simulated using standard Monte Carlo techniques by tracking the net Majorana operators applied at any given time. For this reason, when a model of the type given in Eqs. (6.4) and (6.5) mimics the actual noise in a physical system, it is extremely useful for studying quantum error correction.

In the following, a *noise event* refers to the application of one of the operations of the right hand side of Eqs. (6.4) or (6.5). For simplicity of relating the probabilities defining our noise models to physical processes, we include noise events that apply the same Majorana operator twice (therefore not causing an error). The following presentation of the noise models is tailored for conceptual ease; in Section 6.4 we give a more explicit description of how one can simulate these noise models.

6.2.1 Qubit-based stochastic noise models

We first review three well-known qubit-based stochastic noise models, all of which are built from Pauli operators and measurement bit-flips. In each case, we consider a scenario consisting of a sequence of time steps, where a set of single- and multi-qubit measurements and/or gates are applied in each step.

Throughout the paper, the error probabilities of the Pauli noise models are slightly reweighted compared to their standard presentation by also including the identity operator as a possible error. This allows for an easier comparison with Majorana noise models where noise events can lead to the application of $\gamma_a^2 = 1$.

Pauli noise (or *code capacity noise*). For a given time step and for each qubit:

1. Apply one single-qubit operator (either 1, X, Y, or Z, chosen uniformly) with probability p; otherwise do nothing.

2. Apply all measurement projectors perfectly.

More explicitly, Pauli operators X, Y, or Z are applied with probability $p/4$ and identity is applied with probability $1 - 3p/4$. As noted above, the non-standard normalization is chosen for ease of comparison with the Majorana noise models introduced in the following section. For the remaining noise models, we will not explicitly write "otherwise do nothing."

Pauli noise is defined by the single parameter p. While the model is too simple to provide realistic estimates of an error-correcting code's performance, it serves as a quick first test of

any code.

Pauli noise with bit-flip measurement (or *phenomenological noise*). For a given time step, for each qubit apply step 1 of Pauli noise, then:

2. Apply all measurement projectors perfectly, then flip each measurement outcome with probability p_{mst}.

Note that flipping the measurement outcome does not change the state of the system, only our information about the system.

Pauli noise with bit-flip measurement is defined by two parameters, $\{p, p_{\text{mst}}\}$, which may be taken to be equal, $p = p_{\text{mst}}$, for a simple estimate of a code's pseudo-threshold. We emphasize that the measurement projections are still applied exactly, but the classical bit which stores the measurement outcome can be flipped. This model is motivated on the grounds that qualitatively different error correction approaches are required to handle faulty measurements in addition to errors on the encoded information alone, making this minimal addition to Pauli noise useful for discriminating between codes.

Pauli circuit noise (or *circuit-level noise*) extends the previous two models to account for the different noise processes affecting a qubit during an operation (unitary gate or measurement). For a given time step, each qubit is involved in a k-qubit operation, where $k = 0$ for an idle qubit. For all sets of qubits involved in the same k-qubit operation:

1. Do the following:

(a) For each qubit in the set, apply one single-qubit operator (either 1, X, Y, or Z, chosen uniformly) with probability $p^{(k)}$.

(b) Apply a k-qubit Pauli operator with probability $p_{\text{cor}}^{(k)}$. For $k = 2$, this is any element of the set of 16 operators $\{Z \otimes X, 1 \otimes Y, \dots\}$. For $j \leq 1$, $p_{\text{cor}}^{(j)} = 0$.

2. Apply the measurement projector perfectly, then flip the k-qubit measurement outcome with probability $p_{\text{mst}}^{(k)}$. For an idle qubit, do nothing.

For step 1a, X, Y, or Z are applied with probability $p^{(k)}/4$ and identity is applied with probability $1 - 3p^{(k)}/4$. For step 1b, any given non-trivial Pauli operator is applied with probability $p_{\text{cor}}^{(k)}/16$ and identity is applied with probability $1 - 15p_{\text{cor}}^{(k)}/16$. Again, the non-standard normalization is chosen to simplify comparison with the Majorana noise models in the following section.

Pauli circuit noise is defined by the set of probabilities $\{p^{(0)}, p^{(k)}, p_{\text{cor}}^{(2)}, p_{\text{mst}}^{(k)}\}$ for $k \in \{1, 2\}$. It is for this noise model (slightly renormalized [1]) with the probability of a single-qubit, two-qubit, and measurement bit-flip error equally likely, that the well-known result is found that the qubit surface code has an error threshold value of $p_{\text{th}} \approx 1\%$ [217, 261]. This means that a quantum state can be reliably stored in an (arbitrarily large) surface code for an indefinite period of time for qubits subjected to circuit-level noise with $p < p_{\text{th}}$.

[1] Note that because of the renormalization of probabilities to include the identity operation, this result is found for $p = p_{\text{mst}}^{(k)} = 3/4p^{(0)} = 3/4p^{(1)} = 15/16p_{\text{cor}}^{(2)}$.

6.2.2 Stochastic Majorana noise models

We now present four stochastic Majorana noise models in order of increasing complexity. The first three are analogous to the qubit-based models reviewed above. The fourth is motivated by a particular physical implementation and measurement protocol of a Majorana-based quantum computing architecture [208, 141].

Naively, the simplest stochastic Majorana noise model to consider would simply apply the Majorana operator γ_i with probability p for each $i \in \{1, 2, \ldots, 2n\}$ in each time step, followed by perfect measurements. However, such a model would on average spend an equal amount of time in an even total MZM parity state as in an odd total MZM parity state. In the case of superconducting islands with charging energy, *e.g.*, for the system described in Section 6.3.1, the energy separation of these states is large (on the order of the superconducting gap or the charging energy of the island) and thus physically we would expect the system to spend much more time in the lower-energy state corresponding to a specific MZM parity. To more accurately describe this situation, we go beyond the naive model and introduce the concept of MZM islands.

We assume that the MZMs are naturally split into n/m subsets, each of which contains $2m$ MZMs belonging to the same superconducting island (see Fig. 6.1). We assume that the initial $2m$-MZM parity on each island is even so that, for a given time step, an island has *even parity* if an even number of Majorana operators have been applied in its history, and has *odd parity* otherwise. By keeping track of the parity of the islands, the probability of applying an odd number of Majorana operators can be adjusted depending on whether this would relax the

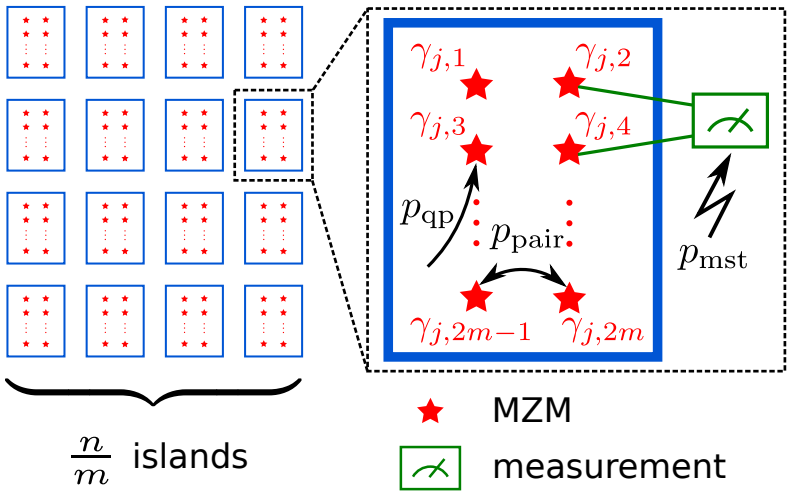

Figure 6.1: Schematic of a quantum computing architecture with $2n$ MZMs (red stars) equally divided among n/m islands (blue boxes). The inset zooms in on the jth island. As an example, we indicate a two-MZM measurement and the possible noise events for the Majorana noise model QpBf when the island begins a time step in the even parity state.

system back to the ground state or lead to an excited state. This is captured by an additional step 0 in Majorana noise models that is not required for the qubit ones.

Each noise model contains up to four types of noise events:

- *Quasiparticle* event: application of a single Majorana operator: $|\psi\rangle_{\text{M}} \to \gamma_{j,a}|\psi\rangle_{\text{M}}$.
- *Pair-wise dephasing* event: application of a pair of Majorana operators belonging to the same island: $|\psi\rangle_{\text{M}} \to \gamma_{j,a}\gamma_{j,b}|\psi\rangle_{\text{M}}$.
- *Correlated* event: application of Majorana operators from multiple islands involved in the same measurement (see later discussion or Table 6.1 for examples).
- *Measurement bit-flip*: flipping of the classical bit storing the outcome of a $2k$-MZM parity measurement: *e.g.*, $\vec{m} \to \vec{m} \oplus (0, 1, 0, \ldots, 0)$.

The naming of the noise events will become clear in Section 6.3 when we describe the phys-

ical processes contributing to each error-type. To simplify combinatorial prefactors, we allow the same Majorana operator to be used multiple times in a given noise event (*e.g.*, pair-wise dephasing includes the identity operator γ_a^2). We also keep track of ordering, so that applying the pairs $\gamma_a\gamma_b$ and $\gamma_b\gamma_a$ are considered different noise events (multiple noise events contribute to the same type of error). Unless otherwise noted, we assume that the Majorana operators corresponding to a given noise event are chosen uniformly over all MZMs on the island.

We note that even if subsets of MZMs are combined into physical qubits, errors involving an odd number of Majorana operators on any given island cannot be described by Pauli operators, motivating the consideration of stochastic Majorana noise models.

Quasiparticle noise (Qp). In a given time step, implement the following sequence for each island:

0. If the island begins the time step with odd parity, apply a quasiparticle event with probability p_{odd}.

1. Apply one single-island noise event: either a quasiparticle event with probability p_{qp} or a pair-wise dephasing event with probability p_{pair}.

2. Apply all measurement projectors perfectly.

We count $2m \times 2m$ different pairs of Majorana operators per island. In step 1, the operator $\gamma_{j,a}$ is applied with probability $p_{\text{qp}}/2m$, the operator $\gamma_{j,a}\gamma_{j,b}$ ($a \neq b$) is applied with probability $p_{\text{pair}}/(2m)^2$, and identity is applied with probability $1 - p_{\text{qp}} - 3p_{\text{pair}}/4$ (because of pair-wise dephasing events with $\gamma_{j,a}^2 = 1$).

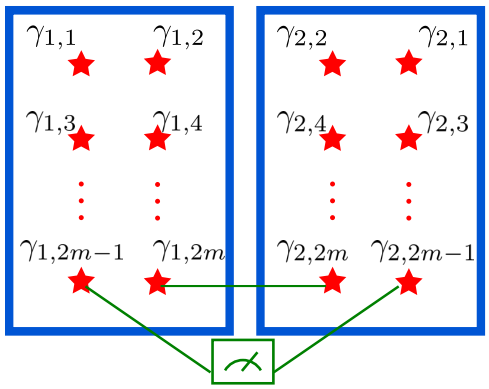

Event	Operator	Qp	QpBf	MC	PMC
qp	$\gamma_{1,1}$	$p_{\text{qp}}/(2m)$	$p_{\text{qp}}/(2m)$	$p^{(2)}_{\text{qp}}/(2m)$	$p^{(0)}_{\text{qp}}/(2m)$
	$\gamma_{1,2m}$	$p_{\text{qp}}/(2m)$	$p_{\text{qp}}/(2m)$	$p^{(2)}_{\text{qp}}/(2m)$	$p^{(2)}_{\text{qp}}/(2m)$
pair	$\gamma_{1,1}\gamma_{1,2}$	$p_{\text{pair}}/(2m)^2$	$p_{\text{pair}}/(2m)^2$	$p^{(2)}_{\text{pair}}/(2m)^2$	$p^{(0)}_{\text{pair}}/(2m)^2$
	$\gamma_{1,1}\gamma_{1,2m}$	$p_{\text{pair}}/(2m)^2$	$p_{\text{pair}}/(2m)^2$	$p^{(2)}_{\text{pair}}/(2m)^2$	$p^{(2)}_{\text{pair}}/(2m)^2$
cor	$\gamma_{1,1}\gamma_{1,2m}\gamma_{2,2m}$	$p_{\text{pair}}p_{\text{qp}}/(2m)^3$	$p_{\text{pair}}p_{\text{qp}}/(2m)^3$	$p_{\text{cor,odd}}/N_{\text{odd}}$	$p^{(2)}_{\text{cor,odd}}/(8m)$
	$\gamma_{1,1}\gamma_{1,2m}\gamma_{2,2m}\gamma_{2,2}$	$p^2_{\text{pair}}/(2m)^4$	$p^2_{\text{pair}}/(2m)^4$	$p_{\text{cor,even}}/N_{\text{even}}$	$p^{(2)}_{\text{cor,even}}/(16m^2)$
mst	$b^{(2)}$	N/A	p_{mst}	$p^{(2)}_{\text{mst}}$	$p^{(2)}_{\text{mst}}$

Table 6.1: *Top*: MZMs (red stars) are grouped into sets of $2m$ on an island (blue box). The operator of ath MZM on the jth island is $\gamma_{j,a}$. For the time step considered here, the two islands are involved in a four-MZM measurement. *Bottom*: Example noise event probabilities when both islands begin the time step with even parity. The table could equivalently be understood as noise event probabilities after the initial step 0 of each noise model accounting for the asymmetry between even and odd parity islands. The left-most column labels the error type, with the abbreviations meaning quasiparticle, pair-wise dephasing, correlated, and measurement bit-flip, respectively. The operators for correlated noise events for models MC and PMC could be applied from two independent single-island noise events, analogously to models Qp and QpBf, or from a single correlated event; for simplicity we only write the probability of the latter. The parameters $N_{\text{even}} = ((2m)^2(2m+1)^{m-2})^2$ and $N_{\text{odd}} = N_{\text{even}}/2m$ in the fifth column are defined to be the number of different odd correlated events and even correlated events, respectively, in the model MC. Note that in model PMC, correlated events must involve a pair of MZMs connected by the measurement, which reduces the combinatorial factors in the denominators. For instance, an odd correlated event has $4m$ possibilities for the initial excitation ($\gamma_{1,1}$ in the table) and only two choices for the pair of MZMs that transfers the excitation to the second island ($\gamma_{1,2m}\gamma_{2,2m}$ in the table).

The set of probabilities $\{p_{\text{odd}}, p_{\text{qp}}, p_{\text{pair}}\}$ defines this model. In an encoding where four MZMs define a physical qubit, Qp reduces to the qubit-based model *Pauli noise* when $p_{\text{qp}} = 0$ (with $p \to p_{\text{pair}}$).

As mentioned above, step 0 accounts for the energy difference between an island with odd parity and even parity: when $p_{\text{qp}} \ll p_{\text{odd}}$, each island in the system spends on average very little time in the odd MZM parity state. We will return to this discussion in Section 6.3.1.

Quasiparticle noise and bit-flip measurement (QpBf). In a given time step, implement steps 0 and 1 from model (Qp) for each island, then:

2. Apply all measurement projectors perfectly, then independently flip each classical bit storing a measurement outcome with probability p_{mst}.

This model is defined by the set of probabilities $\{p_{\text{odd}}, p_{\text{qp}}, p_{\text{pair}}, p_{\text{mst}}\}$. In an encoding where four MZMs define a physical qubit, when $p_{\text{qp}} = 0$, QpBf reduces to the qubit-based model Pauli noise and bit-flip measurement (with $p \to p_{\text{pair}}$ and the same p_{mst}). Example noise events and their corresponding probabilities are schematically depicted in Fig. 6.1 and listed in Table 6.1 for an island beginning a time step in the even parity state.

Correlated events. Models Qp and QpBf do not distinguish the probabilities of noise events involving MZMs on idle islands from those on measured islands. We would now like to account for these differences. Define $\gamma_{j,a}$ to be the operator corresponding to the ath MZM on the jth island. We consider two types of correlated events possible in a multiple-island measurement:

- *Odd correlated event*: application of a string of three or more Majorana operators involving at least two islands, such that an odd number (up to $m-1$) of Majorana operators are applied to one of the islands involved in a k-island measurement. There is an even number (up to m) of Majorana operators applied to the remaining $k-1$ islands involved in the measurement. For example, an odd correlated event in a two-island measurement of islands i and j results in $|\psi\rangle_{\mathrm{M}} \to \gamma_{i,a}\gamma_{j,b}\gamma_{j,c}|\psi\rangle_{\mathrm{M}}$.

- *Even correlated event*: application of a string of four or more Majorana operators involving at least two islands, such that an even number (up to m) of Majorana operators are applied to all the islands involved in the k-island measurement. For example, an even correlated event in a two-island measurement of islands i and j results in $|\psi\rangle_{\mathrm{M}} \to \gamma_{i,a}\gamma_{i,b}\gamma_{j,c}\gamma_{j,d}|\psi\rangle_{\mathrm{M}}$.

In the following, we assume that during a time step each island is either idle or involved in a single measurement. The spread of correlated events can be mitigated by restricting the number of islands involved in a measurement. For instance, for the Bacon-Shor code studied in Section 6.4, correlated events only involve nearest neighbor islands.

Majorana circuit noise (MC). In a given time step, for a set of islands involved in the same k-island measurement ($k=0$ for an idle island), implement the following sequence:

0. For each island that begins the time step with odd parity, apply a quasiparticle event with probability $p_{\mathrm{odd}}^{(k)}$.

1. For the set of islands involved in the same k-island measurement, do the following:

(a) For each island in the set, apply one single-island noise event: either a quasiparticle event with probability $p_{\text{qp}}^{(k)}$ or a pair-wise dephasing event with probability $p_{\text{pair}}^{(k)}$.

(b) Apply a correlated event to the set: either an odd correlated event with probability $p_{\text{cor,odd}}^{(k)}$ or an even correlated event with probability $p_{\text{cor,even}}^{(k)}$. For $j \leq 1$, $p_{\text{cor,odd}}^{(j)} = p_{\text{cor,even}}^{(j)} = 0$.

2. Apply the measurement projector perfectly, then flip the classical bit storing the measurement outcome with probability $p_{\text{mst}}^{(k)}$. For an idle island, do nothing.

MC is defined by the probability set $\{p_{\text{odd}}^{(k)}, p_{\text{qp}}^{(k)}, p_{\text{pair}}^{(k)}, p_{\text{mst}}^{(k)}, p_{\text{cor,odd}}^{(k)}, p_{\text{cor,even}}^{(k)}\}$ for $k \leq k_{\text{max}}$, where k_{max} is the maximum number of islands involved in a measurement. MC has the same action on an idle island ($k = 0$) as Qp, with the probability set $\{p_{\text{odd}}, p_{\text{qp}}, p_{\text{pair}}\} \to \{p_{\text{odd}}^{(0)}, p_{\text{qp}}^{(0)}, p_{\text{pair}}^{(0)}\}$. MC has the same action on an island involved in a single-island measurement ($k = 1$) as QpBf, with the probability set $\{p_{\text{odd}}, p_{\text{qp}}, p_{\text{pair}}, p_{\text{mst}}\} \to \{p_{\text{odd}}^{(1)}, p_{\text{qp}}^{(1)}, p_{\text{pair}}^{(1)}, p_{\text{mst}}^{(1)}\}$. In an encoding where four MZMs define a physical qubit and if the probability of any error involving an odd number of Majorana operators on a given island is set to zero (*i.e.*, $p_{\text{qp}}^{(k)} = p_{\text{cor,odd}}^{(k)} = 0$), MC reduces to the qubit-based model Pauli circuit noise, with the probabilities related by $\{p^{(k)}, p_{\text{cor}}^{(2)}, p_{\text{mst}}^{(k)}\} \to \{p_{\text{pair}}^{(k)}, p_{\text{cor,even}}^{(2)}, p_{\text{mst}}^{(k)}\}$.

In Table 6.1, we compare the probabilities of noise events in step 1 of models Qp, QpBf, and MC. We see that MC allows for the possibility that noise events affecting multiple islands connected by a measurement happen with greater probability than independent noise events on the islands (*e.g.*, when $p_{\text{cor,even}}^{(2)} > p_{\text{pair}}^2$).

Physical Majorana circuit noise (PMC). This model refines MC by considering a specific physical implementation and measurement protocol of the MZM system [208, 141]. Focusing on a specific measurement protocol allows us to drop many of the correlated events included in MC, as well as to separate noise events involving measured MZMs from those only involving unmeasured MZMs. These two modifications enable a more accurate description of this physical system, see Section 6.3.1 for a description of the underlying causes of errors in such a system.

We assume that our measurement protocol allows parity measurements of two MZMs belonging to the same island and joint parity measurements of a set of four MZMs on two islands. During a given time step, each island is now either idle ($k = 0$), involved in a two-MZM measurement ($k = 1$), or involved in a four-MZM measurement ($k = 2$).

The model follows the same steps as MC, with slight modifications of steps 0 and 1(a) for islands that are involved in a measurement, to account for whether particular MZMs are connected to the measurement apparatus or not:

0. For each island that begins the time step with odd parity, apply a quasiparticle event corresponding to:
    - A MZM not involved in the measurement with probability $\frac{2m-2}{2m} p_{\text{odd}}^{(0)}$.
    - A MZM involved in the measurement with probability $\frac{2}{2m} p_{\text{odd}}^{(k)}$.
1. (a) For islands in the set not involved in a measurement ($k = 0$) apply either a quasiparticle of pair-wise dephasing event with respective probabilities $p_{\text{qp}}^{(0)}$ and $p_{\text{pair}}^{(0)}$.

For each island in the set with $k \geq 1$, apply either a quasiparticle event corresponding to:

- A MZM not involved in the measurement with probability $\frac{2m-2}{2m} p_{\text{qp}}^{(0)}$.
- A MZM involved in the measurement with probability $\frac{2}{2m} p_{\text{qp}}^{(k)}$.

or a pair-wise dephasing event corresponding to:

- A pair of MZMs not involved in the measurement with probability $\frac{(2m-2)^2}{(2m)^2} p_{\text{pair}}^{(0)}$.
- A pair of MZMs, with at least one of them involved in the measurement, with probability $\frac{4(2m-1)}{(2m)^2} p_{\text{pair}}^{(k)}$.

Furthermore, we consider a restricted set of correlated events in step 1(b) so that odd correlated events are strings of three Majorana operators $\gamma_{i,a}\gamma_{i,b}\gamma_{j,b}$ and even correlated events are strings of four Majorana operators $\gamma_{i,a}\gamma_{i,b}\gamma_{j,b}\gamma_{j,c}$, such that $i \neq j$ and the indices are chosen such that $\gamma_{i,b}$ and $\gamma_{j,b}$ are involved in a measurement.

PMC is defined by the same set of probabilities as MC, with $k_{\text{max}} = 2$. While MC treated all MZMs on a given island identically, PMC distinguishes between the measured and unmeasured MZMs within the island for single-qubit noise events. Furthermore, correlated events in PMC always involve a pair of MZMs directly coupled by the measurement. In Table 6.1, we compare noise event probabilities for all four models. Only a restricted set of correlated events are considered in PMC, which changes the combinatorial prefactors of the probabilities of these events between MC and PMC.

6.3 Physical system

6.3.1 Example system: tetron array

In the following, we use the two-sided tetron from Chapter 4 as an example to illustrate the different types of errors and to connect them to our noise models. Recall from Fig. 4.14 that the system consists of an array of four-MZM islands with finite charging energy E_C. Each tetron corresponds to a physical qubit, whose states are stored in the two nearly-degenerate ground states within a total parity subspace. In the absence of quasiparticle poisoning, the latter is fixed to be either even or odd. Multiple tetrons are connected to each other by semiconducting wires, which may be gated to allow for measurement by quantum dots [141]. The Hilbert space of a single tetron contains many of the features applicable to a large class of MZM systems, however the measurement protocol is specific to this qubit proposal.

Spectrum and single MZM excitations

The jth tetron can be described by the Hamiltonian [2]

$$H = E_C \left(\hat{n}_s - n_g\right)^2 + \sum_k E_k \, \hat{n}_{\Delta,k} + \sum_{a \neq b} \delta E_{ab} \, i\gamma_{j,a}\gamma_{j,b}, \tag{6.6}$$

where $a, b = 1, 2, 3, 4$. The last two terms (BCS Hamiltonian and MZM hybridization) are present in all MZM systems, while the first term (charging energy Hamiltonian) is present in systems for which the superconducting island is Coulomb-blockaded (*i.e.*, not grounded).

In the charging energy Hamiltonian, the operator $\hat{n}_s$, with integer eigenvalues n_s, is the

[2] In Eq. (6.6) we assumed that "mutual charging energy" terms that could couple pairs of MZMs belonging to different tetrons are perfectly quenched. We will comment more these terms in Section 6.3.2.

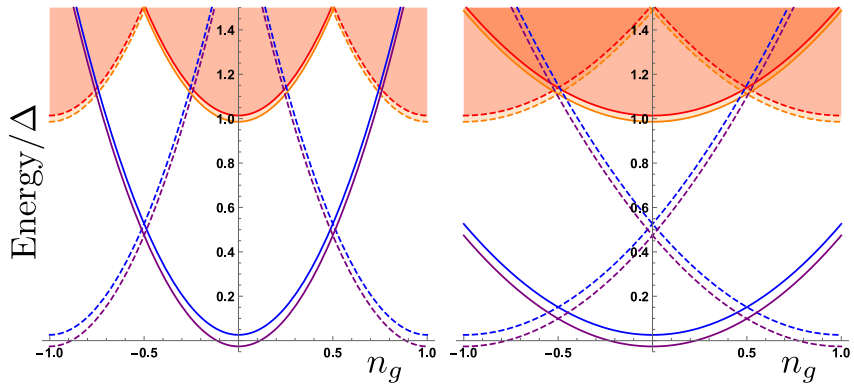

Figure 6.2: Cartoon of the energy levels of a single tetron against dimensionless gate voltage for $E_C = 2\Delta$ (*left panel*) and $E_C = \Delta/2$ (*right panel*), where E_C is the charging energy of the island and Δ is the superconducting gap. For fixed gate volgate $-0.5 < n_g < 0.5$, the system has a nearly-degenerate ground state with an even four-MZM parity. The degeneracy is broken by the MZM hybridization δE_{ab}, leading to distinct states $|g\rangle|\psi_i\rangle_{\rm M}$ denoted by solid blue and purple curves. The energy bands bordered by solid orange and red curves correspond to the states $|e_\Delta\rangle|\bar{\psi}_i\rangle_{\rm M}$ that have total fermion parity even, and odd four-MZM parity. The shaded regions indicate that the bands contain many discrete energy levels, with level spacing $\delta_{\rm is}$. The dashed blue and purple curves correspond to the states $|e_{C,\pm}\rangle|\bar{\psi}_i\rangle_{\rm M}$ that have total fermion parity odd, and odd four-MZM parity. Comparing the right and left panels near $n_g \approx 0$, we see that when E_C is larger (smaller) than Δ, the quasiparticle-poisoned states with one extra or one fewer electron on the superconducting island, $|e_{C,\pm}\rangle|\bar{\psi}_i\rangle_{\rm M}$, are higher (lower) in energy than the lowest energy states with a thermally excited quasiparticle, $|e_\Delta\rangle|\bar{\psi}_i\rangle_{\rm M}$.

number operator for electrons on the superconducting island. Generally the energy will be minimized when n_s is the integer closest to n_g, the dimensionless gate voltage applied to the superconducting island. When n_g is an integer, adding an electron to or subtracting an electron from the island costs a charging energy E_C, which is set by the capacitance of the superconducting island.

The BCS Hamiltonian is written in terms of the quasiparticle number operator $\hat{n}_{\Delta,k}$, with integer eigenvalues $n_{\Delta,k}$. More specifically, $\hat{n}_{\Delta,k}$ counts the number of above-gap quasiparti-

cles on the superconducting island with crystal momentum k, occupying the state with energy

$$E_k = \sqrt{\left(\frac{k^2}{2m} - \mu\right)^2 + \Delta^2}, \tag{6.7}$$

where Δ is the superconducting gap and μ is the chemical potential. Due to the finite size of the island, only a discrete set of momenta, $\{k_i\}$, is allowed. The level spacing of the island, δ_{is}, is the separation between adjacent energies: $\delta_{\text{is}} = E_k - E_{k-\delta k}$.

The last term of Eq. (6.6) describes the MZM hybridization energy, δE_{ab}, between MZMs $\gamma_{j,a}$ and $\gamma_{j,b}$. Generally, δE_{ab} is set by the wavefunction overlap, resulting in a length dependence $\delta E_{ab} \propto e^{-L_{ab}/\xi}$, where L_{ab} is the distance separating $\gamma_{j,a}$ and $\gamma_{j,b}$ and ξ is the superconducting coherence length. The topological protection of the system is manifested as an exponentially small ground state degeneracy splitting and requires $L_{ab} \gg \xi$.

We denote the eigenstates of Eq. (6.6) using the basis $|n_s, \{n_{\Delta,k}\}_\Delta\rangle|i\gamma_{j,1}\gamma_{j,2}, i\gamma_{j,3}\gamma_{j,4}\rangle$. The first set of quantum numbers describes the non-topological degrees of freedom: charge or quasiparticle excitations. The second set denotes the (almost) degenerate MZM subspace. The pairing of Majorana operators into $i\gamma_{j,1}\gamma_{j,2}$ and $i\gamma_{j,3}\gamma_{j,4}$ is an arbitrary choice. Note that the total fermion parity of the island, $2(n_s \bmod 2) - 1$, equals the product of the quasiparticle and four-MZM parity.

To discuss the leading excitations, we compare the energy levels of the system for $E_C = 2\Delta$ and for $E_C = \Delta/2$ in the left and right panels of Fig. 6.2. Solid curves correspond to an even number of particles n_s on the superconducting island, dashed curves to odd n_s. The tetron is operated at an even integer value for the dimensionless gate voltage to maximize protection from quasiparticle poisoning by maximizing the energy separation between solid and dashed

curves. Without loss of generality we assume $n_g \approx 0$. In this regime, there are two nearly degenerate ground states:

$$|g\rangle|\psi_i\rangle_{\rm M} = |0, \{0\}_\Delta\rangle|\psi_i\rangle_{\rm M}, \tag{6.8}$$

with $i = 0, 1$ and corresponding energy given by the solid blue and purple curves centered at $n_g = 0$. We write $\{n_{\Delta,k}\}_\Delta = \{0\}_\Delta$ to denote that there are no quasiparticles occupying energy levels above the superconducting gap. The qubit is stored in the two MZM states $|\psi_i\rangle_{\rm M}$, which are orthogonal linear combinations of the even four-MZM parity basis states $|i\gamma_{j,1}\gamma_{j,2} = \pm 1, i\gamma_{j,3}\gamma_{j,4} = \pm 1\rangle$. When the only non-vanishing hybridizations are δE_{12} and δE_{34}, $|\psi_i\rangle_{\rm M}$ is simply $|\pm 1, \pm 1\rangle$.

There are two bands of lowest excited states with even n_s, that correspond to a single thermally excited quasiparticle. Their energies are shown in Fig. 6.2 by the overlapping shaded regions bordered by solid orange and red curves. Two-quasiparticle excitations require energies of at least 2Δ and are therefore much less likely; in the following, we restrict our attention to $n_{\Delta,k} \in \{0, 1\}$. We denote a single excitation with energy larger than the gap Δ as e_Δ. The two bands are denoted by the states

$$|e_\Delta\rangle|\bar{\psi}_i\rangle_{\rm M} = |0, \{n_{\Delta,k} = 1\}_\Delta\rangle|\bar{\psi}_i\rangle_{\rm M}, \tag{6.9}$$

with $i = 0, 1$. In the above, e_Δ may denote different k states; this does not matter for our discussion as long as we focus on states with energy $\approx \Delta$. Here, the MZM states $|\bar{\psi}_i\rangle_{\rm M}$ are orthogonal linear superpositions of the *odd* four-MZM fermion parity states $|i\gamma_{j,1}\gamma_{j,2} = \pm 1, i\gamma_{j,3}\gamma_{j,4} = \mp 1\rangle$.

Depending on whether n_g is positive or negative, the two lowest excited states with odd total fermion parity contain either an extra electron or one fewer electron, respectively. Such

states are quasiparticle-poisoned. The states with one extra (one fewer) electron are written as

$$|e_{C,\pm}\rangle|\bar{\psi}_i\rangle_{\mathrm{M}} = |\pm 1, \{0\}_{\Delta}\rangle|\bar{\psi}_i\rangle_{\mathrm{M}}, \tag{6.10}$$

with energy levels shown in the dashed blue and purple parabolas centered about $n_g = \pm 1$.

The state of the MZMs is very similar for the two excited states discussed above. In both cases, an excitation process exchanges an electron between the MZMs and other fermionic modes represented by either the excited quasiparticles or by an external environment. The excitation acts by applying a single Majorana operator to the state $|\psi_i\rangle_{\mathrm{M}}$. The ground states $|g\rangle|\psi_i\rangle_{\mathrm{M}}$ and the excited states $|e_{\Delta}\rangle|\bar{\psi}_i\rangle_{\mathrm{M}}$, $|e_{C,\pm}\rangle|\bar{\psi}_i\rangle_{\mathrm{M}}$ are therefore distinguished by their four-MZM parity, with odd parity states separated from the even parity ground states by an energy $\min(\Delta, E_C)$. In our stochastic Majorana noise models, we focus only on these four lowest energy states and can therefore use the four-MZM parity as a measure of whether an island is in a ground or an excited state. In order to include higher excited states, we would need to separately track the four-MZM parity and the quantum numbers n_s and $\{n_{\Delta,k}\}$.

Measurements

For an array of tetrons, parity measurements can be implemented by coupling the MZMs to quantum dots [141] or by a conductance-based readout scheme [158, 208]. Most of the measurement concepts can be used interchangeably between the two approaches. In the following, we focus on quantum-dot based measurements. The most common examples are measuring the parity of a pair of MZMs on a single island, or measuring a four-MZM parity composed out of two MZM-pairs from separate islands. The latter can induce correlated excitations of

different islands. Other Majorana-based quantum computing architectures employ different measurement schemes, which in general will change the correlated events between islands being measured. In Section 6.5, we comment on how the different measurement schemes of other Majorana-based quantum computing architectures affect which types of correlated events the noise model should include.

To measure the parity of a pair of MZMs $\gamma_{1,m}$ and $\gamma_{1,\bar{m}}$ belonging to the same tetron, electrostatic gates in the semiconducting wire adjacent to the MZMs are tuned to form a quantum dot tunnel-coupled to $\gamma_{1,m}$ and $\gamma_{1,\bar{m}}$, as shown in the left panel of Fig. 4.2. To measure the parity of four MZMs (two pairs on two different superconducting islands), the electrostatic gates are tuned to form two quantum dots, each of which is tunnel-coupled to a MZM on each island, as shown in the right panel of Fig. 4.2.

An isolated quantum dot is described by a charging-energy Hamiltonian

$$H_D = E_C^{\mathrm{QD}} \left(d^\dagger d - N_g \right)^2 , \tag{6.11}$$

where d is the fermionic annihilation operator for the quantum dot and N_g is the dimensionless gate voltage on the dot. Writing the eigenvalues of the number operator for quantum dot levels as N_d, the quantum dot Hamiltonian is spanned by the occupation basis $|N_d\rangle_d$. We assume that the quantum dot is in the spin-polarized regime such that the available states are $|0\rangle_d, |1\rangle_d$. When performing a measurement, a tunneling Hamiltonian couples Eqs. (6.6) and (6.11). For instance, for the two-MZM measurement, the tunneling term takes the form

$$H_t = -a^- \left(t_m d^\dagger \gamma_{1,m} + t_{\bar{m}} d^\dagger \gamma_{1,\bar{m}} \right) + \text{H.c.}, \tag{6.12}$$

where t_m is the tunneling amplitude between MZM $\gamma_{1,m}$ and the quantum dot, and a^- is a

bosonic operator removing a single electron charge from the island. Equation (6.12) hybridizes the two quantum dot states $|0\rangle_d$ and $|1\rangle_d$ in a two-MZM parity-dependent manner. By measuring the energy levels, charge occupation, or quantum capacitance of the quantum dot, one can extract the two-MZM parity $i\gamma_{1,m}\gamma_{1,\bar{m}}$ of the system. Such a two-MZM measurement can be used to infer whether the tetron is in computational state $|\psi_0\rangle_M$ or $|\psi_1\rangle_M$. For a more-detailed discussion, see Ref. [141].

In the remainder of this section, we make the following gauge choice: all fermion operators are neutral and the charge on the system is accounted for by the bosonic operator $\hat{n}_s$. We define the neutral creation operator of an above-gap quasiparticle with crystal momentum k as $c_k^\dagger$ (*i.e.*, $c_k^\dagger|n_s, \{n_{\Delta,k}=0\}_\Delta\rangle = |n_s, \{n_{\Delta,k}=1\}_\Delta\rangle$). When an electron enters or leaves the superconducting island, the eigenvalue n_s changes by 1. We account for this change with the ladder operators $a^\pm$, which raise or lower n_s.

6.3.2 Error processes

In this section, we discuss the main physical processes contributing to errors in Majorana-based quantum computing architectures. The corresponding error rates will be independent of which computational (MZM) state the system is in, as such we simplify notation by dropping the MZM labels $|\psi\rangle_{\mathrm{M}}, |\bar{\psi}\rangle_{\mathrm{M}}$ and only writing the energy state $|g\rangle, |e_\Delta\rangle$, or $|e_{C,\pm}\rangle$. When an effect is independent of which excited state the system is in, we will simply write $|e\rangle$.

There are higher energy states, for instance, the state with both an extra electron and an above-gap quasiparticle on the island, that we have not discussed. Throughout this work, our

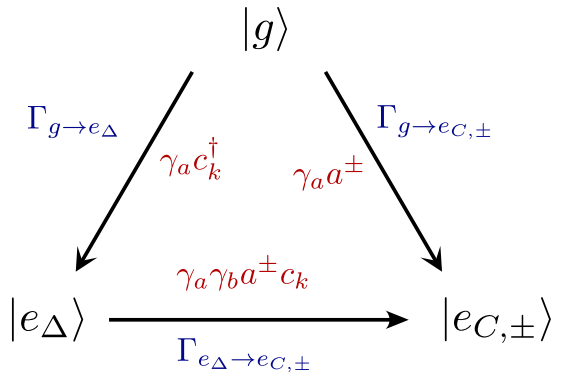

Figure 6.3: Quasiparticle events for a single MZM island. The corners of the triangle correspond to the three energy states we consider: the ground state with even MZM parity (corresponding to the computational states) $|g\rangle = |0, \{0\}_\Delta\rangle$, the thermal excited state with an above-gap quasiparticle $|e_\Delta\rangle = |0, \{1\}_\Delta\rangle$, and the quasiparticle-poisoned states $|e_{C,\pm}\rangle = |\pm 1, \{0\}_\Delta\rangle$. The edges of the triangle denote the quasiparticle event that transitions the system between the given states (thermal excitation of an above-gap quasiparticle or extrinsic quasiparticle poisoning), and are labeled by the corresponding transition rate for that process (in blue) and the operators that act on the system for that given process (in red). Arrows can be reversed by conjugating the operators, but the rates for the opposite processes can be drastically different.

aim will be to identify the *lowest order errors*: the most prominent errors in the system. If the probability of a given error is less than or equal to the product of the probabilities of other errors, and the effect on the Hilbert space of the MZMs is the same for that particular error as for the combination of the other errors, then we call such an error *higher order*. Processes involving excited states other than $|e_\Delta\rangle$ and $|e_{C,\pm}\rangle$ can be described as higher-order errors, see Section 6.7. Note that an error is classified as higher order solely from its probability; it is possible for the physical process causing a particular higher order error to be distinct from the physical processes causing lower order errors.

Figure 6.3 schematically illustrates single island error processes involving quasiparticles. A transition between the ground and an excited state corresponds to the application of a single Majorana operator and thus sets the probability of a quasiparticle event. The combination

of an excitation and a relaxation, or a transition between excited states, corresponds to the application of an even number of Majorana operators. These processes therefore contribute to the probability of a pair-wise dephasing event. We first quantify the transition rates involving quasiparticles in a single island, before discussing correlated events between islands connected during a measurement and error processes that do not involve quasiparticles. In the rates given below, we only quote the parametric dependence and ignore prefactors of $\mathcal{O}(1)$.

Thermally excited quasiparticles

Thermal excitation of an above-gap quasiparticle, the top left process in Fig. 6.3 $|g\rangle \to |e_\Delta\rangle$, is present in all MZM systems. This process occurs, for instance, when a Cooper pair breaks into two electrons, one of which occupies one of the non-local fermionic states formed by the MZMs while the other occupies a state in the continuum above the superconducting gap. Thermal excitation of a quasiparticle preserves the total fermion parity of the island and can therefore occur in an isolated system. [3]

Crucially, in equilibrium, thermal excitation of a single quasiparticle to the state $|e_\Delta\rangle$ is exponentially suppressed in the ratio Δ/T, where T is the temperature of the system. The

[3]There are also thermal excitations that conserve the parity of the MZMs by exciting a pair of quasiparticles to the continuum. These processes have an energy cost greater than twice the superconducting gap and are therefore less likely to occur. In practice, there will be a competition between a power-law enhancement for creating a particle-hole pair since it can happen anywhere in the system, and the additional exponential suppression due to the higher energy cost. Thermally excited particle-hole pairs do not cause errors by themselves, but increase the chance of subsequently transitioning to states that flip the MZM parity. Furthermore, pair-excitation can cause correlated events when nearby superconducting islands are coupled together for a measurement. For now we assume that these effects can be qualitatively captured by the transition rate of a single quasiparticle excitation and the rates describing correlated events.

excitation and relaxation rates take the form

$$\Gamma_{g\to e_\Delta} = \tau_0^{-1}\exp(-\Delta/T) \tag{6.13}$$

$$\Gamma_{e_\Delta\to g} = \tau_0^{-1}, \tag{6.14}$$

where τ_0 is a characteristic time scale describing the electron-phonon coupling of the system. For InAs wires with an Al half-shell, $\tau_0 \sim 50$ns [151]. In the presence of non-equilibrium quasiparticles, the factor $\exp(-\Delta/T)$ is essentially replaced by the number of quasiparticles in the vicinity of the MZMs.

A single thermal excitation event takes the computational (MZM) state of the island from an even parity state to an odd parity state, while a relaxation event does the reverse. Both thermal excitation and relaxation apply a single Majorana operator γ_a to the computational state, although as can be seen from Eqs. (6.13) and (6.14) the corresponding rates are significantly different. This is the underlying reason why all of the noise models of Section 6.2 account for quasiparticle events with two different probabilities, $p_{\text{odd}}^{(j)}$ and $p_{\text{qp}}^{(j)}$: if the island begins a time step in an odd MZM parity state, a relaxation event is much more likely than an excitation event if the island has even MZM parity, indicating a separation of scales between $p_{\text{odd}}^{(j)}$ and $p_{\text{qp}}^{(j)}$. Furthermore, the application of a single quasiparticle event significantly changes the probability of future quasiparticle events, which is why our noise models only allow for a single noise event to occur in step 0, and a single noise event to occur in step 1(a) (this approximation is justified if the errors are sufficiently rare).

A pair-wise dephasing event can result from an excitation and subsequent relaxation of

a thermal quasiparticle. The relaxation event is equally likely for all Majorana operators on the island, regardless of which Majorana operator was applied for the excitation event: this is the underlying reason why we allow for *all* pairs of Majorana operators, including the same Majorana operator twice, when considering pair-wise dephasing in our noise models. Finally, notice that the rates of thermal excitation and relaxation are unaffected by whether or not the superconducting island is involved in a measurement.

Extrinsic quasiparticle poisoning

Extrinsic quasiparticle poisoning, the top right process in Fig. 6.3 $|g\rangle \rightarrow |e_{C,\pm}\rangle$, is when a quasiparticle tunnels onto or off of the superconducting island, thereby changing the total fermion parity and charge of the island. We focus on the lowest-energy poisoning events where quasiparticles tunnel onto (off of) the island and into (out of) one of the fermion states provided by the MZMs. In the following discussion, we will assume $n_g = 0$ so that adding an electron to, or taking an electron off of the superconducting island costs an energy E_C; the following expressions could be made more general by replacing E_C with $E_C\,(1 \mp 2n_g)$. For an external quasiparticle to enter the island, it has to overcome the energy barrier $E_C + \delta\mu$, where $\delta\mu = \mu_{\text{is}} - \mu_{\text{res}}$ denotes a possible difference in the chemical potentials (a voltage bias) of the reservoir and the island.

In the case of tetrons, the most likely source of quasiparticles is the quantum dot explicitly coupled to the MZMs during a parity measurement. When the quantum dot is tuned to resonance [4], the energy difference $\delta\mu = 0$. Transitions between $|g\rangle$ and $|e_{C,\pm}\rangle$ are then described

[4]Tuning the quantum dot to resonance maximizes the measurement visibility, but is not a necessary condition.

by the rates

$$\Gamma^{(k)}_{g\to e_{C,\pm}} = g_T(k)\delta \exp\{-E_C/T\} \tag{6.15}$$

$$\Gamma^{(k)}_{e_{C,\pm}\to g} = g_T(k)\delta \tag{6.16}$$

where $g_T(k)$ is the dimensionless conductance between the quantum dot and MZM island. The parameter δ is either the level spacing of the quantum dot δ_{dot} when an electron transitions from the quantum dot to the island, or the effective MZM level spacing Δ when an electron transitions from the island to the quantum dot. Equations (6.15)-(6.16) can also be generalized to conductance-based measurement schemes [158, 208]. In that case, δ_{dot} is replaced by the temperature T and $g_T(k)$ is the dimensionless conductance between the lead and the MZM island. In the case of a quantum dot connected to the superconducting island, only a single channel with transmission $\mathcal{T}^{(k)}$ contributes to the island-dot coupling, thus $g_T(k) = |\mathcal{T}^{(k)}|^2$. The transmission $\mathcal{T}^{(k)}$ is essentially zero for $k = 0$ (*i.e.*, no measurement), and becomes appreciable for $k = 1, 2$. Notice also that during the measurement, the quantum dot is tuned close to the charge degeneracy point, thus we do not have to pay extra energy to remove a particle from it. If the quantum dot is then tuned to the bottom of its charging parabola when a measurement is not being performed, then $E_C \to E_C + E_C^{\text{QD}}$ in Eq. (6.15), further protecting the system from quasiparticle poisoning. It thus follows that quasiparticle poisoning from the quantum dot is significantly more likely during a measurement. This motivates why the noise models MC and PMC allow for different probabilities of quasiparticle events and pair-wise dephasing when an island is involved in a measurement.

Alternatively, quasiparticles could come from nearby metallic gates, for example those used to tune the MZM island into the topological regime. The transition rates are now independent of whether a measurement is being performed, as this is not expected to change the coupling between the island and the gate. If the metallic gates are kept at a large voltage, the energy $|\delta\mu|$ may become much larger than E_C so that it could be favorable for an extra quasiparticle to be on the superconducting island. In this case, it is essential that the dimensionless conductance between the metallic gate and the island g_{env} is sufficiently small so that the island is not constantly being poisoned by quasiparticles. Since an insulating barrier to the gates suppresses g_{env} exponentially in the thickness of the barrier, sufficiently small values of g_{env} are possible in practice. In the following, we assume that extrinsic quasiparticle poisoning rates are well approximated by Eqs. (6.15) and (6.16).

From Eq. (6.15), we see the benefit of the island having a large charging energy is to suppress the rate of extrinsic quasiparticle poisoning events. Majorana-based quantum computing proposals for which the superconducting island is grounded ($E_C \to 0$) are likely to be more susceptible to quasiparticle and pair-wise dephasing events.

A comment is in order about the fast relaxation of Eq. (6.16). A crucial requirement is that the environment can accept or provide an electron at no energy cost. This is always the case for conductance-based measurements in which the island is connected to leads with no charging energy. For quantum dot-based measurements, it is important to properly initialize and decouple the quantum dots. An example procedure that always allows for fast relaxation is a double-dot measurement (see Fig. 4.2 right panel). By initializing the quantum dots in the

state $|0\rangle_d|1\rangle_d$ and tuning them so that each dot is at its charge degenerate point, the island can relax its charge state by transitioning to the $|1\rangle_d|1\rangle_d$ or $|0\rangle_d|0\rangle_d$ state. Alternatively, we can use the quantum dots to check if a poisoning event has occurred during the measurement by performing an additional charge measurement of the quantum dot(s) after the island is decoupled. This additional measurement could allow immediate correction of extrinsic quasiparticle poisoning events, in which case we would not need to include such events in the noise models.

In terms of the computational state of the island, extrinsic quasiparticle poisoning has the same effect as the corresponding thermal quasiparticle event: an excitation, $|g\rangle \rightarrow |e\rangle$, takes the MZMs from an even parity state to an odd parity state by applying a single Majorana operator γ_a; relaxation, $|e\rangle \rightarrow |g\rangle$, does the reverse; and the combination of an excitation and subsequent relaxation, $|g\rangle \rightarrow |e\rangle \rightarrow |g\rangle$, applies the pair of Majorana operators $\gamma_a\gamma_c$ where a can equal c. Transitions between the excited states $|e_{C,\pm}\rangle$ and $|e_\Delta\rangle$ have the same effect on the computational state as a combined excitation and relaxation. Moreover, a transition between excited states requires two unlikely processes to occur: first, an island must be excited and second, the island must transition to the other excited state before relaxing to the ground state. It follows that such transitions only contribute a small correction to the probability of pair-wise dephasing events and can therefore be neglected.

Correlated events

Quasiparticle poisoning and thermal excitations can lead to correlated events that transfer excitations between two (or more) islands connected during a measurement. An excited charge state can be transferred by a quasiparticle tunneling between two islands through the low-

energy subspace provided by the MZMs. A thermal excitation can be transferred without changing the net particle number by an above-gap quasiparticle tunneling between two islands and a corresponding reverse tunneling of an electron through the low energy subspace. Each time an island transitions between the ground and an excited state, a Majorana operator is applied to the computational state of that island. Thus, a process in which two islands swap being in the ground and excited state,

$$|g\rangle \otimes |e\rangle \to |e\rangle \otimes |g\rangle, \tag{6.17}$$

results in a Majorana operator being applied to each island. The corresponding MZMs are tunnel-coupled to the same quantum dot, as shown in the right panel of Fig. 4.2 (either $\gamma_{2,m}\gamma_{3,m}$ or $\gamma_{2,\bar{m}}\gamma_{3,\bar{m}}$). When this process combines with excitations and relaxations on the two islands, it results in correlated events involving three or four Majorana operators between two islands, described, *e.g.*, by the probabilities $p^{(2)}_{\text{cor,odd}}$ and $p^{(2)}_{\text{cor,even}}$, respectively, in PMC.

The most prominent correlated events come from the processes

$$|g\rangle \otimes |g\rangle \to |e_x\rangle \otimes |g\rangle \to |g\rangle \otimes |e_x\rangle \to |g\rangle \otimes |g\rangle \tag{6.18}$$

$$|g\rangle \otimes |g\rangle \to |e_x\rangle \otimes |g\rangle \to |g\rangle \otimes |e_x\rangle \tag{6.19}$$

$$|e_x\rangle \otimes |g\rangle \to |g\rangle \otimes |e_x\rangle \to |g\rangle \otimes |g\rangle \tag{6.20}$$

where the excited states $|e_x\rangle \in \{|e_{C,\pm}\rangle, |e_\Delta\rangle\}$. Equation (6.18) applies an even number of Majorana operators and is described by the probability $p^{(2)}_{\text{cor,even}}$ in PMC. If relaxation processes are fast compared to the time step τ, this is the most probable type of correlated event. Equa-

tions (6.19) and (6.20) describe odd correlated events captured by $p^{(2)}_{\text{cor,odd}}$ in PMC and can be seen as being part of an even correlated event split up over two time steps. Both odd correlated events have the same effect on the computational subspace and are equally likely. To simplify our noise models, we only take into account the process described by Eq. (6.19). When connecting the probabilities defining PMC to physical processes, we therefore have to overestimate the probability of the event described by Eq. (6.19) by at least a factor of two in order to avoid undercounting odd correlated events. Similarly to the previous discussion of single-island errors, we ignore higher order correlated events between the two islands, *e.g.*, $|e_{C,\pm}\rangle \otimes |g\rangle \to |e_\Delta\rangle \otimes |e_\Delta\rangle$, see Section 6.7.

Assuming the islands are identical, there is no energy difference between the states $|e_x\rangle\otimes|g\rangle$ and $|g\rangle \otimes |e_x\rangle$. As such, the corresponding transition rates have no exponential suppression:

$$\Gamma_{e_{e_{C,\pm}},g\to g,e_{e_{C,\pm}}} = g_{\text{is-is}}\Delta \tag{6.21}$$

$$\Gamma_{e_{e_\Delta},g\to g,e_{e_\Delta}} = g^2_{\text{is-is}}\Delta\delta_{\text{is}}/E_C, \tag{6.22}$$

where $g_{\text{is-is}}$ is the dimensionless conductance between the two islands. The second line originates from the tunneling of an above-gap quasiparticle (level spacing δ_{is}) and a tunneling through the MZMs (effective level spacing Δ) within the time $1/E_C$ of the virtual charge and thermal excited state. Note that for weak coupling to the dots, the interisland conductance $g_{\text{is-is}} \ll g^{(k)}_T$, and grows quadratically with the tunneling amplitude to the dots. Despite the smaller prefactor of Eqs. (6.21) and (6.22), the corresponding rates are expected to be much larger than those given in Eqs. (6.13) and (6.15) due to the absence of exponential suppression. It follows that an excitation on one island moves to the other with higher probability than an

independent relaxation of one island and excitation of the other; this is what is meant by a *correlated event.*

Processes in which $|e_x\rangle \otimes |g\rangle \rightarrow |g\rangle \otimes |e_y\rangle$ with $x \neq y$ are a combination of transitions between excited states $|e_{C,\pm}\rangle \leftrightarrow |e_\Delta\rangle$ and the same-state correlated events of Eqs. (6.21) and (6.22). We thus expect the corresponding transition rates to only contribute a small correction to the correlated event probabilities in PMC, for the same reason that transitions between excited states only contribute a small correction to the probability of a pair-wise dephasing event.

Other errors

Processes that do not involve quasiparticles can also contribute to the probabilities of pair-wise dephasing events and measurement bit-flips. Finite MZM hybridization, δE_{ab} in Eq. (6.6), leads to dephasing of the MZMs associated with operators $\gamma_a\gamma_b$. The MZM hybridization is caused by finite overlap of the MZM wavefunctions when the correlation length of the topological superconductor is not sufficiently smaller than the distance separating the MZMs. The degeneracy splitting can have both a constant and fluctuating piece. The former would be problematic for topological gates that rely on degeneracy of the computational subspace, but will not be explicitly considered here. The latter is problematic even for memory storage. Charge noise in the electrostatic gates and substrate on which the MZM island is sitting can cause fluctuations of the electric field at the topological wire, which in turn results in a noisy time-dependence of the MZM hybridization δE_{ab}. We expect the rate of such errors to scale as

$$\Gamma_{EE} \sim \sqrt{\int d\omega S_{EE}(\omega) e^{-L/\xi}}, \tag{6.23}$$

where $S_{EE}(\omega)$ is the spectral function of electric field fluctuations in the system and L is the typical separation of MZMs in the island. Any computing approach that involves tuning a superconductor into the topological regime with electrostatic gates will likely experience noise described by Γ_{EE}, however, as discussed in Ref. [151], the time scales associated with this dephasing process are predicted to be quite long for reasonably-sized systems (order of minutes for $L/\xi \sim 30$). At these system sizes, the thermal excitations of Eq. (6.13) become the most important source of pairwise dephasing events. For concreteness, we use this limit and neglect hybridization-based errors for the probability estimates in the next section.

Another source of error occurs when the classical bit storing the outcome of a $2k$-MZM parity measurement does not agree with the actual parity of the measured MZMs at the end of the time step. Physically, the measurement is implemented by adding a term to the Hamiltonian with the $2k$ Majorana operators to be measured. This term splits the energy of the two eigenstates of $2k$-MZM parity and the environment then quickly dephases these two states, collapsing the system into one of the eigenstates. The measurement outcome is obtained by gathering statistics throughout the time step as to which eigenstate the system has collapsed.

There are two ways for measurement outcomes to disagree with the state of the system at the end of the time step: (1) the classical bit storing the measurement is flipped, or (2) the state of the system changes between the measurement projection and the end of the time step. Errors from case (1) are described by the probability $p_{\text{mst}}^{(k)}$ in MC and PMC (probability p_{mst} in QpBf). This case either results from statistical error (the integration time of the measurement was too short), or from classical noise in the measurement flipping the bit's outcome. Classical

noise is strongly dependent on the physical implementation of the measurement, as such, we do not further analyze these processes other than to note that a measurement error will be more probable for smaller measurement signals, likely to occur when multiple islands are involved in a single measurement.

Due to our convention that measurement projections are performed at the end of a time step, our models do not describe case (2). In reality, a measurement is performed by collecting statistics throughout the time interval, thus the measurement result will likely reflect a noise event that occurs near the beginning of the time step, but not one that occurs at the end. The latter are instead reflected in the next measurement that occurs. In an error correction protocol in which almost every island is measured in each time step, it is only a small effect (for a large number of time steps) whether we apply projectors at the beginning or the end of a time step, as for one convention the noise events will be reflected in the measurement associated with that time step, and in the other convention the noise events will be reflected in the measurements associated with the subsequent time step.

6.3.3 Error probabilities

We now use the transition rates discussed in the previous section to estimate how the error probabilities in the stochastic Majorana noise model PMC depend on physical parameters of the system. These estimates serve the double purpose of connecting the noise models of the previous section to the underlying physical system, and of simplifying the simulations of

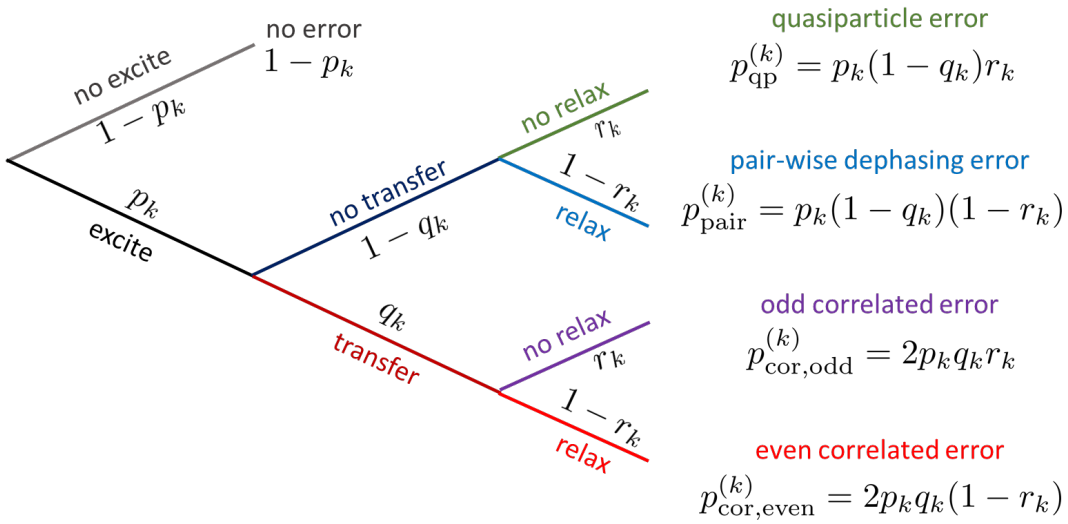

Figure 6.4: Probability tree for the different error types involving quasiparticles for Majorana noise model PMC: p_k is the probability that a MZM on an island in a k-island measurement is excited, q_k is the probability that this excitation is transferred to a different island in the measurement, and r_k is the probability that this excitation does not relax. The probabilities $p^{(k)}_{\text{qp}}$ and $p^{(k)}_{\text{pair}}$ are for single islands, while $p^{(k)}_{\text{cor,odd}}$ and $p^{(k)}_{\text{cor,even}}$ are for both islands in a measurement. In the text, we relate these small, dimensionless parameters to the transition rates discussed in the previous section. When $m = 2$, corresponding to a tetron architecture, and $r_k = 0$, corresponding to no odd Majorana operators, the model PMC reduces to the qubit-based model Pauli circuit noise.

pseudo-thresholds in the next section by reducing the number of independent parameters in PMC. At the end of this section, we discuss the other three Majorana noise models Qp, QpBf, and MC, and the limit in which they reduce to the analogous qubit-based noise models.

In Fig. 6.4, we schematically show that for a k-island measurement, all errors involving quasiparticles are related by three small dimensionless parameters: p_k, the probability that a quasiparticle is excited on one of the islands involved in the measurement; q_k, the probability that the energy from this excitation is transferred to a different island involved in the measurement; and r_k, the probability that an excitation created during the time step does not relax. These dimensionless parameters are related to the three types of transition rates involving

quasiparticles discussed in the previous sections: excitations $\Gamma^{(k)}_{g\to e_x}$, energy transfers between islands $\Gamma^{(2)}_{e_x,g\to g,e_x}$, and relaxations $\Gamma^{(k)}_{e_x\to g}$, respectively. More explicitly, denoting the length of the time step by τ, we find

$$p_k = 2m \sum_x \Gamma^{(k)}_{g\to e_x}\tau \tag{6.24}$$

$$r_k = \max_x \left(\tau\Gamma^{(k)}_{e_x\to g}\right)^{-1} = \tau_{\mathrm{r}}^{(k)}/\tau \tag{6.25}$$

$$q_2 = \max_x \left(\exp\left\{\Gamma^{(2)}_{e_x,g\to g,e_x}\tau_x^{(2)}\right\} - 1\right). \tag{6.26}$$

The factor of $2m$ in Eq. (6.24) comes from any of the $2m$ MZMs on an island initially being excited. We assume that excitations are rare, so that $\Gamma^{(k)}_{g\to e_x}\tau \ll 1$ and p_k is a small parameter. For an idle MZM, we expect extrinsic quasiparticle poisoning to be negligible, thus only $\Gamma^{(0)}_{g\to e_\Delta}$ will contribute to p_0. Generally, we expect $\Gamma^{(0)}_{g\to e_\Delta} \approx \Gamma^{(1)}_{g\to e_\Delta} \approx \Gamma^{(2)}_{g\to e_\Delta}$ and $\Gamma^{(1)}_{g\to e_C} \lesssim \Gamma^{(2)}_{g\to e_C}$, so that $p_0 < p_1 \lesssim p_2$.

In Eq. (6.25), $\tau_{\mathrm{r}}^{(k)} \equiv \max_x \left[1/\Gamma^{(k)}_{e_x\to g}\right]$ is the typical time scale over which the longest living excited state relaxes to the ground state. We assume $\tau_{\mathrm{r}}^{(k)} \ll \tau$ based on physical considerations. The parameter τ is bounded from below by the longest measurement time, a four-MZM parity measurement in the current discussion. We expect this measurement time to be $1-10$ μs for high-fidelity measurements, while typical time scales for the electron-phonon coupling facilitating quasiparticle relaxation are ~ 0.1 μs [180]. Physically, we expect $0 < r_k < 1/10$ and $r_0 \approx r_1 \approx r_2$. The probability of an excitation, created at the beginning of the time step, to not relax is exponentially small in $1/r_k$ and will be neglected through the remainder of the

paper. Equation (6.25) then follows from the probability of a given excitation to happen within the window $\tau_{\mathrm{r}}^{(k)}$ just before the end of the time step. When $r_k = 0$, an island never ends (or begins) a time step in an excited state; for $m = 2$, the noise model then reduces to the qubit-based model Pauli circuit noise. If the assumption of $r_k \ll 1$ is violated, excitations become long-lived. In this case, excitations can travel long distances before relaxing, thereby significantly degrading the effectiveness of error correction. We discuss noise models describing long-lived excitations in Section 6.7.

For simplicity, and to obtain an upper bound on the correlated errors in Eq. (6.26), we maximize the probability for transferring energy over the excited states. Since q_2 is not exponentially suppressed and can therefore be $\mathcal{O}(1)$ when islands involved in a measurement are well-coupled, we did not use the approximation for small transition rates. Physically, we expect the probability of an energy transfer between the two islands to be smaller than the probability that the excitation remains on the same island, so we anticipate $0 < q_2 < 1/2$. For an idle island or single-island measurement, $q_0 = q_1 = 0$.

In the following, we describe the noise model PMC using the parameters introduced above.

Quasiparticle events. The probability $p_{\mathrm{qp}}^{(k)}$ that a single Majorana operator is applied to an island involved in a $2k$-MZM measurement can be obtained from considering an initial excitation (p_k) of a quasiparticle that does not relax (r_k) and does not transition to another island ($1 - q_k$). We

therefore find

$$p_{\text{qp}}^{(k)} \approx p_k \, (1 - q_k) \, r_k \, . \tag{6.27}$$

The probability $p_{\text{odd}}^{(k)}$ of an initially excited state to relax during the time step is given by

$$p_{\text{odd}}^{(k)} \approx 1 - e^{-1/r_k} \tag{6.28}$$

$$p_{\text{odd}}^{(k)} > 1 - p_{\text{qp}}^{(k)}. \tag{6.29}$$

The bound in Eq. (6.29) reflects the assumption of fast relaxation. In that case, it is more likely for an excitation to relax and get re-excited, than for the excitation to remain over the entire time step. Within the fast relaxation limit, we can use the upper bound for $1 - p_{\text{odd}}^{(k)} = p_{\text{qp}}^{(k)}$. We discuss how the noise models can be generalized beyond the fast relaxation limit in Section 6.7.

Pair-wise dephasing events. Pair-wise dephasing events can occur from quasiparticle excitations and relaxations, or from non-quasiparticle processes such as MZM hybridization discussed in Section 6.3.2:

$$p_{\text{pair}}^{(k)} \approx p_k \; (1 - q_k) \; (1 - r_k) + m \, \Gamma_{EE} \, \tau. \tag{6.30}$$

Here, $(1 - q_k)(1 - r_k)$ is the probability of an excited quasiparticle to relax within the same island and thus contribute to pair-wise dephasing. The second term arises from noise in the hybridization, see Eq. (6.23). The combinatoric prefactor of m counts the number pairs of

MZMs whose wavefunction overlap contributes to pair-wise dephasing. In the following, we will assume the MZMs are sufficiently separated that we can drop the second term.

Correlated events. An odd correlated event occurs when one island involved in a measurement is excited and transfers its excess energy to a second island, which remains in the excited state for the rest of the time step. Similar to quasiparticle events, only excitations within a fraction of r_k of the time step contribute significantly to odd correlated events. More explicitly, the probability of an odd correlated event is

$$p^{(2)}_{\text{cor,odd}} \approx 2\, p_2\, q_2\, r_2. \tag{6.31}$$

The factor of two is a result of the initial quasiparticle excitation occurring on either of the two islands involved in the measurement.

An even correlated event occurs when a quasiparticle excitation in one island is transferred to the other island, which subsequently relaxes:

$$p^{(2)}_{\text{cor,even}} \approx 2p_2\, q_2\, (1 - r_2). \tag{6.32}$$

The factor of two again comes from either island initially being excited. When hybridization errors are subleading (*i.e.*, the MZMs are sufficiently well-separated), an even correlated event is essentially a pair-wise dephasing event interrupted by an energy transfer.

Measurement bit-flip. A measurement bit-flip depends only on classical and statistical noise, and is thus independent of the other probabilities in the noise model. The signal-to-noise ratio

Model	Probabilities
Qp	$p_{\text{pair}} = p\,(1-r), p_{\text{qp}} = p\,r,\ p_{\text{odd}} = 1 - p_{\text{qp}}$
QpBf	$p_{\text{pair}} = p\,(1-r), p_{\text{qp}} = p\,r,\ p_{\text{odd}} = 1 - p_{\text{qp}},\ p_{\text{mst}}$
MC & PMC	$p^{(k)}_{\text{pair}} = p_k\,(1-q_k)\,(1-r),\ p^{(k)}_{\text{qp}} = p_k\,(1-q_k)\,r$ $p^{(k)}_{\text{odd}} = 1 - p^{(k)}_{\text{qp}},\ p^{(2)}_{\text{cor,even}} = 2p_2\,q_2\,(1-r)$ $p^{(2)}_{\text{cor,odd}} = 2p_2\,q_2\,r,\ p_{\text{mst}}$

Table 6.2: Probabilities for pair-wise dephasing, quasiparticle, and correlated events in the four stochastic Majorana noise models can be written in terms of an excitation parameter p_k (p), a relaxation parameter r, and a correlation parameter q_k (with $q_0 = q_1 = 0$), see Eqs. (6.24-6.26). The expressions above neglect the contribution of hybridization to pair-wise dephasing events, and assume that quasiparticle relaxation times are fast, *i.e*, $p^{(k)}_{\text{qp}} > \exp(-1/r)$ and similar regardless of whether an island is involved in a measurement. Model PMC is physically motivated when $0 \leq r \lesssim 1/10$ and $0 \leq q_2 \leq 1/2$. When $m = 2$, the limit of $r = 0$ corresponds to the qubit model Pauli circuit noise. The expressions in this table are used in the pseudo-threshold calculations in Section 6.4.

of a measurement typically increases as a square root of the integration time [68]. We assume that τ is essentially given by the integration time of the measurement. The confidence of the measurement outcome therefore behaves as

$$p^{(k)}_{\text{mst}} \approx e^{-\tau/\tau^{(k)}_{\text{mst}}}, \tag{6.33}$$

where τ_{mst} is a characteristic time scale that gives a signal-to-noise ratio of 1. Four-MZM measurements are expected to have lower visibility and thus be more susceptible to statistical and classical error, *i.e.*, $p^{(1)}_{\text{mst}} < p^{(2)}_{\text{mst}}$.

We have shown that the probabilities defining model PMC can be defined in terms of excitation parameters p_k, relaxation parameter r_k, and a correlation parameter q_2. Varying these

parameters over the appropriate ranges and studying the effect on the pseudo-threshold for the system should inform us about the relative importance of single-island vs. two-island errors, as well as errors with an odd vs. even number of Majorana operators. A natural choice for the three other stochastic Majorana noise models is to assume a similar dependence of the probabilities on these parameters. In the next section, for ease of comparing the effects of different errors, we will set $r_k = r$ and use the lower bound of the relaxation probability $p_{\text{odd}}^{(k)} = 1 - p_{\text{qp}}^{(k)}$. We summarize the scaling relations between error probabilities for the four models in Table. 6.2.

Finally, note that if we set $p_0 = p_2$ and restrict our attention to tetrons ($m = 2$), the noise models MC and PMC differ only in that some of the odd correlated events in MC do not occur in PMC. For both MC and PMC, there are only 16 computationally distinct [5] even correlated events, each occurring with equal probability. In contrast, there are 16 computationally distinct odd correlated events that can occur in PMC with equal probability, and 32 computationally distinct odd correlated events that can occur in MC with equal probability. For larger values of m, we expect MC and PMC to differ more substantially.

6.4 Application of noise models

We now apply the noise models presented in Section 6.2 to analyze the error correction performance of the Bacon-Shor code [12, 156, 235] on a small system of tetrons. As explained in Section 6.3, a tetron consists of four MZMs, and therefore stores a single qubit of information

[5] Because the total MZM parity of an island is fixed, some Majorana operators are computationally equivalent, *e.g.* $\gamma_{j,1}\gamma_{j,2}$, $\gamma_{j,2}\gamma_{j,1}$, $\gamma_{j,3}\gamma_{j,4}$, and $\gamma_{j,4}\gamma_{j,3}$.

in the overall even parity state. Although our noise models can be applied to any quantum error correction scheme, there are several motivations for considering this small subsystem code rather than (1) a Majorana fermion code specifically designed to correct for quasiparticle events [48, 255, 122], or (2) a qubit-based stabilizer code (*e.g.*, the surface code). (1) A Majorana fermion code either requires the ability to measure the total parity of all MZMs on an island, or the ability to dynamically adjust the number of MZMs on a given island. We discuss in Section 6.5 why it is experimentally challenging to satisfy these conditions. Furthermore, the codes discussed in Ref. [255] are categorized with a notion of code distance in which the most probable noise events are quasiparticle events, which is not expected to be the case for a tetron architecture. Rather, for low temperatures ($T \ll E_C, \Delta$) and fast relaxation ($r_k \ll 1$), quasiparticle events in a system of tetrons are converted by the environment into Pauli errors, which in turn are correctable by qubit-based codes. As discussed in Section 6.3.1, the odd total-MZM parity state of an island is highly excited above the (even MZM parity) ground state; as such, the environment relaxes the system back to the ground state. In the language of Refs. [122, 255], the environment measures the missing stabilizers of the Majorana fermion code needed to detect errors involving odd numbers of Majorana operators.

Regarding point (2), in the Bacon-Shor code, error correction is built out of two-qubit measurements, which can be simply implemented for tetrons with four-MZM parity measurements. In contrast, typical stabilizer codes involve measurements of at least four-qubit (eight Majorana) operators, which are expected to be more difficult to implement experimentally. While in principle it is possible to implement higher-weight measurements from a sequence of smaller-

weight measurements, the extra operations can significantly increase the noise. For example, a six-MZM measurement for a system of tetrons could be performed using two ancilla tetrons with six four-MZM and four two-MZM measurements [141], or alternatively by preparing ancilla tetrons in a cat state, then doing a sequence of four-MZM measurements [175]. Adding ancilla tetrons and additional measurements provides new locations and opportunities for noise to occur before it can be corrected by the code. Additionally, as is further discussed in Section 6.6, higher-weight measurements can result in a higher probability of correlated errors, with negative effects on the pseudo-threshold. Circumventing higher-weight measurements using subsystem codes is therefore a natural starting point for error correction in Majorana-based quantum computing architectures. Determining optimal error correction procedures by weighing the advantages and disadvantages of higher-weight measurements is an interesting direction for future research.

We review error correction with subsystem codes, focusing on the Bacon-Shor code and how it applies to a system of tetrons. We then analyze the conditions for fault tolerance (*i.e.*, compute pseudo-thresholds) for each of the noise models presented in Section 6.2. The analysis of this section is restricted to quantum memory error correction; analyzing the fault tolerance of logical gates is an important subject that we relegate to future studies. The choice of error correcting code and error correction protocol have not been optimized to minimize the number of resources [58, 56] or to maximize the fault tolerance threshold [99]. As such, the pseudo-threshold values reported here are more informative in their relative magnitude (within a given noise model for different parameter values) than in their absolute value. At the end of this

section, we separately discuss what experimental implications can be drawn from our analysis.

6.4.1 Subsystem error correcting codes

As subsystem codes are less commonly studied compared to stabilizer codes [198], we first review the standard application of a subsystem code to a qubit noise model (*i.e.*, errors involving an even number of Majorana operators in a tetron architecture). For a more extensive discussion of subsystem codes, see Ref. [209]. We then discuss how a subsystem code can also correct for errors involving an odd number of Majorana operators in a tetron architecture. We address measurement bit-flips later when discussing the application of the Bacon-Shor code to the noise models of Section 6.2. An example illustrating the formal concepts introduced below is given in Section 6.4.2.

Subsystem codes are generalizations of stabilizer codes in which information is encoded in a *subsystem* of a *subspace* of the Hilbert space, rather than a *subspace*. More explicitly, the Hilbert space of physical qubits $\mathcal{H}$ can be decomposed into a code space $\mathcal{H}_\mathcal{C}$ and the perpendicular subspace of errors, $\mathcal{H}_\mathcal{E} = \mathcal{H}_\mathcal{C}^\perp$:

$$\mathcal{H} = \mathcal{H}_\mathcal{C} \oplus \mathcal{H}_\mathcal{E}. \tag{6.34}$$

The code space can be further decomposed into a logical subsystem $\mathcal{H}_\mathcal{L}$, the Hilbert space of the logical qubits, and a gauge subsystem $\mathcal{H}_\mathcal{G}$:

$$\mathcal{H}_\mathcal{C} = \mathcal{H}_\mathcal{L} \otimes \mathcal{H}_\mathcal{G}. \tag{6.35}$$

In a stabilizer code, $\mathcal{H}_\mathcal{G}$ is trivial. The benefit of having the gauge subsystem is that error correction only needs to correct an error modulo the gauge subsystem structure; a non-trivial

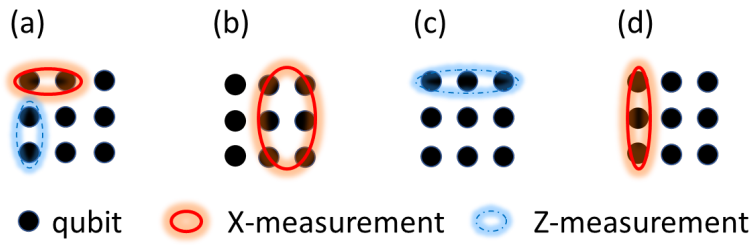

Figure 6.5: The $d = 3$ Bacon-Shor code storing a single logical qubit is implemented by applying X-type (red solid ovals) and Z-type (blue dashed ovals) Pauli operators on a grid of 9 qubits (black dots). (a) Example of gauge generators. X-type (Z-type) gauge generators act on pairs of nearest neighbor qubits in the horizontal (vertical) direction. There are six different X and Z gauge generators. (b) Example of an X-type stabilizer. X stabilizers consist of pairs of X-type Pauli operators applied to an even number of columns. Z stabilizers are pairs of Z-type Pauli operators applied to an even number of rows (not shown). (c) The Z-type bare logical operator is applied to an odd number of rows. (d) The X-type bare logical operator is applied to an odd number of columns.

action on the gauge subsystem does not affect the encoded quantum information. As we detail below, this extra degree of freedom can allow the error correction procedure to be implemented directly with smaller measurements, but comes at the cost of a reduction of the number of inequivalent code states.

More formally, we specify a subsystem code using subgroups of the Pauli group for n physical qubits, $\mathcal{P}_n$:

- The *gauge group*, $\mathcal{G}$: a non-Abelian subgroup of $\mathcal{P}_n$ which defines the subsystem code.
- The *stabilizer group*, $\mathcal{S}(\mathcal{G})$: the largest subgroup of $\mathcal{G}$, excluding -1, consisting of elements which commute with every element of $\mathcal{G}$.
- The group of *bare logical operators*, $\mathcal{L}_B$: Pauli operators that commute with, but do not belong to, the gauge group $\mathcal{G}$.

- The group of *dressed logical operators*, $\mathcal{L}_D = \langle \mathcal{L}_B, \mathcal{G} \rangle$.

The *code space*, $\mathcal{H}_\mathcal{C}(\mathcal{G})$, of a subsystem code with gauge group $\mathcal{G}$ is the $+1$ eigenspace of all stabilizer operators. The *code distance*, d, is defined to be the minimum support of any logically non-trivial element of $\mathcal{L}_D$. We use the standard qubit definition of code distance, not to be confused with the Majorana fermion code distance used in Refs. [48, 122, 255].

Error correction with a subsystem code involves using the measurement outcomes of the generators of the stabilizer group (stabilizers) to infer if any unwanted Pauli noise operators have been applied to the system [6]. One of the most appealing features of subsystem codes is that the eigenvalue of each stabilizer generator can be determined by multiplying together the eigenvalues of some of the gauge generators, which are often easier to measure. For an example of gauge generators and stabilizers, see Fig 6.5.

To model memory error correction, the system is prepared in an eigenstate of one of the logical operators and is periodically measured to check that the state remains unchanged. If at least one, but fewer than d, Pauli errors occur in an error correction round (measurement of all stabilizers), the system will no longer be in $\mathcal{H}_\mathcal{C}(\mathcal{G})$ and some of the stabilizer measurements will have outcome -1. The *syndrome* of a given Pauli error is the corresponding set of stabilizer measurement outcomes. The error correction protocol uses the syndrome to infer which Pauli operators have been applied (under the assumption that the minimal number of errors corresponding to that syndrome has occurred). The errors can then be corrected by appropriate application of Pauli operators, returning the system to its intended state. However, if more than

[6] As stabilizer generators commute, they can be measured simultaneously. This is not the case for gauge generators, which do not necessarily commute.

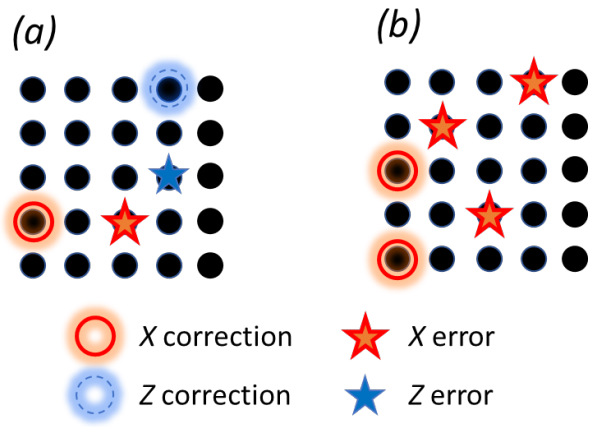

Figure 6.6: Two examples of Pauli errors (red and blue stars) and corresponding error correction (solid red and dashed blue circles). All X errors in the same row and all Z errors in the same column have the same syndrome. (a) Example correction of a single X and a single Z error. The net Pauli operator applied to the system (errors and correction) is in the gauge group and thus does not change the quantum information stored in the code. (b) Example failure of the code for three X errors. They syndrome of the three X errors is the same as the syndrome for two X errors in the third and fifth rows. The correction thus applies X operators to these rows, so that the net operator (error and correction) applied to the system is a dressed logical operator, which changes the quantum information.

$(d-1)/2$ Pauli errors occur in an error correction round, the correction procedure might incorrectly diagnose the error; in this case, the correction procedure might change the logical state of the encoded quantum information, resulting in a failure of the error correction protocol.

6.4.2 Bacon-Shor codes

One particular subsystem code, the distance-d Bacon-Shor code, is implemented on a $d \times d$ grid of qubits, with d odd [12, 156]. Figure 6.5 shows the relevant operators of the $d = 3$ Bacon-Shor code. The generators of the gauge group $\mathcal{G}$ are XX acting on horizontal nearest neighbors and ZZ acting on vertical nearest neighbors, as depicted in Fig. 6.5(a). The stabilizer group $\mathcal{S}(\mathcal{G})$ has $d-1$ X-type and $d-1$ Z-type generators, where each X-type generator consists of X

applied to two columns ($2d$ qubits) and each Z-type generator consists of Z applied to two rows ($2d$ qubits), see Fig. 6.5(b). A Z-type bare logical operator is a string of Z operators applied to a row of qubits [Fig. 6.5(c)], and an X-type logical operator is a string of X operators applied to a column of qubits [Fig. 6.5(d)]. Applying a stabilizer operator to a bare logical operator results in an equivalent bare logical operator. Application of a gauge operator to a bare logical operator results in an equivalent dressed logical operator.

For the distance-d Bacon-Shor code ($d = 3$ in Fig. 6.5), a single X error in a given row will anti-commute with any Z-type stabilizer with support in that row and will therefore have the same syndrome as all other X errors in that row. This ambiguity does not cause any problem for error correction as X errors belonging to the same row differ from each other by a gauge generator, and thus are corrected by the same procedure: applying a single X operator to one qubit in the row. In order to find each stabilizer measurement outcome, it is enough to measure the d two-qubit gauge generators and multiply the outcomes (*e.g.*, three two-qubit measurements for the $d = 3$ code shown in Fig. 6.5). Single-qubit Z errors can similarly be identified by finding the eigenvalues of the stabilizer generators, and corrected by applying a single Z operator to any qubit in the same column.

In the following, we imagine a distance-d Bacon-Shor code implemented in a tetron-like architecture using $4d^2$ MZMs. The jth qubit hosts four MZMs, $\gamma_{j,1}$, $\gamma_{j,2}$, $\gamma_{j,3}$, $\gamma_{j,4}$, and we identify the corresponding Pauli operators as

$$X_j \sim \gamma_{j,2}\gamma_{j,3}, \quad Y_j \sim \gamma_{j,1}\gamma_{j,3}, \quad Z_j \sim \gamma_{j,1}\gamma_{j,2}. \tag{6.36}$$

(When analyzing noise model PMC, we will alter this definition to take into account the

geometric arrangement of the MZMs on the island, see Fig. 6.11. Specifically, we use the parity conservation of the ground state so that $X_j = \gamma_{j,1}\gamma_{j,4}$ or $\gamma_{j,2}\gamma_{j,3}$ depending on whether a tetron is in a joint measurement with its left or right neighbor; similarly $Z_j = \gamma_{j,1}\gamma_{j,2}$ or $\gamma_{j,3}\gamma_{j,4}$ depending on whether a tetron is in a joint measurement with its top or bottom neighbor.) Using Eq. (6.36), we can map each Pauli operator to a MZM-parity measurement. Furthermore, we assume that corrections are applied as *Pauli frame updates*: rather than actually applying an operator to correct an error, we classically track measurement outcomes and appropriately reinterpret subsequent measurement outcomes. As such, we can assume corrections are perfect, since faulty measurements are already taken into account.

We can choose to apply all Z corrections (Pauli frame changes) to the qubit in the appropriate column in the top row and all X corrections to the qubit in the appropriate row in the left column. The stabilizer measurements are decoded by assuming that the minimal number of Pauli errors corresponding to a given syndrome have occurred (we will explain how to treat measurement bit-flips in the next section). For the $d = 5$ Bacon-Shor code, any two-qubit Pauli error can be corrected in this way [12], see Fig. 6.6(a) for an example. However, some three-qubit Pauli errors will be misdiagnosed by this decoding scheme, and can result in a logical operator being applied to the system after the correction step, see Fig. 6.6(b). In this case, the quantum information stored in the code has changed, resulting in a failure of the protocol.

Note that the stabilizer measurements do not distinguish between the even and odd parity subspaces of the qubits: this can be seen with the mapping in Eq. (6.36) by noting that $\gamma_{j,4}$ does not change any of the stabilizer outcomes. Therefore, every error involving an odd number of

Majorana operators has the same syndrome as some error involving an even number of Majorana operators. Using the decoder described in the previous paragraph, all syndromes will be interpreted as corresponding to an error involving an even number of Majorana operators, thus the correction step (applying an X operator to a qubit in the left column or a Z operator to a qubit in the top row) will not return the system to the even parity subspace. However, when the system relaxes back to the ground state in a later time step, it either does this through application of a Majorana operator that does not change the stabilizer measurement outcomes (in which case the environment has self-corrected), or the stabilizer measurements are altered and the error correction procedure now identifies the Pauli error resulting from the combined initial excitation-intermediate correction steps-relaxation processes. Note that when the excitation-relaxation process extends over more than one time step the outcome of subsequent stabilizer measurements might disagree. For example, an initial $\gamma_{j,2}$ excitation would be interpreted as a Y_j error. If there is a subsequent relaxation to, say, $\gamma_{j,3}$ the combined process corresponds to an X_j error. The above process can lead to misinterpretation of the error and can therefore be thought as contributing to measurement errors, which we discuss more in Section 6.4.4. We say that the protocol works if the correction step after the system has returned to the even parity subspace (possibly in a later time step) has applied a stabilizer operator. Conversely, if the correction step after the qubit returns to the even parity subspace results in a logical error, the protocol fails.

6.4.3 Fault tolerant error correction

A distance-d error correcting code could be used to protect against up to $(d-1)/2$ errors with a single round of perfect measurements. To account for the fact that some noise models can have imperfect measurements, a framework known as fault-tolerant error correction has been developed. This framework distinguishes between *faults* and *errors*:

- A *fault* is any noise event that adversely disturbs the system or the measurements.
- An *error* is any non-trivial operator applied to a qubit.

For a qubit-based model, a fault corresponds to any non-trivial noise event (including measurement bit-flips) and an error is some single-qubit Pauli operator (we will generalize the discussion to Majorana noise models at the end of this section and clarify what is meant by a noise event that "adversely disturbs the system"). Faults are defined with respect to a given noise model; we illustrate this point by considering the qubit-based noise models Pauli noise with bit-flip measurement and Pauli circuit noise. For the former, a single fault is either a single-qubit Pauli operator or a measurement bit-flip. For the latter, a single fault can be a single-qubit Pauli operator, a two-qubit Pauli operator, or a measurement bit-flip. Notice that if a noise model includes correlated events, a single fault can result in multiple errors.

For a given qubit-based noise model, the requirement that the error correction procedure is *fault-tolerant* amounts to satisfying the following conditions [112]:

1. (EC A): For any initial state (irrespective of whether or not it is a code state), a single fault that can occur anywhere during the error correction procedure results in an output

which differs from a code state by at most $(d-1)/2$ errors.

2. (EC A'): For an initial error-free code state, a single fault that can occur anywhere during the error correction procedure outputs the error-free code state.

3. (EC B): If the error correction proceeds without additional faults, any code state with $(d-1)/2$ errors will be corrected.

If the noise is sufficiently weak, information stored in a fault-tolerant error correcting code is better-protected than information stored directly in a physical qubit. The performance of a fault-tolerant error correction scheme can be quantified by the *pseudo-threshold*, defined for a noise model characterized by a single parameter p by

$$p_{\text{th}} \equiv \max\{p | p_{\text{err}}(p) \leq p\}, \tag{6.37}$$

where p_{err} is the logical error rate, *i.e.*, the probability of an uncorrectable error remaining in the system after the application of strength-p noise and error correction. The pseudo-threshold will depend on the noise model, the error correcting code, and the error-correction protocol. A pseudo-threshold is defined for a particular error correcting code on a fixed number of qubits, in contrast to a *threshold* which is defined for a family of error correcting codes, each for different system size (*i.e.*, a different number of physical qubits). The threshold is the limit of the pseudo-threshold for infinitely large system size. The Bacon-Shor code family does not have a finite threshold.

For a Majorana-based system, any non-trivial string of Majorana operators applied to a single island results in an error. A fault is more subtle. For instance, some noise events are a

result of the system relaxing back to the even parity ground state. This relaxation does not necessarily occur within the same time step as excitation, which is why our models include noise events involving an odd number of Majorana operators (*i.e.*, quasiparticle and odd correlated events). When using a qubit-based code (*i.e.*, a code that only corrects for Pauli errors on the qubits) to error correct a Majorana-based system, it is essential for the environment to relax the system to the even parity ground state so that the net operator applied to any island involves an even number of Majorana operators (and therefore corresponds to some Pauli operator). This motivates a careful specification of what is considered "adversely disturbing the system" in the definition of a fault. If an island begins a time step in the odd parity state and a quasiparticle event relaxes the island back to the even parity state, this noise event is beneficial to the error correction protocol and is thus *not* considered a fault. Conversely, if an island begins or ends a time step in the odd parity state, the lack of a relaxation *is* a fault. For all the Majorana noise models presented in Section 6.2, any non-trivial noise event applied during steps 1 or 2 correspond to a fault; a quasiparticle event applied in step 0 is not a fault; and not applying a quasiparticle event in step 0 is a fault.

With the above understanding of what constitutes a fault and what constitutes an error, fault tolerance conditions (EC A)-(EC B) apply to a Majorana-based system. Note that "a single fault" in conditions (EC A) and (EC A') implies that if the fault corresponds to a quasiparticle or odd correlated event in a time step, the excitation is immediately relaxed in the subsequent time step. Similarly, "without additional faults" in condition (EC B) implies that if the code state with $(d-1)/2$ errors is in an odd parity state, then the system is relaxed to the even parity

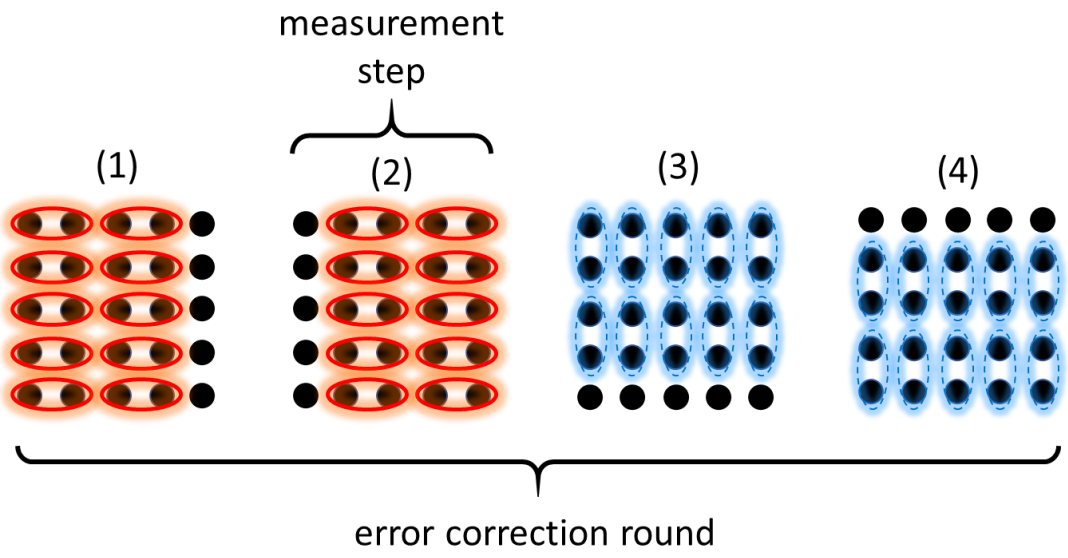

Figure 6.7: Measurement steps for a single error correction round of the $d = 5$ Bacon-Shor code. Same legend as Fig. 6.5, black dots correspond to qubits, red ovals denote X measurements, blue dashed ovals denote Z measurements. Each step involves the measurement of two stabilizers built out of five gauge generator measurements. Four measurement steps are necessary (for arbitrary d) for a single error correction round. As discussed in the main text, faulty measurements can be corrected by repeating each error correction round at least four times. One might, in principle, be able to do multiple measurements on a single qubit and thereby reduce the number of measurement steps required; however, this is inadvisable as it allows correlated errors to spread over longer distances.

state in the subsequent time step.

6.4.4 Numerical results

In this section, we analyze fault-tolerant error correction circuits for storing a qubit using the $d = 5$ Bacon-Shor code under the Majorana noise models presented in Section 6.2. We define the parameters of each noise model according to Table 6.2, so that we can easily scale the probability of a logical error p_{err} as a function of the probability p_0 of an excitation of an idle island. The analogous qubit noise models are found by setting the probability of all errors

involving an odd number of Majorana operators to zero (equivalently, by setting the relaxation parameter r from Section 6.3.3 to zero).

An exhaustive simulation of all possible errors to find the exact pseudo-threshold p_{th}^{A} of a noise model A quickly becomes intractable. We therefore follow a Monte Carlo approach of simulating n_{trials} runs for a single error correction round to estimate $p_{\text{err}}(p_0)$ from the fraction of trials which result in a logical error we extract

$$p_{\text{err}}(p_0) = \frac{n_{\text{fail}}}{n_{\text{trials}}}. \tag{6.38}$$

The uncertainty of $p_{\text{err}}(p_0)$ for a given p_0 is of order $1/\sqrt{n_{\text{trials}}}$.

The Majorana noise models Qp, QpBf, and MC are designed without respect to a specific physical measurement protocol. Thus, when simulating pseudo-thresholds for these three models, we define measurements according to Eq. (6.36), *i.e.*, without considering the geometric arrangement of MZMs within a tetron. In contrast, model PMC is designed with the measurement protocol of Section 6.3.1 in mind; as such when analyzing this model we redefine the measurements to account for a convenient physical implementation of the Bacon-Shor code.

There are three main differences between our simulations of models MC and PMC and the most realistic approach to estimating optimal pseudo-threshold values. (The simple models Qp and QpBf will clearly not estimate realistic pseudo-threshold values as they do not include all lowest order noise events in a Majorana-based system.) Firstly, to help the simulations run faster, we do many trial runs of a single error correction round, rather than simulating many rounds and analyzing the frequency of logical errors being applied. [7] The latter approach is

[7] This approach allows us to speed up the run time by using importance sampling for the first error.

a more accurate description of noise in an actual system because it feeds the errors from a previous error correction round into the next. However, feeding errors into the next time step is only important when the system has the unlucky combination of an error going undetected (*e.g.*, from occurring in one of the later time steps of an error correction round and thus being identified as a measurement bit-flip) followed by enough additional errors occurring in the next error correction round to result in a logical error. When the noise event rate is sufficiently small, the difference between simulating many error correction rounds and repeatedly simulating a single round will only result in a small correction to the pseudo-threshold estimates. Details of the code used for simulating the pseudo-thresholds can be found in Ref. [152].

Secondly, to correct for faulty measurements, we use the Shor error correction approach [235] of repeating stabilizer measurements multiple times in a single error correction round. Generally, Steane error correction [243], which uses entangling gates (*e.g.*, CNOTs) of the logical data qubit with logical ancilla qubits to locate errors, results in higher threshold estimates (in part because the effort of error correction is shifted from operations on the data qubits to preparation of ancillas [112]). Steane error correction is only known to apply to stabilizer codes, which means that in order to do Steane error correction on the Bacon-Shor code we must fix the gauge subsystem and thereby lose the ability to build stabilizer measurements out of two-qubit measurements. Furthermore, the logical ancillas (tripling the number of tetrons) and multiple CNOT gates (each using an additional ancilla tetron and multiple measurements [141]) needed for Steane error correction quickly complicate the pseudo-threshold simulations.

Finally, we include correlated events, which reduces the number of faults that can be cor-

rected for models MC and PMC because two faults can result in a logical error (*e.g.*, a correlated event plus a pair-wise dephasing event can implement Pauli errors on three islands). We could have avoided correlated events reducing the code distance by using measurement gadgets [112], which use CNOT gates and ancilla tetrons to ensure that any correlated event only affects one data tetron. However, measurement gadgets introduce more opportunities for a fault to occur within an error correction round due to both the introduction of ancilla tetrons and because CNOT gates require three measurements for a tetron architecture [141]. It is therefore not clear whether measurement gadgets would improve the error correction for tetron-based architectures.

Given the above considerations, we believe the pseudo-threshold estimates for models MC and PMC in this section are below their optimal values and should not be taken as experimental targets. Our analysis should rather be taken as indication of the relative importance of the different noise events (quasiparticle, measurement, correlated, and pair-wise dephasing) on the pseudo-threshold. In Section 6.6, we identify future directions of study that could improve simulations of the noise models presented in this paper and result in more accurate pseudo-threshold estimates. We explicitly discuss experimental implications of our analysis at the end of this section.

Quasiparticle noise with perfect measurement (Qp)

Model Qp is the simplest stochastic Majorana noise model given in Section 6.2, in which only pair-wise dephasing events or quasiparticle events can occur. We define measurements according to Eq. (6.36). The relative distribution of quasiparticle events and pair-wise dephasing

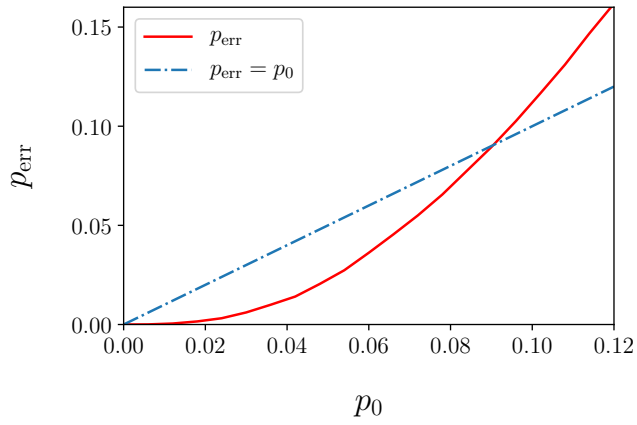

Figure 6.8: Logical error rate p_{err} (solid red curve) as a function of the noise event rate p_0 for the Qp noise model (see Table 6.2). The dot-dashed blue line indicates no error correction. The pseudo-threshold is the intersection of the two curves: $p_{\text{th}}^{\text{Qp}} \approx 0.09$. This plot was generated for 10^5 Monte Carlo trials per data point.

events can be adjusted by varying the relaxation parameter r, see Table 6.2. In the limit $r = 0$, Qp reduces to the qubit model Pauli noise (or code capacity noise).

The standard procedure for calculating pseudo-thresholds for Pauli noise is to consider a noisy time step, followed by perfect application of all stabilizer measurements (*i.e.*, errors cannot occur between the four different measurement steps displayed in Fig. 6.7). We implement the same procedure for Qp, however, since the syndrome of a quasiparticle event after a single time step is identical to that of some pair-wise dephasing event, a single time step of Qp is not able to distinguish quasiparticle events from pair-wise dephasing events. The r-dependence of the model will therefore only become apparent after simulating multiple time steps, for instance by considering several error correction rounds or by modeling application of a logical gate (not included in this paper). We do not simulate multiple time steps for Qp, as the simulations of QpBf and MC clearly indicate that the pseudo-threshold only has weak r dependence.

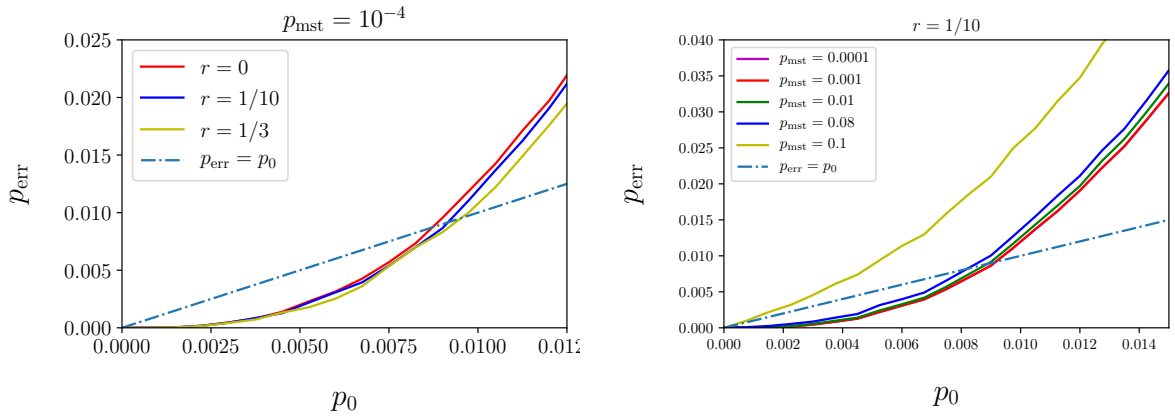

Figure 6.9: Pseudo-threshold simulation results for the QpBf noise model varying r (*top*) and p_{mst} (*bottom*) (see Table 6.2). Solid curves are the logical error rate as a function of the noise event rate p_0, dot-dashed blue lines indicate no error correction, and the pseudo-threshold for each choice of parameters r and p_{mst} is their intersection. These plots were generated for 1.5×10^5 Monte Carlo trials per data point. See text for discussion of results.

The pseudo-threshold estimate under Qp (and Pauli noise) for a single time step is $p_{\text{th}}^{\text{Qp}} \approx 0.09$ (see Fig 6.8).

Quasiparticle noise with bit-flip measurement (QpBf)

The model QpBf builds on the previous model Qp by allowing the classical bit storing the measurement outcome to be flipped. We define the error probabilities in Table 6.2 and the measurements according to Eq. (6.36). For this noise model, we repeat the four measurement steps comprising a single round of error correction in order to avoid introducing errors into the code state from a single measurement bit-flip (*i.e.*, we use a Shor error correction scheme). Our procedure is to consider a single (noisy) time step preceding each error correction round, repeated four times. We again apply all stabilizer measurements simultaneously, as in the Qp simulation. If the repetition rounds result in different syndromes, we accept the last syndrome

which repeats for two consecutive rounds. When multiple errors occur, it is possible that no two consecutive rounds will have the same syndrome. In this case, we assume the syndrome for the fourth round.

The pseudo-threshold dependence on r and p_{mst} is shown in Fig. 6.9. In the top panel, we see weak dependence on r, with $p_{\text{th}}^{\text{QpBf}} \approx 8 \times 10^{-3}$ for $0 \leq r \leq 1/3$ and $p_{\text{mst}} = 10^{-4}$. It follows that under this noise model, the $d = 5$ Bacon-Shor code is insensitive to the relative distribution of quasiparticle and pair-wise dephasing events. Intuitively, we can understand this result as follows: in the parameter regime considered, the environment relaxes each island with high probability, thereby converting quasiparticle events in one time step to pair-wise dephasing events in the subsequent time step. A pair-wise dephasing event in one time step does not have a significantly different effect than a pair-wise dephasing event broken into two time steps. As noted in Section 6.3.3, larger r is not captured by model QpBf and would be highly problematic (see Sections 6.5 and 6.7), requiring a Majorana fermion code to efficiently correct a single excitation [48, 122, 255].

The bottom panel of Fig. 6.9 shows the pseudo-threshold dependence on p_{mst} for $r = 1/10$. The logical error rate, and therefore the pseudo-threshold, have much weaker dependence on p_{mst} than on p_0. Intuitively, this insensitivity to measurement bit-flip can be understood as a direct consequence of the repetition of stabilizer measurements: a measurement bit-flip must be repeated in order to show up in the accepted syndrome, whereas a quasiparticle or pair-wise dephasing event occurring in the first time step will affect all subsequent syndromes. We expect p_{mst} to contribute significantly to p_{err} when $p_{\text{mst}} \gtrsim \mathcal{O}\left(\sqrt{p_0}\right)$ [8]. This estimate is consistent with

[8] One example scenario in which measurement bit-flips contribute to a failure of the error correction protocol

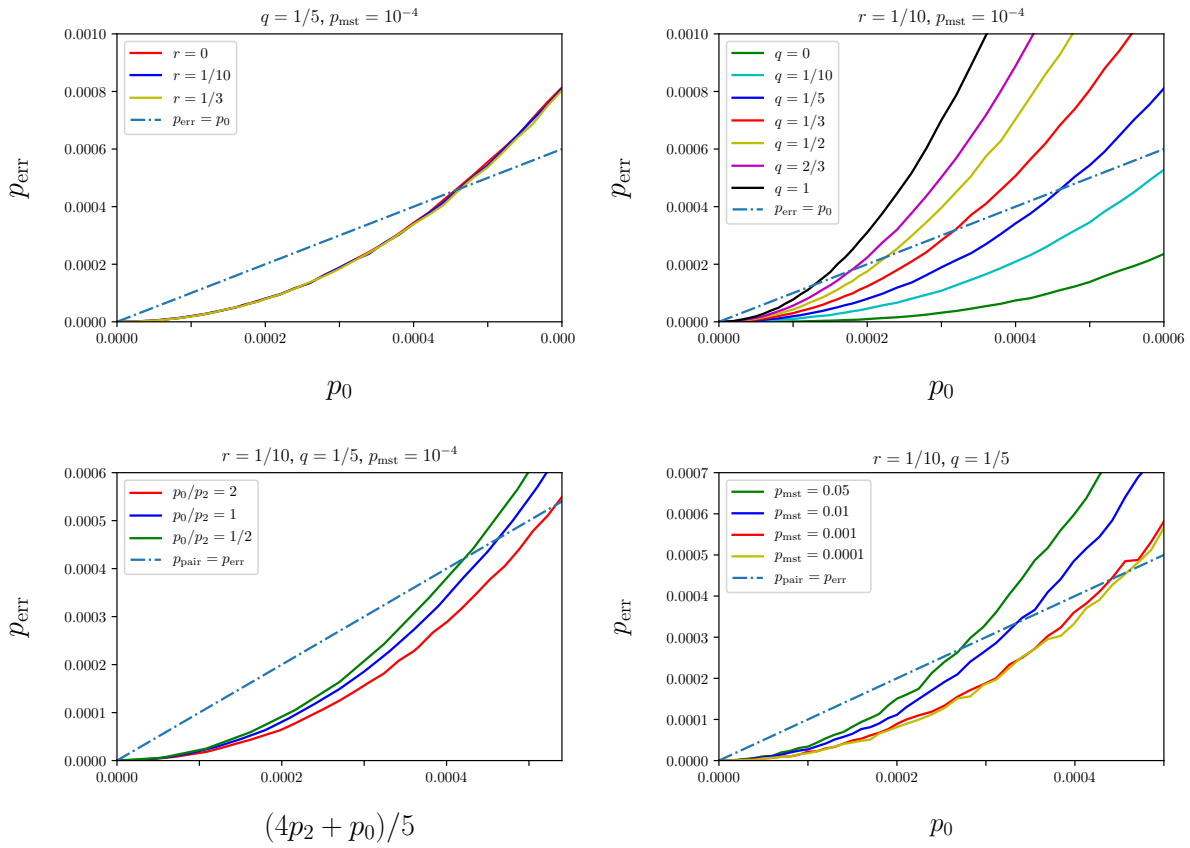

Figure 6.10: Pseudo-threshold simulation results for the MC noise model varying r (*top left*), q (*top right*), p_2 (*bottom left*), and p_{mst} (*bottom right*) (see Table 6.2). Solid curves are the logical error rate as a function of the noise event rate per qubit (averaged over the 20 measured qubits and 5 idle qubits in the system), dot-dashed lines indicate no error correction, and their intersections denote the pseudo-threshold for those parameter choices. In the top right panel, the pseudo-threshold for $q = 1/10$ is $\approx 6.5 \times 10^{-4}$, and for $q = 0$ is $\approx 9.8 \times 10^{-4}$. See text for discussion of the results. The first three plots were generated for 10^8 effective Monte Carlo trials per data point and the bottom right plot was generated for 10^7 effective Monte Carlo trials per data point.

the approximately constant value $p_{\text{th}}^{\text{QpBf}} \approx 8 \times 10^{-3}$ for $p_{\text{mst}} = 10^{-4} - 10^{-2} \ll \sqrt{p_{\text{th}}^{\text{QpBf}}}$, and the sharp pseudo-threshold decrease when $p_{\text{mst}} = 0.08 \approx \sqrt{p_{\text{th}}^{\text{QpBf}}}$. The insensitivity to p_{mst} is

is if two single qubit errors occur in the first time step, *e.g.*, x errors on qubits in different columns, and a measurement bit-flip occurs for a qubit in a different column in *both* the second and third time step (or both the third and fourth time steps). The same logical error could instead occur if three x errors affecting qubits in different columns occur in the first, second, or third time steps. The two scenarios are similarly probable when $p_{\text{mst}}^2 \sim \mathcal{O}(p_0)$.

independent of whether or not there are MZMs in the system and should apply generally to any error correction scheme that relies on repetition to correct for measurement bit-flips. A similar result was found in the context of the surface code built from qubits subjected to Pauli noise with bit-flip measurement in Ref. [119]: for small Pauli error probability ($p_0 < 0.01$), the probability of a stabilizer measurement bit-flip could approach 50% without strongly affecting the logical error rate. In comparison, the probability of a stabilizer measurement bit-flip here is $1 - (1 - p_{\text{mst}})^{10}$, which equals 50% for $p_{\text{mst}} \approx 0.07$.

Finally, we note that in the regime of weak p_{mst} dependence, the pseudo-threshold estimate for QpBf is approximately consistent with the simulation of Qp if the logical error rate is plotted as a function of $p_0/4$. If we ignore measurement bit-flips, the simulation for QpBf mainly differs from Qp in that there are four time steps before applying the decoder, thus the QpBf simulation roughly quadruples the probability of a noise event compared to the Qp simulation [9].

Majorana circuit noise (MC)

The error probabilities for MC are given in Table 6.2 (here we write q_2 as q). Because we are restricting our analysis to the operations necessary for error correction of quantum memory, during any given time step every island is either idle or involved in a four-MZM measurement with another island. Measurements are still defined according to Eq. (6.36). It is now important to keep track of which islands are involved in a given measurement, therefore we can

[9] This argument is not exact as only errors occurring during the first three time steps will be actively corrected by the error correction protocol.

no longer assume that all stabilizers are applied simultaneously. Rather, each set of stabilizer measurements (see Fig. 6.7) is preceded by a noisy time step, so that a single error correction round is comprised of four time steps and four measurement steps. As for QpBf, faults in the measurement process require repetition and we use the same protocol as before: we accept the last repeated syndrome, or if no syndrome repeats, we assume the syndrome for the last round. Ref. [152] shows this repetition scheme satisfies the conditions for fault tolerance.

The simulation results are plotted in Fig. 6.10. The top left panel shows the dependence on r for $q = 1/5$ (single-qubit errors four times more likely than two-qubit errors), $p_0 = p_2$, and $p_{\text{mst}} = 10^{-4}$. The pseudo-threshold dependence on r is even weaker than was the case for QpBf, and is within noise of the simulation for realistic choices of r (including unphysical values of $r = 1/2$ and 1 does reveal a weak r-dependence). This indicates that the code is insensitive to a redistribution of errors involving an even or odd number of Majorana operators. We stress that the insensitivity of the pseudo-threshold to changes in r is highly dependent on the assumption $e^{-1/r_k} < p_k$ (see Section 6.3.3) that went into the construction of the circuit noise models. If this were not the case, a single excitation in one island could spread throughout the system through correlated events occurring with probability $q \sim \mathcal{O}(1)$. We comment further on architectures where this inequality is not satisfied in Sections 6.5 and 6.7.

The pseudo-threshold's dependence on q is shown in the top right panel of Fig. 6.10 for $r = 1/10$, $p_0 = p_2$, and $p_{\text{mst}} = 10^{-4}$. As is expected from similar studies using qubit noise models, we see that a higher weight of correlated events significantly lowers the pseudo-threshold [248]. When all initial excitations in an island lead to correlated events, *i.e.*, $q = 1$, the pseudo-

threshold $p_{\text{th}}^{\text{MC}} \approx 1.2 \times 10^{-4}$. When half of the errors on a measured island are from correlated event processes, *i.e.*, $q = 1/2$, the pseudo-threshold increases to the $p_{\text{th}}^{\text{MC}} \approx 4.5 \times 10^{-4}$. Finally, in the limit of no correlated events, *i.e.*, $q = 0$, the pseudo-threshold is $p_{\text{th}}^{\text{MC}} \approx 9.8 \times 10^{-4}$. This last limit agrees with the simulation results for Qp and QpBf by scaling the x-axes of Figs. 6.8 and 6.9 by factors of $1/16$ and $1/4$, respectively, to account for the factor of four increase in the number of time steps that can contribute to a logical error compared to the QpBf simulation.

The bottom left panel of Fig. 6.10 plots the pseudo-threshold for $p_2 = p_0/2,\ p_0,$ and $2p_0$ with $r = 1/10$, $q = 1/5$, and $p_{\text{mst}} = 10^{-4}$. In order to keep the total probability of an error fixed, the x-axis is now given by $(p_0 + 4p_2)/5$, the average rate of creating an excitation in the $d = 5$ system. The pseudo-threshold is lower for $p_2 > p_0$, which is consistent with our expectation that a higher percentage of correlated events should decrease the pseudo-threshold. This dependence is not especially strong, which can be understood as resulting from the small ratio (1/5) of islands that are idle in any given time step.

Finally, we show the pseudo-threshold dependence on p_{mst} in the bottom right panel of Fig. 6.10 for $r = 1/10$, $q = 1/5$, and $p_0 = p_2$. The curves for $p_{\text{mst}} = 10^{-4}$ and $p_{\text{mst}} = 10^{-3}$ are essentially within noise of each other, and only for $p_{\text{mst}} \gtrsim 10^{-2} \sim \mathcal{O}\left(\sqrt{p_0}\right)$ does the pseudo-threshold depend noticeably on p_{mst}. The intuition is the same as for model QpBf: measurement bit-flips must be repeated over successive stabilizer measurements in order to affect the accepted syndrome and influence the correction procedure.

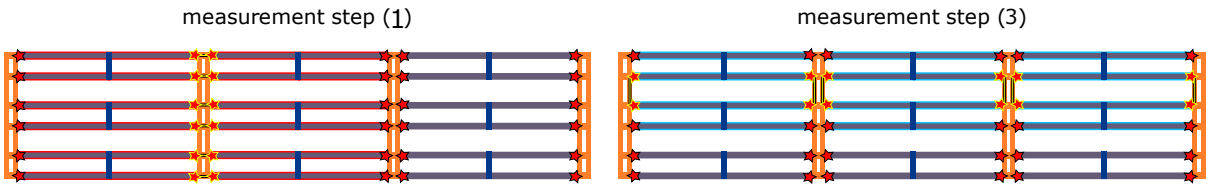

Figure 6.11: Measurement steps (1) (*top panel*) and (3) (*bottom panel*), see Fig. 6.7, for the $d = 3$ Bacon-Shor code implemented for a system of tetrons. Measured MZMs are highlighted in yellow. Tetrons involved in XX measurements between horizontal nearest neighbors are highlighted in red, tetrons involved in ZZ measurements between vertical nearest neighbors are highlighted in blue. The PMC simulation takes into account the geometrical arrangement of MZMs on a tetron, so that different MZMs on the left and right islands are measured in an XX measurement, and different MZMs on the top and bottom islands are measured in a ZZ measurement, see Eqs. (6.39) and (6.40).

Physical Majorana circuit noise (PMC)

For PMC, we follow the same protocol as for MC: every time step is followed by a stabilizer measurement and we repeat the error correction round four times (for a total of 16 time steps, 16 stabilizer measurements, and four sets of syndromes). We assume the last syndrome which repeats twice is correct; if no two syndromes are repeated, we assume the last syndrome.

As noted at the end of Section 6.3.3, models PMC and MC applied to a system of tetrons with $p_0 = p_2$ only differ in a slight redistribution of the odd correlated events. However, since PMC is defined with a particular physical implementation in mind and keeps track of which MZMs are involved in a measurement, we now take into account the geometric arrangement of MZMs on an island to define the measurements. We replace Eq. (6.36) with the following definitions of an XX measurement of horizontal nearest neighbor tetrons and a ZZ measurement

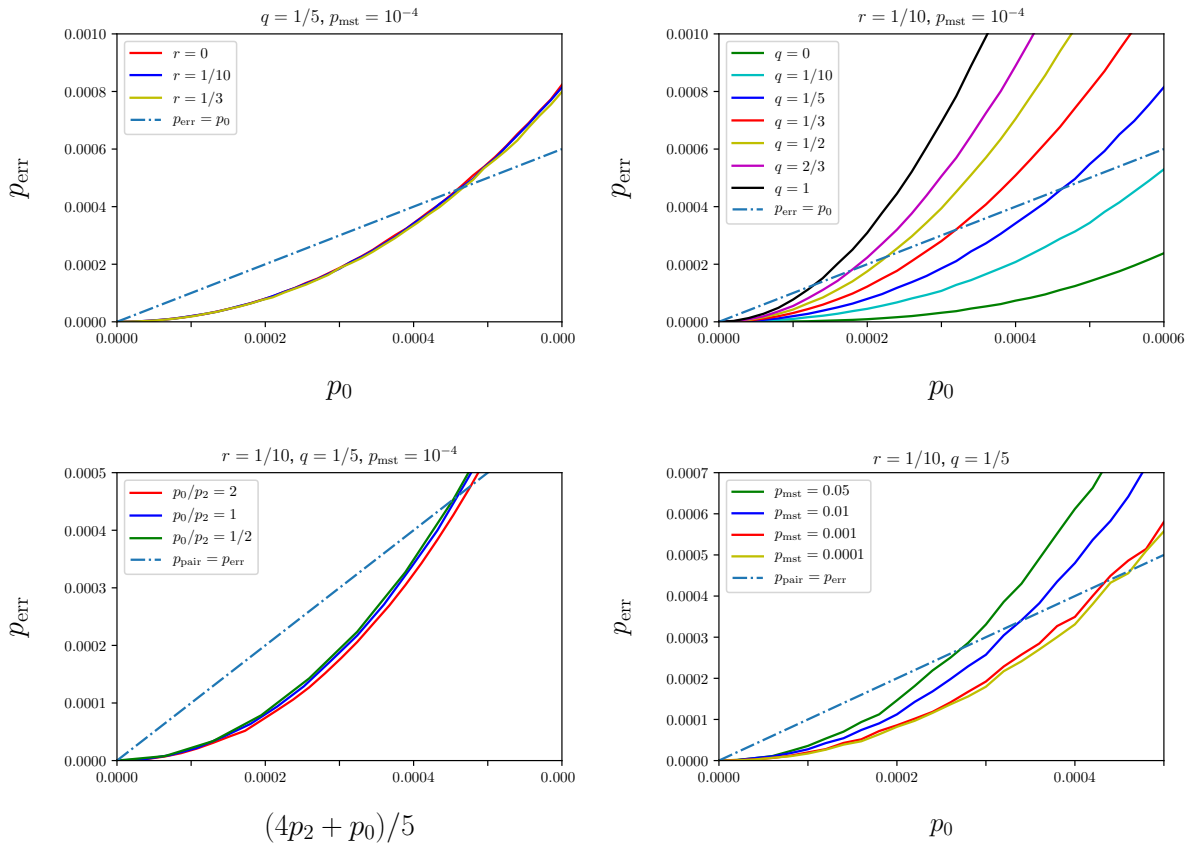

Figure 6.12: Pseudo-threshold simulation results for the PMC noise model varying r (*top left*), q (*top right*), p_2 (*bottom left*), and $p_{\rm mst}$ (*bottom right*) see Table 6.2). Solid curves are the logical error rate as a function of the noise event rate per qubit (averaged over the 20 measured qubits and 5 idle qubits in the system), dot-dashed lines indicate no error correction, and their intersections denote the pseudo-threshold for those parameter choices. See text for discussion of the results. The first three plots were generated for 10^8 effective Monte Carlo trials per data point and the bottom right plot was generated for 10^7 effective Monte Carlo trials per data point.

of vertical nearest neighbor tetrons (see Fig. 6.11):

$$X_j X_{j+1} = \gamma_{j,2}\gamma_{j,3}\gamma_{j+1,1}\gamma_{j+1,4} \tag{6.39}$$

$$Z_j Z_{j+5} = \gamma_{j,3}\gamma_{j,4}\gamma_{j+5,1}\gamma_{j+5,2}. \tag{6.40}$$

Note that now, for every tetron not located at a corner, each MZM on that tetron is involved in at least one measurement. This is a departure from the case where one MZM (e.g., $\gamma_{j,4}$) is not touched by any measurement and prevents a one-to-one mapping of quasiparticle events and Pauli errors. In particular, a single-MZM error can lead to measurement syndromes that are not described by a local Pauli error. Equations (6.39) and (6.40) are more convenient measurements to implement physically; however, there is no fundamental limitation to implementing measurements described by Eq. (6.36) if the tetron architecture includes additional ancilla islands to facilitate longer-range measurements [141].

The PMC simulation results are shown in Fig. 6.12. The r-dependence, q-dependence, and p_{mst}-dependence of the logical error rate are shown in the top-right, top-left, and bottom-right panels, respectively. These plots are not noticeably different from those in Fig. 6.10 for the MC noise model, indicating that the redistribution of odd correlated errors (due to the difference between models MC and PMC) and the measurement redefinition have little effect on the pseudo-thresholds.

The bottom-left panel of Fig. 6.12 plots the logical error for $p_0/p_2 = 2, 1, 1/2$ with $r = 1/10$, $q = 1/5$, and $p_{\text{mst}} = 10^{-4}$. The x-axis, $(4p_2 + p_0)/5$, is chosen for easy comparison to model MC but is no longer the average rate of creating an excitation (the probability some of the noise events in PMC on a measured island are independent of p_2). As expected, increasing p_2 worsens the logical error rate because it increases the relative distribution of correlated events, but it does so to a smaller degree than for MC since fewer of the noise events depend on p_2.

6.4.5 Experimental implications

The pseudo-threshold calculations in the previous section have important implications for experimental realizations of a tetron-based quantum computing architecture. In the limit of a hard superconducting gap and large charging energy, *i.e.*, $T \ll \min(\Delta, E_C)$, quasiparticle events are rare and the noise model PMC is a reasonable description of the most-likely error sources in the system. The weak dependence of the pseudo-threshold on r in this regime indicates that once quasiparticle events are sufficiently rare and the relaxation time is less than one tenth of the four-MZM measurement time, it is not essential to further suppress the quasiparticle poisoning rate.

A second important experimental implication regards the tradeoff between correlated and measurement errors. Statistical errors in the measurement contribute to the probability p_{mst} in our noise models. For the same length of measurement time, larger measurement visibility, which is controlled by the tunneling amplitude between the quantum dot and MZMs (see Section 6.3.1), results in smaller statistical error and hence smaller p_{mst}. Conversely, the parameter q controlling the relative distribution of single-qubit and two-qubit errors increases with tunneling amplitude [see Eqs. (6.21), (6.22) and (6.26)]. Thus, we see a tradeoff in which reducing the tunneling amplitude can suppress correlated events at the expense of increasing measurement errors. However, the pseudo-threshold results indicate that, at least for Shor error correction of quantum memory, correlated events have a much stronger effect on the pseudo-threshold than do measurement bit-flips. Therefore, it is desirable to work with a smaller tunneling amplitude from the point of view of the pseudo-threshold. Reference [248] reached a similar conclu-

sion about the relative importance of two-qubit errors compared to measurement errors for small-distance surface codes. The tradeoff of measurement and correlated errors is particularly interesting when also considering different error correcting codes that might provide certain advantages but introduce stronger correlated errors due to higher-weight measurements.

As noted earlier, the pseudo-threshold estimates in this paper prioritize simplicity of simulation over optimal magnitude, and should therefore not be interpreted as quantitative experimental targets. However, if the correlation parameter q can be reasonably estimated for a given system, then previous studies using the qubit-based model Pauli circuit noise are applicable. For instance, if $q \sim 1/15$, then Ref. [72] suggests a pseudo-threshold for the $d = 5$ Bacon-Shor code $\mathcal{O}\left(10^{-3}\right)$ (with Steane error correction).

6.5 Extensions

We now discuss how the noise models can be modified to describe other Majorana-based systems. The physical error sources we considered (thermal excitation, extrinsic quasiparticle poisoning, fluctuations in the MZM hybridization energies, error in the measurements) are ubiquitous to all Majorana-based quantum computing architectures. Therefore, quasiparticle events, pair-wise dephasing events, and measurement bit-flips, as well as the corresponding probabilities $p_{\text{qp}}^{(k)}, p_{\text{pair}}^{(k)}$, and $p_{\text{mst}}^{(k)}$, respectively, should be present in any realistic stochastic Majorana noise model. The maximal number of MZMs involved in a parity measurement will vary depending on the proposal, therefore the allowed integer values of k will be system-dependent. Furthermore, the degree to which a particular proposal is susceptible to these errors will depend

on experimental parameters of the system, including the size and gap of the superconducting islands, whether or not the island has a charging energy, and what potential quasiparticle reservoirs (*e.g.*, metal or superconducting leads, quantum dots) are present.

The main assumption of all four Majorana noise models introduced in Section 6.2 regards the energy separation between even and odd parity states of the underlying quantum computing architecture. More specifically, we assume the system is divided into superconducting islands and that the environment relaxes islands with odd Majorana parity to the even parity subspace within a time step with high probability. When this is not the case, *e.g.*, for grounded superconducting islands [120, 252, 129], step 0 of the Majorana noise models needs to be modified. In such systems, a single quasiparticle excitation can be long-lived, and multi-island stabilizer measurements can propagate the excitation throughout the system, see Section 6.7.

Qubit-based error correcting codes are less effective in a MZM system with long-lived quasiparticle excitations. If the error correcting measurements introduce connected paths of islands spanning the system, a single quasiparticle excitation can cause a logical error within a time step. Therefore, in this scenario, the measurements must be carefully designed to minimize the spread of high-weight errors through quasiparticle excitations. Provided there is still a finite relaxation rate, the probability for an excitation not to relax over a full time step is $\exp\{-1/r\}$. Thus, if measurements are designed so that excitations can only travel to neighboring islands in a time step [10], the probability for a single excitation to travel through d (the code distance) islands (possibly resulting in a logical error) is $\exp\{-(d-1)/2r\}$. For d-large, this probability becomes vanishingly small and the qubit-based code retains some error cor-

[10] Note that the Bacon-Shor code already utilizes this clever design by only using two-qubit measurements.

recting ability.

Alternatively, one could use a Majorana fermion code [48, 122, 255] to distinguish odd and even parity states, thereby correcting quasiparticle excitations before they can spread throughout the system. Such codes require the ability to either (1) measure the total parity of the MZMs on an island, or (2) dynamically adjust the number of MZMs on an island, both of which are experimentally challenging for the following reasons. (1) Proposals to date are not able to distinguish the total fermion parity of an island from the total parity associated with the MZMs. The measurements proposed in Refs. [120, 252, 129, 1] measure the total charge on the island, and are thus unable to identify the presence of a thermally excited quasiparticle. Charge measurements of the islands are therefore helpful only if the charge excitations are long-lived while thermal excitations relax sufficiently fast. (2) Dynamically adjusting the number of MZMs on an island requires sufficient tunability of certain experimental parameters (*e.g.*, Josephson energy) to transition from the fully disconnected regime to the fully connected regime: residual coupling in the former can lead to increased probability of correlated events; non-fully connected regions within an island in the latter can result in mutual capacitances leading to higher weight errors, see Section 6.7. Furthermore, the tuning procedure must be done sufficiently slowly and smoothly to avoid introducing diabatic errors into the system [59, 138, 229, 123, 153].

Model PMC was built on the further assumption of single or two-island quantum dot-based measurements involving at most two MZMs per island [208, 141]. Additional correlated events can arise for alternate measurement schemes [120, 252, 129, 175, 255] or if more than

two islands are connected during a measurement. For instance, surface code implementations that rely on eight-MZM stabilizer measurements connecting four islands [158] could result in a correlated event involving any subset of the four islands.

Finally, the pseudo-threshold calculations in Section 6.4 are specific to Shor error correction of quantum memory for a system with four MZMs per island. The pseudo-threshold estimates would likely change for a Steane error correction analysis, if logical operations on the system are included, or if islands have more than four MZMs (*e.g.*, a hexon architecture [141]). The benefit of the Bacon-Shor code is lost for Steane error correction, since the stabilizers could no longer be implemented from two-island measurements. Generally, for a stabilizer code, Steane error correction will estimate higher pseudo-thresholds, however we do not anticipate the change from Shor to Steane error correction to affect the relative importance of quasiparticle and correlated events (r and q dependence). Including logical operations would probably result in a greater dependence on the relative magnitudes of p_0, p_1, and p_2, as the majority of islands would no longer be involved in two-island measurements for each time step. With hexons ($m = 3$), the percentage of correlated events that do not commute with all stabilizer measurements is greater than for the case of tetrons; therefore we expect the pseudo-threshold to have a stronger q dependence. Furthermore, since physical considerations can constrain the number of allowed correlated events in PMC relative to MC, more substantial differences in the pseudo-threshold estimates are possible than were found for the tetron case considered here.

6.6 Conclusions and outlook

The primary goal of this chapter is to connect the underlying physical processes causing errors in a Majorana-based quantum computing architecture to the noise models used for fault tolerance analysis of the system. We developed stochastic Majorana noise models in close analogy to the standard qubit-based noise models generally used in threshold calculations. These Majorana noise models allow for errors involving an odd number of Majorana operators to occur, and have different probability distributions depending on whether a MZM island begins a time step in an even or odd parity state. The result of our analysis is that for quasiparticle-poisoning-protected qubits, the pseudo-threshold estimate for the $d = 5$ Bacon-Shor code under each of the Majorana noise models is well-approximated by the estimate using the analogous qubit-based model. Essentially, when the relaxation parameter $r \lesssim 1/5$, a quasiparticle event in one time step relaxes with high probability in the subsequent time step; the cumulative effect is to apply a Pauli error broken-up over two time steps, which does not dramatically alter the error correcting code's performance. This result does not depend on any particular feature of the Bacon-Shor code, thus we expect it to apply more generally to larger error correcting codes, as well as to error correction of logical gates. It is a positive result that MZM systems with short-lived quasiparticle excitations (*e.g.*, charging-energy-protected qubits) can be analyzed with the simpler qubit-based noise models, as this simplifies numerical simulations and allows for studies of larger error-correction schemes.

Conversely, a MZM system with long-lived quasiparticles cannot be accurately described by a qubit-based noise model. In such a system, an excitation could travel between islands

connected by measurements over several time steps with $\mathcal{O}(1)$ probability, thereby spreading throughout the system. In order to prevent excitations traveling long distances, it is therefore beneficial when performing measurements in parallel to avoid creating connected paths of islands spanning the system. The Majorana noise models developed here could be extended to systems with long-lived excitations (see Section 6.7). The latter make qubit-based codes less efficient and might require a Majorana fermion code for error correction [48, 122, 255] (see discussion in Section 6.5).

A useful observation is that in a Shor error correction scheme, in which stabilizer measurements are repeated to protect against a single measurement bit-flip, the error correcting code can sustain high probabilities of measurement errors without affecting the pseudo-threshold. This result applies equally well to conventional qubit systems. While generally Steane error correction results in higher pseudo-thresholds, if measurement error is a limiting obstacle, Shor error correction could be an attractive alternative.

Our pseudo-threshold analysis further demonstrates that there is a strong dependence on the relative distribution of single-island and correlated events. It is therefore essential that any realistic noise analysis of a given system carefully estimate the rate of transferring excitations between islands so as to choose an appropriate distribution of single-island and correlated events. Furthermore, proposals involving higher-weight measurements (*e.g.*, four-island stabilizer measurements in the surface code) will be subject to higher-weight correlated events that could significantly affect the threshold estimate. The relative importance of correlated errors compared to measurement errors also indicates that it is worth optimizing the measurement

processes so that correlated errors are suppressed even if this reduces the measurement fidelity.

This work is a first step towards comprehensive analysis of the fault tolerance of Majorana-based quantum computing architectures. Future directions of study include understanding to what extent our results hold for both larger error correcting codes and logical gate error correction. Additionally, an important open question is to determine the optimal error correction procedure for Majorana-based quantum computation. This analysis should weigh the experimental feasibility of the quantum error correcting codes under consideration (*e.g.*, ability to perform stabilizer measurements and whether the underlying system needs to be charging-energy-protected) and the physical noise sources affecting the underlying architecture in addition to the usual fault tolerance criteria (*e.g.*, threshold values and ratio of physical to logical qubits). We believe the connections elucidated here between physical error processes in MZM systems and noise models would aid in such an analysis.

6.7 Other errors

We address higher order errors and errors arising from long-lived excitations, which are not essential for the discussion in the main text but could be important in different devices.

6.7.1 Higher order errors

The probabilities defining PMC correspond to the lowest order error processes occurring in a tetron architecture. These lowest order processes include measurement bit-flips and all noise events that involve only a single excitation (one factor of p_k in the language of Fig. 6.4 and

Table 6.2): quasiparticle, pair-wise dephasing, and correlated events. All other errors in the model occur at higher order, that is, with a probability that is the product of probabilities explicitly defined in the model (*i.e.*, a probability $\mathcal{O}\left(p_k^2\right)$). We now justify why other error processes (transitions into higher excited states, other correlated events, or mutual capacitance terms) that are physically present in the system can be absorbed into these higher order terms.

Throughout our discussion, we have only considered the excited states $|e_\Delta\rangle$ and $|e_{C,\pm}\rangle$. In particular, we have neglected an extrinsic quasiparticle tunneling into an above-gap state, states with multiple above-gap quasiparticles, or states with charge $2e$ or higher. Let $\Gamma_{g\to e} = \max\left(\Gamma_{g\to e_\Delta}, \Gamma_{g\to e_{C,\pm}}\right)$. Transitions into all higher energy states are additionally suppressed compared to $\Gamma_{g\to e}$ by a factor $\exp\{-\delta\varepsilon/T\}$, where $\delta\varepsilon$ is the energy difference between the higher excited state and $\max\left(\Delta, E_C\right)$. As $\delta\varepsilon \geq \min\left(\Delta, E_C\right)$, this additional exponential factor makes such a transition a higher order process. For the same reason, a correlated event involving the process $|e_x\rangle \otimes |g\rangle \to |e_x\rangle \otimes |e_x\rangle$ ($|e_x\rangle \in \{|e_\Delta\rangle, |e_{C,\pm}\rangle\}$), is also a higher order process, as it requires two excitations.

For a noise model that gives conservative threshold estimates, it is sometimes beneficial, for the sake of keeping the model simple, to overestimate the probability of lowest order errors, so that multiple lowest order errors capture the effects of additional error processes. As an example, we note that the presence of interactions in the MZM system can lead to an additional error source that we have not explicitly included in our model. So far we have neglected mutual charging energies within a superconducting island, *e.g.*, between the two MZM nanowires comprising a tetron. In the case of tetrons, mutual capacitances are exponentially suppressed in

the number of channels in the superconducting backbone (blue line in the left panel of Fig. **??**) connecting the two MZM nanowires. The remaining small but finite mutual capacitances, however, would add four-(or more)-MZM terms to Eq. (6.6) that involve pairs of MZMs belonging to different tetrons. This capacitance can, depending on the screening properties of the system, fall off as a powerlaw with distance, and could therefore give rise to high-weight errors (errors involving products of $2n$ MZMs with $n \geq 2$) in the MZM system. To justify ignoring these high-weight errors at lowest order in the noise model, we could overestimate the probability $p_{\text{pair}}^{(k)}$ of pair-wise dephasing events so that the probability of an error involving $2n$ MZMs is given by $\left(p_{\text{pair}}^{(k)}\right)^n$.

6.7.2 Long-lived excitations

The Majorana noise models presented in Section 6.2 need to be modified when the system has long-lived excitations (*e.g.*, in the case of islands with small charging energies) to include an additional type of correlated event:

- *Hopping event*: application of two Majorana operators involving two islands connected by a measurement. A hopping event for islands i and j is of the form $\gamma_{i,a}\gamma_{j,b}$.

A hopping event can occcur when an island involved in a k-island measurement begins a time step in the odd parity state and transfers its excitation to another island involved in the same measurement. Such a process is more likely to occur when an excitation is long-lived. Models MC and PMC can be generalized to account for long-lived excitations by modifying step 0 as follows:

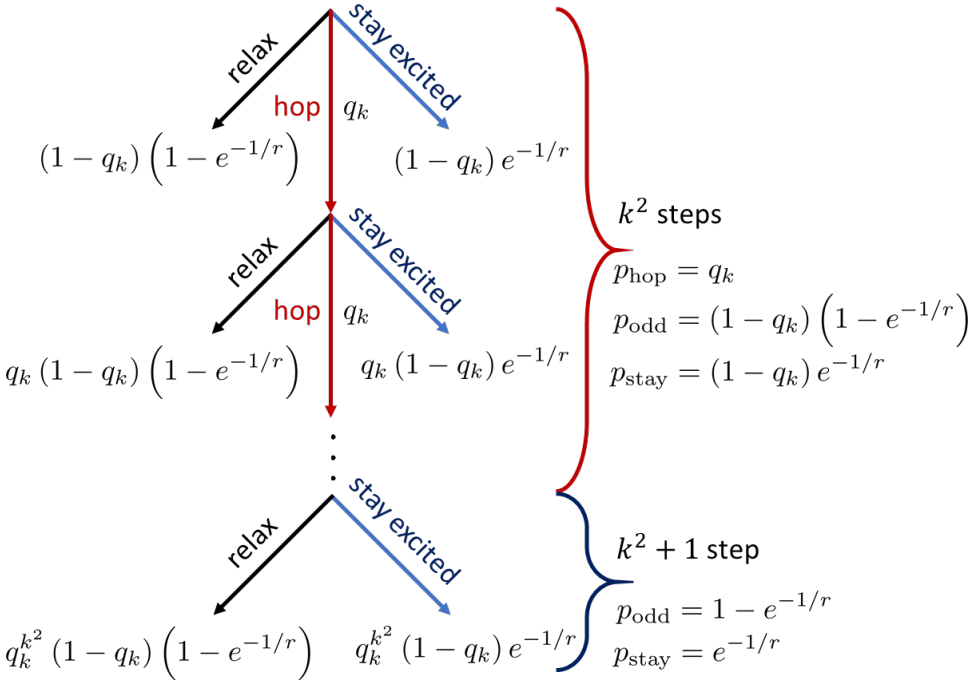

Figure 6.13: Decision tree for the generalized step 0 for models MC and PMC in the case of long-lived excitations. If an island involved in a k-island measurement begins in the odd parity state, it can either relax (left black line) with probability p_{odd}, hop to another island involved in the measurement (center red line) with probability p_{hop}, or remain excited throughout the time step (right blue line) with probability p_{stay}. In the first or the last case, the noise model proceeds as described in the main text to allow for single island noise events, correlated events, or measurement bit-flips. In the latter case, if at least one of the islands involved in the measurement is still in the odd parity state, it again proceeds to the next step of the decision tree (relax, hop, or stay excited). Even for $q_k \sim 1$, the tree can be truncated after k^2 steps where all k island have been visited by the excitation. In the final step the excitation can then be assumed to either relax or stays excited. The probabilities for p_{odd} and p_{stay} are modified for the final step of the decision tree as shown.

0. For the set of islands involved in the same k-island measurement, if at least one of the islands begins the time step with odd parity, do one of the following:

   (a) Apply a hopping event involving an odd parity island with probability p_{hop}, and return to the beginning of step 0.

   (b) Apply a quasiparticle event to an island with odd parity with probability p_{odd}, and proceed to step 1.

   (c) Do not apply any noise events with probablity $p_{\text{stay}} = 1 - p_{\text{hop}} - p_{\text{odd}}$, and proceed to step 1.

The generalized step 0 results in the decision tree depicted in Fig. 6.13. The chance for a large number n_{hop} of hopping events is exponentially suppressed by $q_k^{n_{\text{hop}}}$. Moreover, even for large $q_k \sim 1$, the tree can be truncated, with the final step modified to not include step 0a. For instance, if every island is only directly connected to at most two other islands (as in a tetron measurement), then a hopping event is a random walk through the connected path of islands. After k^2 steps, the average path includes the path involving all islands in the measurement; therefore all possible noise events occurring after $k^2 + 1$ steps can be captured by a more-probable process in a smaller number of steps.

In the language of Section 6.3, the probabilities for the modified step 0 are given by

$$p_{\text{hop}} = q_k, \tag{6.41}$$

$$p_{\text{odd}} = (1 - q_k)\left(1 - e^{-1/r}\right), \tag{6.42}$$

$$p_{\text{stay}} = (1 - q_k)\, e^{-1/r}. \tag{6.43}$$

(If truncating the modified step 0, the probabilities for the final step do not involve q_k, see Fig. 6.13.) Recall that q_k is the probability of an energy transfer between islands connected by a measurement, while r is the probability that an excitation occurring during a time step does not relax before the end of the time step. The probability that an island beginning a time step in the odd parity state does not relax is $e^{-1/r}$.

In the main text, we set $p_{\text{hop}} = 0$. The justification for this approximation is that we assume r is small enough (quasiparticle excitations are short-lived enough) that noise events resulting from a sequence of hopping events are already captured by a sequence of correlated and single qubit noise events. More concretely, one might worry that not including hopping events neglects the possibility that a single excitation can result in a high-weight error spread over several time steps from a quasiparticle traveling between different islands connected by subsequent measurements. Consider, for instance, the following two scenarios leading to a weight-three error: (1) An idle island is initially excited in the first time step, the excitation is transferred to a second island in the second time step and does not relax, and the excitation is transferred to a third island in the third time step and then relaxes. This process applies a pair of Majorana operators on all three islands involved. In an alternative scenario (2) an

idle island experiences no noise events in the first time step, the first and second islands are involved in an even correlated error in the second time step, and the third island undergoes a pair-wise dephasing event in the third time step. Process (1) only requires a single excitations to cause a weight-three error, while process (2) is the most probable implementation of a weight-three error over three time steps that does not involve hopping events. Process (1) occurs with probability

$$p_{\text{qp}} \left(p_{\text{hop}} p_{\text{stay}}\right) \left(p_{\text{hop}} p_{\text{odd}}\right) \tag{6.44}$$

and process (2) occurs with probability

$$\left(1 - p_{\text{qp}} - \frac{3}{4} p_{\text{pair}}\right) p^{(2)}_{\text{cor,even}} p^{(2)}_{\text{pair}}. \tag{6.45}$$

(We assume the first island is idle in the first time step for simplicity, the argument naturally extends if the island is instead involved in a measurement.) Processes (1) and (2) result in the same computational effect for the MC simulation discussed in Section 6.4.4, because the net application of Majorana operators at the end of the third time step are equivalent for (1) and (2), and intermediate steps are interpreted as measurement errors. We are therefore justified in neglecting process (1) when the probability (6.44) is much less than (6.45). This is the case provided

$$p_0 \gg \frac{q}{1-q} \frac{r}{(1-r)^2} e^{-1/r} \left(1 - e^{-1/r}\right) \approx q r e^{-1/r}. \tag{6.46}$$

The simplifying approximation holds for small q and r. For $q = 1/5$ and $p_0 = 10^{-3}$ condition (6.46) is valid provided $r < 1/5$, and for $q = 1/5$ and $p_0 = 10^{-4}$ is valid provided

$r = 1/7$. Note that the r values in Fig. 6.10 were chosen to exaggerate the r dependence of the noise model and do not strictly fall into this regime. Including additional time steps does not result in a stronger condition on the relative size of p_0 and r.

When r is too large to satisfy Eq. (6.46), we need to use the more complicated step 0. In this regime, a single excitation can result in a high-weight error by continually spreading to new islands with each multi-island measurement.

In scenarios with long-lived excitations it becomes crucial to devise a careful measurement protocol to avoid introducing paths of connected islands spanning the system. If errors can only hop to $\mathcal{O}(k)$ nearby islands in a single time step, an excitation will eventually relax before traversing the system if the system size becomes sufficiently large. This implies that, while being less efficient, large qubit-based codes will still be able to correct for long-lived excitations. At some point it might, however, be more practical to use Majorana fermion codes to be able to detect whether an island is in the odd parity state before the excitation can propagate.

Finally, if the quantum computing architecture is built from grounded superconducting islands, an island can spend an equal amount of time in the even and odd parity states. In this case, the probabilities of different noise events are the same regardless of in which parity state the system begins. In this regime, excitations are dominated by extrinsic quasiparticle poisoning events and Eq. (6.24) is modified to

$$p_k = 2m \left(\exp \left\{ \Gamma^{(k)}_{g \to e_C} \tau \right\} - 1 \right). \tag{6.47}$$

In particular, p_k is not exponentially suppressed and all noise events become more likely.

Chapter 7

Review: Fractional Chern Insulators

There is nothing like looking, if you want to find something. You certainly usually find something, if you look, but it is not always quite the something you were after.

-J.R.R. Tolkien, *The Hobbit*

Previous chapters have focused on the potential realization of and challenges facing Majorana-based topological quantum computing. We now turn to a different platform that can host non-Abelian topological defects: fractional Chern insulators (FCIs). We begin by reviewing the fractional quantum Hall (FQH) effect. We are particularly interested in the field theory description of Abelian FQH states, which will be useful for the discussion in the next chapter. We explain how bilayer FQH states can host non-Abelian topological defects known as genons. Next, we consider FCIs, which can be understood as lattice analogs of FQH states. We illustrate some of the interesting properties of FCIs using a toy model introduced by Hofstadter [127].

We then review a recent experiment that observed FCIs in graphene [238], and comment on its implications for future directions.

7.1 Fractional quantum Hall effect

Electrons confined to move in two dimensions in the presence of a magnetic field $\mathbf{B} = B\hat{z}$ develop an off-diagonal component to the resistivity ρ_{xy} known as the Hall resistivity. In addition to current flowing in the direction of an applied electric field $\mathbf{E}$, the Lorentz force on the electrons due to the magnetic field also pushes electrons perpendicular to $\mathbf{E}$. Classically, the Hall resistivity is expected to increase linearly with B. However, for clean samples at low temperature ρ_{xy} instead forms plateaus, while the longitudinal resistivity ρ_{xx} vanishes (except when transitioning between plateaus) as shown in Fig. 7.1. Furthermore, the plateaus are precisely quantized (to one part in a billion) despite the presence of disorder in the sample. This striking departure from the classically expected behavior is known as the *quantum Hall effect*, and we now understand its precise quantization as indicative of underlying topological physics. At the plateaus, the Hall conductance (given by the inverse of the resistance matrix) takes values

$$\sigma_{xy} = \nu \frac{e^2}{h}, \tag{7.1}$$

where ν is an integer or rational fraction. The integer and fractional quantum Hall effects, referring to ν taking integer or fractional values respectively, were the first [258, 249] and re-

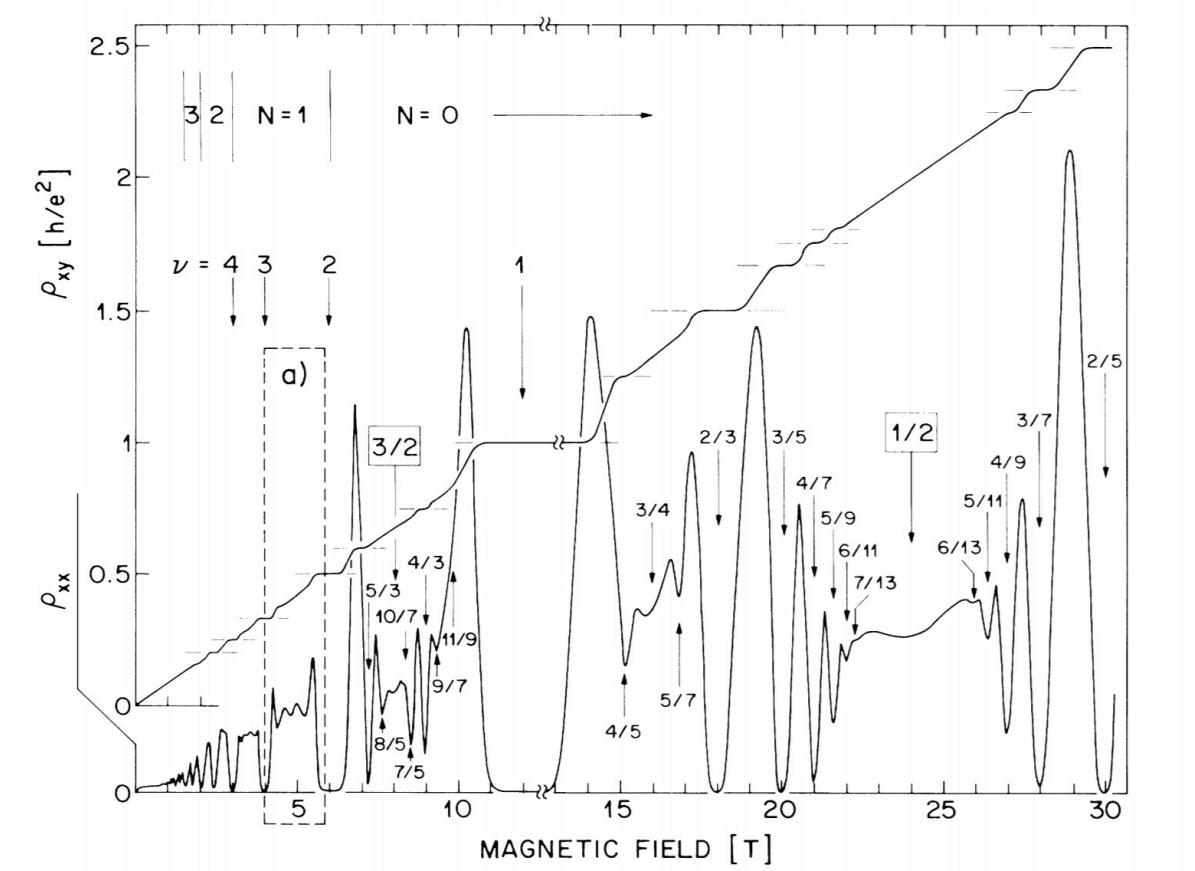

Figure 7.1: Quantum Hall trace. The Hall resistivity ρ_{xy} forms plateaus, which are labeled by the corresponding filling factor. The longitudinal resistivity ρ_{xx} vanishes at each plateau. From Ref. [266], reprinted with permission from American Physical Society.

main the best-studied examples of topological phases. Here, we review a few key aspects of quantum Hall physics that are useful for understanding their lattice analogs, fractional Chern insulators. We refer the reader interested in a more comprehensive review to the classic textbook, Ref. [211].

7.1.1 Landau levels, Chern number, trial wavefunctions

We begin by ignoring Coulomb interactions and considering an electron confined to two dimensions subject to a perpendicular magnetic field B. Working in Landau gauge, $\mathbf{A} = xB\hat{y}$, the Hamiltonian for the system is

$$H = \frac{1}{2}\left(k_x^2 + (k_y + exB)^2\right)^2. \tag{7.2}$$

(Above and for the remainder of this thesis we set $\hbar = 1$.) In particular, the Hamiltonian is independent of y, and quadratic in x. The first point implies that eigenstates are plane-waves in y, $\psi_{k_y,n}(x,y) = e^{ik_y y} f_{k_y,n}(x)$, while the second implies that the function $f_{k_y,n}(x)$ is a harmonic oscillator eigenstate with a k_y-dependent shift:

$$\left(\frac{k_x^2}{2m} + \frac{m\omega_c^2}{2}\left(x + k_y \ell_B^2\right)^2\right) f_{k_y,n}(x) = \varepsilon_n f_{k_y,n}(x). \tag{7.3}$$

We have introduced a length scale $\ell_B = \sqrt{\frac{1}{eB}}$ known as the *magnetic length*. The energies ε_n are given by

$$\varepsilon_n = \omega_c\left(n + \frac{1}{2}\right), \tag{7.4}$$

where $\omega_c = \frac{eB}{m}$ is the *cyclotron frequency*. In the Landau-gauge, eigenfunctions are called *Landau-gauge orbitals* and are given by

$$\psi_{k_y,n}(x,y) \propto e^{ik_y y} e^{-(x+k_y\ell_B^2)^2/2\ell_B^2} H_n\left(\frac{x+k_y\ell_B^2}{\ell_B}\right), \tag{7.5}$$

where H_n is the nth Hermite polynomial (familiar from the solution to the Harmonic oscillator).

Importantly, the system forms a band insulator with completely flat (momentum-independent) energy levels known as *Landau levels*. We can rewrite the Hamiltonian in momentum space as

$$H = \int d^2k c_{\mathbf{k}}^\dagger h(\mathbf{k}) c_{\mathbf{k}}, \tag{7.6}$$

where the dimension of the matrix $h(\mathbf{k})$ is the number of Landau levels in the system and $c_{\mathbf{k},j}$ creates an electron with momentum $\mathbf{k}$ in the jth band. Let $|\mathbf{k}\rangle$ denote the Bloch state of an occupied Landau level. The Berry phase gauge field for that Landau level is defined as $a_i(\mathbf{k}) = -i\langle\mathbf{k}|\partial_{k_i}|\mathbf{k}\rangle$. A two dimensional band has an associated topological invariant known as the *Chern number* C,

$$C = \frac{1}{2\pi}\int d^2k \varepsilon^{ij}\partial_i a_j(\mathbf{k}). \tag{7.7}$$

One can check that all Landau levels have $C = 1$, and are thus topologically non-trivial bands.

The Chern number has crucial implications for the edge states of the system. Non-zero C

implies the band has C chiral edge modes, each contributing conductance $2\pi e^2$ (in units where $\hbar = 1$). When the current is carried by chiral edge states (as is the case when the difference in Fermi energy between either edge of the sample is smaller than the spacing between Landau levels), disorder-induced scattering between different edge states does not change the total current. Thus, the Chern number underlies the precise quantization of σ_{xy} in the IQH effect: each occupied Landau level contributes a chiral edge mode, thus $\nu = C$ is the number of filled Landau levels.

From Fig. 7.1, we see that there are also Hall plateaus occurring for fractional ν, corresponding to partial filling of a Landau level. In this case, the *filling factor* ν is the fraction of available single-particle states that are occupied. Landau levels are extensively degenerate, with one state per flux quantum $\phi_0 = 2\pi/e$ piercing the sample for degeneracy $N = BA/\phi_0$ (A is the area). Defining j_0 as the particle density, the filling factor is therefore

$$\nu = \frac{2\pi j_0}{eB}. \tag{7.8}$$

The single-particle analysis thus far cannot explain the presence of incompressible states at fractional ν, thus interaction effects (e.g., Coulomb repulsion) are essential for understanding these FQH states.

Solving for exact many body ground states with interactions is no longer feasible, however progress was made in 1983 when Laughlin proposed a trial wavefunction for the FQH ground state at $\nu = 1/m$, with m odd [161]. Switching to the symmetric gauge, $\mathbf{A} = -\frac{1}{2}\mathbf{r} \times B\hat{z}$, the single particle orbitals can be written in terms of complex coordinates $z = x + iy$ as

$\psi(z,\bar{z}) \propto ze^{-|z|^2/(4\ell_B^2)}$. A filled Landau level should therefore have many-body ground state $\Psi(\{z\}) \propto \prod_{i<j}(z_i - z_j)e^{-\frac{1}{4\ell_B^2}\sum_i |z_i|^2}$, where z_i is the complex coordinate of the ith electron. Laughlin proposed the trial wavefunction at $\nu = 1/m$

$$\Psi_m(\{z\}) \propto \prod_{i<j}(z_i - z_j)^m e^{-\frac{1}{4\ell_B^2}\sum_i |z_i|^2}. \tag{7.9}$$

The Laughlin wavefunction has several desirable features: it is antisymmetric under particle exchange; it is an analytic function of the coordinates; it recovers the IQH ground state wavefunction when $m = 1$; and the wavefunction vanishes rapidly when two electrons approach, as we would expect for a ground state of a system with repulsive interactions. Laughlin showed that his wavefunction has good overlap with the exact ground state of $\nu = 1/3$ with three particles [161].

It is also possible to study the QH effect in multilayer systems (e.g. double layer quantum wells or bilayer or trilayer graphene). The simplest bilayer FQH states are generalizations of the Laughlin states known as (lmn) Halperin states, with many body ground state wavefunction

$$\Psi_{lmn}(\{z,w\}) \propto \prod_{i<j}(z_i - z_j)^l (w_i - w_j)^m \prod_{i,j}(z_i - w_j)^n e^{-\frac{1}{4\ell_B^2}\sum_i \left(|z_i|^2 + |w_i|^2\right)}, \tag{7.10}$$

where z_i is the complex coordinate of the ith particle in layer 1 and w_j is the complex coordinate of the jth particle in layer 2. The integers l, m (both odd) characterize intralayer particle interactions, while the integer n (even or odd) characterizes interlayer interactions.

There are many FQH states beyond the Laughlin and Halperin states presented above. It is

useful for studying the FQH more generally to move from trial wavefunctions to a field theory description of the low energy physics, which we do in the next section.

7.1.2 Field theory description: bulk

Universal properties of Abelian FQH states are succinctly captured by a field theory description. We first motivate the form of the Lagrangian by considering the $1/m$ Laughlin state, following the presentation in Ref. [262]. We then summarize the relevant formulas of the more general theory.

Recall that the Lagrangian for a charged particle in a magnetic field is

$$\mathcal{L} = e\mathbf{A} \cdot \mathbf{J} + \text{ kinetic energy}, \tag{7.11}$$

where e is the electron charge, $\mathbf{A}$ is the electromagnetic vector potential, and $\mathbf{J}$ is the particle current. We would like to write down a Lagrangian such that the Euler-Lagrange equations of motion imply

$$-e\delta J_\nu = \sigma_{xy}\varepsilon^{\mu\nu\lambda}\partial_\nu \delta A_\lambda, \tag{7.12}$$

where $\delta\mathbf{A}$ is a change in the electromagnetic fields and $\sigma_{xy} = e^2/(2\pi m)$ is the Hall conductance for filling factor $\nu = 1/m$ (setting $\hbar = 1$). Greek indices label spacetime coordinates and repeated indices are summed.

It is useful to introduce a $U(1)$ gauge field a_μ such that the current is

$$J_\mu = \frac{1}{2\pi}\partial_\nu a_\lambda \varepsilon^{\mu\nu\lambda}. \tag{7.13}$$

Then, Eq. (7.12) is implied by the equations of motion for

$$\mathcal{L} = \frac{m}{4\pi} a_\mu \partial_\nu a_\nu \varepsilon^{\mu\nu\lambda} + \frac{1}{2\pi} A_\mu \partial_\nu a_\lambda \varepsilon^{\mu\nu\lambda}. \tag{7.14}$$

The first term is known as the Chern Simons Lagrangian, originally studied in the context of pure differential geometry [264]. The second term encodes the linear response to an external electromagnetic field.

Adding a source term to Eq. (7.14)

$$\ell a_\mu j_\mu, \tag{7.15}$$

corresponds to adding a quasiparticle with current j_μ carrying "a_μ charge" ℓ and "a_μ flux" ℓ/m. That is, the gauge field carries a fictitious charge and flux, separate from the electromagnetic quantities. The electric charge carried by the quasiparticle is given by the coupling of a_μ to A_μ. The equation of motion $\frac{\delta \mathcal{L}}{\delta a_0} = 0$ implies

$$j_0 = \frac{1}{2\pi m}\varepsilon_{ij}\partial_i a_j = \frac{e}{2\pi m} B + \frac{\ell}{m}\delta(\mathbf{x} - \mathbf{x}_0). \tag{7.16}$$

The second term tells us that the quasiparticle carries fractional electric charge $e\ell/m$. The first

term recovers $\nu = 1/m$, using the definition of the filling factor $\nu = 2\pi j_0/(eB)$.

We can further calculate the phase accrued when interchanging a pair of identical quasiparticles described by Eq. (7.15). There is an Aharonov-Bohm phase associated with an a_μ charge circling an a_μ flux, which for Eq. (7.15) is

$$\theta = \pi \frac{\ell^2}{m}. \tag{7.17}$$

Therefore, the Chern-Simons term implies anyonic statistics (when ℓ^2/m is non-integer). We immediately see that $\ell = m$ for an electron.

The Lagrangian in Eq. (7.14) encodes the universal information about the anyonic quasiparticles of the Laughlin phase at $\nu = 1/m$. More generally, all Abelian fractional quantum Hall states are classified by an integer matrix K_{IJ}, a charge vector t_I, and a spin vector s_I, with the corresponding Lagrangian

$$\mathcal{L} = \frac{1}{4\pi} K_{IJ} a_{I,\mu} \partial_\nu a_{J,\lambda} \varepsilon^{\mu\nu\lambda} + e A_\mu t_I \partial_\nu a_{I,\lambda} \varepsilon^{\mu\nu\lambda} + \ell_I a_{I,\mu} j_\mu. \tag{7.18}$$

(The spin vector is necessary to distinguish some phases for which the K-matrix and charge vector are related by an $SL(2,\mathrm{Z})$ transformation, but will not be important for our discussion.) The capital letter indices label different species of gauge field. For instance, hierarchical states at $\nu = \frac{p}{pq+1}$ (q even) can be understood by successive condensation of different FQH liquids, each associated to its own gauge fields. Only the gauge field $a_{1,\mu}$ couples to the external electromagnetic field (i.e., $\mathbf{t} = (1, 0, \dots)$). More relevant to the discussion in the next chapter,

multilayer quantum Hall systems have a gauge field associated to each layer, with charge vector $\mathbf{t} = (1, 1, \dots)$. The K-matrix essentially encodes the interactions between different species of gauge fields. The filling factor is given by

$$\nu = \mathbf{t} K^{-1} \mathbf{t}. \tag{7.19}$$

The last term in Eq. (7.18) describes a quasiparticle of species ℓ, with charge Q and statistical angle θ given by

$$Q = e \mathbf{t}^T K^{-1} \ell \tag{7.20}$$

$$\theta = \pi \ell K^{-1} \ell. \tag{7.21}$$

The Halperin (lmn) states (Eq. (7.10)) are characterized by

$$K = \begin{pmatrix} l & n \\ n & m \end{pmatrix}, \qquad \mathbf{t} = \begin{pmatrix} 1 \\ 1 \end{pmatrix}. \tag{7.22}$$

We see that the diagonal elements of the K-matrix characterize the intralayer electron interactions, while off-diagonal elements characterize the interlayer electron interactions.

7.1.3 Field theory description: edge

Edge physics provides one of the most powerful experimental probes of QH systems. As discussed at the beginning of this section, transport of QH systems is determined by their gapless edge states. Quantum point contacts at which tunneling between edges occur can be used to infer the K-matrix and charge vector introduced above. Furthermore, edge states can be used for interferometry to probe quasiparticle content of the bulk [40]. It is therefore desirable to have a description of the universal low energy physics of QH edge states. Fortunately, the K-matrix description of the bulk carries over to the edge physics [262].

The edge of a FQH state with K-matrix K_{IJ} and charge vector $\mathbf{t}$ is described by the chiral Luttinger liquid action [1]

$$S_{\text{edge}} = \frac{1}{4\pi} \int dt dx \left(K_{IJ} \partial_t \phi_I \partial_x \phi_J - V_{IJ} \partial_x \phi_I \partial_x \phi_J \right). \tag{7.23}$$

The ϕ_I are 2π-periodic bosonic fields constrained to live on the edge of the sample. The K-matrix is the same as for the bulk of the phase, while the positive-definite integer matrix V encodes microscopic details of the edge physics and is generally non-universal.

For every bulk quasiparticle characterized by ℓ, there is a corresponding edge excitation

$$\psi_\ell \sim e^{i \ell_I \phi_I}. \tag{7.24}$$

The excitation ψ_ℓ has the same charge as its bulk counterpart, $Q_\ell = e \ell_I \left(K^{-1}\right)_{IJ} t_J$, but statis-

[1] The action S_{edge} is similar to the Luttinger liquid action used to describe the Majorana nanowire in Chapter 5, except now all fields propagate in the same direction. See Appendix A for a review of field-theoretic bosonization.

tics are no longer well-defined. For electrons confined to the edge, ℓ corresponds to a row of the K-matrix:

$$\psi_{e,I} \sim e^{iK_{IJ}\phi_J}. \tag{7.25}$$

It follows that there are multiple types of edge electrons when dim$K > 1$. We will primarily be interested in bilayer (lmn) states, for which the two electrons correspond to the layers of the system.

When two edges are brought close together, tunneling between the edges can occur. Given the form of Eq. 7.24, tunneling is described by cosine terms:

$$\psi^\dagger_\ell \psi_{\ell'} \sim \cos\left(\ell_I \phi_I - \ell'_J \phi_J\right). \tag{7.26}$$

Such a term is allowed when charge is conserved and the left and right scaling dimensions are equal [2]. When the edges are separated by a FQH liquid, for instance at a quantum point contact between edges of the same sample, quasiparticles supported by that liquid can tunnel between the edges through the bulk. This process will generally be dominated by the quasiparticle with the lowest scaling dimension, and can therefore be used as a partial probe of the quasiparticle content. When edges are separated by the trivial phase, e.g. for two adjacent QH liquids, only electrons can tunnel. When this tunneling term is relevant, the two edges can gap out.

[2]The term is relevant when the total scaling dimension is less than two. In general, when K has both positive and negative eigenvalues the scaling dimension will depend on the non-universal interaction matrix V.

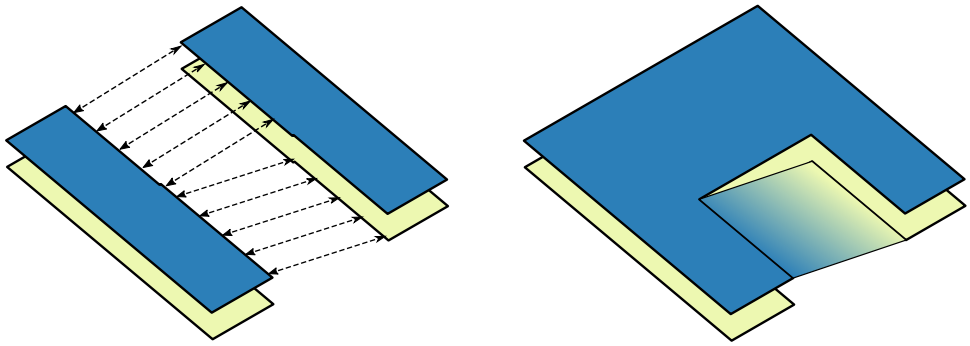

Figure 7.2: Schematic for realizing a genon in a bilayer QH system [22]. For a bilayer FQH state with layer-exchange symmetry, tunneling between edges belonging to the same layer or edges belonging to different layers (left panel) can gap out the edges, effectively healing the system into a single surface (right panel). The intersection of the two distinct tunneling terms corresponds to a defect of the layer exchange symmetry, a genon. Pairs of genons effectively increase the genus of the surface, thereby increasing the ground state degeneracy. For ease of visualization, we only show tunneling between one pair of layers.

7.1.4 Genons

An attentive reader might wonder why we have focused on Abelian FQH states, when the motivation of this thesis has been to study platforms for topological quantum computing, which necessarily require non-Abelian statistics. Our reasons are two-fold. (1) Non-Abelian FQH phases are significantly more challenging to study. While theoretical arguments and numerical studies indicate that non-Abelian FQH states exist when $\nu = 5/2$ and $12/3$ (see e.g., Ref. [193] for a review), experimental verification has been limited. Such experiments are notoriously difficult to conduct, requiring exceptionally clean samples and difficult interferometric or thermal conductance measurements [82, 214, 267, 14]. (2) Abelian FQH phases can support a topologically protected ground state degeneracy when the system is realized on a higher genus surface (see discussion in Chapter 1).

Reference [22] proposed one way of effectively engineering a higher genus surface using a

bilayer QH system in the Halperin $(mm0)$ phase. Such a phase has a layer-exchange symmetry. Consider two bilayer QH systems adjacent to each other, as shown in Fig. 7.2. Introducing tunneling terms can gap out the edges. If tunneling in one region is between edges belonging to the same layer, while in a different region it is between edges belonging to different layers, then the intersection of these two regions corresponds to a defect of the layer exchange symmetry. This defect introduces a non-contractible cycle to the surface, effectively increasing the genus and thereby increasing the ground state degeneracy. For the $(mm0)$ phase, there are m Abelian quasiparticles that can circle the defect, thus the ground state degeneracy is now m. A pair of layer-exchange defects are necessary to increase the genus by one, thus each defect has quantum dimension $d = \sqrt{m}$. These defects are called "genons"- while they are easiest to visualize in the bilayer scenario, they can arise in any system with a layer-exchange symmetry [20].

While probably easier than realizing a QH system on a torus, the inter-layer tunneling terms proposed in Ref. [22] are experimentally challenging and have not gained much traction. We now turn our attention to a different system supporting genons, fractional Chern insulators [21]. The next chapter will present an experimental proposal for realizing and detecting genons in fractional Chern insulators in graphene.

7.2 Fractional Chern insulators

In the previous section, we saw that Landau levels of a QH system all have Chern number $C = 1$. IQH states are a particular example of a *Chern insulator*: an insulator whose occupied bands have non-trivial Chern number. An incompressible state at partial filling of a non-trivial

Chern band is a *fractional Chern insulator* (FCI), thus FQH states are examples of FCIs. By adding a periodic potential (e.g., a lattice) to a QH system, it is possible to realize bands with $|C| > 1$. It is not even strictly necessary to have a net magnetic field provided that time reversal symmetry is broken: a lattice model with complex hopping amplitudes can realize non-trivial Chern bands [115]. For a lattice system, the relevant parameter is the not the total magnetic field, but rather the flux per plaquette, which is only defined modulo the flux quantum.

For the remainder of this thesis, we will distinguish FQH states, which can arise in the continuum and whose Landau levels all have $C = 1$, from FCIs which arise in lattice systems and can have $|C| > 1$. We first consider a toy model [127] in which bands are characterized by two topological invariants: the Chern number C, and S which characterizes the strength of lattice effects. We then review a recent experiment [238] which observed FCIs in graphene subject to a Moiré pattern. Our main interest in FCIs is in the non-trivial interplay between their topological degrees of freedom and the lattice symmetries. In the next chapter, we will see that lattice dislocations in FCIs can host genons, with potential applications to topological quantum computing.

7.2.1 Hofstadter model

The Hofstadter model describes a perpendicular magnetic field applied to a square lattice with lattice constant a.

$$H = -t \sum_{\langle m,n \rangle} \left\{ c_n^\dagger c_m e^{i2\pi \int_m^n \mathbf{A}\cdot d\ell} + h.c. \right\}. \tag{7.27}$$

Working in Landau gauge $\mathbf{A} = Bx\hat{y}$ at flux density $Ba^2 = \phi = p/q$ (p and q coprime), we can write the Hamiltonian in momentum space on the infinite plane as

$$H = \sum_{\mathbf{k}} \mathbf{c}_{\mathbf{k}}^{\dagger} \mathcal{H}_{\mathbf{k}} \mathbf{c}_{\mathbf{k}}, \tag{7.28}$$

where $\mathbf{c}_{\mathbf{k}} = (c_{\mathbf{k},1}, c_{\mathbf{k},2}, \ldots, c_{\mathbf{k},q})^T$ and $\mathcal{H}(\mathbf{k})$ is the $q \times q$ matrix

$$\mathcal{H}(\mathbf{k})_{m,n} = \cos\left(k_y a + 2\pi n\phi\right) \delta_{m,n} + e^{ik_x a/q} \delta_{m+1,n} + h.c.. \tag{7.29}$$

The magnetic unit cell has q sites in the y direction and one site in the x direction. This model is famous for its fractal spectrum, which forms the Hofstadter butterfly when energy is plotted as a function of flux density ϕ.

Each band has two topological invariants associated with it: the Chern number C and S, which characterizes the strength of lattice effects. For a fixed $\phi = p/q$, the rth band of the Hofstadter model is described by the TKNN Diophantine equation [247]

$$t_r p + s_r q = r \tag{7.30}$$

which under $|t_r| < q/2$ has unique integer solution (s_r, t_r). The invariants of the rth band (C_r, S_r) are $(t_r - t_{r-1}, s_r - s_{r-1})$, respectively. As an example, when $\phi = 2/3$, the solutions are $(t_1 = -1, s_1 = 1)$, $(t_2 = 1, s_2 = 0)$, and $(t_3 = 0, s_3 = 1)$, corresponding to $(C_1 = -1, S_1 = 1)$, $(C_2 = 2, S_2 = -1)$, and $(C_3 = -1, S_3 = 1)$. Note that (1) $\sum_r C_r = 0$, and

(2) the middle band has $|C_2| > 1$. The first observation is true for any closed system: the sum of all Chern numbers must be zero. The second observation indicates that, as promised, in the presence of a lattice it is possible to realize higher Chern bands.

Using $(C_r, S_r) = (t_r - t_{r-1}, s_r - s_{r-1})$, Eq. (7.30) can be rewritten for a filled band as $C\frac{p}{q} + S = \frac{1}{q}$. A filled band has one electron per magnetic unit cell, and therefore has electron density $n_e = 1/q$. Equation (7.30) can be expressed as

$$n_e = C\phi + S. \tag{7.31}$$

This equation holds more generally for FCIs beyond the Hofstadter model [238].

7.2.2 Realization in graphene

The magnetic length $\ell_B = \sqrt{\frac{1}{eB}}$ sets the relevant scale for QH physics. Experimentally, the maximum magnetic field for observing QH physics is $\mathcal{O}(15\,\mathrm{T})$, corresponding to $\ell_B \sim \mathcal{O}(10\,\mathrm{nm})$. As the atomic lattice of the system is on the order of angstroms, lattice effects can usually be neglected and FCI physics is not observed.

Clearly, if a new potential is introduced with lattice constant on the order of the magnetic length, the above argument will no longer hold. For instance, graphene subject to a Moiré pattern (either with hexagonal Boron Nitride (hBN) or from misalignment with another graphene layer), can experience a periodic potential whose lattice constant is much larger than the underlying graphene unit cell. When the period approaches the magnetic length, FCI physics becomes accessible.

Reference [238] fabricated a bilayer graphene sample with one layer closely aligned ($\sim 1^\circ$ rotation) to neighboring hBN, resulting in a superlattice constant $\mathcal{O}(10\,\text{nm})$. They mapped out the incompressible states in the electron density versus flux density plane (controlled via backgate voltage and magnetic field strength, respectively) using capacitance measurements between top and bottom graphite gates.

Equation (7.31) indicates that filled Chern bands should appear as lines in the n_e versus ϕ plane. Generalizing to partially filled Chern bands,

$$n_e = t\phi + s, \tag{7.32}$$

where $t = \frac{\partial n_e}{\partial \phi}|_{N_S}$ describes the change in electron density with respect to flux density when the number of superlattice unit cells N_S is held constant; and $s = N_S \frac{\partial n_e}{\partial N_S}|_{N_\phi}$ is the change in the number of electrons when the number of superlattice unit cells is changed, holding the number of magnetic flux quanta N_ϕ constant. Essentially, $t = 2\pi\sigma_{xy}/e^2$ is a measure of the Hall conductance, while s is a measure of how much charge is glued to a unit cell.

Figure 7.3 shows the results, plotting n_ϕ versus n_e. At low magnetic field, a sequence of states emanating from the origin with integer inverse slope have the largest gaps (highest capacitance). These correspond to IQH states. The difference in inverse slope between neighboring IQH states is 1, indicating once again that Landau levels have $C = 1$. We also see states emanating from the origin with fractional inverse slope (and lower capacitance, indicating smaller gaps). These correspond to FQH states.

More interestingly, at higher magnetic field, states emerge with non-zero y-intercept, i.e.,

non-zero S. The wedge formed between a pair of such states describes a Chern band, with $(C, S) = (\Delta t, \Delta s)$. Reference [238] observed bands with $C = \pm 1, \pm 2, \pm 3, \pm 5$. Additional states appear at partial filling of these bands with fractional inverse slope and fractional y intercept. Using numerical evidence, Ref. [238] argued that these states are FCIs.

This experiment is the first observation of FCIs in a solid state system. It demonstrates that graphene is a viable platform for exploring FCI physics. The bilayer nature of the experiment was not strictly necessary, one could instead implement a Moiré pattern with hBN using monolayer graphene. Further, it might be possible to go beyond Moiré superlattices and introduce an artificially patterned lattice potential; this would allow greater control over the lattice symmetries, lattice constant (possibly facilitating observation of FCIs with lower magnetic fields), and even accommodate patterning defects into the lattice. The last point is especially interesting, as such defects can interact non-trivially with the topological degrees of freedom of the FCI and host genons. In the next chapter, we propose an experiment that allows for realization and detection of genons in graphene FCIs.

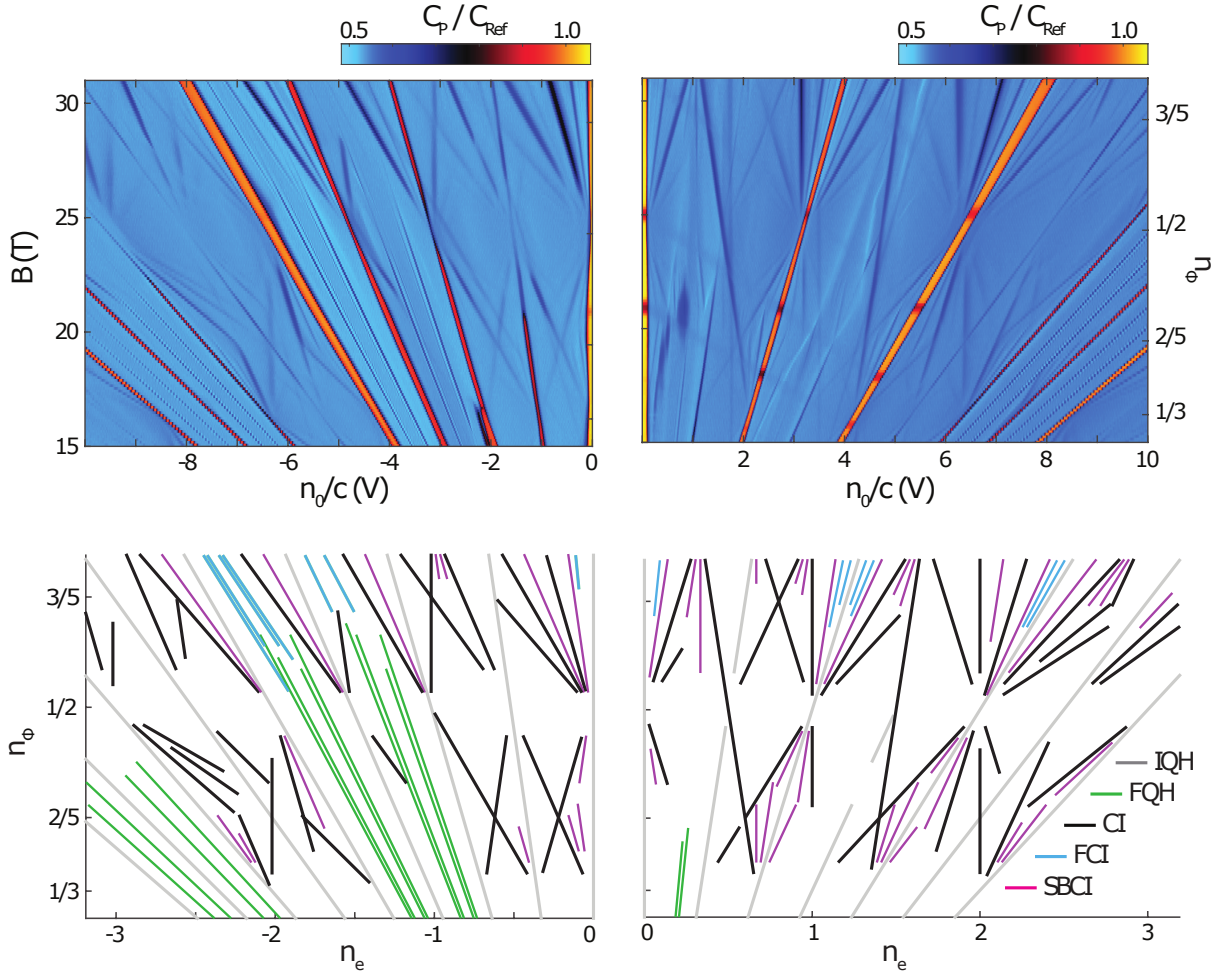

Figure 7.3: Experimental observation of FCIs in bilayer graphene. Top panel: capacitance C_p/C_{Ref} plotted as a function of magnetic field B and electron density $n_0 = c(V_T + V_B)$, where $V_{T/B}$ are the top and bottom gate voltages and c is the geometric capacitance to the gates. Higher capacitance indicates incompressible states. Bottom panel: identification of the states on the left with IQH, FQH, and FCI states. Gate voltage measurements have been converted to electron density n_e and magnetic field to flux density n_ϕ. From Ref. [238], reprinted with permission from AAAS.

Chapter 8

Fractional Chern insulator edges for genon detection

Because when you are imagining, you might as well imagine something worth while.

-L.M. Montgomery, *Anne of Green Gables*

Fractional Chern insulators (FCIs) realized in fractional quantum Hall systems subject to a periodic potential are topological phases of matter for which space group symmetries play an important role. In particular, lattice dislocations in an FCI can host non-Abelian topological defects, known as genons. Genons can increase the ground state degeneracy of the system and are thus potentially useful for topological quantum computing. In this work, we study FCI edges and how they can be used to detect genons. We find that translation symmetry can impose a quantized momentum difference between the edge electrons of a partially-filled Chern

band. We propose *layer-resolved lattice contacts*, which utilize this momentum difference to selectively contact a particular FCI edge electron. The relative current between FCI edge electrons can then be used to detect the presence of genons in the bulk FCI. Recent experiments have demonstrated graphene is a viable platform to study FCI physics. We describe how the lattice contacts proposed here could be implemented in graphene subject to an artificial lattice, thereby outlining a path forward for experimental detection of non-Abelian topological defects.

The results presented here were originally published in "Fractional Chern Insulator Edges and Layer-Resolved Lattice Contacts," by Christina Knapp, Eric M. Spanton, Andrea F. Young, Chetan Nayak, and Michael P. Zaletel in Physical Review B **99**, 081114.

8.1 Introduction

The subject of this thesis has been exploring how to utilize non-Abelian topological physics for quantum computing. An alternative to the Majorana zero modes (MZMs) studied in Chapters 2-6, are genons- topological defects whose presence effectively changes the genus of the system [17, 18, 16, 71]. Genons can increase the ground state degeneracy of an otherwise Abelian topological phase, enhancing the computational power of the system. One system predicted to host genons are fractional Chern insulators (FCIs), reviewed in the previous chapter. The ground state of a partially filled Chern-C band can be mapped to a $|C|$-layer FQH state in which different lattice sites are analogous to layers [213, 269, 21, 117, 130]. Lattice symmetries are thus interwoven with internal component labels of the FCI; translations have a non-trivial ac-

tion on layer index which can result in genons localized at lattice dislocations [21].

Recent experiments have demonstrated that FCIs can be realized in graphene, where interference between the graphene and dielectric lattices forms a Moiré lattice [238]. These experiments indicate that graphene is a viable platform in which to pursue non-Abelian physics, however the Moiré potential is not readily applicable to genons as it is difficult to controllably insert lattice dislocations into the Moiré superlattice. Alternatively, the lattice potential can be engineered, *e.g.*, by patterning holes into a neighboring metallic gate or dielectric [4, 124, 98]. An artificial lattice is an appealing route towards realizing FCIs hosting genons because (1) the lattice itself can be used to tune to the desired phase, and (2) there is no additional cost associated with patterning dislocations.

Even after genons have been engineered, there remains a final hurdle of how to detect their presence, which is the focus of this work. To understand why this is challenging, consider the analogy of an FCI in a Chern-2 band to a bilayer QH system, depicted in Fig. 8.1. When the FCI ground state satisfies the microscopic lattice symmetries, sublattices are analogous to layers. Crucially, under this mapping, unit cell translations and plaquette-centered rotations interchange the two sublattices, therefore lattice dislocations play the same role as layer-exchange defects in the bilayer system. In the bilayer case, layer-exchange defects can be detected using the difference in the edge current of the two layers [22], which in turn can be measured by separately contacting each layer's edge. In the FCI case, the difference in the current associated with the edge electrons again carries a signature of the genon; however, we must devise a way to selectively contact edge electrons residing in the same physical sample.

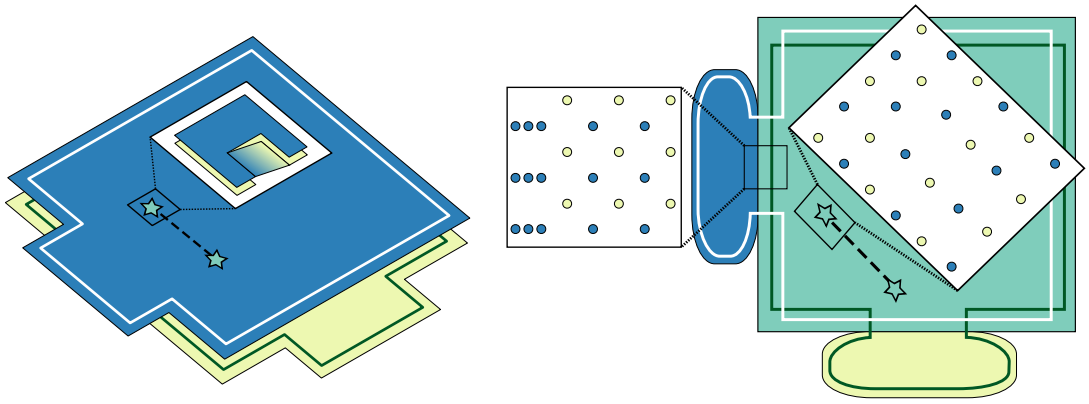

Figure 8.1: Analogy between a bilayer QH system (*left*) and an FCI in a $C = 2$ band (*right*). Both systems contain a pair of genons (stars) and a blue and yellow region to selectively contact the two edge electrons (white and green lines). A genon in the bilayer system exchanges the layers. *Right panel.* An FCI (green) with two layer-resolved lattice contacts (blue and yellow). Each lattice contact gaps out one of the FCI's edge electrons, rerouting that electron along the exterior of the contact and allowing for selective voltage-bias and current measurement. The FCI is in a partially-filled $C = 2$ band subject to a square lattice potential, such that it realizes the two-component (mml) phase. The two components, 'layers', are localized on the blue and yellow sublattices. The contacts are in a $C = 1$ band. The unit cell area of the rectangular lattice is half that of the bulk, and is lattice-matched with the bulk along the interface.

In this chapter, we study FCI edges in a partially filled $C > 1$ band and propose *layer-resolved lattice contacts* that can be used to detect genons. The main idea is depicted in the left panel of Fig. 8.1. Essentially, translation symmetry along the edge constrains the allowed perturbations from electron tunneling between the FCI (green) and lattice contacts (blue/yellow). By appropriately designing the lattices in the three regions, the two contact interfaces can gap out different edge electrons of the FCI, thereby spatially separating them and allowing independent measurement of their electrical properties. The relative current can then be used to detect genons in the bulk [22], providing a path forward for experimental detection of non-Abelian topological defects in graphene.

The remainder of this chapter is organized as follows. We review the mapping of an FCI

ground state to a $|C|$-layer QH state. We next study the FCI edge physics, elucidating the additional constraints translation symmetry imposes on electron tunneling across the interface. We then discuss how the lattice itself can be used as a tuning parameter to simultaneously realize different phases in the same sample. Finally, we synthesize the above discussion to propose layer-resolved lattice contacts and illustrate how these contacts provide the missing link in experimental detection of genons.

8.2 Chern band as $|C|$-layer QH system

Consider a square lattice with unit cell area a^2 and flux density $\phi = p/q$, with p and q coprime integers. In the previous chapter we saw that Chern bands are characterized by topological invariants C and S given by the TKNN Diophantine equation [247]

$$n_e = C\phi + S, \tag{8.1}$$

where n_e is the electron density per unit cell. We now show that the single particle orbitals of the band can be mapped to Landau-gauge orbitals of a $|C|$-layer QH system at flux density $\bar{\phi} = \phi + S/C$, with effective magnetic length $\bar{\ell}_B = a/\sqrt{2\pi\bar{\phi}}$ [213, 269, 21, 117, 130]. This mapping allows us to write candidate FCI states from FQH wavefunctions, and to apply the field theoretic description of Abelian FQH states to the FCI case with an additional symmetry action.

8.2.1 Single-particle orbital mapping

Recall that in Landau gauge $\mathbf{A} = -By\hat{x}$, single-particle orbitals are uniquely labeled by their momentum k_x. The key idea is that in an appropriate basis, single particle orbitals $|\tilde{k}_x, \beta\rangle$ of a Chern-C band have a continuum index $\tilde{k}_x \in \mathrm{R}$ analogous to the momentum k_x in Landau-gauge orbitals, and an internal index $\beta \in \mathrm{Z}_C$ analogous to a layer index of a multilayer QH system. This identification is most clearly seen by considering the action of magnetic translations on the single-particle orbitals.

Magnetic translations by lattice vectors do not commute due to the non-integer flux density:

$$T_x T_y = e^{i2\pi\phi} T_y T_x, \tag{8.2}$$

where $T_{x/y} = e^{i\left(k_{x/y} - eA_{x/y}/c\right)a}$. It is therefore useful to consider a magnetic unit cell containing p flux quanta, such that translations along the magnetic unit cell, *e.g.*, T_x, T_y^q, do commute. For this choice of magnetic unit cell, translations act on the single-particle momentum states as

$$T_x|k_x, k_y\rangle = e^{ik_x a}|k_x, k_y\rangle \tag{8.3}$$

$$T_y|k_x, k_y\rangle = e^{ik_y a}|k_x + \phi G_x, k_y\rangle. \tag{8.4}$$

In the above, $k_x \in [0, G_x)$, $k_y \in [0, G_y)$, and $G_x = 2\pi/a$, $G_y = 2\pi/qa$.

A partial Fourier transform on the momentum eigenstates results in Wannier orbitals

$$|k_x, b\rangle = \int_{-G_y/2}^{G_y/2} \frac{dk_y}{\sqrt{2\pi}} e^{ik_y bqa} e^{i\varphi(k_x,k_y)} |k_x, k_y\rangle, \tag{8.5}$$

where b denotes the y coordinate. Wannier orbitals satisfy twisted boundary conditions $|k_x + G_x, b\rangle = |k_x, b + C\rangle$. There are several choices for the phase $\varphi(k_x, k_y)$ [269], which will not

be important for the present discussion.

A convenient basis change on Eq. (8.5) allows us to map the single-particle orbitals to Landau-gauge orbitals of a $|C|$-layer QH system at the effective flux density $\bar{\phi}$ and magnetic length $\bar{\ell}_B$ defined above. We denote the new basis by $|\tilde{k}_x, \beta\rangle$, where

$$\tilde{k}_x = k_x + G_x \frac{b}{C} \in \mathrm{R}, \qquad \beta = b - C\lfloor \frac{b}{C} \rfloor \in \mathrm{Z}_C. \tag{8.6}$$

Translations act on single particle states in this new basis as

$$T_x|\tilde{k}_x, \beta\rangle = e^{i\tilde{k}_x a} e^{i2\pi\beta/C} |\tilde{k}_x, \beta\rangle \tag{8.7}$$

$$T_y|\tilde{k}_x, \beta\rangle = |\tilde{k}_x + \bar{\phi} G_x, \beta + S\rangle. \tag{8.8}$$

In particular, we can factor translations into a continuum and internal part, $T_j = \tilde{T}_j \otimes \tau_j$ for $j = x, y$. We see that $\tilde{T}_j$ transforms $\tilde{k}_x$ as

$$\tilde{T}_x|\tilde{k}_x\rangle = e^{i\tilde{k}_x a}|\tilde{k}_x\rangle, \qquad \tilde{T}_y|\tilde{k}_x, \beta\rangle = |\tilde{k}_x + \bar{\phi} G_x, \beta\rangle, \tag{8.9}$$

which is exactly how magnetic translations act on the momentum k_x of a Landau level in the continuum at flux density $\bar{\phi}$. In contrast, the layer index β is acted on by

$$\tau_x = e^{-2\pi i \hat{\beta}/C}, \qquad \tau_y = |\beta + S\rangle\langle\beta|. \tag{8.10}$$

When S and C are coprime, the internal parts, denoted with a greek letter, act non-trivially

on the layer index: $\tau_x\tau_y = e^{2\pi iS/C}\tau_y\tau_x$. This implies that the Wannier orbitals $|\tilde{k}_x, \beta\rangle$ can be identified with Landau-gauge orbitals of a $|C|$-layer QH system for which magnetic translations along y act non-trivially on the layer-index. This corresponds to the "topological nematic state" introduced by Ref. [21].

The square lattice additionally has a plaquette-centered (p) and site-centered (s) C_4 symmetry, related by $C_{4,s} = T_x C_{4,p}$. Plaquette-centered C_4 symmetry satisfies $C_{4,p}^{-1} T_x C_{4,p} = T_y$ and $C_{4,p}^{-1} T_y C_{4,p} = T_x^{-1}$. These rotations factor into continuum and internal parts, $\tilde{C}_{4,s/p} \otimes \gamma_{4,s/p}$, where the continuum part $\tilde{C}_{4,p}$ has the same action as C_4 acting on Landau-gauge orbitals in a continuum Landau level, while the internal part $\gamma_{4,p}$ acts on the layer indices as

$$\gamma_{4,p} = \sum_{\beta,\beta'} \frac{1}{\sqrt{C}} |\beta\rangle e^{2\pi i \beta\beta'/C} \langle\beta'|. \tag{8.11}$$

8.2.2 Many-body state mapping

In the limit that $a/\bar{\ell}_B \to 0$, equivalently when $\phi \to -\frac{S}{C}$, the bands become flat and the system has a Landau level-like continuum limit. Given any $|C|$-layer FQH state in this limit, an analogous FCI state is given by replacing the Landau-gauge orbitals with the single-particle basis states $|\tilde{k}_x, \beta\rangle$. This construction is particularly simple on the cylinder, for which the n_ith Landau-gauge orbital sits at the n_ith lattice site in the compact direction. For example, on a

cylinder compact in the x-direction with circumference L_x, the (lmn) wavefunction is

$$\Psi_{lmn}\{z_i, w_j\} = \Omega_z \Omega_w \prod_{i<j} \left(e^{2\pi z_i/L_x} - e^{2\pi z_j/L_x}\right)^l \left(e^{2\pi w_i/L_x} - e^{2\pi w_j/L_x}\right)^m \times \prod_{i,j} \left(e^{2\pi z_i/L_x} - e^{2\pi w_j/L_x}\right)^n e^{-\sum_i (y_i^2+v_i^2)/2\ell_B^2}, \tag{8.12}$$

where $z_i = x_i + iy_i$ is the complex coordinate of the ith electron in the top layer, $w_j = u_j + iv_j$ is the complex coordinate of the jth electron in the bottom layer, and $\Omega_{z/w}$ are normalization factors. We can rewrite the wavefunction in the occupation basis as

$$\Phi_{lmn}\{l_i, m_j\} = \Omega_{l,m} \int \prod_i{}' \prod_j{}' dx_i dy_i du_j dv_j \psi^*_{\tilde{k}_{x,l_i}}(x_i, y_i) \psi^*_{\tilde{k}_{x,m_j}}(u_j, v_j) \Psi_{lmn}\{z_i, w_j\}, \tag{8.13}$$

where $\Omega_{l,m}$ is a normalization factor, the primes on the products denote they are restricted to $\{i | l_i \in \{l_i\}\}$ and $\{j | m_j \in \{m_j\}\}$. We have written the Landau-gauge wavefunction as $\psi^*_{\tilde{k}_x}$, and defined $\tilde{k}_{x,l_i} = G_x l_i / L_x$. The many-body state is then

$$|lmn\rangle = \sum_{\{l_i, m_j\}} \Phi_{lmn}\left(\{l_i, m_j\}\right) \prod_i{}' \prod_j{}' |\tilde{k}_{x,l_i}, 0\rangle |\tilde{k}_{x,m_j}, 1\rangle. \tag{8.14}$$

8.2.3 C_4-symmetric basis

In writing Eq. (8.14), we only relied on the fact that the continuum variable $\tilde{k}_x$ is analogous to momentum in a Landau level. This fixes the definition of $\tilde{k}_x$, but we are free to rotate the basis of the layer index (the basis of the τ_j) provided that $\tilde{k}_x$ is unaffected. We refer to the *layer basis* as the single-particle basis choice in Eq. (8.14), for which $\beta = 0, 1$ corresponds

to the layer indices l, m of the many-body state. When the τ_j in the layer basis are given by Eq. (8.10), translations along y permute the layers while translations along x do not; this corresponds to the topological nematic states proposed in Ref. [21]. We show below that if in the layer basis $\tau_x = \sigma_x$ and $\tau_y = \sigma_y$, then the (mml) many-body ground state preserves C_4 symmetry. Whereas for a QH system the different components correspond to different layers or spin species, for an FCI the components are associated with different lattice sites (*e.g.*, a checkerboard arrangement for the C_4-symmetric layer basis and a stripe arrangement for the topological nematic states).

As the continuum translation operators $\tilde{T}_j$ act on the single particle basis in the same way as magnetic translations on Landau-gauge orbitals, we know that translations acting on the many-body state $|lmn\rangle$ can only differ in the actions of the internal part of translation τ_j. When $\tau_x = \sigma_z$ and $\tau_y = \sigma_x$ (*i.e.*, for the basis given in Eq. (8.10) with $C = 2$ and S odd),

$$\tau_x|lmn\rangle = (-1)^{|\{m_j\}|}|lmn\rangle, \tag{8.15}$$

$$\tau_y|lmn\rangle = |mln\rangle. \tag{8.16}$$

In this basis, τ_y exchanges the layers, but τ_x does not: this many-body state does not preserve the microscopic C_4 symmetry of the lattice.

Conversely, if we rotate the component basis by the unitary $U = (1 - i\sigma_y)(1 - i\sigma_z)/2$, then

$\tau_x = \sigma_x$ and $\tau_y = \sigma_y$. When this corresponds to the layer basis, we have

$$\tau_x |lmn\rangle = |mln\rangle, \tag{8.17}$$

$$\tau_y |lmn\rangle = (-i)^{|\{l_i\}|} i^{|\{m_j\}|} |mln\rangle. \tag{8.18}$$

Assuming both layers have equal occupation, *i.e.* $|\{l_i\}| = |\{m_j\}|$, then both τ_x and τ_y exchange the layers. When $l = m$, this many-body state is a C_4 eigenstate.

8.2.4 Field theory

In the limit that $\bar{\phi} \to 0$, the system has a continuum limit and admits a field theoretic description. For concreteness, we consider a partially filled $C = 2$, S odd band whose ground state realizes an Abelian, C_4-symmetric (mml) state. At the topological level the system is described by the Lagrangian of Eq. (7.18), with K-matrix and charge-vector

$$K = \begin{pmatrix} m & l \\ l & m \end{pmatrix}, \qquad \mathbf{t} = \begin{pmatrix} 1 \\ 1 \end{pmatrix}. \tag{8.19}$$

The topological field theory must then be supplemented with the symmetry action (accounting for non-trivial action of τ_j, $\gamma_4^{(k)}$ on the internal index β).

The electron current in layer I is $j^\mu_{e,I} = \frac{1}{2\pi} \partial_\nu a_{I,\lambda} \varepsilon^{\mu\nu\lambda}$, while the electron operator $\psi_{e,I}$ generates a corresponding flux in the Chern-Simons gauge field $a_{I,\lambda}$. We demand that the $\psi_{e,I}$

transform under the lattice symmetries just like the single-particle orbitals of a $C = 2$ band; specifically they transform under translations as $\tau_j = \sigma_j$ where $\sigma_{x/y}$ are Pauli matrices, and under rotations as $\gamma_{4,p} = (\tau_x + \tau_y)/\sqrt{2}$. This implicitly defines the action of the symmetry on the Chern-Simons fields, as detailed below. Note that by a change of basis in the layer space β, we could have instead chosen (say) $\tau_x = \sigma_z$; this corresponds to a *distinct* implementation of the symmetry (the "topological nematic" state of Ref. [17]). Our choice is C_4 symmetric. When $|m - l| \geq 2$, interchanging the layers permutes the anyons, and consequently [63] such twists defects are genons with quantum dimension $d = \sqrt{|m - l|}$ [17, 21]. For $\tau_j = \sigma_j$, a lattice dislocation with a Burger's vector along *either* x or y permutes the layers, so will carry this degeneracy.

8.3 FCI edges

The interplay of translation symmetry and the component labels of the many-body state has interesting implications for FCI edges. Recall from our review of the field theory description of FQH edge states that the Lagrangian associated with the edge of the system is [262]

$$\mathcal{L}_{\text{edge}} = \frac{1}{4\pi} \int dx \left\{ K_{IJ} \partial_t \phi_I \partial_x \phi_J - V_{IJ} \partial_x \phi_I \partial_x \phi_J \right\}, \tag{8.20}$$

where the matrix K_{IJ} is that of the bulk theory, while the edge potential V_{IJ} is non-universal. An edge along the (u, v) direction has translation symmetry $T_{(u,v)} = \tilde{T}_{(u,v)} \otimes \tau_{(u,v)}$. The "internal" part of the translation acts on electron operators $\psi_{e,I} \sim \exp\{iK_{IJ}\phi_J\}$ as $\tau_{(u,v)} \left(\psi_{e,1}, \psi_{e,2}\right)^T$.

For instance, in the (mml) phase an x-edge [$(u,v)=(1,0)$] interchanges the bosonic modes: $\tau_x\phi_{1/2}=\phi_{2/1}$.

Translation symmetry imposes additional constraints on the allowed perturbations to Eq. (8.20). Consider a translationally invariant interface between two phases described by $K^{L/R}$. When these phases are not related by anyon condensation, only perturbations arising from electron tunneling across the interface are allowed. These perturbations take the form

$$t_{gh}\cos\left(g_I K^L_{IJ}\phi^L_J - h_I K^R_{IJ}\phi^R_J\right), \tag{8.21}$$

where g_I and h_I are integer vectors satisfying $\sum_I g_I = \sum_I h_I$ from charge conservation. For QH systems, Eq. (8.21) can gap out the edge modes $e^{ig_I K^L_{IJ}\phi^L_J}, e^{ih_I K^R_{IJ}\phi^R_J}$ when the left and right scaling dimensions are equal and the total scaling dimension is less than two. For the FCI interface, Eq. (8.21) must additionally be invariant under the component translation symmetries of the left/right phases, $\tau^{L/R}_{(u,v)}$.

This additional constraint implies that the interplay of translation symmetry and layer index introduces an edge electron momentum difference that is not present for the analogous FQH state. Consider the (mml) state with $\tau_{x/y}=\sigma_{x/y}$. The $(1,1)$ edge has $\tau_{(1,1)}=\sigma_z$. When V_{IJ} is a symmetric matrix, layer-exchange symmetry implies that the two edge electrons for a bilayer FQH state have the same momenta; this implies that for an FCI, both edge electrons $\psi_{e,1/2}$ have the same $\tilde{k}_{(1,1)}$. However, the *internal* part of the translation introduces a quantized momentum

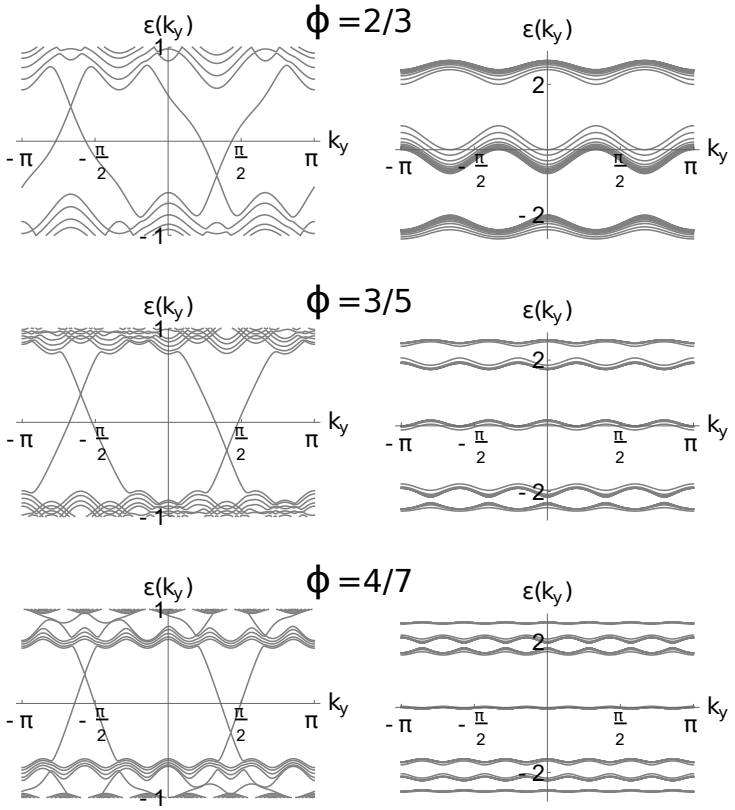

Figure 8.2: Energy spectrum for the Hofstadter model near $\phi = 1/2$. *Left panel.* Edge state momentum difference for the Hofstadter model on the infinite cylinder at $\phi = 2/3$, $3/5$, and $4/7$. The two halves of the cylinder differ by filling a band with $C = 2$, $S = -1$, with left and right movers corresponding to opposite edges. The edge state momentum difference at $\varepsilon = 0$ is $\frac{\pi}{a}(1 + 1/q)$ for flux density p/q. As $p/q \to 1/2$, the edge state momentum difference approaches quantization, corresponding to the limit that the system admits a field theory description. *Right panel.* Energy plotted against k_y for different values of k_x for the infinite plane. As $\phi \to 1/2$, the middle band becomes flatter. This agrees with the perturbation theory discussion of the Hofstadter model in Ref. [117].

difference of $\pi/\left(\sqrt{2}a\right)$:

$$\tilde{T}_{(1,1)} \otimes \tau_{(1,1)} \begin{pmatrix} \\ \psi_{e,1} \\ \\ \\ \psi_{e,2} \\ \\ \end{pmatrix} = e^{i\tilde{k}_{(1,1)}\sqrt{2}a} \begin{pmatrix} \\ \psi_{e,1} \\ \\ \\ -\psi_{e,2} \\ \\ \end{pmatrix}. \tag{8.22}$$

This momentum difference will no longer be quantized in the presence of non-symmetric perturbations to V_{IJ}. Figure 8.2 shows this momentum difference approaches quantization in the limit $\phi \to -S/C$ for the Hofstadter model [127, 118].

We can explore the momentum difference of the edge states in more detail by considering two types of edges, as shown in Fig. 8.3: 'A-type' edges run along the $(1,0)$ and $(0,1)$ directions, while 'B-type' edges run along the $(1,1)$ and $(1,-1)$ directions. The internal part of translation acts on the electron operators for A-type edges as

$$\sigma_x \begin{pmatrix} \psi_{e,1} \\ \\ \psi_{e,2} \end{pmatrix} = \begin{pmatrix} \psi_{e,2} \\ \\ \psi_{e,1} \end{pmatrix} \tag{8.23}$$

$$\sigma_y \begin{pmatrix} \psi_{e,1} \\ \\ \psi_{e,2} \end{pmatrix} = \begin{pmatrix} -i\psi_{e,2} \\ \\ i\psi_{e,1} \end{pmatrix}, \tag{8.24}$$

and on the electron operators for B-type edges as

$$\pm\sigma_z \begin{pmatrix} \psi_{e,1} \\ \\ \psi_{e,2} \end{pmatrix} = \pm \begin{pmatrix} \psi_{e,1} \\ \\ -\psi_{e,2} \end{pmatrix}. \tag{8.25}$$

Previously, we argued that for symmetric edge potential $V_{IJ} = V_{JI}$ the edge electrons

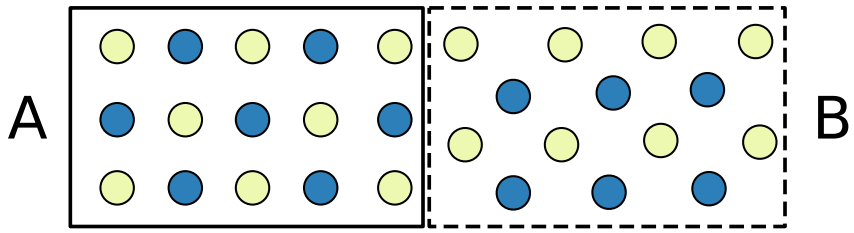

Figure 8.3: The left half of the sample has 'A-type' edges, oriented along the $(1,0)$ and $(0,1)$ directions, with corresponding internal translations $\tau_x = \sigma_x$ and $\tau_y = \sigma_y$. The right half has 'B-type' edges, oriented along the $(1,1)$ and $(1,-1)$ directions, with internal translations $\tau_{x/y} = \pm\sigma_z$. When translation symmetry is preserved along the edges, the interface has a gapless edge mode due to the lattice mismatch.

should have momentum difference $\pi/(\sqrt{2}a)$ along a B-type edge. Along an A-type edge with $\tau_z = \sigma_x$, the component translation eigenmodes are the symmetric and antisymmetric combinations of the electron operators,

$$T_{x/y}\begin{pmatrix} \psi_{e,1}+\psi_{e,2} \\ \\ \psi_{e,1}-\psi_{e,2} \end{pmatrix} = e^{i\tilde{k}_{x/y}a}\begin{pmatrix} \psi_{e,1}+\psi_{e,2} \\ \\ -\psi_{e,1}+\psi_{e,2} \end{pmatrix}, \tag{8.26}$$

indicating that the momentum separation of the edge electrons is π/a. Therefore, when translation symmetry is preserved, an interface between an A-type and B-type edge of the same bulk phase, as depicted in Fig. 8.3, cannot simultaneously gap out both edge electrons.

We can check the momentum difference of the edge electrons explicitly for the bilayer checkerboard tight binding model [271]. This model has two bands with Chern numbers $C =$

± 2, where each site on a square lattice has both an a and a b orbital,

$$H = t_1 \sum_{\langle i,j \rangle} \left(e^{i\phi_{ij}} a_i^\dagger b_j + h.c \right) + \sum_{\langle\langle i,j \rangle\rangle} t_{ij} \left(a_i^\dagger a_j - b_i^\dagger b_j \right). \tag{8.27}$$

Equation (8.27) describes a bilayer checkerboard lattice. We work with the parameters $\phi_x = \phi_{-x} = \pi/4$, $\phi_y = \phi_{-y} = -\pi/4$, and second nearest neighbor hoppings $t_{++} = t_{--} = t_2$, and $t_{+-} = t_{-+} = -t_2$. On the infinite plane, the Hamiltonian can be written in momentum space as

$$H = \sum_{\vec{k}} \left(a_{\vec{k}}^\dagger, b_{\vec{k}}^\dagger \right) H_{\vec{k}} \begin{pmatrix} a_{\vec{k}} \\ \\ b_{\vec{k}} \end{pmatrix}, \tag{8.28}$$

$$H_{\vec{k}} = \sqrt{2} t_1 \left(\cos k_x + \cos k_y \right) \sigma_x - \sqrt{2} t_1 \left(\cos k_x - \cos k_y \right) \sigma_y - 4 t_2 \sin k_x \sin k_y \sigma_z. \tag{8.29}$$

In order to investigate the edge modes, we can put the model on a strip finite in x and infinite in y. The Hamiltonian then is given by

$$\begin{aligned} H = \sum_{x=1}^{n} \sum_{k_y} \Big\{ & t_1 a_{x,k_y}^\dagger \left(e^{i\pi/4} b_{x+1,k_y} + e^{i\pi/4} b_{x-1,k_y} + e^{-i\pi/4} 2 \cos k_y b_{x,k_y} \right) + h.c. \\ & + t_2 2i \sin k_y \left[a_{x,k_y}^\dagger \left(a_{x+1,k_y} - a_{x-1,k_y} \right) - b_{x,k_y}^\dagger \left(b_{x+1,k_y} - b_{x-1,k_y} \right) \right] \Big\}. \end{aligned} \tag{8.30}$$

We plot the energy spectrum of Eq. (8.30) in the left panel of Fig. 8.3. As expected, the

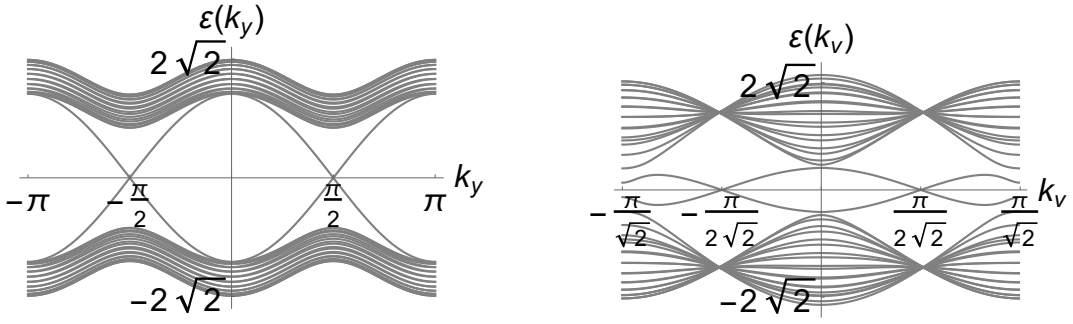

Figure 8.4: Energy versus momentum for the bilayer checkerboard lattice model on the infinite strip with edges parallel to the y-axis $(0,1)$ (*left panel*) and with edges parallel to the v-axis $(1,1)$ (*right panel*). Right and left movers correspond to opposite edges. The edge state momentum difference is quantized to π/a, where a is the lattice spacing along the edge (*i.e.*, $a=1$ for the y edge and $a=\sqrt{2}$ for the v edge).

momentum difference of the edge modes is π/a. Adding an orbital-dependent edge potential

$$H_a = \sum_{x=1}^{n} \sum_{k_y} \mu_a(x) a^\dagger_{x,k_y} a_{x,k_y}, \tag{8.31}$$

affects both edge modes, therefore we conclude that the edge modes are mixtures of the two orbitals.

Additionally, we can consider an infinite strip with B-type edges. Denoting the $(1,1)$ coordinate by v and the $(1,-1)$ coordinate by u, the Hamiltonian is given by

$$\begin{aligned} H = \sum_{u=1}^{n} \sum_{k_v} \Big\{ 2t_1 \Big[& \cos\left(\frac{k_v}{\sqrt{2}} + \frac{\pi}{4}\right) \left(a^\dagger_{u,k_v} b_{u+\frac{1}{\sqrt{2}},k_v} + b^\dagger_{u,k_v} a_{u-\frac{1}{\sqrt{2}},k_v} \right) \\ & + \cos\left(\frac{k_v}{\sqrt{2}} - \frac{\pi}{4}\right) \left(a^\dagger_{u,k_v} b_{u-\frac{1}{\sqrt{2}},k_v} + b^\dagger_{u,k_v} a_{u+\frac{1}{\sqrt{2}},k_v} \right) \\ & + t_2 \Big[a^\dagger_{u,k_v} \left(a_{u+\sqrt{2},k_v} + a_{u-\sqrt{2},k_v} - 2\cos(\sqrt{2}k_v) a_{u,k_v} \right) \\ & - b^\dagger_{u,k_v} \left(b_{u+\sqrt{2},k_v} + b_{u-\sqrt{2},k_v} - 2\cos(\sqrt{2}k_v) b_{u,k_v} \right) \Big] \Big\}. \end{aligned} \tag{8.32}$$

We plot the energy spectrum of Eq. (8.32) in the right panel of Fig. 8.3. Now, the lattice spacing along the edge is $\sqrt{2}a$, and we see that the momentum difference of the edge modes is $\pi/\sqrt{2}a$. Adding the orbital-dependent edge potential of Eq. (8.31) only affects one left-moving and one-right moving mode, thus we conclude that each edge mode can be identified with a single orbital.

For these parameter values, the flux is tuned exactly to $\phi = 1/2 = -S/C$, which is why the edge momentum difference is well quantized to π/a ($\pi/\sqrt{2}a$) for A-type (B-type) edges.

8.3.1 Corner MZMs

When the system satisfies plaquette-centered C_4 symmetry, the $(1, -1)$ edge has component translation $\tau_{(1,-1)} = \gamma_{4,p}^{-1}\tau_{(1,1)}\gamma_{4,p} = -\sigma_z$, and the momenta of the edge electrons are swapped compared to Eq. (8.22) (assuming $\tilde{k}_{(1,1)} = \tilde{k}_{(1,\pm 1)}$). For the (331) state (or any (mml) state satisfying $|m - l| = 2$), there is a MZM at the corner, which interchanges the two layers of the FCI.

The edge Lagrangian written in terms of the charged $(+)$ and neutral $(-)$ boundary modes $\psi_\pm \sim e^{i(\phi_1 \pm \phi_2)}$ is

$$L_0 = \int dx \left\{ v_- \psi_- \partial_x \psi_- + v_+ \psi_+ \partial_x \psi_+ \right\}. \tag{8.33}$$

Note that ψ_- is a fermion (has scaling dimension $1/2$). The component plaquette-centered

component C_4 symmetry $\gamma_{4,p} = (\sigma_x + \sigma_y)/\sqrt{2}$ implies that the edge modes transform as

$$\gamma_{4,p} \begin{pmatrix} \phi_1 \\ \\ \phi_2 \end{pmatrix} = \begin{pmatrix} \phi_2 - \frac{\pi}{8} + 2\pi b \\ \\ \phi_1 + \frac{\pi}{8} + 2\pi c \end{pmatrix}. \tag{8.34}$$

The constants $b = (3j - k)/8$ and $c = (3k - j)/8$ for $j, k \in \mathrm{Z}$ come from the compactness of the fields $\phi_{1/2}(x) + 2\pi = \phi_{1/2}(x)$. Different values of b and c correspond to different symmetry fractionalization classes [63].

The boundary Lagrangian [54, 90] that enforces the C_4 symmetry at a corner (*e.g.*, the Northwest corner at $z = 0$) is

$$\begin{aligned} L_b = &- v_- \left\{ e^{-i\alpha_-} \psi_-^{\mathrm{W}}(0) \psi_-^{\mathrm{N}}(0) + e^{i\alpha_-} \bar{\psi}_-^{\mathrm{W}}(0) \bar{\psi}_-^{\mathrm{N}}(0) \right\} \\ &- v_+ \left\{ e^{-i\alpha_+} \bar{\psi}_+^{\mathrm{W}}(0) \psi_+^{\mathrm{N}}(0) + e^{i\alpha_+} \psi_+^{\mathrm{W}}(0) \bar{\psi}_+^{\mathrm{N}}(0) \right\}. \end{aligned} \tag{8.35}$$

The phase factors $\alpha_\pm$ are defined by Eq. (8.34), and are unimportant for the present discussion. Equation (8.35) describes Andreev reflection of the neutral edge electron ψ_-, indicating Majorana zero modes (MZMs) at the corner of the system. For $b = c = 0$, ψ_+ is invariant under $\gamma_{4,p}$ (the charged mode is insensitive to the MZM), while ψ_- transforms as $\gamma_{4,p}\psi_- \to \bar{\psi}_- e^{-i\frac{\pi}{4}}$. These MZMs are exponentially localized to the edges of the system due to the bulk gap, but are only power-law localized to the corners because the edges are gapless.

Alternatively, when the system satisfies site-centered C_4 symmetry, then

$$\gamma_{4,s}\begin{pmatrix}\phi_1\\ \\ \phi_2\end{pmatrix}=\begin{pmatrix}\phi_1+\frac{\pi}{8}+2\pi b\\ \\ \phi_2-\frac{\pi}{8}+2\pi c\end{pmatrix}. \tag{8.36}$$

In particular, the rotation symmetry does not interchange the layers. The boundary Lagrangian that enforces this symmetry is

$$\begin{aligned}L_b=&-v_-\left\{e^{-i\alpha_-}\bar{\psi}_-^{\mathrm{W}}(0)\psi_-^{\mathrm{N}}(0)+e^{i\alpha_-}\psi_-^{\mathrm{W}}(0)\bar{\psi}_-^{\mathrm{N}}(0)\right\}\\ &-v_+\left\{e^{-i\alpha_+}\bar{\psi}_+^{\mathrm{W}}(0)\psi_+^{\mathrm{N}}(0)+e^{i\alpha_+}\psi_+^{\mathrm{W}}(0)\bar{\psi}_+^{\mathrm{N}}(0)\right\},\end{aligned} \tag{8.37}$$

where $\alpha_\pm$ are redefined compared to Eq. (8.35). In this case, both $\psi_\pm$ satisfy normal reflection, therefore there is no corner MZM.

Finally, we note that a system with plaquette-centered C_4 symmetry with A-type edges should not be interpreted as having corner MZMs, as all translation interchange the edge components and thus there is nothing special about the corner compared to the middle of the edge. More explicitly, we could write a boundary Lagrangian to enforce the translation symmetry at

the midpoint of a $(1,0)$ or $(0,1)$ edge. Comparing

$$\sigma_x \begin{pmatrix} \phi_1 \\ \\ \phi_2 \end{pmatrix} = \begin{pmatrix} \phi_2 + 2\pi b \\ \\ \phi_1 + 2\pi c \end{pmatrix} \tag{8.38}$$

$$\sigma_y \begin{pmatrix} \phi_1 \\ \\ \phi_2 \end{pmatrix} = \begin{pmatrix} \phi_2 - \frac{\pi}{4} + 2\pi b \\ \\ \phi_1 + \frac{\pi}{4} + 2\pi c \end{pmatrix}, \tag{8.39}$$

to Eq (8.34), we see this boundary Lagrangian has the same form as Eq. (8.35), up to a re-definition of the phases $\alpha_\pm$. An equivalent statement is that in the case of B-type edges with plaquette-centered C_4 symmetry, there is a boundary entropy of $\ln\sqrt{2}$ associated with the corners that is not present mid-edge. For A-type edges, the corners and mid-edges have the same boundary entropy. We only identify a corner MZM when there is a $\ln\sqrt{2}$ boundary entropy difference between a mid-edge point and the corner [2, 89, 90].

8.4 Lattice as a tuning parameter

We now focus on the particular realization of an FCI in graphene subject to an artificial lattice, depicted in Fig. 8.5. As reviewed in the previous chapter, insulating phases correspond to lines in the flux density ϕ versus electron density n_e plane [238]. The phase of the system can be tuned by: (1) applying a voltage to the sample to vary n_e, (2) applying a perpendicular

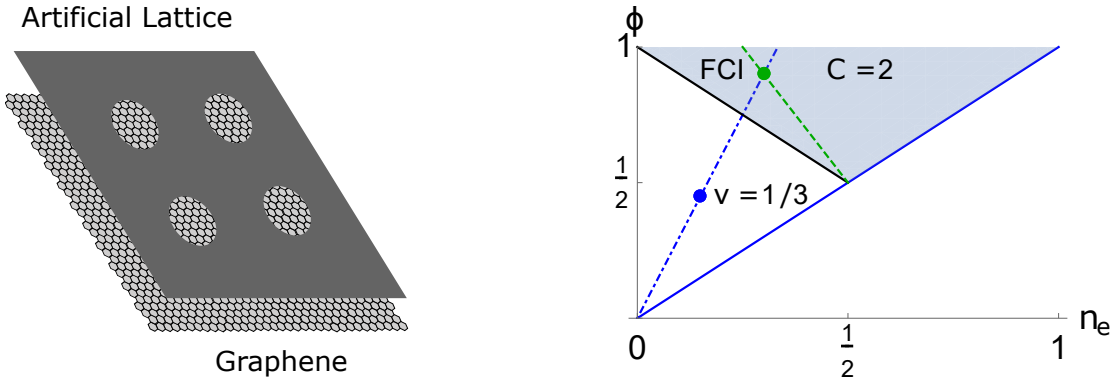

Figure 8.5: *Left panel.* The FCI can be engineered in graphene subject to an artificial lattice, *e.g.* by patterning holes in a neighboring dielectric or metal gate (see Fig. 8.6). *Right panel.* Flux density versus electron density phase space. The dot-dashed blue line corresponds to the FQH phase $\nu = 1/3$. The dashed green line corresponds to an FCI at quarter filling of a $C = 2$, $S = -1$ band (shaded region). The pair of points depict that for the different lattices shown in Fig. 8.1, the green and blue/yellow regions can be tuned to distinct phases for the same global backgate voltage and magnetic field.

magnetic field to vary ϕ, and (3) changing the unit cell area of the lattice to change (n_e, ϕ) simultaneously. The third option provides a convenient way of realizing distinct phases within the same sample by defining the artificial lattice differently in separate spatial regions. We consider edges defined by the artificial lattice, as the physical graphene edge is too dirty.

Consider the right panel of Fig. 8.1: the unit cell area in the green region is twice as large as the unit cell area in the blue/yellow regions. Therefore, for the same magnetic field and backgate voltage, $2(n_e, \phi)_{\text{b/y}} = (n_e, \phi)_{\text{g}}$. When these points lie on lines characterizing distinct phases, the green and blue/yellow regions are in different phases. Figure 8.5 shows an example. The dashed green line corresponds to an FCI at quarter filling of a $C = 2, S = -1$ band (shaded region). A possible ground state of this phase is the Abelian (331) state, which hosts genons at lattice dislocations. The dot-dashed blue line corresponds to the FQH phase $\nu = 1/3$. When the green region is tuned to the point $(3/10, 9/10)$, the blue/yellow regions are at $(3/20, 9/20)$.

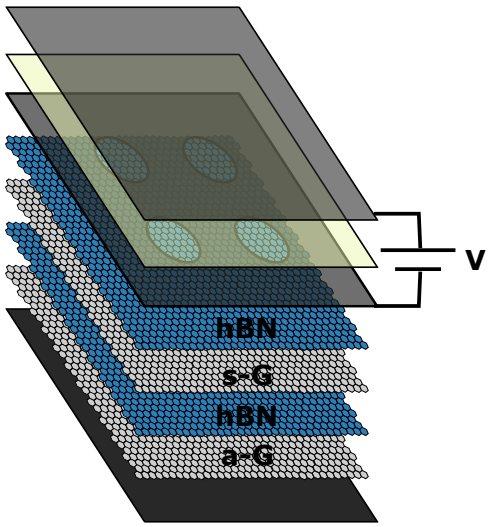

Figure 8.6: Artificial lattice proposal: a dielectric layer (yellow) separates two metal gates (gray) held at a potential difference V. The bottom metal gate has a square lattice patterned into it, which applies a periodic potential to all lower layers. A sacrificial graphene layer (s-G) is used to screen noise from the metal gates, so that only the periodic potential from the artificial lattice is applied to the active graphene layer (a-G) hosting the FCI. The graphene layers are sandwiched between hexagonal Boron Nitride (h-BN), and a graphite bottom gate (black) varies the electron density of the sample.

Generally, for large ϕ FCI phases have larger energy gaps than competing FQH phases [238], therefore for these parameter values we would expect the bulk and lattice contacts to be in an FCI and FQH phase, respectively.

Figure 8.6 illustrates one approach to engineering an artificial lattice applied to graphene. The lattice is patterned into a metal gate (third layer). The potential from this lattice can be made larger by increasing the voltage difference between two metal gates, separated by a dielectric (yellow). A sacrificial graphene layer (s-G) screens the metal gates to avoid introducing additional noise. For large enough potential difference V, only the periodic potential from the artificial lattice passes through the screening layer to affect the active graphene layer (a-G). The electron density of the system can be tuned using a graphite bottom gate (black).

8.5 Layer-resolved lattice contacts

We now propose the layer-resolved lattice contacts shown in Fig. 8.1. We assume the bulk (green) is in the plaquette-centered C_4-symmetric ground state of the (331) phase so that the layer basis corresponds to the blue and yellow sublattices (see insets). The two contacts (blue/yellow) are in the $\nu = 1/3$ phase. Possible parameter values for the bulk and contacts are given by the green and blue dots, respectively, in Fig. 8.5. Furthermore, we assume that the FCI-contact interface is sufficiently long that translation symmetry is preserved, and located in the middle of the edge so that corner physics may be neglected.

The white/green lines indicate the edge electrons $\psi_{e,1/2}$ associated with the FCI layer index. These electrons are eigenstates of the translation operators $T_{(1,\pm 1)}$, and thus have well-defined momenta. The C_4 symmetry guarantees the momentum of $\psi_{e,1/2}$ along the yellow contact interface is equal to the momentum of $\psi_{e,2/1}$ along the blue contact interface. If the energy gaps of the (331) and $\nu = 1/3$ phases are compatible (*i.e.*, the contact's edge electron has the same momentum as either $\psi_{e,1/2}$ for an appropriate value of the electrochemical potential), then $\psi_{e,1}$ and $\psi_{e,2}$ can be gapped out along opposite contacts. The Supplement describes a tuning procedure for checking that the contact's edge electron has the necessary momentum. We do not show the edge electron associated with the filled $C = -1$ band (solid black line in Fig. 8.5); generically this edge electron's momentum will be different than that of the $\psi_{e,1/2}$ and does not change under C_4 rotation, thus it can be safely ignored. Effectively, gapping out an FCI's edge electron along the contact's interface reroutes that edge electron along the exterior of the contact, spatially separating the FCI's two edge electrons. A current measurement or

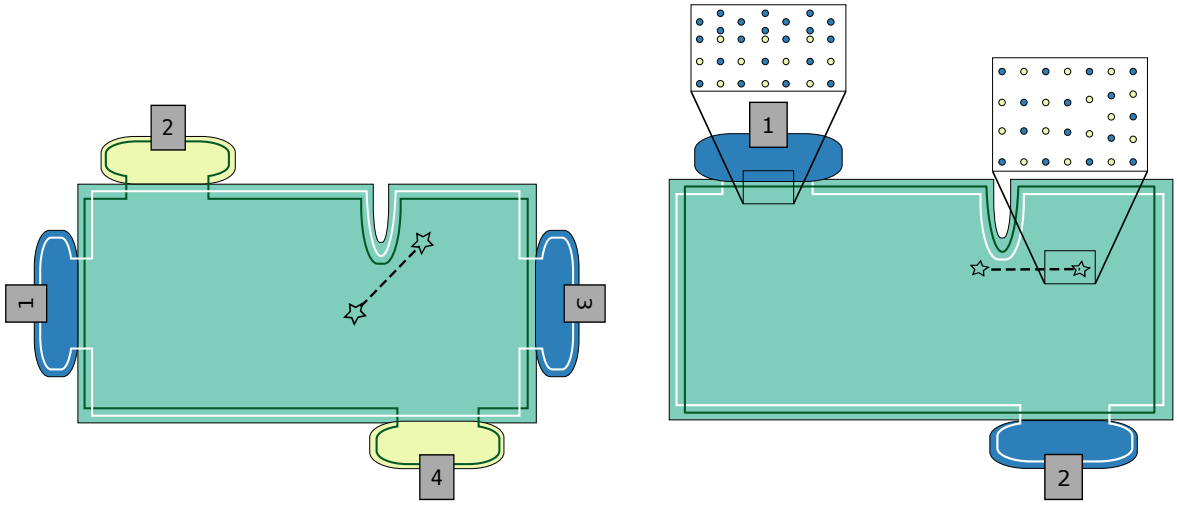

Figure 8.7: Detecting genons using FCI edges. *Left panel.* The two edge electrons (white/green lines) are interchanged at a genon (star), resulting in a signature in the differential conductance dI_r/dV_r [22]. When all contacts are held to the same chemical potential, electrodes 1 and 3 selectively couple to one of the FCI's edge electrons, while 2 and 4 couple to the other. By measuring the voltage drop between 1 and 3, as well as 2 and 4, we can determine the relative current I_r. The differential conductance dI_r/dV_r can then be determined by varying the voltage applied to any of the four electrodes. *Right panel.* The same experiment, using lattice contacts for A-type edges. The white line now depicts the edge electron associated with $\psi_{e,1} - \psi_{e,2}$, which can be gapped out by appropriately tuning the chemical potential of the contacts. The current associated with this edge electron is the relative current $I_r = I_1 - I_2$.

voltage applied to the outer edge of the lattice contact will only affect one of the FCI's edge electrons, hence the name *layer-resolved lattice contacts*.

Given the ability to separately contact the two FCI edge electrons, we can use their relative current to detect genons localized at lattice dislocations in the bulk. The left panel of Fig. 8.7 generalizes an experimental proposal in Ref. [22] for a bilayer QH system with layer exchange defects. Let $I_{1/2}$ denote the current associated with $\psi_{e,1/2}$. The relative current $I_r = I_1 - I_2$ is inverted across a genon. The layer-resolved lattice contacts allow separate control of the voltage and measurement of the current for the two edge electrons, thereby allowing readout of their relative conductance, dI_r/dV_r. The relative conductance peaks for small edge-genon

separation; therefore by comparing multiple samples that vary this separation distance, we can obtain spatial resolution of the relative conductance and detect the genon. The quantum point contact interferometer of Ref. [22] can be similarly generalized to the FCI context.

The right panel of Fig. 8.7 shows an alternate realization of the experiment described above using lattice contacts for A-type edges. Recall that for A-typed edges, translation eigenstates are $\psi_{e,\pm} = \psi_{e,1} \pm \psi_{e,2}$ for $\tau_x = \sigma_x$. When the contact is tuned to gap out $\psi_{e,-}$, a current measurement gives the exciton current I_r, which should carry the signature of the genon. It is still important in this case that the FCI-contact interface is long enough that translation symmetry is preserved, and that the contact is unaffected by corner physics.

There are many other choices for the FCI and lattice contact phases; the two phases can be realized simultaneously for constant magnetic field and backgate voltage provided the line connecting $(n_e, \phi)_{\text{g}}$ and $(n_e, \phi)_{\text{b/y}}$ intersects the origin. Furthermore, while we focused on C_4-symmetric lattices, this proposal could be generalized to lattices satisfying other spatial symmetries.

8.5.1 Calibration experiments

In order to ascertain that the layer-resolved lattice contacts are working as intended, we propose the following calibration experiments. Each experiment could be first done with the bulk and contacts in filled $C = 2$ and $C = 1$ bands, respectively, then applied to the (331) phase. Here, we assume that in both cases the energy gaps of the bulk and contacts are compatible so that the relative chemical potential can be used to tune the lattice contact's edge momentum

equal to the momentum of either of the bulk's edge electrons.

Testing interface length. The layer-resolved lattice contacts rely on the contact-bulk interface being long enough so that translation symmetry is preserved. To test this lengthscale, two bulk phases can be engineered such that their lattices are rotated by $\pi/4$ from each other, corresponding to an interface between an A-type and a B-type edge, as depicted in Fig. 8.3. When translation symmetry is preserved, there is a gapless edge mode running along the interface, since the two phases have different momentum separation. When the interface is too short to preserve translation symmetry, the interface should be gapped out since the lattice orientation is unimportant for the physics.

Testing separation from corners. The next test is for the setup shown in Fig. 8.1: all edges are B-type, with the West and South edges corresponding to blue and yellow sublattices, respectively. By changing the displacement of the lattice contacts from the Southwest corner (by using different samples), we can check that the corner physics is not affecting the lattice contacts. When the lattice contact is far away from the corners, the momentum difference between the two edge states should be $\pi/(\sqrt{2}a)$. When the contact is at the corner, there is no momentum difference between the two edge states. By varying the lattice contact displacement from the edge and measuring the amount by which we need to tune the lattice contact's chemical potential to change from gapping out one edge mode to gapping out the other, we can measure the length scale over which the corner physics is important. Once the lattice contacts are far-

enough separated from the corner, the momentum difference between edge states will be fixed. A potential difficulty of this experiment is that we need to compare different samples, thus this calibration will only work if the edge potential does not vary strongly between samples. Up to four displacements can be tested on the same sample by placing lattice contacts on different edges.

Testing layer-selectivity. The final calibration test is again for the setup in Fig. 8.1, where one lattice contact controls voltage and the other measures current. When the contacts are equilibrated with the FCI edge, the current injected at the contact should be equal to the voltage measured at that edge multiplied by the expected Hall conductance. For a long contact, this should only happen when the contact's and FCI's edge electrons have the same momentum. When the system is tuned so that the contacts gap out opposite edge electrons, varying V on the blue contact should not affect the I measured on the yellow contact. When the contacts are tuned such that they should gap out the same edge electron, varying V on the blue contact should directly affect the I measured on the yellow contact. The first case corresponds to the lattice contacts held at the same electrochemical potential for the geometry shown (South and West edges corresponding to opposite sublattices). The electrochemical potential of one contact can then be tuned (using an additional gate) to achieve the second case.

8.6 Summary and outlook

In this chapter, we proposed layer-resolved lattice contacts for FCI edges. The lattice contacts utilize the interplay of translation symmetry with internal component labels of the FCI state to selectively couple to one of the FCI's edge electrons. Lattice contacts facilitate genon detection in the bulk by measuring the differential conductance associated with the relative current between the edge electrons, which in our proposal becomes a standard four terminal conductance measurement. The experimental proposal in this paper could be realized using graphene subject to an artificial lattice.

For the (331) phase, the genons are MZMs; more exotic topological defects are possible for (mml) phases with $|m - l| > 2$ [17]. Open questions include determining the energy gaps, ground states, and symmetries, of fractionally filled Chern bands. Additionally, the role of disorder, and whether it causes FCI edge modes to equilibrate, could affect our proposal. More broadly, FCIs realized with an artificial lattice provide a playground for studying interfaces of different topological phases, including the transfer and sharing of information across the interface.

Chapter 9

Future directions

There was no telling what people might find out once they felt free to ask whatever questions they wanted to.

-Joseph Heller, *Catch-22*

The work contained in this thesis has been motivated by understanding the challenges facing topological quantum computing and presenting solutions for overcoming them. We found that diabatic errors in anyon braiding scale polynomially in the ratio of the gap to the operational times and are thus not topologically protected in the usual sense. We proposed a measurement-based protocol to correct these errors. We presented scalable designs for Majorana-based qubits that avoided many of the experimental challenges of previous designs, used a large charging energy to suppress quasiparticle errors, and are operated using a measurement-based protocol to avoid the previously mentioned diabatic errors. We studied

the charge distribution of these qubits to analyze their dephasing times. We further developed physically motivated noise models for analyzing the fault tolerance of a Majorana-based quantum computer.

The near-term devices proposed at the end of Chapter 4 are the focus of current experiments. An unforeseen difficulty in fabricating these devices has to do with the superconducting backbone: it is necessary for the backbone to be thin enough that the magnetic field line can go around it and that the charging energy remains large, and for the presence of the backbone not to introduce subgap states in the superconductor. While depositing thin layers of Al is by now standard practice on semiconductor nanowires, deposition becomes more challenging without semiconductor underneath. One hope is that advances in 2DEG or SAG wire technology may facilitate fabricating the backbone. Once these devices are fabricated, it should be possible to test the quantum dot-based measurement, measure dephasing times, and obtain a better understanding of the noise environment in semiconductor-superconductor heterostructures. Another important open question is better understanding the fault tolerance requirements for a measurement-only topological quantum computer; this question could be addressed by extending the analysis in Chapter 6 beyond quantum memory.

In the latter part of this thesis we turned our attention to an alternate platform for non-Abelian topological defects: fractional Chern insulators in graphene. Recent experiments have indicated that graphene is a viable platform for exploring fractional Chern insulators, and an exciting next step is to engineer genons. We proposed how genons in the bulk could be detected using the edge physics, provided there is sufficient control over the lattice governing the

fractional Chern insulator physics. This control could be provided by patterning an artificial lattice. The experiment is now testing whether an artificial lattice applied to graphene can be made clean enough to observe fractional Chern insulator states.

We now conclude by noting two other future directions we plan to pursue.

9.1 Analyzing measurement-based braiding of MZMs in a number conserving formalism

Recent papers have raised the troubling possibility that MZMs in a topological superconductor might have non-universal corrections to the braiding phase [172, 173]. Their key concern is that most studies analyzing braiding for p+ip superconductors rely on a mean-field Bogoliubov-de Gennes (BdG) analysis, that could miss number-conserving corrections to the braiding phase. Modifying the standard mean-field arguments by working in a number-projected BdG formalism suggest that the MZM couples to a Cooper pair operator, which in turn couples in a non-universal manner to environmental noise and is sensitive to the braiding trajectory.

We would like to apply the number conserving bosonized formalism used to analyze dephasing times in Chapter 5 to examine whether measurement-based braiding suffers from non-universal corrections. In particular, from the analysis there, we know that topologically encoded information (MZM parity) only couples to the difference fields between the semiconductor and superconductor. We expect that by analyzing how the quantum-dot based measurement proposed in Chapter 4 couples to these fields, we should be able to derive the bosonized expres-

sion for the MZM parity. If this expression only depends on the topological difference fields, we would expect that the measurement-based braiding protocol is topologically protected and not susceptible to number-conserving corrections.

9.2 FCI corner modes and higher order topological insulators

In Chapter 8 we saw that FCIs with a plaquette-centered C_4 symmetry in the (331) state support MZMs at the corners of the sample. These corner modes had important implications for how the momentum difference between edge states changed between neighboring edges, but are not expected to be exponentially localized due to the presence of gapless edge states.

Recently, corner modes have gained much interest in the context of higher order topological insulators (HOTIs) [26, 230]: topological insulators whose codimension 1 surfaces are gapped, but that can support zero energy corner modes (for 2D or 3D) or gapless hinge modes (for 3D). HOTIs differ from FCIs in that they have no intrinsic topological order (e.g., no anyonic quasiparticles), but are similar in the sense that rotational symmetries have been show to be necessary to protect the corner modes or hinge states.

We would like to study corner modes in FCIs more generally, and explore their connection to HOTIs. We believe that the defect network description developed in Ref. [87] could be applied to this problem to identify for what phases and symmetries corner modes appear. An especially interesting question would be whether we expect interesting corner states to appear

in graphene subject to a Moiré lattice, and if so whether there are experimental signatures of these states that survive edge disorder.

Appendix A

Diagrammatic anyon models

In this appendix, we review the description of anyon models on a sphere [148, 40, 43]. Since punctures may be represented by anyons existing on their boundaries, this section also applies to spheres with punctures, e.g., a disk. This formalism has been extended to higher genus surfaces [42].

This Appendix previously appeared in "Anyonic Entanglement and Topological Entanglement Entropy" by Parsa Bonderson, Christina Knapp, and Kaushal Patel, *Annals of Physics* **385**, arXiv:1706.09420.

A.1 Fusion algebra

Anyon models, or modular tensor categories (MTCs), consist of a finite set of objects, or *anyons*, which obey a commutative, associative fusion algebra:

$$a \times b = \sum_c N_{ab}^c c, \tag{A.1}$$

where N_{ab}^c is a non-negative integer that specifies the number of different ways anyons a and b can fuse to c. An anyon a is *non-Abelian* if $\sum_c N_{ab}^c > 1$ for some b, and *Abelian* otherwise.

The fusion algebra must obey certain conditions. There must exist a unique *vacuum* anyon 0 such that $N_{a0}^c = \delta_{ac}$, and each anyon a must have a *dual* anyon $\bar{a}$ such that $N_{ab}^0 = \delta_{b\bar{a}}$. We also have the important relation

$$d_a d_b = \sum_c N_{ab}^c d_c, \tag{A.2}$$

where d_a, the *quantum dimension* of a, is the largest eigenvalue of the fusion matrix N_a, (whose elements are $[N_a]_{bc} = N_{ab}^c$.) For non-Abelian anyons, $d_a > 1$, while for Abelian anyons, $d_a = 1$.

The total quantum dimension of an anyon model $\mathcal{C}$ is

$$\mathcal{D} = \sqrt{\sum_{a \in \mathcal{C}} d_a^2}. \tag{A.3}$$

A.2 Anyonic Hilbert space

The *anyonic Hilbert space* of topological system consists of all of its possible topologically distinct states. It can be constructed and expressed diagrammatically as follows.

Basis

The building blocks of the anyonic Hilbert space for the sphere is the space V_c^{ab} of two anyons a and b with definite total charge c, which is spanned by the vectors

$$|a,b;c,\mu\rangle = \left(\frac{d_c}{d_a d_b}\right)^{1/4} \quad , \tag{A.4}$$

where $\mu = 1, \ldots, N_{ab}^c$. The dual space V_{ab}^c is spanned by the covectors

$$\langle a,b;c,\mu| = \left(\frac{d_c}{d_a d_b}\right)^{1/4} \quad . \tag{A.5}$$

Larger spaces are constructed by taking tensor products. For example, the space V_d^{abc} of three anyons a, b, and c with definite total charge d can be constructed as

$$V_d^{abc} \cong \bigoplus_e V_e^{ab} \otimes V_d^{ec}, \tag{A.6}$$

which is spanned by

$$|a,b;e,\mu\rangle|e,c;d,\nu\rangle = \left(\frac{d_d}{d_a d_b d_c}\right)^{1/4} \quad , \tag{A.7}$$

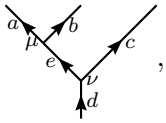

where $\mu = 1, \ldots, N_{ab}^e$, $\nu = 1, \ldots, N_{ec}^d$, and e is any anyon such that $N_{ab}^e \geq 1$ and $N_{ec}^d \geq 1$. The space V_d^{abc} can also be constructed as

$$V_d^{abc} \cong \bigoplus_e V_e^{bc} \otimes V_d^{ae}, \tag{A.8}$$

which is spanned by

$$|b,c;e,\mu\rangle|a,e;d,\nu\rangle = \left(\frac{d_d}{d_a d_b d_c}\right)^{1/4} \quad . \tag{A.9}$$

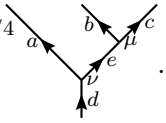

where $\mu = 1, \ldots, N_{bc}^e$, $\nu = 1, \ldots, N_{ae}^d$, and e is any anyon such that $N_{bc}^e \geq 1$ and $N_{ae}^d \geq 1$.

These constructions are isomorphic, and their basis vectors are related by an F-*move*:

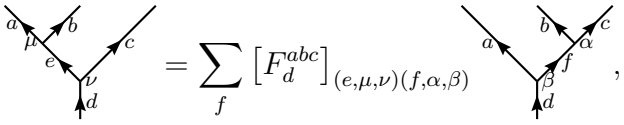

$$= \sum_f \left[F_d^{abc}\right]_{(e,\mu,\nu)(f,\alpha,\beta)} \quad , \tag{A.10}$$

where the F-*symbols* F_d^{abc} are unitary matrices that must satisfy the Pentagon consistency equations.

In general, the space $V_c^{a_1 \ldots a_n}$ of anyons $a_1, \ldots, a_n$ with definite combined charge c can be constructed as

$$V_c^{a_1 \ldots a_n} \cong \bigoplus_{\vec{b}} V_{b_2}^{a_1 a_2} \otimes V_{b_3}^{b_2 a_3} \otimes \cdots \otimes V_c^{b_{n-1} a_n}, \tag{A.11}$$

which is spanned by

$$\begin{aligned} |\vec{a}, \vec{b}, \vec{\alpha}; c\rangle &= |a_1, a_2; b_2, \alpha_2\rangle \cdots |b_{n-1}, a_n; c, \alpha_n\rangle \\ &= \left(\frac{d_c}{d_{a_1} \cdots d_{a_n}}\right)^{1/4} \end{aligned}$$

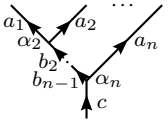

. (A.12)

where $\vec{b}$ and $\vec{\alpha}$ take values that are allowed by fusion.

We can also write the F-move with two lower and two upper legs. This basis change is given by

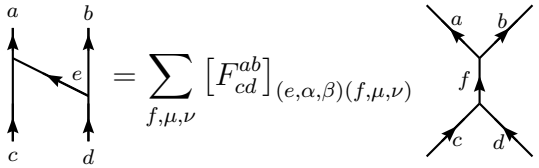

$$= \sum_{f,\mu,\nu} \left[F_{cd}^{ab}\right]_{(e,\alpha,\beta)(f,\mu,\nu)} \quad , \tag{A.13}$$

where the F-symbol in the above equation is related to the regular F-symbol by

$$\left[F_{cd}^{ab}\right]_{(e,\alpha,\beta)(f,\mu,\nu)} = \sqrt{\frac{d_e d_f}{d_a d_d}} \left[F_f^{ceb}\right]^*_{(a,\alpha,\mu)(d,\beta,\nu)} \tag{A.14}$$

and is also a unitary transformation.

Dimension

The dimension of $V_c^{a_1 \cdots a_n}$ is given by

$$\dim(V_c^{a_1 \cdots a_n}) = \sum_{\vec{b}} N_{a_1 a_2}^{b_2} N_{b_2 a_3}^{b_3} \cdots N_{b_{n-1} a_n}^{c} \equiv N_{a_1 \ldots a_n}^{c}. \tag{A.15}$$

The total dimension of the space of anyons $a_1, \ldots, a_n$ is

$$\sum_c \dim(V_c^{a_1 \cdots a_n}) = \sum_c N_{a_1 \ldots a_n}^{c} \equiv N_{a_1 \ldots a_n}, \tag{A.16}$$

In particular, if $a_1 = \cdots = a_n = a$, then the dimension grows as $N_{a \ldots a} \sim d_a^n$ for large n. Note that a collection of Abelian anyons can only produce 1-dimensional spaces, but non-Abelian anyons can give rise to higher dimensional spaces. When considered by itself, a single anyon does not possess a multi-dimensional Hilbert space, so, from the perspective of individual anyons, the meaning of the quantum dimension is not so clear. We also define

$$d_{\vec{a}} \equiv d_{a_1} \cdots d_{a_n} = \sum_c N_{a_1 \ldots a_n}^{c} d_c. \tag{A.17}$$

Note that $N_{a_1 \ldots a_n} = \mathrm{Tr}(1_{a_1 \ldots a_n})$ and $d_{\vec{a}} = \widetilde{\mathrm{Tr}}(1_{a_1 \ldots a_n})$, where Tr and $\widetilde{\mathrm{Tr}}$ are defined below, and that they both grow with the same scaling as $n \to \infty$.

Inner Product

Inner products can be evaluated by stacking diagrams, e.g. the fact that

$$\langle a', b'; c', \mu' | a, b; c, \mu \rangle = \delta_{a,a'} \delta_{b,b'} \delta_{c,c'} \delta_{\mu,\mu'} 1_c \tag{A.18}$$

can be expressed as

$$\left(\frac{d_c^2}{d_a d_b d_{a'} d_{b'}}\right)^{1/4}$$ 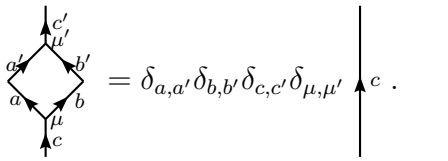 $$= \delta_{a,a'}\delta_{b,b'}\delta_{c,c'}\delta_{\mu,\mu'}$$. (A.19)

Note that in the diagrammatic notation, $\delta_{a,a'}$ and $\delta_{b,b'}$ ensure that the branches of the splitting vertex can be joined with those of the fusion vertex, while $\delta_{c,c'}$ enforces the conservation of anyonic charge. More complicated diagrams can be similarly evaluated.

Operators

The space $V_{a_1 \ldots a_n}^{a'_1 \ldots a'_n}$ of operators acting on anyons $a_1, \ldots, a_n$ can be constructed as

$$V_{a_1 \ldots a_n}^{a'_1 \ldots a'_n} = \bigoplus_c V_{a_1 \ldots a_n}^{c} \otimes V_c^{a'_1 \ldots a'_n}, \tag{A.20}$$

which is spanned by

$$|\vec{a}', \vec{b}', \vec{\alpha}'; c\rangle\langle \vec{a}, \vec{b}, \vec{\alpha}; c| = \left(\frac{d_c^2}{d_{\vec{a}} d_{\vec{a}'}}\right)^{1/4}$$ 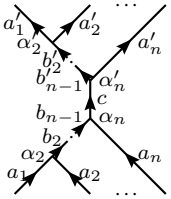 , (A.21)

where $\vec{b}$, $\vec{\alpha}$, $\vec{b}'$, and $\vec{\alpha}'$ take values that are allowed by fusion.

For example, the identity operator for a pair of anyons a and b is

$$1_{ab} = \sum_{c,\mu} |a, b; c, \mu\rangle\langle a, b; c, \mu|, \tag{A.22}$$

or, diagrammatically,

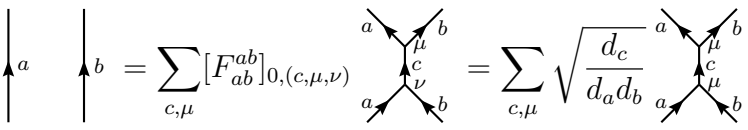 (A.23)

and the braiding operator for the pair is

$$R^{ab} = \sum_{c,\mu} [R_c^{ab}]_{\mu\nu} |a, b; c, \mu\rangle\langle b, a; c, \nu|, \tag{A.24}$$

or, diagrammatically,

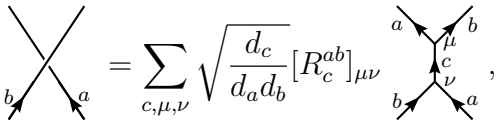

(A.25)

where the R *symbols* R_c^{ab} are unitary matrices that must satisfy the Hexagon consistency equations.

$\mathcal{S}$-matrix

The topological S-matrix is defined by

$$S_{ab} = \frac{1}{\mathcal{D}} \widetilde{\text{Tr}} \left(R^{b\bar{a}} R^{\bar{a}b} \right). \tag{A.26}$$

The quantum dimension is related to the S-matrix by

$$d_a = \frac{S_{0a}}{S_{00}}. \tag{A.27}$$

For a modular tensor category (MTC), the S-matrix is unitary and provides a unitary projective representation of the modular $\mathcal{S}$-transformations. In this case, the fusion coefficients can be expressed in terms of the $\mathcal{S}$-matrix by the Verlinde formula

$$N_{ab}^c = \sum_x \frac{\mathcal{S}_{ax} \mathcal{S}_{bx} \mathcal{S}_{cx}^*}{\mathcal{S}_{0x}}. \tag{A.28}$$

It follows that the dimension of $V_c^{a_1 \cdots a_n}$, given in Eq. (A.15), can also be expressed in terms of

the $\mathcal{S}$-matrix as

$$N^c_{a_1 \ldots a_n} = \sum_x \mathcal{S}_{0x}^{1-n} \mathcal{S}_{a_1 x} \cdots \mathcal{S}_{a_n x} \mathcal{S}^*_{cx}. \tag{A.29}$$

ω_a-loops

The ω_a-loop is defined by

ω_a 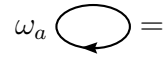 $= \sum_x \mathcal{S}_{0a} \mathcal{S}^*_{ax}$ 

, (A.30)

and acts a projector on all charges threading the loop,

ω_a 

$= \delta_{ab}$ 

. (A.31)

Trace

The *trace* of an operator is defined, as usual, to be the sum of its diagonal elements, e.g.

$$\mathrm{Tr}(|a', b'; c, \mu'\rangle\langle a, b; c, \mu|) = \delta_{a,a'} \delta_{b,b'} \delta_{\mu,\mu'} \tag{A.32}$$

Its diagrammatic equivalent is the *quantum trace* $\widetilde{\mathrm{Tr}}$, (also called the *anyonic trace*,) which is obtained by joining the outgoing anyon lines of the operator's diagram back onto the corresponding incoming lines, e.g.

$\widetilde{\mathrm{Tr}}\left(\left(\frac{d_c^2}{d_a d_b d_{a'} d_{b'}} \right)^{1/4}$ 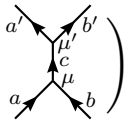

$\right) = \left(\frac{d_c^2}{d_a d_b d_{a'} d_{b'}} \right)^{1/4}$ 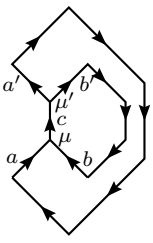

$$= d_c \delta_{a,a'} \delta_{b,b'} \delta_{\mu,\mu'}, \tag{A.33}$$

which agrees with Eq. (A.32) except for the factor of d_c. In general, the anyonic trace of an operator $X \in V_{a'_1 \ldots a'_n}^{a_1 \ldots a_n}$ is related to its ordinary trace by

$$\widetilde{\mathrm{Tr}}(X) = \sum_c d_c \mathrm{Tr}([X]_c), \tag{A.34}$$

$$\mathrm{Tr}(X) = \sum_c \frac{1}{d_c} \widetilde{\mathrm{Tr}}([X]_c) \tag{A.35}$$

where $[X]_c = \Pi_c X \Pi_c \in V_c^{a_1 \ldots a_n} \otimes V_{a'_1 \ldots a'_n}^c$ is the projection of X onto definite total charge c, with $X = \sum_c [X]_c$.

The *partial anyonic trace* is obtained by joining only the outgoing and incoming lines of the anyons being traced over, e.g.

$$\widetilde{\mathrm{Tr}}_b \left(\left(\frac{d_c^2}{d_a d_b d_{a'} d_{b'}} \right)^{1/4} \right.$$

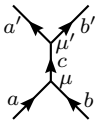

$$\left. \right) = \left(\frac{d_c^2}{d_a d_b d_{a'} d_{b'}} \right)^{1/4}$$

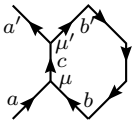

$$= \frac{d_c}{d_a} \delta_{a,a'} \delta_{b,b'} \delta_{\mu,\mu'}$$

. (A.36)

Before computing the partial trace, all the anyons being traced over must moved to the edge of the diagram by braiding them past the other anyons, a process which is not necessarily unique. In general, the partial anyonic trace of $X \in V_{a'_1 \ldots a'_n b'_1 \ldots b'_m}^{a_1 \ldots a_n b_1 \ldots b_m}$ over the anyons $b_1, \ldots, b_m$ is related

to its ordinary partial trace by

$$\widetilde{\mathrm{Tr}}_{b_1\ldots b_m}(X) = \sum_{c,a} \frac{d_c}{d_a} [\mathrm{Tr}_{b_1\ldots b_m}([X]_c)]_a, \tag{A.37}$$

$$\mathrm{Tr}_{b_1\ldots b_m}(X) = \sum_{c,a} \frac{d_a}{d_c} [\widetilde{\mathrm{Tr}}_{b_1\ldots b_m}([X]_c)]_a. \tag{A.38}$$

A.3 Anyonic density matrix

An *anyonic density matrix* $\tilde{\rho}$ is an anyonic operator normalized by the quantum trace $\widetilde{\mathrm{Tr}}\tilde{\rho} = 1$, that describes the topological state of the system. The anyonic density matrix $\tilde{\rho}$ determines the expectation value of anyonic operators acting on the system, $\langle X \rangle = \widetilde{\mathrm{Tr}}(\tilde{\rho} X)$. For example, the density matrix describing a pair of anyons a and b with definite total charge c is

$$\tilde{\rho}_{ab} = \frac{1}{d_c} |a, b; c, \mu\rangle\langle a, b; c, \mu| = \frac{1}{\sqrt{d_a d_b d_c}}$$

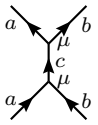

, (A.39)

which is normalized such that $\widetilde{\mathrm{Tr}}(\tilde{\rho}^{ab}) = 1$, while the most general state for the pair is given by

$$\begin{aligned} \tilde{\rho}_{ab} &= \sum_{\substack{a,b,\mu \\ c \\ a',b',\mu'}} \frac{\rho_{(a,b;c,\mu)(a',b';c,\mu')}}{d_c} |a, b; c, \mu\rangle\langle a', b'; c, \mu'| \\ &= \sum_{\substack{a,b,\mu \\ c \\ a',b',\mu'}} \frac{\rho_{(a,b;c,\mu)(a',b';c,\mu')}}{(d_a d_b d_{a'} d_{b'} d_c^2)^{1/4}} \end{aligned}$$

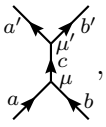

, (A.40)

where the coefficients are normalized such that $\sum_{a,b,\mu,c} \rho_{(a,b;c,\mu)(a,b;c,\mu)} = 1$.

For a collection of anyons $a_1, \ldots, a_n, b_1, \ldots, b_n$, the reduced anyonic density matrix

$$\tilde{\rho}_{a_1 \ldots a_n} = \widetilde{\mathrm{Tr}}_{b_1 \ldots b_n}(\tilde{\rho}_{a_1 \ldots a_n b_1 \ldots b_n}) \tag{A.41}$$

describes the topological state of the anyons $a_1, \ldots, a_n$, i.e. for any operator $X \in V_{a'_1 \ldots a'_n}^{a_1 \ldots a_n}$,

$$\langle X \rangle = \widetilde{\mathrm{Tr}}(\tilde{\rho}_{a_1 \ldots a_n b_1 \ldots b_n} X) = \widetilde{\mathrm{Tr}}(\tilde{\rho}_{a_1 \ldots a_n} X). \tag{A.42}$$

Appendix B

Field theoretic bosonization

In this appendix, we review the field theoretic bosonization used in Chapter 5 to model a Majorana nanowire and in Chapters 7 and 8 to study chiral edge states of FQH and FCI phases.

B.1 Basic definitions

The essential idea behind field theoretic bosonization is that fermionic fields can be described by exponentiated bosonic fields. While somewhat strange at first glance, this mapping allows one to reexpress terms in the action that are quartic in the fermionic fields, such as density-density interactions, as quadratic terms for the bosonic fields. Thus interacting problems in the fermionic language become soluble with bosonization. The derivation of these expressions can be found in many places (see e.g., Ref. [107]) and we will not reproduce it here, but rather quote the resulting expressions.

In 1D, a fermionic operator can be decomposed into left and right-moving parts,

$$\psi(x) = e^{ik_F x}\psi_R(x) + e^{-ik_F x}\psi_L(x). \tag{B.1}$$

We begin by considering a spinless system. The left and right-moving fields can be written as

$$\psi_r(x) = \frac{1}{\sqrt{2\pi a}} e^{i\theta(x)+ir\phi(x)}, \tag{B.2}$$

where a is the short distance cutoff and the bosonic fields $\theta(x)$ and $\phi(x)$ satisfy commutation relations

$$[\phi(x), \theta(x')] = i\pi\Theta(x - x'), \tag{B.3}$$

$$[\partial_x\phi(x), \theta(x')] = i\pi\delta(x - x'). \tag{B.4}$$

The fields ϕ and θ commute with themselves. We have written $r = \pm$ to denote right or left mover, respectively. (Equation (B.4) implies that ϕ and θ are dual fields to each other; Eq. (B.3) is sometimes defined as $i\pi\text{Sign}(x-x')/2$, in which case the left/right moving fermions require a Klein factor U_r to impose the correct anticommutation relations, see e.g. Ref. [107].) To see that the above commutation relations imply anticommutation of the fermionic fields $\psi_{R/L}(x)$,

note

$$\begin{aligned}\psi_R(x)\psi_L(x') &\sim e^{i\theta(x)+i\phi(x)}e^{i\theta(x')-i\phi(x')} \\ &= e^{i\theta(x')-i\phi(x')}e^{i\theta(x)+i\phi(x)}e^{-[\theta(x)+\phi(x),\theta(x')-\phi(x')]} \\ &= e^{-i\pi(\Theta(x-x')-\Theta(x'-x))}\psi_L(x')\psi_R(x) \\ &= -\psi_L(x')\psi_R(x) \qquad \text{(B.5)} \\ \psi_R(x)\psi_R(x') &\sim e^{i\theta(x)+i\phi(x)}e^{i\theta(x')+i\phi(x')} \\ &= e^{i\theta(x')+i\phi(x')}e^{i\theta(x)+i\phi(x)}e^{-[\theta(x)+\phi(x),\theta(x')+\phi(x')]} \\ &= \psi_R(x')\psi_R(x)e^{-i\pi(\Theta(x-x')+\Theta(x'-x))} \\ &= -\psi_R(x')\psi_R(x). \qquad \text{(B.6)}\end{aligned}$$

In the above, we used the commutation relation

$$e^A e^B = e^B e^A e^{[A,B]}, \qquad \text{(B.7)}$$

for operators A, B satisfying $[A,[A,B]] = [B,[A,B]] = 0$.

In our convention, the field ϕ is related to the particle density j_0, while θ is related to the current j_1:

$$\frac{1}{\pi}\partial(x) = \rho_R(x) + \rho_L(x) = j_0(x), \qquad \text{(B.8)}$$

$$\frac{1}{\pi}\theta(x) = \rho_R(x) - \rho_L(x) = j_1(x). \qquad \text{(B.9)}$$

A fermionic Hamiltonian with density-density interaction bosonizes to a Luttinger liquid,

$$H = \frac{v}{2\pi} \int dx \left(K(\partial_x \theta)^2 + K^{-1} (\partial_x \phi)^2 \right), \tag{B.10}$$

where v is the Fermi velocity and K is the Luttinger parameter. The Luttinger parameter characterizes the strength of the interactions: $K = 1$ corresponds to a non-interacting system, $K < 1$ to repulsive interactions, and $K > 1$ to attractive interactions.

When the system is spinful, a fermion with spin σ is bosonized

$$\psi_\sigma \sim e^{ik_F x} \psi_{R,\sigma} + e^{-ik_F x} \psi_{L,\sigma} \tag{B.11}$$

$$\psi_{r,\sigma} = \frac{U_r}{\sqrt{2\pi a}} e^{\frac{i}{\sqrt{2}}(\theta_\rho + r\phi_\rho + \sigma(\theta_\sigma + r\phi_\sigma))}. \tag{B.12}$$

The subscript ρ indicates a charge field, $\theta_\rho = \frac{1}{\sqrt{2}}(\theta_\uparrow + \theta_\downarrow)$ while subscript σ indicates a spin field, $\theta_\sigma = \frac{1}{\sqrt{2}}(\theta_\uparrow - \theta_\downarrow)$ (and similarly for ϕ_μ). Spin and charge fields commute, i.e., commutator in Eq. (B.4) acquires a $\delta_{\mu\nu}$ on the right.

The Luttinger liquid action for spinful fields is

$$H = \sum_{\mu=\rho,\sigma} \frac{v_\mu}{2\pi} \int dx \left(K_\mu (\partial_x \theta_\mu)^2 + K_\mu^{-1} (\partial_x \phi_\mu)^2 \right) + \frac{\Delta_\sigma}{(2\pi a)^2} \int dx \cos(2\sqrt{2}\phi_\sigma). \tag{B.13}$$

When the spin modes become massive (ϕ_σ orders), the Luttinger liquid is called a Luther-Emergy liquid. The Luther-Emergy liquid is a 1D analog of a superconductor.

B.2 Majorana nanowire description

We now derive the Lagrangian used to study a Majorana nanowire in Chapter 5. We begin with a nanowire Hamiltonian

$$H_{\text{NW}} = \int dx \psi_\sigma^\dagger(x) \left(-\frac{\partial_x^2}{2m} - \mu + i\alpha\sigma_y\partial_x + V_z\sigma_z \right)_{\sigma\sigma'} \psi_{\sigma'}(x) \tag{B.14}$$

and model the superconductor with the attractive Hubbard model

$$H_{\text{SC}} = \int dx \left\{ -\sum_\sigma \eta_\sigma^\dagger(x)\partial_x\eta_\sigma + U\rho_\uparrow(x)\rho_\downarrow(x) \right\}. \tag{B.15}$$

Above, we have written the density as $\rho_\sigma(x) =: \eta_\sigma^\dagger(x)\eta_\sigma(x) :$. For large Zeeman gap, the nanowire can be written as spinless Luttinger liquid while the superconductor is a Luther-Emery liquid (Eqs. (B.10) and (B.13), respectively).

We assume the semiconductor-superconductor interface is clean and thus electrons can tunnel across it:

$$H_T = t\sum_\sigma \int dx \left(\psi_\sigma^\dagger \eta_\sigma + h.c. \right). \tag{B.16}$$

Since ϕ_σ for the superconductor is pinned, single electron tunneling is not allowed. We can expand the tunneling term to second order in perturbation theory, resulting in the action

$$S_{\text{PT}} = -t^2 \sum_\sigma \int dx dx' d\tau d\tau' \left\{ \psi_\sigma^\dagger(x,\tau)\psi_{-\sigma}^\dagger(x',\tau')\eta_\sigma(x,\tau)\eta_{-\sigma}(x',\tau') + h.c. \right\}. \tag{B.17}$$

Expanding ψ and η in Eq. (B.17) into left and right movers, we note that terms involving odd numbers of left and right movers average to zero because they contain oscillating exponentials $\exp\left\{i\left(k_F + k_F^{(\rho)}\right)x\right\}$. The field θ_σ for the superconductor is highly disordered (because its dual field is pinned), thus averaging over this field sets $(x,\tau) = (x',\tau')$. The spinless assumption for the semiconductor allows us to replace $\sqrt{2}\theta_\rho \to 2\theta$. Therefore, pair tunneling contributes a term

$$\frac{\Delta}{2\pi a}\int dx \cos\left(\sqrt{2}\theta_\rho - 2\theta\right), \tag{B.18}$$

where as in Chapter 5, θ refers to the semiconductor while θ_ρ is the charge field of the superconductor. (An alternative derivation begins from assuming the Luttinger liquid describes a helical nanowire, so that tunneling only involves terms $\eta_\downarrow^\dagger\psi_L + h.c.$ and $\eta_\uparrow^\dagger\psi_R + h.c.$.)

As noted in Chapter 5, in the ground state the difference field $\theta_- = \theta_\rho/\sqrt{2} - \theta$ is pinned to $n\pi$, $n \in \mathrm{Z}$ to minimize the pairing term. The commutator

$$[\phi_-(x), \theta_-(x')] = \frac{i\pi}{2}\mathrm{Sign}(x - x'), \tag{B.19}$$

implies that the parity operator

$$(-1)^N = (-1)^{N_-} = e^{i\pi N_-} \qquad = e^{i\pi(\phi_-(L) - \phi_-(0))} \tag{B.20}$$

changes θ_- by π. Therefore, the parity eigenstates for a single wire are

$$|\pm\rangle = \frac{1}{\sqrt{2}} \left(|\theta_- = 0\rangle \pm |\theta_- = \pi\rangle \right). \tag{B.21}$$

Finally, in Chapter 5 we assumed that the charging energy was large enough to ignore quasiparticle poisoning. If we wanted to account for the charging energy explicitly, we could add terms to the action

$$S_C = -E_C \int d\tau \left(N_{\text{sm}}(\tau) + N_{\text{sc}}(\tau) - N_g \right)^2 \tag{B.22}$$

$$= -\frac{E_C}{\pi^2} \int d\tau \left(\phi(\tau, L) - \phi(\tau, 0) + \phi_\rho(\tau, L) - \phi_\rho(\tau, 0) - N_g \right)^2. \tag{B.23}$$

In terms of the sum and difference fields, S_C only depends on ϕ_+ and therefore does not couple to the topological degrees of freedom.

B.3 Chiral fields

The Luttinger liquid Hamiltonian, Eq. (B.10) can be diagonalized by the fields

$$\phi_R = K\theta - \phi \tag{B.24}$$

$$\phi_L = K\theta + \phi, \tag{B.25}$$

satisfying commutation relations

$$[\phi_r(x), \phi_{r'}(x')] = \pm i\pi K \text{Sign}(x - x')\delta_{r,r'}, \tag{B.26}$$

where again $r = R, L$.

We can define operators

$$\tilde{\rho}_{R/L} = \pm \frac{1}{2\pi} \partial_x \phi_{R/L}. \tag{B.27}$$

When $K = 1$, $\tilde{\rho}_{R/L}$ are the densities of $\psi_{R/L}$. Note that

$$\partial_t \tilde{\rho}_r = \mp \partial_x \tilde{\rho}_r, \tag{B.28}$$

therefore $\tilde{\rho}_r$ are only functions of $x \mp vt$ and are therefore chiral fields. The field theory used to describe quantum Hall edges is written in terms of these chiral fields, with the K matrix determining the number of left/right movers.

Bibliography

[1] D. Aasen, M. Hell, R. V. Mishmash, A. Higginbotham, J. Danon, M. Leijnse, T. S. Jespersen, J. A. Folk, C. M. Marcus, K. Flensberg, and J. Alicea. Milestones Toward Majorana-Based Quantum Computing. *Phys. Rev. X*, 6(3):031016, July 2016.

[2] Ian Affleck and Andreas W. W. Ludwig. Universal noninteger "ground-state degeneracy" in critical quantum systems. *Phys. Rev. Lett.*, 67:161–164, Jul 1991.

[3] T. Albash and D. A. Lidar. Decoherence in adiabatic quantum computation. *Phys. Rev. A*, 91(6):062320, June 2015.

[4] C. Albrecht, J. H. Smet, K. von Klitzing, D. Weiss, V. Umansky, and H. Schweizer. Evidence of hofstadter's fractal energy spectrum in the quantized hall conductance. *Phys. Rev. Lett.*, 86:147–150, Jan 2001.

[5] S. M. Albrecht, A. P. Higginbotham, M. Madsen, F. Kuemmeth, T. S. Jespersen, J. Nygård, P. Krogstrup, and C. M. Marcus. Exponential protection of zero modes in Majorana islands. *Nature*, 531:206, March 2016.

[6] J. Alicea. New directions in the pursuit of Majorana fermions in solid state systems. *Rep. Prog. Phys.*, 75(7):076501, July 2012.

[7] J. Alicea, Y. Oreg, G. Refael, F. von Oppen, and M. P. A. Fisher. Non-Abelian statistics and topological quantum information processing in 1D wire networks. *Nature Physics*, 7:412–417, May 2011.

[8] A. Altland and R. Egger. Multiterminal Coulomb-Majorana Junction. *Phys. Rev. Lett.*, 110(19):196401, May 2013.

[9] Andrey E. Antipov, Arno Bargerbos, Georg W. Winkler, Bela Bauer, Enrico Rossi, and Roman M. Lutchyn. Effects of Gate-Induced Electric Fields on Semiconductor Majorana Nanowires. *Phys. Rev. X*, 8(3):031041, Jul 2018.

[10] III Avignone, Frank T., Steven R. Elliott, and Jonathan Engel. Double beta decay, Majorana neutrinos, and neutrino mass. *Reviews of Modern Physics*, 80(2):481–516, Apr 2008.

[11] D. Bacon and S. T. Flammia. Adiabatic Gate Teleportation. *Phys. Rev. Lett.*, 103(12):120504, September 2009.

[12] Dave Bacon. Operator quantum error-correcting subsystems for self-correcting quantum memories. *Phys. Rev. A*, 73:012340, Jan 2006.

[13] E. Bakkers and L. Kouwenhoven. *private communication*.

[14] M. Banerjee, M. Heiblum, V. Umansky, D. E. Feldman, Y. Oreg, and A. Stern. Observation of half-integer thermal Hall conductance. *Nature*, 559:205, July 2018.

[15] R. Barends, J. Kelly, A. Megrant, A. Veitia, D. Sank, E. Jeffrey, T. C. White, J. Mutus, A. G. Fowler, B. Campbell, Y. Chen, Z. Chen, B. Chiaro, A. Dunsworth, C. Neill, P. O'Malley, P. Roushan, A. Vainsencher, J. Wenner, A. N. Korotkov, A. N. Cleland, and J. M. Martinis. Superconducting quantum circuits at the surface code threshold for fault tolerance. *Nature*, 508:500–503, April 2014.

[16] M. Barkeshli and M. Freedman. Modular transformations through sequences of topological charge projections. *Phys. Rev. B*, 94(16):165108, October 2016.

[17] M. Barkeshli, C.-M. Jian, and X.-L. Qi. Twist defects and projective non-Abelian braiding statistics. *Phys. Rev. B*, 87(4):045130, January 2013.

[18] M. Barkeshli and J. D. Sau. Physical Architecture for a Universal Topological Quantum Computer based on a Network of Majorana Nanowires. September 2015.

[19] Maissam Barkeshli, Parsa Bonderson, Meng Cheng, and Zhenghan Wang. Symmetry, Defects, and Gauging of Topological Phases. page arXiv:1410.4540, 2014.

[20] Maissam Barkeshli, Chao-Ming Jian, and Xiao-Liang Qi. Twist defects and projective non-abelian braiding statistics. *Phys. Rev. B*, 87:045130, Jan 2013.

[21] Maissam Barkeshli and Xiao-Liang Qi. Topological nematic states and non-abelian lattice dislocations. *Phys. Rev. X*, 2:031013, Aug 2012.

[22] Maissam Barkeshli and Xiao-Liang Qi. Synthetic topological qubits in conventional bilayer quantum hall systems. *Phys. Rev. X*, 4:041035, Nov 2014.

[23] C. Barthel, M. Kjærgaard, J. Medford, M. Stopa, C. M. Marcus, M. P. Hanson, and A. C. Gossard. Fast sensing of double-dot charge arrangement and spin state with a radio-frequency sensor quantum dot. *Phys. Rev. B*, 81:161308, Apr 2010.

[24] C. W. J. Beenakker. Search for Majorana fermions in superconductors. *Annu. Rev. Condens. Matter Phys.*, 4:113, 2013.

[25] Gilad Ben-Shach, Arbel Haim, Ian Appelbaum, Yuval Oreg, Amir Yacoby, and Bertrand I. Halperin. Detecting Majorana modes in one-dimensional wires by charge sensing. *Phys. Rev. B*, 91(4):045403, January 2015.

[26] Wladimir A. Benalcazar, B. Andrei Bernevig, and Taylor L. Hughes. Electric multipole moments, topological multipole moment pumping, and chiral hinge states in crystalline insulators. *Phys. Rev. B*, 96(24):245115, Dec 2017.

[27] C. H. Bennet and G. Brassard. Quantum cryptography: Public key distribution and coin tossing. *IEEE Conf. Proc.*, 175:8, 1984.

[28] B. Béri and N. R. Cooper. Topological Kondo Effect with Majorana Fermions. *Phys. Rev. Lett.*, 109:156803, October 2012.

[29] Michael V. Berry. Quantal phase factors accompanying adiabatic changes. *Proc. Roy. Soc. Lond.*, A392:45–57, 1984.

[30] W. Bishara, P. Bonderson, C. Nayak, K. Shtengel, and J. K. Slingerland. The non-abelian interferometer. *Phys. Rev. B*, 80:155303, 2009.

[31] P. Bonderson. Splitting the topological degeneracy of non-Abelian anyons. *Phys. Rev. Lett.*, 103:110403, 2009.

[32] P. Bonderson. Measurement-only topological quantum computation via tunable interactions. *Phys. Rev. B*, 87(3):035113, January 2013.

[33] P. Bonderson, D. J. Clarke, C. Nayak, and K. Shtengel. Implementing Arbitrary Phase Gates with Ising Anyons. *Phys. Rev. Lett.*, 104(18):180505, May 2010.

[34] P. Bonderson, M. Freedman, and C. Nayak. Measurement-only topological quantum computation. *Phys. Rev. Lett.*, 101:010501, 2008.

[35] P. Bonderson, M. Freedman, and C. Nayak. Measurement-only topological quantum computation via anyonic interferometry. *Ann. Phys.*, 324:787, 2009.

[36] P. Bonderson, A. Kitaev, and K. Shtengel. Detecting non-Abelian statistics in the $\nu = 5/2$ fractional quantum Hall state. *Phys. Rev. Lett.*, 96(1):016803, 2006.

[37] P. Bonderson and R. M. Lutchyn. Topological Quantum Buses: Coherent Quantum Information Transfer between Topological and Conventional Qubits. *Phys. Rev. Lett.*, 106(13):130505, April 2011.

[38] P. Bonderson and C. Nayak. Quasi-topological phases of matter and topological protection. *Phys. Rev. B*, 87(19):195451, May 2013.

[39] P. Bonderson, K. Shtengel, and J. K. Slingerland. Interferometry of non-Abelian anyons. *Ann. Phys.*, 323(11):2709–2755, November 2008.

[40] P. H. Bonderson. *Non-Abelian anyons and interferometry*. PhD thesis, California Institute of Technology, 2007.

[41] Parsa Bonderson, Colleen Delaney, César Galindo, Eric C. Rowell, Alan Tran, and Zhenghan Wang. On invariants of Modular categories beyond modular data. May 2018.

[42] Parsa Bonderson, Christina Knapp, and Kaushal Patel. Anyonic entanglement and topological entanglement entropy. *Ann. Phys.*, 385:399–468, Oct 2017.

[43] Parsa Bonderson, Kirill Shtengel, and J. K. Slingerland. Interferometry of non-abelian anyons. *Ann. Phys.*, 323:2709, 2008.

[44] M. Born and V. Fock. Beweis des Adiabatensatzes. *Zeitschrift fur Physik*, 51:165–180, March 1928.

[45] P. O. Boykin, T. Mor, M. Pulver, V. Roychowdhury, and F. Vatan. On Universal and Fault-Tolerant Quantum Computing. June 1999.

[46] S. Bravyi and J. Haah. Magic state distillation with low overhead. *Phys. Rev. A*, 86(5):052329, 2012.

[47] S. Bravyi and A. Kitaev. Universal quantum computation with ideal Clifford gates and noisy ancillas. *Phys. Rev. A*, 71(2):022316, February 2005.

[48] S. Bravyi, B. M. Terhal, and B. Leemhuis. Majorana fermion codes. *New J. Phys.*, 12(8):083039, August 2010.

[49] Sergey Bravyi. Universal quantum computation with the $\nu = 5/2$ fractional quantum Hall state. *Phys. Rev. A*, 73:042313, 2006.

[50] C. G. Brell, S. Burton, G. Dauphinais, S. T. Flammia, and D. Poulin. Thermalization, Error Correction, and Memory Lifetime for Ising Anyon Systems. *Phys. Rev. X*, 4(3):031058, July 2014.

[51] Jan Carl Budich, Stefan Walter, and Bjrn Trauzettel. Failure of protection of Majorana based qubits against decoherence. *Phys. Rev. B*, 85(12):121405, March 2012.

[52] E. T. Campbell, H. Anwar, and D. E. Browne. Magic-State Distillation in All Prime Dimensions Using Quantum Reed-Muller Codes. *Phys. Rev. X*, 2(4):041021, October 2012.

[53] Earl T. Campbell and Mark Howard. Unified framework for magic state distillation and multiqubit gate synthesis with reduced resource cost. *Phys. Rev. A*, 95:022316, Feb 2017.

[54] J. Cardy. Boundary Conformal Field Theory. November 2004.

[55] C. Cesare, A. J. Landahl, D. Bacon, S. T. Flammia, and A. Neels. Adiabatic topological quantum computing. *Phys. Rev. A*, 92(1):012336, July 2015.

[56] Christopher Chamberland and Michael E. Beverland. Flag fault-tolerant error correction with arbitrary distance codes. *Quantum*, 2:53, February 2018.

[57] W. Chang, S. M. Albrecht, T. S. Jespersen, F. Kuemmeth, P. Krogstrup, J. Nygård, and C. M. Marcus. Hard Gap in Epitaxial Superconductor-Semiconductor Nanowires. *Nature Nanotechnology*, 10:232, November 2015.

[58] Rui Chao and Ben W. Reichardt. Fault-tolerant quantum computation with few qubits. *npj Quantum Information*, 4:42, Sep 2018.

[59] M. Cheng, V. Galitski, and S. Das Sarma. Nonadiabatic effects in the braiding of non-Abelian anyons in topological superconductors. *Phys. Rev. B*, 84(10):104529, September 2011.

[60] M. Cheng, R. M. Lutchyn, V. Galitski, and S. Das Sarma. Tunneling of anyonic Majorana excitations in topological superconductors. *Phys. Rev. B*, 82(9):094504, September 2010.

[61] Meng Cheng, Roman M. Lutchyn, Victor Galitski, and S. Das Sarma. Splitting of majorana-fermion modes due to intervortex tunneling in a p_x+ip_y superconductor. *Phys. Rev. Lett.*, 103:107001, Aug 2009.

[62] Meng Cheng and Hong-Hao Tu. Majorana edge states in interacting two-chain ladders of fermions. *Phys. Rev. B*, 84:094503, Sep 2011.

[63] Meng Cheng, Michael Zaletel, Maissam Barkeshli, Ashvin Vishwanath, and Parsa Bonderson. Translational symmetry and microscopic constraints on symmetry-enriched topological phases: A view from the surface. *Phys. Rev. X*, 6:041068, Dec 2016.

[64] C.-K. Chiu, J. D. Sau, and S. Das Sarma. Conductance of a superconducting Coulomb blockaded Majorana nanowire. February 2017.

[65] H. O. H. Churchill, V. Fatemi, K. Grove-Rasmussen, M. T. Deng, P. Caroff, H. Q. Xu, and C. M. Marcus. Superconductor-nanowire devices from tunneling to the multichannel regime: Zero-bias oscillations and magnetoconductance crossover. *Phys. Rev. B*, 87(24):241401, June 2013.

[66] D. J. Clarke, J. D. Sau, and S. Das Sarma. A Practical Phase Gate for Producing Bell Violations in Majorana Wires. *Phys. Rev. X*, 6(2):021005, April 2016.

[67] D. J. Clarke and K. Shtengel. Improved phase-gate reliability in systems with neutral Ising anyons. *Phys. Rev. B*, 82(18):180519, November 2010.

[68] A. A. Clerk, M. H. Devoret, S. M. Girvin, Florian Marquardt, and R. J. Schoelkopf. Introduction to quantum noise, measurement, and amplification. *Rev. Mod. Phys.*, 82(2):1155, April 2010.

[69] William S. Cole, Jay D. Sau, and S. Das Sarma. Proximity effect and Majorana bound states in clean semiconductor nanowires coupled to disordered superconductors. *Phys. Rev. B*, 94(14):140505, Oct 2016.

[70] J. I. Colless, A. C. Mahoney, J. M. Hornibrook, A. C. Doherty, H. Lu, A. C. Gossard, and D. J. Reilly. Dispersive Readout of a Few-Electron Double Quantum Dot with Fast rf Gate Sensors. *Phys. Rev. Lett.*, 110(4):046805, January 2013.

[71] I. Cong, M. Cheng, and Z. Wang. On Defects Between Gapped Boundaries in Two-Dimensional Topological Phases of Matter. *Phys. Rev. B*, 96:195129, 2017.

[72] Andrew W. Cross, David P. Divincenzo, and Barbara M. Terhal. A comparative code study for quantum fault tolerance. *Quantum Info. Comput.*, 9(7):541–572, July 2009.

[73] Łukasz Cywiński, Roman M. Lutchyn, Cody P. Nave, and S. Das Sarma. How to enhance dephasing time in superconducting qubits. *Phys. Rev. B*, 77:174509, May 2008.

[74] A. Das, Y. Ronen, Y. Most, Y. Oreg, M. Heiblum, and H. Shtrikman. Zero-bias peaks and splitting in an Al-InAs nanowire topological superconductor as a signature of Majorana fermions. *Nat. Phys.*, 8:887, 2012.

[75] S. Das Sarma, M. Freedman, and C. Nayak. Majorana zero modes and topological quantum computation. *NPJ Quantum Information*, 1(15001), 2015.

[76] S. Das Sarma, Jay D. Sau, and Tudor D. Stanescu. Splitting of the zero-bias conductance peak as smoking gun evidence for the existence of the majorana mode in a superconductor-semiconductor nanowire. *Phys. Rev. B*, 86:220506, Dec 2012.

[77] G. de Lange, B. van Heck, A. Bruno, D. J. van Woerkom, A. Geresdi, S. R. Plissard, E. P. A. M. Bakkers, A. R. Akhmerov, and L. DiCarlo. Realization of Microwave Quantum Circuits Using Hybrid Superconducting-Semiconducting Nanowire Josephson Elements. *Phys. Rev. Lett.*, 115(12):127002, September 2015.

[78] M. T. Deng, S. Vaitieknas, E. B. Hansen, J. Danon, M. Leijnse, K. Flensberg, J. Nygrd, P. Krogstrup, and C. M. Marcus. Majorana bound state in a coupled quantum-dot hybrid-nanowire system. *Science*, 354(6319):1557, December 2016.

[79] M. T. Deng, C. L. Yu, G. Y. Huang, M. Larsson, P. Caroff, and H. Q. Xu. Anomalous zero-bias conductance peak in a nb–insb nanowire–nb hybrid device. *Nano Lett.*, 12(12):6414, 2012.

[80] M. T. Deng, C. L. Yu, G. Y. Huang, M. Larsson, P. Caroff, and H. Q. Xu. Parity independence of the zero-bias conductance peak in a nanowire based topological superconductor-quantum dot hybrid device. *Scientific Reports*, 4:7261, 2014.

[81] S. Deser, R. Jackiw, and S. Templeton. Three-dimensional massive gauge theories. *Phys. Rev. Lett.*, 48(15):975–978, Apr 1982.

[82] M. Dolev, M. Heiblum, V. Umansky, A. Stern, and D. Mahalu. Observation of a quarter of an electron charge at the $\nu = 5/2$ quantum Hall state. *Nature*, 452:829–834, April 2008.

[83] Fernando Domnguez, Jorge Cayao, Pablo San-Jose, Ramn Aguado, Alfredo Levy Yeyati, and Elsa Prada. Zero-energy pinning from interactions in Majorana nanowires. *NPJ Quant. Mat.*, 2(1):13, March 2017.

[84] Y. Dovzhenko, J. Stehlik, K. D. Petersson, J. R. Petta, H. Lu, and A. C. Gossard. Nonadiabatic quantum control of a semiconductor charge qubit. *Phys. Rev. B*, 84:161302, Oct 2011.

[85] G. Duclos-Cianci and K. M. Svore. Distillation of nonstabilizer states for universal quantum computation. *Phys. Rev. A*, 88(4):042325, October 2013.

[86] T. Duty, G. Johansson, K. Bladh, D. Gunnarsson, C. Wilson, and P. Delsing. Observation of Quantum Capacitance in the Cooper-Pair Transistor. *Phys. Rev. Lett.*, 95(20):206807, November 2005.

[87] Dominic V. Else and Ryan Thorngren. Crystalline topological phases as defect networks. *Phys. Rev. B*, 99(11):115116, Mar 2019.

[88] V. J. Emery, S. A. Kivelson, and O. Zachar. Classification and stability of phases of the multicomponent one-dimensional electron gas. *Phys. Rev. B*, 59:15641, June 1999.

[89] P. Fendley, M. P. A. Fisher, and C. Nayak. Topological Entanglement Entropy from the Holographic Partition Function. *Journal of Statistical Physics*, 126:1111–1144, March 2007.

[90] P. Fendley, M. P. A. Fisher, and C. Nayak. Boundary conformal field theory and tunneling of edge quasiparticles in non-Abelian topological states. *Ann. Phys.*, 324:1547–1572, July 2009.

[91] R. P. Feynman. Simulating physics with computers. *International Journal of Theoretical Physics*, 21:467, 1982.

[92] L. Fidkowski and A. Kitaev. Topological phases of fermions in one dimension. *Phys. Rev. B*, 83(7):075103, February 2011.

[93] L. Fidkowski, R. M. Lutchyn, C. Nayak, and M. P. A. Fisher. Majorana zero modes in one-dimensional quantum wires without long-ranged superconducting order. *Phys. Rev. B*, 84(19):195436, November 2011.

[94] Lukasz Fidkowski, Jason Alicea, Netanel H. Lindner, Roman M. Lutchyn, and Matthew P. A. Fisher. Universal transport signatures of majorana fermions in superconductor-luttinger liquid junctions. *Phys. Rev. B*, 85:245121, Jun 2012.

[95] A. D. K. Finck, D. J. Van Harlingen, P. K. Mohseni, K. Jung, and X. Li. Anomalous Modulation of a Zero-Bias Peak in a Hybrid Nanowire-Superconductor Device. *Phys. Rev. Lett.*, 110:126406, Mar 2013.

[96] K. Flensberg. Non-Abelian Operations on Majorana Fermions via Single-Charge Control. *Phys. Rev. Lett.*, 106(9):090503, March 2011.

[97] Karsten Flensberg. Tunneling characteristics of a chain of majorana bound states. *Phys. Rev. B*, 82:180516, Nov 2010.

[98] C. Forsythe, X. Zhou, T. Taniguchi, K. Watanabe, A. Pasupathy, P. Moon, M. Koshino, P. Kim, and C. R. Dean. Band structure engineering of 2D materials using patterned dielectric superlattices. *Nature Nanotechnology*, 13:566–571, July 2018.

[99] Austin G. Fowler, Ashley M. Stephens, and Peter Groszkowski. High-threshold universal quantum computation on the surface code. *Phys. Rev. A*, 80:052312, Nov 2009.

[100] E. Fradkin, C. Nayak, A. Tsvelik, and F. Wilczek. A Chern-Simons effective field theory for the Pfaffian quantum Hall state. *Nucl. Phys. B*, 516(3):704, 1998.

[101] M. Freedman, M. B. Hastings, C. Nayak, X.-L. Qi, K. Walker, and Z. Wang. Projective ribbon permutation statistics: A remnant of non-Abelian braiding in higher dimensions. *Phys. Rev. B*, 83(11):115132, March 2011.

[102] L. Fu. Electron Teleportation via Majorana Bound States in a Mesoscopic Superconductor. *Phys. Rev. Lett.*, 104(5):056402, February 2010.

[103] L. Fu and C. L. Kane. Superconducting Proximity Effect and Majorana Fermions at the Surface of a Topological Insulator. *Phys. Rev. Lett.*, 100(9):096407, March 2008.

[104] Suhas Gangadharaiah, Bernd Braunecker, Pascal Simon, and Daniel Loss. Majorana Edge States in Interacting One-Dimensional Systems. *Phys. Rev. Lett.*, 107(3):036801, Jul 2011.

[105] L.M. Garrido and F.J. Sancho. Degree of approximate validity of the adiabatic invariance in quantum mechanics. *Physica*, 28(6):553–560, 1962.

[106] Sasa Gazibegovic, Diana Car, Hao Zhang, Stijn C. Balk, John A. Logan, Michiel W. A. de Moor, Maja C. Cassidy, Rudi Schmits, Di Xu, Guanzhong Wang, Peter Krogstrup, Roy L. M. Op Het Veld, Kun Zuo, Yoram Vos, Jie Shen, Daniël Bouman, Borzoyeh Shojaei, Daniel Pennachio, Joon Sue Lee, Petrus J. van Veldhoven, Sebastian Koelling, Marcel A. Verheijen, Leo P. Kouwenhoven, Chris J. Palmstrøm, and Erik P. A. M. Bakkers. Epitaxy of advanced nanowire quantum devices. *Nature*, 548(7668):434–438, Aug 2017.

[107] T. Giamarchi. *Quantum Physics in One Dimension*. Clarendon Press, 10th edition, 2004.

[108] G. Goldstein and C. Chamon. Decay rates for topological memories encoded with Majorana fermions. *Phys. Rev. B*, 84(20):205109, November 2011.

[109] D. Gottesman. *Stabilizer codes and quantum error correction*. PhD thesis, California Institute of Technology, 1997.

[110] D. Gottesman. The Heisenberg Representation of Quantum Computers. July 1998.

[111] D. Gottesman. Theory of fault-tolerant quantum computation. *Phys. Rev. A*, 57(1):127, Jan 1998.

[112] D. Gottesman. An Introduction to Quantum Error Correction and Fault-Tolerant Quantum Computation. April 2009.

[113] Önder Gül, Hao Zhang, Jouri D. S. Bommer, Michiel W. A. de Moor, Diana Car, Sébastien R. Plissard, Erik P. A. M. Bakkers, Attila Geresdi, Kenji Watanabe, Takashi Taniguchi, and Leo P. Kouwenhoven. Ballistic Majorana nanowire devices. *Nature Nanotechnology*, 13:192–197, 2018.

[114] Önder Gül, Hao Zhang, Jouri D. S. Bommer, Michiel W. A. de Moor, Diana Car, Sébastien R. Plissard, Erik P. A. M. Bakkers, Attila Geresdi, Kenji Watanabe, Takashi Taniguchi, and Leo P. Kouwenhoven. Ballistic Majorana nanowire devices. *Nature Nanotechnology*, 2018.

[115] F. D. M. Haldane. Model for a quantum hall effect without landau levels: Condensed-matter realization of the "parity anomaly". *Phys. Rev. Lett.*, 61:2015–2018, Oct 1988.

[116] B. I. Halperin, Y. Oreg, A. Stern, G. Refael, J. Alicea, and F. von Oppen. Adiabatic manipulations of Majorana fermions in a three-dimensional network of quantum wires. *Phys. Rev. B*, 85(14):144501, April 2012.

[117] F. Harper, S. H. Simon, and R. Roy. Perturbative approach to flat Chern bands in the Hofstadter model. *Phys. Rev. B*, 90(7):075104, August 2014.

[118] P G Harper. The general motion of conduction electrons in a uniform magnetic field, with application to the diamagnetism of metals. *Proceedings of the Physical Society. Section A*, 68(10):879, 1955.

[119] J. W. Harrington. *Analysis of quantum error-correcting codes: Symplectic lattice codes and toric codes*. PhD thesis, California Institute of Technology, 2004.

[120] F. Hassler, A. R. Akhmerov, and C. W. J. Beenakker. The top-transmon: a hybrid superconducting qubit for parity-protected quantum computation. *New J. Phys.*, 13(9):095004, September 2011.

[121] F. Hassler, A. R. Akhmerov, C.-Y. Hou, and C. W. J. Beenakker. Anyonic interferometry without anyons: how a flux qubit can read out a topological qubit. *New J. Phys.*, 12(12):125002, December 2010.

[122] M. B. Hastings. Small Majorana Fermion Codes. March 2017.

[123] M. Hell, J. Danon, K. Flensberg, and M. Leijnse. Time scales for Majorana manipulation using Coulomb blockade in gate-controlled superconducting nanowires. *Phys. Rev. B*, 94(3):035424, July 2016.

[124] T. Hensgens, U. Mukhopadhyay, P. Barthelemy, S. Fallahi, G. C. Gardner, C. Reichl, W. Wegscheider, M. J. Manfra, and L. M. K. Vandersypen. Capacitance spectroscopy of gate-defined electronic lattices. September 2017.

[125] A. P. Higginbotham, S. M. Albrecht, G. Kirsanskas, W. Chang, F. Kuemmeth, P. Krogstrup, T. S. Jespersen, J. Nygard, K. Flensberg, and C. M. Marcus. Parity lifetime of bound states in a proximitized semiconductor nanowire. *Nature Physics*, 11:1017, January 2015.

[126] S. Hoffman, C. Schrade, J. Klinovaja, and D. Loss. Universal quantum computation with hybrid spin-majorana qubits. *Phys. Rev. B*, 94:045316, Jul 2016.

[127] Douglas R. Hofstadter. Energy levels and wave functions of bloch electrons in rational and irrational magnetic fields. *Phys. Rev. B*, 14:2239–2249, Sep 1976.

[128] Ying Hu, Zi Cai, Mikhail A. Baranov, and Peter Zoller. Majorana fermions in noisy Kitaev wires. *Phys. Rev. B*, 92(16):165118, 2015.

[129] T. Hyart, B. van Heck, I. C. Fulga, M. Burrello, A. R. Akhmerov, and C. W. J. Beenakker. Flux-controlled quantum computation with Majorana fermions. *Phys. Rev. B*, 88(3):035121, July 2013.

[130] Matteo Ippoliti, Meng Cheng, and Michael P. Zaletel. *to appear*, 2018.

[131] Matteo Ippoliti, Matteo Rizzi, Vittorio Giovannetti, and Leonardo Mazza. Quantum memories with zero-energy majorana modes and experimental constraints. *Phys. Rev. A*, 93:062325, Jun 2016.

[132] D. A. Ivanov. Non-abelian statistics of half-quantum vortices in p-wave superconductors. *Phys. Rev. Lett.*, 86:268–271, Jan 2001.

[133] L. Jiang, C. L. Kane, and J. Preskill. Interface between Topological and Superconducting Qubits. *Phys. Rev. Lett.*, 106(13):130504, April 2011.

[134] A. Joye and C. . Pfister. Exponential Estimates in Adiabatic Quantum Evolution, July 1998.

[135] A. Joye and C. Pfister. Exponentially small adiabatic invariant for the Schrodinger eqn. *Commun. Math. Phys.*, 140:15–41, 1991.

[136] A. Joye and C. Pfister. Full asymptotic expansion of transition probabilities in the adiabatic limit. *J. Phys. A: Math. Gen*, 24:753–766, 1991.

[137] T. Karzig, Y. Oreg, G. Refael, and M. H. Freedman. Universal Geometric Path to a Robust Majorana Magic Gate. *Phys. Rev. X*, 6(3):031019, July 2016.

[138] T. Karzig, F. Pientka, G. Refael, and F. von Oppen. Shortcuts to non-Abelian braiding. *Phys. Rev. B*, 91(20):201102, May 2015.

[139] T. Karzig, A. Rahmani, F. von Oppen, and G. Refael. Optimal control of Majorana zero modes. *Phys. Rev. B*, 91(20):201404, May 2015.

[140] T. Karzig, G. Refael, and F. von Oppen. Boosting Majorana Zero Modes. *Phys. Rev. X*, 3(4):041017, October 2013.

[141] Torsten Karzig, Christina Knapp, Roman M. Lutchyn, Parsa Bonderson, Matthew B. Hastings, Chetan Nayak, Jason Alicea, Karsten Flensberg, Stephan Plugge, Yuval Oreg, Charles M. Marcus, and Michael H. Freedman. Scalable designs for quasiparticle-poisoning-protected topological quantum computation with Majorana zero modes. *Phys. Rev. B*, 95(23):235305, June 2017.

[142] Torsten Karzig, Yuval Oreg, Gil Refael, and Michael H. Freedman. Robust Majorana magic gates via measurements. page arXiv:1812.10498, Dec 2018.

[143] Ivan Kassal, James D. Whitfield, Alejandro Perdomo-Ortiz, Man-Hong Yung, and Aln Aspuru-Guzik. Simulating chemistry using quantum computers. *Annual Review of Physical Chemistry*, 62(1):185–207, 2011. PMID: 21166541.

[144] G. Kells, D. Meidan, and P. W. Brouwer. Near-zero-energy end states in topologically trivial spin-orbit coupled superconducting nanowires with a smooth confinement. *Phys. Rev. B*, 86(10):100503, Sep 2012.

[145] V. Khemani, R. Nandkishore, and S. L. Sondhi. Nonlocal adiabatic response of a localized system to local manipulations. *Nature Physics*, 11:560–565, July 2015.

[146] A. Y. Kitaev. Unpaired majorana fermions in quantum wires. *Phys. Usp.*, 44:131, October 2001.

[147] A. Y. Kitaev. Fault-tolerant quantum computation by anyons. *Ann. Phys.*, 303:2, January 2003.

[148] Alexei Kitaev. Anyons in an exactly solved model and beyond. *Ann. Phys.*, 321(1):2–111, Jan 2006.

[149] Alexei Kitaev and John Preskill. Topological entanglement entropy. *Phys. Rev. Lett.*, 96:110404, 2006.

[150] Morten Kjaergaard, Konrad Wölms, and Karsten Flensberg. Majorana fermions in superconducting nanowires without spin-orbit coupling. *Phys. Rev. B*, 85:020503, Jan 2012.

[151] C. Knapp, T. Karzig, R. M. Lutchyn, and C. Nayak. Dephasing of Majorana-based qubits. *Phys. Rev. B*, 97(12):125404, March 2018.

[152] Christina Knapp, Michael Beverland, Dmitry I. Pikulin, and Torsten Karzig. Modeling noise and error correction for Majorana-based quantum computing. *Quantum*, 2:88, Jun 2018.

[153] Christina Knapp, Michael Zaletel, Dong E. Liu, Meng Cheng, Parsa Bonderson, and Chetan Nayak. The nature and correction of diabatic errors in anyon braiding. *Phys. Rev. X*, 6:041003, Oct 2016.

[154] E. Knill. Quantum computing with realistically noisy devices. *Nature*, 434:39, 2005.

[155] Jens Koch, Terri M. Yu, Jay Gambetta, A. A. Houck, D. I. Schuster, J. Majer, Alexandre Blais, M. H. Devoret, S. M. Girvin, and R. J. Schoelkopf. Charge-insensitive qubit design derived from the cooper pair box. *Phys. Rev. A*, 76:042319, Oct 2007.

[156] D. W. Kribs, R. Laflamme, D. Poulin, and M. Lesosky. Operator quantum error correction. April 2005.

[157] P. Krogstrup, N. L. B. Ziino, W. Chang, S. M. Albrecht, M. H. Madsen, E. Johnson, J. Nygård, C. M. Marcus, and T. S. Jespersen. Epitaxy of semiconductor–superconductor nanowires. *Nature Mater.*, 14(4):400, 2015.

[158] L. A. Landau, S. Plugge, E. Sela, A. Altland, S. M. Albrecht, and R. Egger. Towards Realistic Implementations of a Majorana Surface Code. *Phys. Rev. Lett.*, 116(5):050501, February 2016.

[159] Lev Landau. Zur theorie der energieubertragung. ii. *Physikalische Zeitschrift der Sowjetunion*, 2:4651, 1932.

[160] T. W. Larsen, K. D. Petersson, F. Kuemmeth, T. S. Jespersen, P. Krogstrup, J. Nygârd, and C. M. Marcus. Semiconductor-Nanowire-Based Superconducting Qubit. *Phys. Rev. Lett.*, 115(12):127001, September 2015.

[161] R.B. Laughlin. Anomalous quantum Hall effect: An incompressible quantum fluid with fractional excitations. *Phys. Rev. Lett.*, 50:1395, 1983.

[162] K. T. Law, Patrick A. Lee, and T. K. Ng. Majorana fermion induced resonant andreev reflection. *Phys. Rev. Lett.*, 103:237001, Dec 2009.

[163] Eduardo J. H. Lee, Xiaocheng Jiang, Manuel Houzet, Ramón Aguado, Charles M. Lieber, and Silvano de Franceschi. Spin-resolved Andreev levels and parity crossings in hybrid superconductor-semiconductor nanostructures. *Nature Nanotechnology*, 9(1):79–84, Jan 2014.

[164] K. W. Lehnert, B. A. Turek, K. Bladh, L. F. Spietz, D. Gunnarsson, P. Delsing, and R. J. Schoelkopf. Quantum charge fluctuations and the polarizability of the single-electron box. *Phys. Rev. Lett.*, 91:106801, Sep 2003.

[165] M. Leijnse and K. Flensberg. Introduction to topological superconductivity and Majorana fermions. *Semiconductor Science Technology*, 27(12):124003, December 2012.

[166] Michael Levin and Xiao-Gang Wen. Detecting topological order in a ground state wave function. *Phys. Rev. Lett.*, 96:110405, 2006.

[167] Y. Li. Fault-tolerant fermionic quantum computation based on color code. *Phys. Rev. A*, 98(1):012336, July 2018.

[168] Ying Li. Noise threshold and resource cost of fault-tolerant quantum computing with majorana fermions in hybrid systems. *Phys. Rev. Lett.*, 117:120403, Sep 2016.

[169] D. A. Lidar, A. T. Rezakhani, and A. Hamma. Adiabatic approximation with exponential accuracy for many-body systems and quantum computation. *Journal of Mathematical Physics*, 50(10):102106, October 2009.

[170] C.-H. Lin, J. D. Sau, and S. Das Sarma. Zero-bias conductance peak in Majorana wires made of semiconductor/superconductor hybrid structures. *Phys. Rev. B*, 86(22):224511, December 2012.

[171] H.-H. Lin, L. Balents, and M. P. A. Fisher. N-chain Hubbard model in weak coupling. *Phys. Rev. B*, 56:6569, September 1997.

[172] Yiruo Lin and Anthony J. Leggett. Effect of Particle Number Conservation on the Berry Phase Resulting from Transport of a Bound Quasiparticle around a Superfluid Vortex. Aug 2017.

[173] Yiruo Lin and Anthony J. Leggett. Towards a Particle-Number Conserving Theory of Majorana Zero Modes in p+ip Superfluids. Mar 2018.

[174] D. Litinski and F. von Oppen. Braiding by Majorana tracking and long-range CNOT gates with color codes. *Phys. Rev. B*, 96(20):205413, November 2017.

[175] Daniel Litinski, Markus S. Kesselring, Jens Eisert, and Felix von Oppen. Combining Topological Hardware and Topological Software: Color-Code Quantum Computing with Topological Superconductor Networks. *Phys. Rev. X*, 7(3):031048, September 2017.

[176] Daniel Litinski and Felix von Oppen. Quantum computing with Majorana fermion codes. *Phys. Rev. B*, 97(20):205404, May 2018.

[177] Chun-Xiao Liu, Jay D. Sau, Tudor D. Stanescu, and S. Das Sarma. Andreev bound states versus majorana bound states in quantum dot-nanowire-superconductor hybrid structures: Trivial versus topological zero-bias conductance peaks. *Phys. Rev. B*, 96:075161, Aug 2017.

[178] Chun-Xiao Liu, F. Setiawan, Jay D. Sau, and S. Das Sarma. Phenomenology of the soft gap, zero-bias peak, and zero-mode splitting in ideal majorana nanowires. *Phys. Rev. B*, 96:054520, Aug 2017.

[179] R. M. Lutchyn, E. P. A. M. Bakkers, L. P. Kouwenhoven, P. Krogstrup, C. M. Marcus, and Y. Oreg. Majorana zero modes in superconductor-semiconductor heterostructures. *Nature Reviews Materials*, 3:52–68, May 2018.

[180] R. M. Lutchyn and L. I. Glazman. Kinetics of quasiparticle trapping in a Cooper-pair box. *Phys. Rev. B*, 75(18):184520, May 2007.

[181] R. M. Lutchyn, J. D. Sau, and S. Das Sarma. Majorana Fermions and a Topological Phase Transition in Semiconductor-Superconductor Heterostructures. *Phys. Rev. Lett.*, 105(7):077001, August 2010.

[182] Roman M. Lutchyn, Georg W. Winkler, Bernard van Heck, Torsten Karzig, Karsten Flensberg, Leonid I. Glazman, and Chetan Nayak. Topological superconductivity in full shell proximitized nanowires. *arXiv e-prints*, Sep 2018.

[183] O. Madelung. *Semiconductors: Data Handbook*. Springer, Berlin, 2004.

[184] J. Majer, J. M. Chow, J. M. Gambetta, J. Koch, B. R. Johnson, J. A. Schreier, L. Frunzio, D. I. Schuster, A. A. Houck, A. Wallraff, A. Blais, M. H. Devoret, S. M. Girvin, and R. J. Schoelkopf. Coupling superconducting qubits via a cavity bus. *Nature*, 449:443, September 2007.

[185] J. M. Martinis and M. R. Geller. Fast adiabatic qubit gates using only σ_z control. *Phys. Rev. A*, 90(2):022307, August 2014.

[186] L. Mazza, M. Rizzi, M. D. Lukin, and J. I. Cirac. Robustness of quantum memories based on Majorana zero modes. *Phys. Rev. B*, 88(20):205142, 2013.

[187] Michaël Mignard and Peter Schauenburg. Modular categories are not determined by their modular data. Aug 2017.

[188] C. Moore and M. Nilsson. Parallel Quantum Computation and Quantum Codes. *eprint arXiv:quant-ph/9808027*, August 1998.

[189] G. Moore and N. Read. Nonabelions in the fractional quantum hall effect. *Nuclear Physics B*, 360:362, 1991.

[190] V. Mourik, K. Zuo, S. M. Frolov, S. R. Plissard, E. P. A. M. Bakkers, and L. P. Kouwenhoven. Signatures of Majorana fermions in hybrid superconductor-semiconductor nanowire devices. *Science*, 336:1003, 2012.

[191] Stevan Nadj-Perge, Ilya K. Drozdov, Jian Li, Hua Chen, Sangjun Jeon, Jungpil Seo, Allan H. MacDonald, B. Andrei Bernevig, and Ali Yazdani. Observation of majorana fermions in ferromagnetic atomic chains on a superconductor. *Science*, 346(6209):602–607, 2014.

[192] Y. Nakamura, Y. A. Pashkin, T. Yamamoto, and J. S. Tsai. Charge Echo in a Cooper-Pair Box. *Phys. Rev. Lett.*, 88(4):047901, January 2002.

[193] C. Nayak, S. H. Simon, A. Stern, M. Freedman, and S. Das Sarma. Non-Abelian anyons and topological quantum computation. *Rev. Mod. Phys.*, 80:1083, July 2008.

[194] G. Nebe, E. M. Rains, and N. J. A. Sloane. The invariants of the Clifford groups, January 2000.

[195] G. Nebe, E. M. Rains, and N. J. A. Sloane. *Self-Dual Codes and Invariant Theory*. Springer-Verlag Berlin Heidelberg, 2006.

[196] G Nenciu. Linear Adiabatic Theory. Exponential Estimates. *Commun. Math. Phys.*, 152:479–496, 1993.

[197] F. Nichele, A. C. C. Drachmann, A. M. Whiticar, E. C. T. O'Farrell, H. J. Suominen, A. Fornieri, T. Wang, G. C. Gardner, C. Thomas, A. T. Hatke, P. Krogstrup, M. J. Manfra, K. Flensberg, and C. M. Marcus. Scaling of Majorana Zero-Bias Conductance Peaks. *Phys. Rev. Lett.*, 119(13):136803, September 2017.

[198] Michael A. Nielsen and Isaac L. Chuang. *Quantum Computation and Quantum Information: 10th Anniversary Edition*. Cambridge University Press, New York, NY, USA, 10th edition, 2011.

[199] B. Nijholt and A. R. Akhmerov. Orbital effect of magnetic field on the Majorana phase diagram. *Phys. Rev. B*, 93(23):235434, June 2016.

[200] Y. Oreg, G. Refael, and F. von Oppen. Helical Liquids and Majorana Bound States in Quantum Wires. *Phys. Rev. Lett.*, 105(17):177002, October 2010.

[201] T. Ota, T. Hayashi, K. Muraki, and T. Fujisawa. Wide-band capacitance measurement on a semiconductor double quantum dot for studying tunneling dynamics. *App. Phys. Lett.*, 96(3):032104, January 2010.

[202] E. Paladino, Y. M. Galperin, G. Falci, and B. L. Altshuler. 1/f noise: Implications for solid-state quantum information. *Rev. Mod. Phys.*, 86:361, April 2014.

[203] Fabio L. Pedrocchi, N. E. Bonesteel, and David P. DiVincenzo. Monte Carlo studies of the self-correcting properties of the Majorana quantum error correction code under braiding. *Phys. Rev. B*, 92(11):115441, 2015.

[204] K. D. Petersson, J. R. Petta, H. Lu, and A. C. Gossard. Quantum coherence in a one-electron semiconductor charge qubit. *Phys. Rev. Lett.*, 105:246804, Dec 2010.

[205] J. R. Petta, A. C. Johnson, C. M. Marcus, M. P. Hanson, and A. C. Gossard. Manipulation of a single charge in a double quantum dot. *Phys. Rev. Lett.*, 93:186802, Oct 2004.

[206] Falko Pientka, Anna Keselman, Erez Berg, Amir Yacoby, Ady Stern, and Bertrand I. Halperin. Topological superconductivity in a planar josephson junction. *Phys. Rev. X*, 7:021032, May 2017.

[207] S. Plugge, L. A. Landau, E. Sela, A. Altland, K. Flensberg, and R. Egger. Roadmap to Majorana surface codes. *Phys. Rev. B*, 94(17):174514, November 2016.

[208] S. Plugge, A. Rasmussen, R. Egger, and K. Flensberg. Majorana box qubits. *New J. Phys.*, 19(1):012001, January 2017.

[209] David Poulin. Stabilizer formalism for operator quantum error correction. *Phys. Rev. Lett.*, 95:230504, Dec 2005.

[210] E. Prada, P. San-Jose, and R. Aguado. Transport spectroscopy of NS nanowire junctions with Majorana fermions. *Phys. Rev. B*, 86(18):180503, November 2012.

[211] R.E. Prange and S.M. Girvin. *The Quantum Hall Effect*. Springer-Verlag, New York, 1987.

[212] J. Preskill. Lecture notes for physics 219:quantum computation. available at http://www.theory.caltech.edu/∼preskill/ph219/ph219_2004.html, 2004.

[213] X.-L. Qi. Generic Wave-Function Description of Fractional Quantum Anomalous Hall States and Fractional Topological Insulators. *Phys. Rev. Lett.*, 107(12):126803, September 2011.

[214] Iuliana P. Radu, J. B. Miller, C. M. Marcus, M. A. Kastner, L. N. Pfeiffer, and K. W. West. Quasi-particle properties from tunneling in the $\nu = 5/2$ fractional quantum hall state. *Science*, 2008.

[215] D. Rainis, L. Trifunovic, J. Klinovaja, and D. Loss. Towards a realistic transport modeling in a superconducting nanowire with Majorana fermions. *Phys. Rev. B*, 87(2):024515, January 2013.

[216] Diego Rainis and Daniel Loss. Majorana qubit decoherence by quasiparticle poisoning. *Phys. Rev. B*, 85(17):174533, May 2012.

[217] R. Raussendorf and J. Harrington. Fault-Tolerant Quantum Computation with High Threshold in Two Dimensions. *Phys. Rev. Lett.*, 98(19):190504, May 2007.

[218] N. Read and D. Green. Paired states of fermions in two dimensions with breaking of parity and time-reversal symmetries and the fractional quantum Hall effect. *Phys. Rev. B*, 61:10267, April 2000.

[219] D. J. Reilly, C. M. Marcus, M. P. Hanson, and A. C. Gossard. Fast single-charge sensing with a rf quantum point contact. *App. Phys. Lett.*, 91(16):162101, 2007.

[220] L. P. Rokhinson, X. Liu, and J. K. Furdyna. The fractional a.c. Josephson effect in a semiconductor-superconductor nanowire as a signature of Majorana particles. *Nat. Phys.*, 8:795, 2012.

[221] Eric C. Rowell and Zhenghan Wang. Localization of Unitary Braid Group Representations. *Communications in Mathematical Physics*, 311(3):595–615, May 2012.

[222] Michael Ruby, Falko Pientka, Yang Peng, Felix von Oppen, Benjamin W. Heinrich, and Katharina J. Franke. End States and Subgap Structure in Proximity-Coupled Chains of Magnetic Adatoms. *Phys. Rev. Lett.*, 115(19):197204, Nov 2015.

[223] Daniel Sank. *Fast, Accurate State Measurement in Superconducting Qubits*. PhD thesis, University of California, Santa Barbara, 9 2014.

[224] J. D. Sau, R. M. Lutchyn, S. Tewari, and S. Das Sarma. Generic New Platform for Topological Quantum Computation Using Semiconductor Heterostructures. *Phys. Rev. Lett.*, 104(4):040502, January 2010.

[225] J. D. Sau, S. Tewari, R. M. Lutchyn, T. D. Stanescu, and S. Das Sarma. Non-Abelian quantum order in spin-orbit-coupled semiconductors: Search for topological Majorana particles in solid-state systems. *Phys. Rev. B*, 82(21):214509, December 2010.

[226] Jay D. Sau, David J. Clarke, and Sumanta Tewari. Controlling non-abelian statistics of majorana fermions in semiconductor nanowires. *Phys. Rev. B*, 84:094505, Sep 2011.

[227] Jay D. Sau, B. I. Halperin, K. Flensberg, and S. Das Sarma. Number conserving theory for topologically protected degeneracy in one-dimensional fermions. *Phys. Rev. B*, 84:144509, Oct 2011.

[228] Jay D. Sau, Sumanta Tewari, and S. Das Sarma. Universal quantum computation in a semiconductor quantum wire network. *Phys. Rev. A*, 82:052322, Nov 2010.

[229] M. S. Scheurer and A. Shnirman. Nonadiabatic processes in Majorana qubit systems. *Phys. Rev. B*, 88(6):064515, August 2013.

[230] Frank Schindler, Ashley M. Cook, Maia G. Vergniory, Zhijun Wang, Stuart S. P. Parkin, B. Andrei Bernevig, and Titus Neupert. Higher-order topological insulators. *Science Advances*, 4(6):0346, Jun 2018.

[231] G. Schön and A. D. Zaikin. Quantum coherent effects, phase transitions, and the dissipative dynamics of ultra small tunnel junctions. *Physics Reports*, 198(5):237, 1990.

[232] K. Sengupta, Igor Žutić, Hyok-Jon Kwon, Victor M. Yakovenko, and S. Das Sarma. Midgap edge states and pairing symmetry of quasi-one-dimensional organic superconductors. *Phys. Rev. B*, 63(14):144531, Apr 2001.

[233] J. Shabani, M. Kjaergaard, H. J. Suominen, Younghyun Kim, F. Nichele, K. Pakrouski, T. Stankevic, R. M. Lutchyn, P. Krogstrup, R. Feidenhans'l, S. Kraemer, C. Nayak, M. Troyer, C. M. Marcus, and C. J. Palmstrøm. Two-dimensional epitaxial superconductor-semiconductor heterostructures: A platform for topological superconducting networks. *Phys. Rev. B*, 93(15):155402, April 2016.

[234] Zhan Shi, C. B. Simmons, Daniel R. Ward, J. R. Prance, R. T. Mohr, Teck Seng Koh, John King Gamble, Xian Wu, D. E. Savage, M. G. Lagally, Mark Friesen, S. N. Coppersmith, and M. A. Eriksson. Coherent quantum oscillations and echo measurements of a si charge qubit. *Phys. Rev. B*, 88:075416, Aug 2013.

[235] P. W. Shor. Fault-tolerant quantum computation. May 1996.

[236] Peter W. Shor. Polynomial-Time Algorithms for Prime Factorization and Discrete Logarithms on a Quantum Computer. *Proc. 35th Annual Symposium on Foundations of Computer Science*, pages 124–134, Aug 1994.

[237] A. A. Soluyanov, D. Gresch, M. Troyer, R. M. Lutchyn, B. Bauer, and C. Nayak. Optimizing spin-orbit splittings in InSb Majorana nanowires. *Phys. Rev. B*, 93(11):115317, March 2016.

[238] E. M. Spanton, A. A. Zibrov, H. Zhou, T. Taniguchi, K. Watanabe, M. P. Zaletel, and A. F. Young. Observation of fractional Chern insulators in a van der Waals heterostructure. *Science*, 360:62–66, April 2018.

[239] T. D. Stanescu, R. M. Lutchyn, and S. Das Sarma. Majorana fermions in semiconductor nanowires. *Phys. Rev. B*, 84(14):144522, October 2011.

[240] T. D. Stanescu, R. M. Lutchyn, and S. Das Sarma. Dimensional crossover in spin-orbit-coupled semiconductor nanowires with induced superconducting pairing. *Phys. Rev. B*, 87(9):094518, March 2013.

[241] T. D. Stanescu and S. Tewari. Majorana fermions in semiconductor nanowires: fundamentals, modeling, and experiment. *Journal of Physics Condensed Matter*, 25(23):233201, June 2013.

[242] Tudor D. Stanescu and Sumanta Tewari. Nonlocality of zero-bias anomalies in the topologically trivial phase of majorana wires. *Phys. Rev. B*, 89:220507, Jun 2014.

[243] A. M. Steane. Active Stabilization, Quantum Computation, and Quantum State Synthesis. *Phys. Rev. Lett.*, 78:2252, March 1997.

[244] A. Stern and B. I. Halperin. Proposed experiments to probe the non-Abelian $\nu = 5/2$ quantum Hall state. *Phys. Rev. Lett.*, 96(1):016802, 2006.

[245] B. M. Terhal. Quantum error correction for quantum memories. *Rev. Mod. Phys.*, 87:307–346, Apr 2015.

[246] B. M. Terhal, F. Hassler, and D. P. DiVincenzo. From majorana fermions to topological order. *Phys. Rev. Lett.*, 108:260504, Jun 2012.

[247] D. J. Thouless, M. Kohmoto, M. P. Nightingale, and M. den Nijs. Quantized hall conductance in a two-dimensional periodic potential. *Phys. Rev. Lett.*, 49:405–408, Aug 1982.

[248] Y. Tomita and K. M. Svore. Low-distance surface codes under realistic quantum noise. *Phys. Rev. A*, 90(6):062320, December 2014.

[249] D.C. Tsui, H.L. Stormer, and A.C. Gossard. Two-dimensional magnetotransport in the extreme quantum limit. *Phys. Rev. Lett.*, 48:1559–1562, 1982.

[250] S. Vaitiekėnas, M. T. Deng, P. Krogstrup, and C. M. Marcus. Flux-induced Majorana modes in full-shell nanowires. *arXiv e-prints*, Sep 2018.

[251] S. Vaitiekėnas, A. M. Whiticar, M. T. Deng, F. Krizek, J. E. Sestoft, C. J. Palmstrøm, S. Marti-Sanchez, J. Arbiol, P. Krogstrup, L. Casparis, and C. M. Marcus. Selective Area Grown Semiconductor-Superconductor Hybrids: A Basis for Topological Networks. *arXiv e-prints*, Feb 2018.

[252] B. van Heck, A. R. Akhmerov, F. Hassler, M. Burrello, and C. W. J. Beenakker. Coulomb-assisted braiding of Majorana fermions in a Josephson junction array. *New J. Phys.*, 14(3):035019, March 2012.

[253] B. van Heck, R. M. Lutchyn, and L. I. Glazman. Conductance of a proximitized nanowire in the coulomb blockade regime. *Phys. Rev. B*, 93:235431, Jun 2016.

[254] S. Vijay and L. Fu. Physical implementation of a Majorana fermion surface code for fault-tolerant quantum computation. *Phys. Scr.*, (1):014002, December 2016.

[255] S. Vijay and L. Fu. Quantum Error Correction for Complex and Majorana Fermion Qubits. March 2017.

[256] S. Vijay, T. H. Hsieh, and L. Fu. Majorana Fermion Surface Code for Universal Quantum Computation. *Phys. Rev. X*, 5(4):041038, October 2015.

[257] G. E. Volovik. Fermion zero modes on vortices in chiral superconductors. *Soviet Journal of Experimental and Theoretical Physics Letters*, 70:609–614, November 1999.

[258] K. von Klitzing, G. Dorda, and M. Pepper. New method for high-accuracy determination of the fine-structure constant based on quantized hall resistance. *Phys. Rev. Lett*, 45, 1980.

[259] A. Vuik, D. Eeltink, A. R. Akhmerov, and M. Wimmer. Effects of the electrostatic environment on the Majorana nanowire devices. *New J. Phys.*, 18(3):033013, 2016.

[260] I. Vurgaftman, J. R. Meyer, and L. R. Ram-Mohan. Band parameters for iiiv compound semiconductors and their alloys. *J. Appl. Phys.*, 89(11):5815–5875, 2001.

[261] David S. Wang, Austin G. Fowler, and Lloyd C. L. Hollenberg. Surface code quantum computing with error rates over 1%. *Phys. Rev. A*, 83:020302, Feb 2011.

[262] Xiao-Gang Wen. Theory of the edge states in fractional quantum hall effects. *International Journal of Modern Physics B*, 06(10):1711–1762, 1992.

[263] N. Wiebe and N. S. Babcock. Improved error-scaling for adiabatic quantum evolutions. *New J. Phys.*, 14(1):013024, January 2012.

[264] F. Wilczek. Fractional statistics and anyon superconductivity. *World Scientific*, 1990.

[265] Frank Wilczek and A. Zee. Appearance of gauge structure in simple dynamical systems. *Phys. Rev. Lett.*, 52:2111–2114, Jun 1984.

[266] R. Willett, J. P. Eisenstein, H. L. Störmer, D. C. Tsui, A. C. Gossard, and J. H. English. Observation of an even-denominator quantum number in the fractional quantum hall effect. *Phys. Rev. Lett.*, 59:1776–1779, Oct 1987.

[267] R. L. Willett, L. N. Pfeiffer, and K. W. West. Alternation and interchange of e/4 and e/2 period interference oscillations consistent with filling factor 5/2 non-abelian quasiparticles. *Phys. Rev. B*, 82:205301, Nov 2010.

[268] G. W. Winkler, Q. Wu, M. Troyer, P. Krogstrup, and A. A. Soluyanov. Topological Phases in $\mathrm{InAs}_{1-x}\mathrm{Sb}_x$: From Novel Topological Semimetal to Majorana Wire. *Phys. Rev. Lett.*, 117(7):076403, August 2016.

[269] Yang-Le Wu, N. Regnault, and B. Andrei Bernevig. Gauge-fixed wannier wave functions for fractional topological insulators. *Phys. Rev. B*, 86:085129, Aug 2012.

[270] Z.-Y. Xue. Measurement based controlled not gate for topological qubits in a majorana fermion quantum-dot hybrid system. *Eur. Phys. J. D*, 67:89, 2013.

[271] S. Yang, Z.-C. Gu, K. Sun, and S. Das Sarma. Topological flat band models with arbitrary Chern numbers. *Phys. Rev. B*, 86(24):241112, December 2012.

[272] Man-Hong Yung, James D. Whitfield, Sergio Boixo, David G. Tempel, and Alán Aspuru-Guzik. Introduction to Quantum Algorithms for Physics and Chemistry. 2012.

[273] Clarence Zener. Non-adiabatic crossing of energy levels. *Proc. R. Soc. Lond A*, 137(833):696–702, 1932.

[274] H. Zhang, C.-X. Liu, S. Gazibegovic, D. Xu, J. A. Logan, G. Wang, N. van Loo, J. D. S. Bommer, M. W. A. de Moor, D. Car, R. L. M. Op Het Veld, P. J. van Veldhoven, S. Koelling, M. A. Verheijen, M. Pendharkar, D. J. Pennachio, B. Shojaei, J. S. Lee, C. J. Palmstrøm, E. P. A. M. Bakkers, S. D. Sarma, and L. P. Kouwenhoven. Quantized Majorana conductance. *Nature*, 556:74–79, April 2018.